An X-ray Bicrystal Truncation Rod Study of a Si Σ13 Symmetric Tilt Grain Boundary and Design and Commissioning of a Holography Endstation at Beamline I06

Thesis submitted for the degree of
Doctor of Philosophy
at the University of Leicester

by

Stephen David Rhead MPhys (Leicester)
Department of Physics and Astronomy
University of Leicester

June 2011

An X-ray Bicrystal Truncation Rod Study of a Si Σ13 Symmetric Tilt Grain Boundary and Design and Commissioning of a Holography Endstation at Beamline I06

Stephen Rhead

Abstract

Naturally occurring grain boundary interfaces greatly influence important characteristics of many materials including their mechanical, electrical and magnetic properties. The atomic structure of such grain boundaries, while crucial to their behaviour, are inaccessible to most experimental techniques as they are internal to the material. Theoretical studies are complicated by the existence of multiple structures for a given grain boundary. Data from an X-ray diffraction experiment is presented, along with the model used for simulated scattering from Keating energy minimised grain boundary structures.

The X-ray diffraction data was measured using a (2+3)-type diffractometer on beamline I07 of the Diamond Light Source. The traditional way to measure the integrated intensity from an X-ray diffraction experiment is to perform a rocking scan. By use of a large 2D area PILATUS detector, an alternative method of measuring diffraction data, where the sample remains fixed, can be implemented. A comparison of the different techniques shows that the stationary scan improves the reliability and shortens the measuring time by almost an order of magnitude.

The theory of crystal truncation rod scattering is extended to account for the bicrystallography of the sample, which gives rise to two overlapping rods; one from each crystal. Simulated X-ray scattering from Keating energy minimised grain

boundaries is compared with experimental data. The simulated scattering, which has atomic sensitivity, is used to discriminate between potential structures based on the statistical goodness of fit with the data.

Finally, a custom designed diffraction chamber was built allowing users to perform lensless Fourier transform holography experiments on the branchline of I06 at the Diamond Light Source. Preliminary data is presented and data analysis techniques discussed. Phase retrieval algorithms do not yield any further high resolution reconstructions due to the noise levels of the hologram.

Acknowledgements

There are many people that have contributed to the work presented here and to my life outside of the university and I wish to take this opportunity to extend my gratitude to all of them.

First, I would like to thank Paul Howes for his excellent supervision. Throughout my PhD he has always given me the freedom and support to develop this thesis and my own research interests. He has always been available to give good advice and his expertise of X-ray diffraction, especially when stuck during the very early hours of the morning at beamlines, has been absolutely vital. I would like to thank Stuart Thornton for his excellent engineering and his designing of the holography chamber; without his input, the project would not have gone anywhere. I extend my thanks to all staff and students of the CMP group for providing advice during my studies and coffee time discussions that were a welcome diversion from work.

I am thankful to all the Diamond Light Source staff and scientists who collaborated with the synchrotron experiments. I am especially grateful to Sarnjeet Dhesi, who not only provided us with in house beam time but whose ideas should lead to some very interesting collaborations.

I would like to thank my parents Barbara and Michael; siblings Peter, Katie and Debbie; Nana Bollington and the rest of my family and friends for their unconditional support. Hopefully this thesis will help explain what I've been doing for the past three and half years and prove I'm not a particle physicist!

Finally, to my fiancé Hazel, the words “thank you” don't do you justice but at least its something tangible! You deserve more gratitude than I can express here for the love and support you've given me and I hope I can make it up to you. This thesis is dedicated to you.

Contents

List of Tables

List of Figures

Chapter 1

Introduction

1.0 Introduction

X-ray diffraction is an important tool for the study of structural properties of crystalline and amorphous materials on the atomic scale. One of the major advantages of X-ray diffraction compared with other techniques is that X-rays interact with matter weakly and a single scattering approach is often sufficient to analyse the diffraction data. The major drawback of the low scattering cross-section is the weak scattering signal, which can be overcome by the brightness (the photon flux per unit phase space volume) of synchrotron radiation.

Synchrotron radiation generated by relativistic electrons in circular accelerators is little more than 60 years old. Third generation synchrotron light sources use an insertion device called an undulator, which consists of a periodic structure of dipole magnets. The static magnetic field alternates along the length of the undulator with a defined periodicity. Electrons traversing the periodic magnet structure are forced to undergo oscillations and thus to radiate energy. The radiation produced in an undulator is very intense and concentrated in narrow energy bands in the spectrum and a large portion of the flux is coherent. The experiments presented in this thesis were performed at such a third generation synchrotron; the Diamond Light Source located at Didcot (UK).

Two diverse, novel X-ray diffraction techniques for probing structure are presented in this thesis. The first is bicrystal truncation rod scattering and the second is lensless Fourier transform holography. As well as high brightness, holography also requires a large coherence length of at least several microns so that each point in the object interferes with the reference source. This coherence length is easily obtainable using undulators.

1.1 Grain Boundaries

Grain boundaries (GBs) in semiconductors have been of interest for some time [1-3] due to the importance of polycrystalline semiconductors in the microelectronic industry and the interest in micromechanical materials, in solar energy applications, and in nanocrystalline Si [4]. The GBs can provide preferential sites for dopants [3, 5, 6], and act as low energy diffusion pathways. For low-energy tilt boundaries, which usually retain the fourfold coordination of the bulk [1, 3], the dominant electronic effects are assumed to be due to dopant segregation to the GB; however, intrinsic gap states localized to the GB may occur if the bonding is sufficiently distorted [2, 3, 7].

Understanding the GBs at an atomic level is therefore crucial. Symmetric tilt GBs have received extensive experimental and theoretical treatment. Experimentally, high resolution transmission microscopy (HRTEM) is widely used in studying GBs [8-11], but the resolution required to examine the atomic structure of the GB is still difficult to achieve. Theoretical studies are complicated by the existence of multiple structures for a given GB [2, 12-15]. First principle calculations are computationally very costly and classical potentials, although fast, need to be checked for their accuracy [2, 12-15].

In this thesis the study of X-ray scattering from the GB of a Si Σ13 bicrystal is presented. X-ray scattering is a powerful, non-destructive probe of surface and interface structures. X-rays have a large penetration depth and can access buried structures that are otherwise inaccessible by standard surface science techniques. Because X-ray scattering is weak, the analysis of X-ray diffraction data is rarely complicated by multiple scattering. X-ray scattering is therefore a suitable method to study buried GBs.

1.2 Lensless Fourier Transform Holography

X-ray microscopy is is an attractive prospect for the study of many nanoscale systems [16-19]. It offers many advantages over other methods including element specific imaging and the ability to non-destructively image the interior of complex structures. It is a promising method of imaging the magnetic structure of thin films when combined with X-ray magnetic circular dichroism, the polarisation dependence of

X-ray scattering at certain absorption edges of magnetic materials.

Direct imaging with X-rays is, however, usually hindered by familiar phase problem and the lack of effective X-ray lenses. In a typical X-ray scattering experiment, a CCD detector measures the scattered intensity in the far-field, Fraunhofer plane but the phase is lost making direct inversion by a Fourier transform impossible. Various holographic techniques offer solutions to this loss of information. Fourier transform holography (FTH) is a lensless technique in which X-rays transmitted through the sample combine with a reference beam to form an interference pattern on the detector [20, 21]. By careful design of a sample mask and spatial separation of the sample aperture and reference pinhole, a direct image can be obtained by the simple application of a Fourier transform to the measured scattering pattern [20, 21]. The resolution is limited by the size of the reference hole, typically 70 nm. Because soft x-ray holography is a lensless technique with no optical elements to degrade the coherence of the beam it ought to be possible to obtain much higher resolution data, even in principle approaching the X-ray wavelength.

1.3 Thesis Overview

Chapter 2 reviews the theory of X-ray scattering, starting from first principles and leads to the concepts of crystal truncation rods and lensless Fourier transform holography. Both are interference techniques and detailed structure of the scatterers can be extracted. There is a discussion on the required coherence of the X-ray source, and a description of bicrystallography and the parameters that define it.

Chapter 3 presents the commissioning of beamline I07 of the Diamond Light Source Synchrotron. The diffractometer, and alignment procedure, are discussed in detail. Crystal truncation rod data, from a Si bicrystal, obtained using various different modes are compared and assessed in terms of their practicality.

Chapter 4 introduces the method of minimising the Keating energy of various grain boundary structures to determine the positions of the atoms. The model of bicrystal truncation rod scattering is developed and used to simulate scattering from the relaxed grain boundaries. The simulated bicrystal truncation rod scattering is compared with experimental measurements and subsequent analysis allowed us to discriminate

between potential grain boundary structures and correctly determine the buried structure, highlighting the success of our approach.

Chapter 5 describes several lensless Fourier transform holography experiments performed on beamline I06. The suitability of the beamline is discussed along with the preparation of samples. A custom built diffraction chamber was designed and commissioned and holograms are presented. There is also a discussion on data analysis techniques.

A summary of the results and conclusions are discussed in chapter 6 and future work is suggested.

Chapter 2

Background Theory

2.1 Introduction

The first part of this chapter introduces the theory of x-ray diffraction, starting from the most simple case of scattering from an electron, leading to the concepts of crystal truncation rods. These ideas were used in the experiments in chapters 3 and 4 and the subsequent data analysis.

In section 2.3 the theory behind bicrystallography is introduced. The concepts of grain boundaries, as well as the mechanisms that create them are discussed.

Finally there is the introduction of Fourier transform holography, which builds upon the basic diffraction theory, and the required coherence properties of the X-ray source in order to perform such an experiment. These concepts are used in chapter 5.

2.2.1 Scattering from Electrons and Atoms

This section contains a brief introduction to basic X-ray diffraction. For a more detailed approach the reader is directed to standard textbooks on X-ray diffraction [22, 23]. The derivation of the scattering process is taken from [24].

The scattering of X-rays from an electron is given by the Thomson scattering formula. The scattered field E_e observed at distance R away from the electron at $\mathbf{r}$ has the amplitude

$$E_e e^{-i\mathbf{k}_f \cdot \mathbf{r}} = E_0 \left(\frac{e^2}{mc^2 R} \right) P^{\frac{1}{2}} e^{-i\mathbf{k}_i \cdot \mathbf{r}} \quad , (2.1)$$

where E_0 is the amplitude of the incoming wave, $\mathbf{k}_f$ and $\mathbf{k}_i$ are the wavevectors of the scattered and incident wave respectively, and for elastic scattering $|k_f| = |k_i| = 2\pi/\lambda$ where

λ is the wavelength. P is the polarization factor of the incoming wave and is equal to 1 if E_0 is normal to the scattering plane and $\cos^2\theta$ when it is in the scattering plane. The scattering angle, θ, is explained in fig. 2.1. Using the definition of the momentum transfer, $\mathbf{q} = \mathbf{k}_f - \mathbf{k}_i$, equation 2.1 becomes

$$E_e = E_0\left(\frac{e^2}{mc^2 R}\right)P^{\frac{1}{2}}e^{i\mathbf{q}\cdot\mathbf{r}} \quad . (2.2)$$

Now scattering from an atom is considered. The Z electrons are distributed around the nucleus to give an atomic electron density $\rho(\mathbf{r})$, The scattering from an atom is then

$$E_a = E_0\frac{e^2}{mc^2 R}P^{\frac{1}{2}}\int \rho(\mathbf{r})e^{i\mathbf{q}\cdot\mathbf{r}}dV \quad , (2.3)$$

where the integral is over the entire volume of the atom.

2.2.2 Atomic Form Factor

The atomic scattering factor, *the atomic form factor*, $f(q)$ is defined as

$$f(q) = \int \rho(\mathbf{r})e^{i\mathbf{q}\cdot\mathbf{r}}dV \quad , (2.4)$$

where the integral is over one atom. As $\mathbf{q}$ tends towards 0 all electrons scatter in phase and $f(q)$ is simply Z.

The atomic scattering factors for all atoms have been calculated and tabulated in the International Tables for X-ray crystallography [25]. A convenient, parametrised version of the atomic form factor can be given by a series of Gaussians by the following expansion

$$f(q) = \sum_{i=1}^{4} a_i e^{\left(\frac{-b_i^2 q^2}{16\pi^2}\right)} + c \quad , (2.5)$$

where a, b and c are constants defined in [25]. This expansion works over the range $0 < q < 8\pi$ Å^{-1}. The value of q in this scope of work does not exceed these limits and equation 2.5 is used throughout.

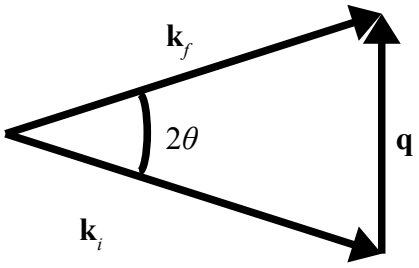

Figure 2.1: The scattering triangle.

2.2.3 Scattering from a Crystal Lattice

A crystal is a three-dimensional repetition of some unit of cell atoms. The essential features are illustrated in fig. 2.2. Atoms, represented by the circles, are repeated identically. The scheme of repetition is defined by three vectors $\mathbf{a}_1$, $\mathbf{a}_2$ and $\mathbf{a}_3$, called the crystal axes. The parallelopiped defined by the three axes $\mathbf{a}_1\mathbf{a}_2\mathbf{a}_3$ is the smallest volume which, repeated, will make up the crystal. This smallest volume is called the unit cell. The unit cell volume is given by $v_a = \mathbf{a}_1 \,.\, \mathbf{a}_2 \times \mathbf{a}_3$.

The different atoms in the unit cell are numbered 1, 2, 3, ..., n, and the positions of the atoms relative to the unit cell origin are given by the vectors $\mathbf{r}_1$, $\mathbf{r}_2$, $\mathbf{r}_3$, ..., $\mathbf{r}_n$. The different unit cells are designated by three integers m_1, m_2, m_3, such that the cell $m_1m_2m_3$ is the one whose origin is displaced from the crystal origin by $m_1\mathbf{a}_1 + m_2\mathbf{a}_2 + m_3\mathbf{a}_3$. Finally the position of atom n in the unit cell $m_1m_2m_3$ is given by the vector

$$\mathbf{R}_m^n = m_1\mathbf{a}_1 + m_2\mathbf{a}_2 + m_3\mathbf{a}_3 + \mathbf{r}_n = \mathbf{R}_m + \mathbf{r}_n \quad . (2.6)$$

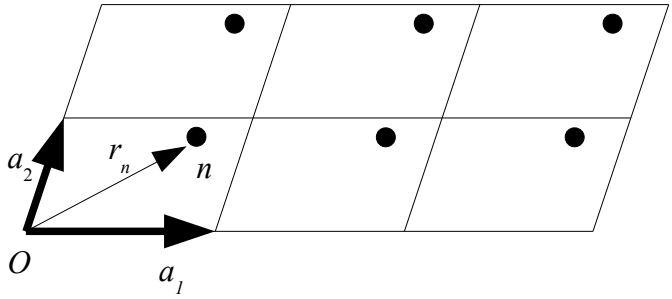

Figure 2.2: Two-dimensional representation of the periodic property of a crystal.

The scattering from the lattice is calculated by first summing over all the atoms in the unit cell, which is given by the structure factor $F(\mathbf{q})$:

$$F(\mathbf{q}) = \sum_n f_n(q) e^{i\mathbf{q}\cdot\mathbf{r}_n} \quad . (2.7)$$

Then each point in the lattice can be summed over to give

$$F_{crystal}(\mathbf{q}) = F_{unitcell}(\mathbf{q}) \sum_{\boldsymbol{R}_m} e^{i\mathbf{q}\cdot\mathbf{R}_m} \quad . (2.8)$$

The intensity of the scattered wave is found by squaring equation 2.3:

$$I(q) = I_0 \frac{e^4}{m^2 c^4 R^2} P |F(q)|^2 \frac{\sin^2(N_1\phi_1)}{\sin^2(\phi_1)} \frac{\sin^2(N_2\phi_2)}{\sin^2(\phi_2)} \frac{\sin^2(N_3\phi_3)}{\sin^2(\phi_3)} \quad , (2.9)$$

where $\varphi_{(1,\,2,\,3)} = \mathbf{q}.\mathbf{a}_{(1,\,2,\,3)} / 2$ and $N_{(1,\,2\,,3)}$ are the extensions of the crystal in $\mathbf{a}_{(1,\,2,\,3)}$. $I(q)$ peaks when the *Laue conditions* are fulfilled

$$\mathbf{q}.\mathbf{a}_1 = 2\pi h \quad , \quad \mathbf{q}.\mathbf{a}_2 = 2\pi k \quad \text{and} \quad \mathbf{q}.\mathbf{a}_3 = 2\pi l \quad , (2.10)$$

where h, k and l are the *Miller indices* and are integers. These conditions are satisfied when $\mathbf{q}$ lies on a point in the reciprocal lattice. The reciprocal lattice is defined by a set of basis vectors $\mathbf{b}_1$, $\mathbf{b}_2$ and $\mathbf{b}_3$ and lattice points on the reciprocal lattice are given by:

$$\mathbf{G} = h\,\mathbf{b}_1 + k\,\mathbf{b}_2 + l\,\mathbf{b}_3 \quad . (2.11)$$

The Laue conditions are satisfied when **q** = **G**. The sharp peaks of the scattered intensity that occur at the Laue conditions are known as *Bragg Peaks*.

The reciprocal lattice vectors are related to the real space vectors by

$$\mathbf{b}_1 = 2\pi \frac{\mathbf{a}_2 \times \mathbf{a}_3}{\mathbf{a}_1 . (\mathbf{a}_2 \times \mathbf{a}_3)} \quad , (2.12)$$

$$\mathbf{b}_2 = 2\pi \frac{\mathbf{a}_3 \times \mathbf{a}_1}{\mathbf{a}_1 . (\mathbf{a}_2 \times \mathbf{a}_3)} \quad , (2.13)$$

$$\mathbf{b}_3 = 2\pi \frac{\mathbf{a}_1 \times \mathbf{a}_2}{\mathbf{a}_1 . (\mathbf{a}_2 \times \mathbf{a}_3)} \quad . (2.14)$$

2.2.4 The Ewald Sphere

A very powerful and useful way of representing the satisfying of the Laue conditions is given by the Ewald sphere. The reciprocal lattice is shown in fig. 2.3. The direction of the incoming wave, $\mathbf{k}_i$, terminates on the origin, *O*, of the reciprocal lattice. A sphere of radius $|\mathbf{k}_i|$ centred on the starting point of the incoming wave passes through the origin. Any reciprocal lattice points *hkl* which happen to fall on the surface of the sphere, represents a set of planes *hkl* for which the Laue conditions are satisfied. The direction of the outgoing wave, $\mathbf{k}_f$, is from the centre of the sphere to the point *hkl*. Although fig. 2.3. is shown in two-dimensions, the Ewald sphere construction is valid in three-dimensions, and the point *hkl* can be at any point on the surface of the sphere.

In terms of the Ewald sphere, the Laue conditions are satisfied for a set of planes *hkl* provided that the reciprocal lattice point *hkl* falls on the surface of the sphere.

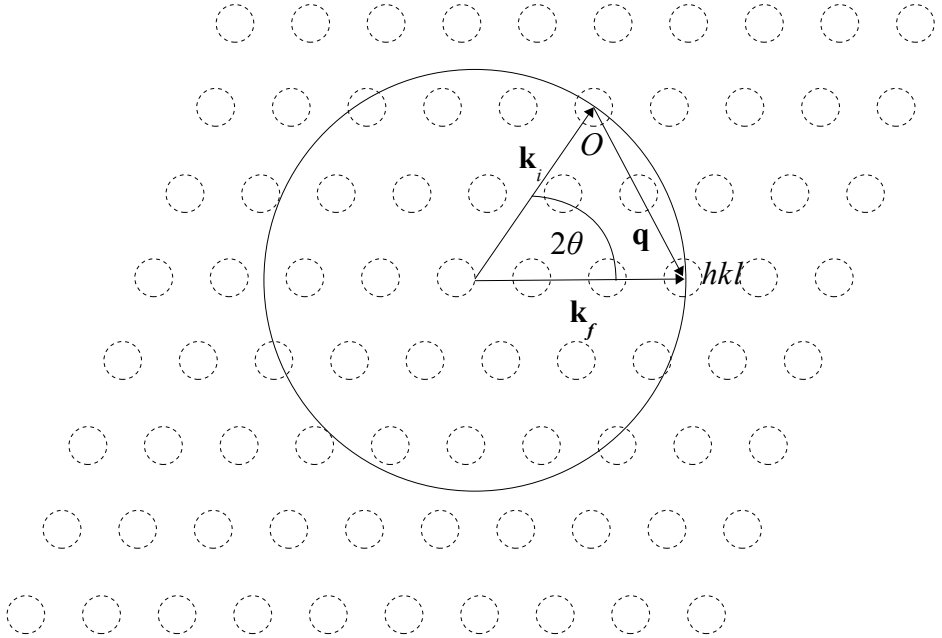

Figure 2.3: Two-dimensional representation of the Ewald sphere in the reciprocal lattice. The Laue conditions are satisfied for any set of planes whose point *hkl* falls on the surface of the sphere.

2.2.5 Crystal Truncation Rods

In the the limit of an infinite crystal, the diffraction peaks are perfect δ functions. However, in materials one is often interested in the surface of a crystal or a buried interface. As a result of this the crystal is semi-infinite; it is an infinite crystal in two-dimensions that is truncated at the surface or interface. When finite-size effects are included, the peaks are found to be broadened by an amount inversely related to the dimension of the diffracting region of the crystal [26]. For crystals with sharp boundaries, a significant amount of intensity is always scattered far away from the Bragg peaks and is spread right across the Brillouin zone. The order of magnitude of this intensity is the same as that arising from a single layer of atoms.

For a crystal with infinite extensions in the directions given by $\mathbf{q}_1$ and $\mathbf{q}_2$, N_1 and N_2 become infinite and equation (2.9) is sharply peaked when the Laue conditions are met. The third basis vector $\mathbf{a}_3$ is assumed to be perpendicular to the surface spanned by $\mathbf{a}_1$ and $\mathbf{a}_2$. This gives the scattered intensity from a slab of crystal with thickness $N_3 a_3$. The scattering from a semi-infinite crystal is obtained by letting N_3 tend to a very large

but finite number:

$$I(q)=I_0\frac{e^4}{m^2c^4R^2}P|F(q)|^2N_1^2N_2^2\frac{1}{2\sin^2(\phi_3)} \quad , (2.16)$$

for $\mathbf{q}.\mathbf{a}_3 \neq 2\pi l$ and where the rapid oscillations in the numerator are averaged out over the limit. The intensity is still peaked where the Laue condition $\mathbf{q}.\mathbf{a}_3 = 2\pi l$ is fulfilled and l is an integer, but because there is no translational symmetry in the direction perpendicular to the surface or interface, there are additional diffuse streaks connecting all the Bragg peaks. Close to the Bragg peaks the intensity tails off as $1/(\Delta q_z)^2$ where Δq_z is the distance from the Bragg peak.

The scattering is sharp in two-dimensions but a diffuse streak perpendicular to the surface or interface (referred to as a "rod" of scattering) arises from the truncation of the crystal at the surface or interface. This rod of scattering is known as the *crystal truncation rod* (CTR) [26]. The intensity of the CTR is approximately 10^5 times smaller than that of the Bragg peak [26].

Different terminations of the crystal surface alter the shape of the CTR. For example, if the termination is more smooth than a step-function, the intensity of the CTR will fall off more rapidly than $1/(\Delta q_z)^2$. An example is shown in fig. 2.4 for the case of a Pt(111) crystal [26]. The dashed line represents the scattering given by equation (2.16) but it does not describe the data very well. If instead of a sharp termination an extra layer of atoms was added on top with a fractional occupancy β ($0 < \beta < 1$), adding a second layer with occupancy β^2 (etc.) and equation (2.16) is modified to account for roughness [26]; the modified CTR is given by the solid line, which predicts the data very well.

A determination of a crystal structure means determining both the size and shape of the unit cell and the atomic positions within the unit cell. In many cases the former is simple in surface crystallography because the surface structure is commensurate with the underlying substrate.

The atomic structure within the unit cell must be determined from the structure factors, since it is only in the structure factor that the atomic positions appear. The structure factors can be obtained from the measured CTR intensities after geometric

correction factors have been applied. The intensities are also affected by the crystal quality of the sample and the collimation of the incoming X-ray beam. The correction factors are discussed in more detail in the next chapter.

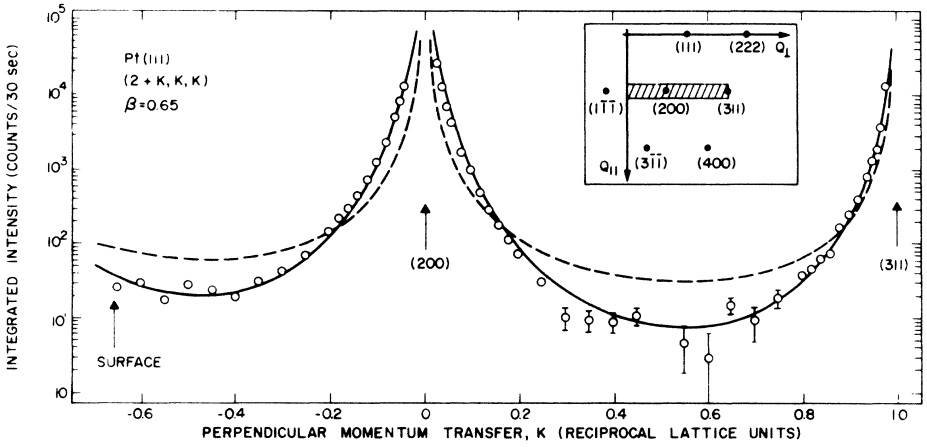

Figure 2.4: Crystal truncation rod of an etched Pt(111) crystal under He atmosphere. The reciprocal lattice notation in the inset is with normal bulk Miller indices. The dashed line represents the CTR for a sharp terminated surface, whereas the solid line is the CTR from a rough surface. After I.K. Robinson [26].

2.3 Bicrystallography

This thesis is concerned not with surfaces but the much more challenging problem of the crystalline interface structure. It extends the CTR formulation to bicrystals.

For the purposes of this work the definition of a bicrystal is taken from Pond (1979) [27] to be two semi-infinite crystals separated by a unique plane, the interface. This section introduces the concept of the formation of idealized bicrystals, grain boundary interfaces and the dislocations that lead to the formation of different grain boundaries. For a more detailed discussion on the formation of bicrystals and symmetry operations the reader is directed towards references [3, 27-31].

2.3.1 Outline of the Crystallographic Methodology

A bicrystal is a composite object of two crystals. There are two types: a heterophase bicrystal, in which the component crystals do not share the same structure, and a homophase bicrystal, in which the component crystals have the same structure. In general the symmetry of the bicrystal will be lower than the symmetries of the the component crystals and this lowering of symmetry is known as *dissymmetrization.* However, in the case of the homophase crystal additional symmetry elements may be created that do not exist in the component crystals in isolation.

Pond [29] introduces a systematic method for the derivation of the symmetry of a interface consisting of four stages. At each stage the symmetry of the object is either the same or lower than the symmetry at the previous stage.

Firstly the notion of *colour* is introduced. This distinguishes between the operations relating sites in the same crystal from those relating sites in different crystals. Firstly one assigns a colour to either crystal, in this case one crystal is labelled black and the other red. *Ordinary* operations relate black sites to black sites and red sites to red, while *antisymmetry* operations relate black sites to red and vice versa. Antisymmetry operations only exist in homophase bicrystals. The initial stage of dissymmetrization is to allow the black and red lattices to interpenetrate to form a *dichromatic pattern.* In the second stage one lattice is rotated to introduce the relative orientation of the two crystals that will exist in the final interface. Both ordinary and antisymmetry operations may exist in the dichromatic pattern. The space group of the dichromatic pattern may therefore contain both types of operation and such a group is called a colour group.

Up until now the interface between the crystals has still not been introduced. The third stage consists of sectioning the dichromatic pattern on the interface plane and to place one crystal lattice on one side of the section and the other crystal lattice on the other. This is the unrelaxed bicrystal.

The forth and final step is to introduce the grain boundary by the insertion of additional material at the interface and the interatomic forces are “switched on” to minimise the energy of the bicrystal giving a relaxed structure. During the relaxation process there is a possibility that a rigid body translation of one crystal to the other may occur. In general the rigid body translation has components both parallel and

perpendicular to the interface; the perpendicular component is called the interfacial expansion and the parallel component is known as the in-plane translation.

2.3.2 Coincidence-Site Lattice

When the crystals are allowed to interpenetrate in the previous section they have complete self-coincidence. However, partial self-coincidence can occur for certain other rotations about an axis. Two crystal lattices related by such an angular rotation about an axis have certain common sites, located on a single lattice of larger cell dimensions. This larger lattice is known as the *coincidence-site lattice* (CSL) [32]. The misorientation relationship between two crystals can be given as an axis-angle pair.

The procedure for obtaining CSLs for rotations about [100] is taken from [32]. A lattice point is chosen as the origin and a square cell is constructed on each line joining the origin to a visible point, and illustrates that there are no other points on the line between the given lattice point and the origin. This square cell is much larger than those of the original unit cell and can be used to generate a CSL. The ratio of the area of the new unit cell to that of the original lattice is $x^2 + y^2$, where (x,y) are the Cartesian coordinates of the lattice point which is joined to the origin. This ratio is also equal to the multiplicity, Σ, of the CSL, which may be defined as the reciprocal of the density of common points [3]. However, the rotation of 180° around [*hkl*] in the cubic system gives rise to the following CSLs of

$$\Sigma = h^2 + k^2 + l^2 \quad , (2.17)$$

if $h^2+k^2+l^2$ is odd or

$$\Sigma = \frac{h^2 + k^2 + l^2}{2} \quad , (2.18)$$

if $h^2+k^2+l^2$ is even.

The CSL of a Σ13(501) grain boundary is shown in fig. 2.5. In this diagram the crystals have interpenetrated and the black crystal rotated with respect to the red crystal.

The rotation angle between the two crystals is given by $\theta = 2 \tan^{-1}(1/5) = 22.6^{o}$.

2.3.3 Grain Boundaries

In a real bicrystal the two lattices are not interpenetrating, but are separated by a grain boundary, which may require the introduction of a dislocation vector **b** in order to ensure compatibility at the interface. A grain boundary is a homophase interface involving a misorientation between the adjoining crystal lattice.

A grain boundary is called a *tilt boundary* when the axis of rotation that can bring the crystals into the same orientation is parallel to the boundary plane, a *twist boundary* when the axis is perpendicular to the boundary plane, and a *mixed boundary* in other cases [1].

A boundary between two grains *A* and *B* of the same material, but of different orientation, is fully determined by the axis of rotation *l*, the angle of rotation θ, and the orientation of the plane of contact *N*. Whereas the axis *l* has the same orientation with respect to the lattices of *A* and *B*, the boundary plane *N* may have different orientations N_A and N_B with respect to these reference systems. It is often useful to give the orientation of *N* with respect to a third lattice *C*, which is known as the median lattice [1]. This lattice is obtained from *A* or *B* by a rotation of $\pm \theta/2$ about *l*. This orientation N_C is the *median plane*. For a pure twist boundary $N_A = N_B = N_C$.

A pure tilt boundary is *symmetrical* if the median plane is a macroscopic symmetry plane of the crystal which in the diamond lattice is a {100} or {110} plane. When the rotation axis is parallel to one or more of these symmetry planes there will be one or more symmetrical positions of the boundary plane [1].

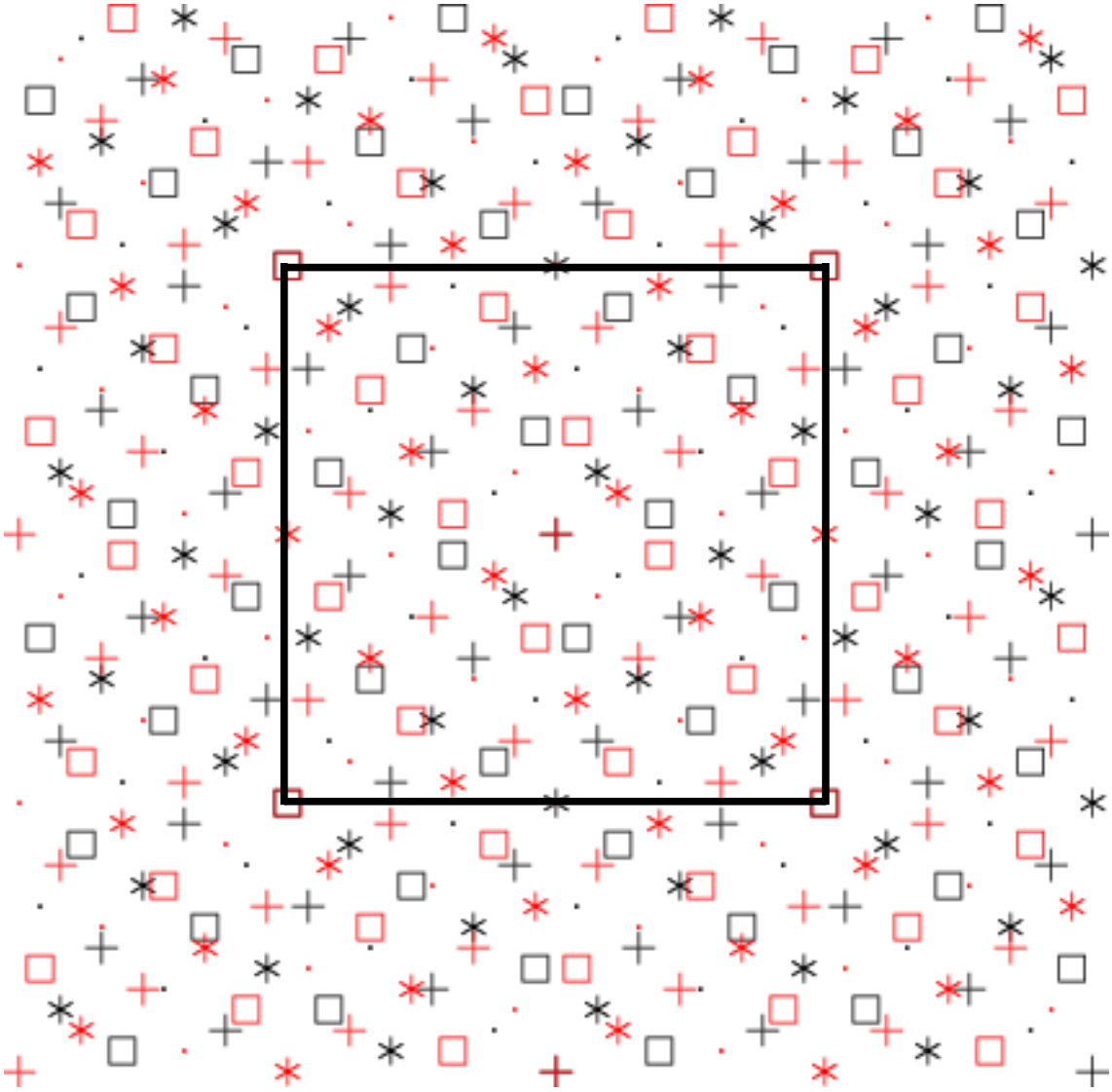

Figure 2.5: (001) projection for the Σ13 boundary in the diamond cubic structure. The black shapes represent the atoms of the black crystal and the red the atoms of the red crystal. The squares represent atoms that are in the plane of the paper, the asterisks are atoms that are ¼ [001] above it, the crosses are atoms ½ [001] above it and the dots are atoms ¾ [001] above it. The CSL is represented by the large square.

2.3.4 Edge Dislocations

A dislocation is a crystallographic defect or irregularity, within a crystal structure. Generally speaking, grain boundaries are composed of an array of dislocations and their properties and structure depends on the angle of rotation. The simplest type of

dislocation is obtained when it is imagined that a cut is made over a certain area of a plane perpendicular to (e.g.) an *x*-axis in an originally perfect lattice, and along this cut either a layer of atoms has been removed or inserted [33]. The insertion of the extra layer of atoms will cause an expansion in the lattice in the immediate vicinity of the cut (fig. 2.6). This type of dislocation is known as an *edge* dislocation. This dislocation has a line direction (also known as the *dislocation line*), which is in the plane perpendicular to the direction of the extra layer of atoms (the *slip* vector).

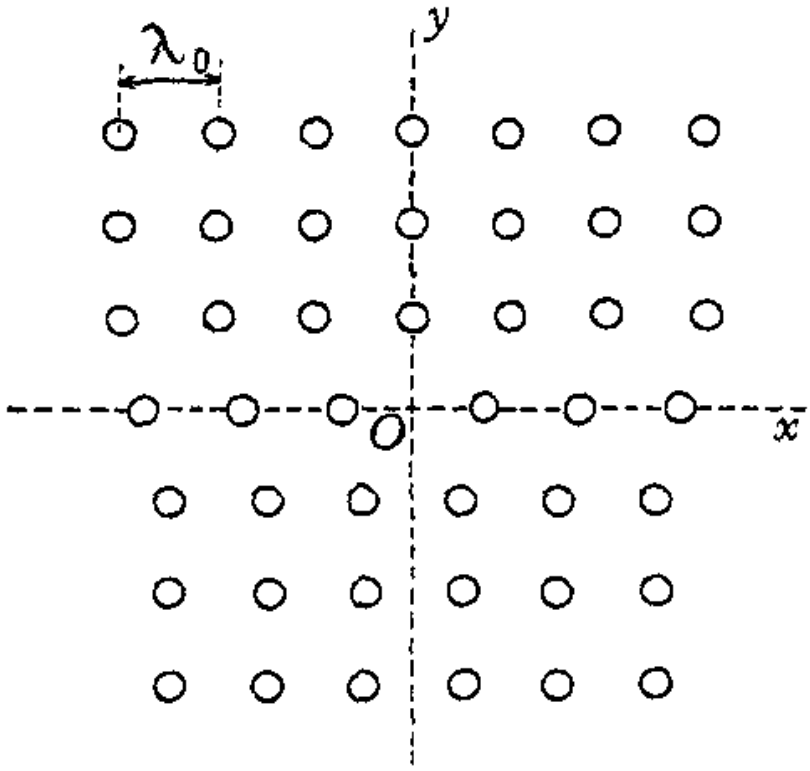

Figure 2.6: An illustration of a two-dimensional edge dislocation [33]. This dislocation has been obtained by the insertion of an extra layer of atoms along the *y*-axis. The line direction is along the *x*-axis.

2.3.5 Screw dislocations

It is also possible to have dislocations with a dislocation line parallel to the slip vector [34]. Figure 2.7 shows a screw dislocation parallel to a cube edge in a simple

cubic crystal; the unit cells are shown as distorted cubes. This figure also illustrates why this dislocation is called screw: *the crystal is not made up of parallel atomic planes one above the other; rather it is a single atomic plane in the form of a spiral ramp.* Figure 2.8 shows the atomic planes above and below the slip plane; the open circles represent atoms just above the slip plane, and the solid circles atoms just below.

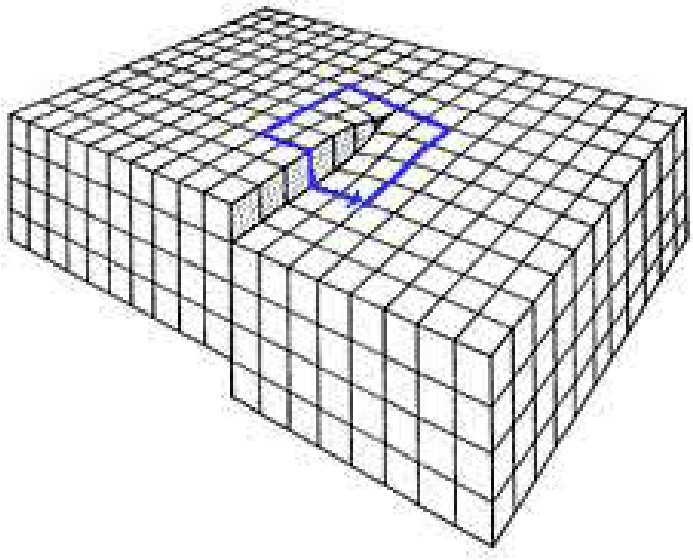

Figure 2.7: The screw dislocation. The atoms are represented by the distorted cubes. The crystal is a single atomic plane in the form of a spiral ramp. The Burgers vector is given by the blue circuit. After [35].

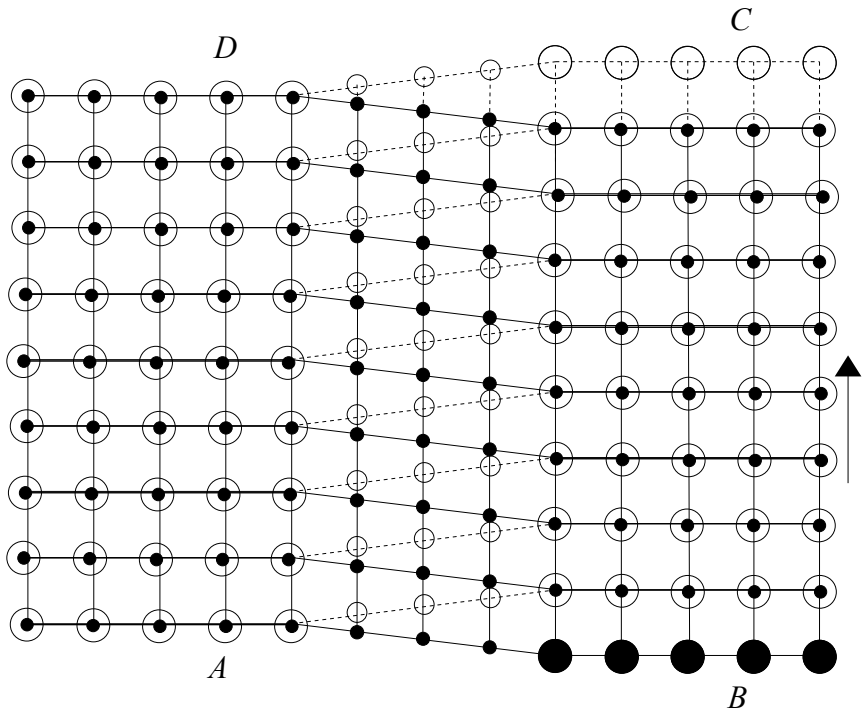

Figure 2.8: Arrangement of atoms around the screw dislocation. The plane of the figure is parallel to the slip plane (the slip vector is denoted by the arrow). *AD* is the dislocation and *ABCD* is the area of the slip.

2.3.6 Burgers Circuit and Vector

In order to describe a dislocation line as completely as possible it is necessary only to specify the position of the dislocation line within the crystal and to indicate the character of each segment of the line [36]. The position of any segment of a dislocation line can be described by a vector **r**, as shown in fig. 2.9.

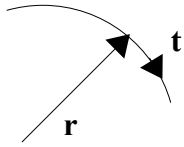

Figure 2.9: Tangent vector **t** of a dislocation segment at position **r**. The vector **t** is a unit vector tangent to the dislocation line. Thus $\mathbf{t} = d\mathbf{r}/dr$.

In order to describe the character of each segment of the line *Burgers vectors* are used. The Burgers vector of the edge dislocation in fig. 2.6 is shown in fig. 2.10. Two circuits have been drawn in this figure. The upper circuit is drawn around the edge dislocation; the lower circuit avoids the dislocation. In each circuit the same number of jumps from atom to atom are made up as are made down, to the left as to the right. The starting and finishing point are the same atom in the circuit that does not include the dislocation. However, for the circuit that includes the dislocation the starting and finishing atoms are different points. Thus there is a failure to close the circuit. The Burgers vector, **b**, is defined to be the closure failure. The sense of the vector is from the finishing atom to the starting atom. The Burgers vector is perpendicular to the line dislocation for an edge dislocation and parallel for a screw dislocation.

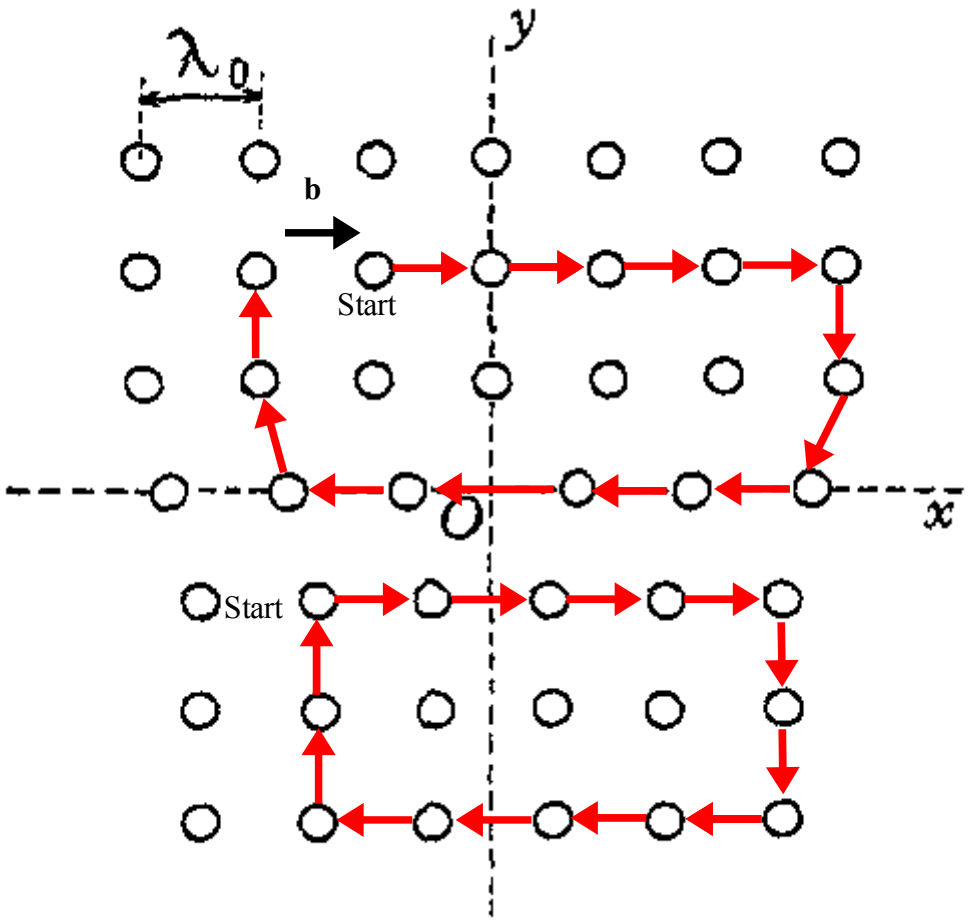

Figure 2.10: Burgers circuit around an edge dislocation.

2.4 Fourier Transform Holography: Conceptual

In this section the concept of Fourier transform holography and reconstruction techniques is introduced. For more detailed discussions the reader is directed towards the following text-books [37-39].

Holography is an *interference* method of recording the light waves diffracted from an object by a subject illuminated with coherent light. The diffracted waves interfere with a phase-related reference wave. If the waves are highly coherent, the relative phase between the object and reference wave remains constant in time producing an observable effect on the intensity distribution of the resulting interference pattern. This pattern, the *hologram*, contains sufficient information about both the phase and the amplitude of the diffracted waves to permit their reconstruction.

Let $\mathbf{o} = o_0\exp(i\varphi_o)$ be the complex amplitude of the light arriving at the hologram plane from the object and $\mathbf{r} = r_0\exp(i\varphi_r)$ the complex amplitude from the reference wave at the hologram, where φ_o and φ_r are the phases of the object and reference waves respectively and o_0, r_0 the amplitudes. The interference between the two waves gives the intensity, I, of the hologram to be

$$I=(\mathbf{o}+\mathbf{r})(\mathbf{o}^*+\mathbf{r}^*)=\mathbf{o}.\mathbf{o}^*+\mathbf{r}.\mathbf{r}^*+\mathbf{o}.\mathbf{r}^*+\mathbf{r}.\mathbf{o}^* \quad , (2.19)$$

where the * denotes the complex conjugate. This can be rewritten as

$$I=o_0^2+r_0^2+2\,o_0 r_0\cos(\varphi_r-\varphi_o) \quad , (2.20)$$

where the interference term is $2o_0r_0\cos(\varphi_r-\varphi_o)$. When the object and reference points are in the same plane, the coordinates of the object O are $(x_o, 0, z_o)$ and the coordinates of the reference R are $(x_r, 0, z_o)$. The phase difference in equation (2.20) becomes

$$\varphi_r-\varphi_o=\frac{-2\pi}{\lambda}\left(\frac{x_r}{z_o}-\frac{x_o}{z_o}\right)x_2 \quad . (2.21)$$

Differentiation of $(\varphi_o - \varphi_r)/2\pi$ with respect to x_2, the x component in the plane of the

hologram, yields the constant fringe frequency

$$\epsilon = \frac{x_o - x_r}{z_o \lambda} \quad . (2.22)$$

Since the fringes are independent of *y*, the fringes are vertical and uniformly spaced, linear fringes.

From fig. 2.11, the ratio of $x_r/z_o = \tan \theta_r \sim \theta_r$ and $x_o/z_o \sim \theta_o$. Equation 2.21 can be rewritten as

$$\varphi_r - \varphi_o = \frac{2\pi}{\lambda}(\theta_o - \theta_r) x_2 \quad , (2.23)$$

and the phase difference now only depends on the angle subtended at the hologram by the difference between the object and the reference. If the object and reference are an infinite distance away from where the hologram is formed, equation (2.23) holds true. The waves arriving at the hologram from point sources at infinity are plane waves. They are far-field pattern or Fourier transforms of the point source. Hence the linear fringe system of equation (2.23) can be regarded as the interference of a plane wave reference with the Fourier transform of the object source. Taking this into consideration equation (2.19) can be amended to become:

$$I = RR^* + OO^* + O R^* + RO^* = |R|^2 + |O|^2 + O R^* + RO^* \quad , (2.24)$$

where *R* is the Fourier transform of *r* and *O* is the Fourier transform of *o* (see appendix A.1) . The terms $|R|^2$ and $|O|^2$ are the autocorrelation terms and arise from the object and reference alone whilst the cross-correlation terms OR^* and RO^* arise from the interference of the object and reference waves giving rise to fringes.

Real space images are reconstructed by calculating the two dimensional Fourier transform of the hologram:

$$\mathcal{F}[I] = \mathcal{F}[|R|^2] + \mathcal{F}[|O|^2] + \mathcal{F}[O R^*] + \mathcal{F}[RO^*] \quad , (2.25)$$

The real space image, I_{real}, has four components

$$I_{real} = r*r + o*o + o*r + r*o \quad , (2.26)$$

The cross-correlation terms give rise to identical, twin images.

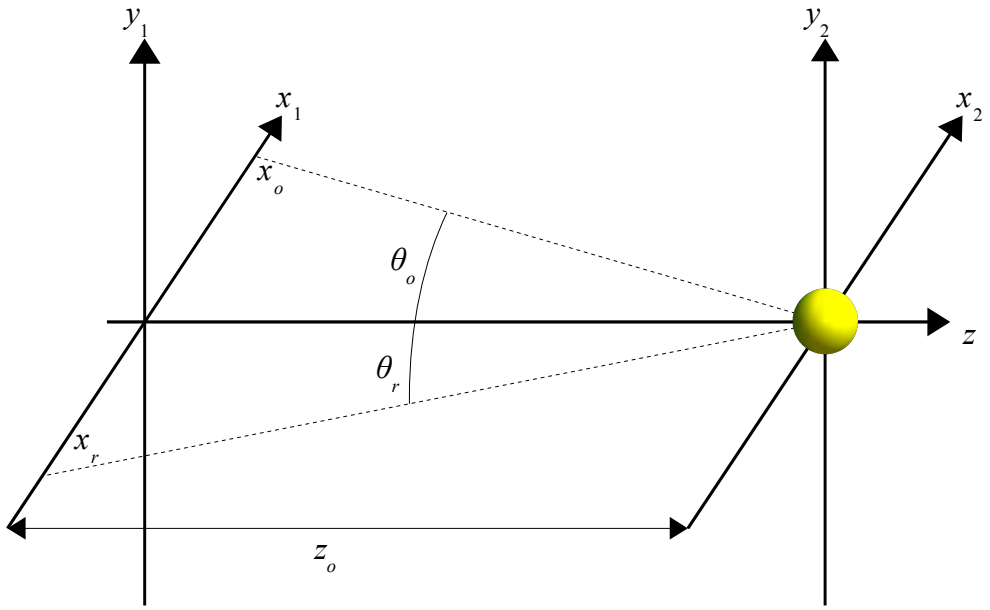

Figure 2.11: Lensless Fourier transform configuration.

2.4.1 Conditions for Interference

If two beams are to interfere to produce a stable pattern, they must have very nearly the same frequency. A significant frequency difference would result in a rapidly varying, time dependent phase difference, which in turn would cause the interference terms in equations (2.20) and (2.24) to average to zero during the detection interval.

Thus far in our treatment of holography we have assumed illumination from a monochromatic plane wave produced by a point source. Under these conditions the phase difference for two fixed points along a ray direction is time independent, or equivalently, the difference in the phase measured at a single point in space at the beginning and end of a fixed time interval Δt does not change with time. These are statements of perfect temporal coherence. Similarly, the phase difference for two fixed

points in a plane normal to a ray direction is time independent. This is perfect *spatial coherence.*

Light from a real physical source is never strictly monochromatic, since even the sharpest spectral line has a finite width, so partially coherent waves are used to illuminate samples. Coherence gives a measure of the correlation between two points P_1 and P_2 in the wave field.

2.4.2 Complex Degree of Coherence

The general subject of partial coherence is treated extensively in Chapter 10 of Born and Wolf [40]. Rather than reproduce proofs of these results the necessary relations are summarized here as basic concepts.

Suppose as in fig. 2.12, that light waves emerge from pinholes P_1 and P_2 and interfere on an observation screen S. An extended partially coherent source illuminates the pinholes. The intensity at point Q on S is represented by equation (2.19) where **o** and **r** are the complex electric fields of the waves from P_1 and P_2 arriving at Q. It is shown by Born and Wolf that the time average of the interference term

$$\langle \mathbf{o}\,\mathbf{r}^* + \mathbf{o}^*\,\mathbf{r} \rangle = 2\Re[\langle \mathbf{o}\,\mathbf{r}^* \rangle] \quad , (2.27)$$

can be written in terms of a complex degree of coherence $\gamma_{12}(\tau)$ and $\Re$ denotes the real part of the operator. $\gamma_{12}(\tau)$ relates the correlation of the electric fields at P_1 and P_2 to the time average of the interference at Q. Since the latter is measurable in terms of visibility, $\gamma_{12}(\tau)$ has the merit of expressing coherence as a measurable quantity. The light intensities at points P_1 and P_2 are $2\langle \mathbf{o}(t)\mathbf{o}^*(t) \rangle$ and $2\langle \mathbf{r}(t)\mathbf{r}^*(t) \rangle$. The complex degree of coherence $\gamma_{12}(\tau)$ is defined as the normalised coherence of $\mathbf{o}(t)$ and $\mathbf{r}(t)$

$$\gamma_{12}(\tau)=\frac{\langle \mathbf{o}(t+\tau)+\mathbf{r}^{*}(t)\rangle}{[\langle \mathbf{o}(t)+\mathbf{o}^{*}(t)\rangle+\langle \mathbf{r}(t)+\mathbf{r}^{*}(t)\rangle]^{1/2}}$$

$$=\frac{\lim_{T\to\infty}\frac{1}{2\mathrm{T}}\int_{-T}^{T}\mathbf{o}(t+\tau)\mathbf{r}^{*}(t)\,dt}{\left[\left(\lim_{T\to\infty}\frac{1}{2\mathrm{T}}\int_{-T}^{T}\mathbf{o}(t)\mathbf{o}^{*}(t)dt\right)\left(\lim_{T\to\infty}\frac{1}{2\mathrm{T}}\int_{-T}^{T}\mathbf{r}(t)\mathbf{r}^{*}(t)\,dt\right)\right]^{1/2}} \quad , (2.28)$$

where T is the observation time. They then relate $\gamma_{12}(\tau)$ to equation (2.27) through

$$2\,\Re[\langle \mathbf{o}\,\mathbf{r}^{*}\rangle]=2o_0r_0\,\Re[\gamma_{12}(\tau)]=2o_0r_0|\gamma_{12}(\tau)|\cos\beta_{12}(\tau) \quad , (2.29)$$

where τ is the difference in light transit time between P_1 and Q compared to that from P_2 and Q, and β_{12} is the phase of $\gamma_{12}(\tau)$. The quantity of $\gamma_{12}(\tau)$ is a measure of the coherence between light at P_1 and P_2 and encompasses both temporal and spatial aspects. Substitution of equation (2.29) into equation (2.19) gives the minimum and maximum intensities:

$$I_{max}=o_0^2+r_0^2+2o_0r_0|\gamma_{12}| \quad \text{when} \quad \cos\beta_{12}=1 \quad (2.30)$$

and

$$I_{min}=o_0^2+r_0^2-2o_0r_0|\gamma_{12}| \quad \text{when} \quad \cos\beta_{12}=-1 \quad . (2.31)$$

Therefore the time averaged components produce different results in the case of partial coherence from that obtained in the case of perfect coherence. This will assert itself in the *visibility* of fringes V defined by

$$V=\frac{I_{max}-I_{min}}{I_{max}+I_{min}}=\frac{2|\gamma_{12}|}{(o_0^2/r_0^2)^{1/2}+(r_0^2/o_0^2)^{1/2}} \quad . \quad (2.32)$$

When the interfering waves are of equal intensity, the absolute value of the degree of

coherence is equal to the observed visibility of the interference fringes.

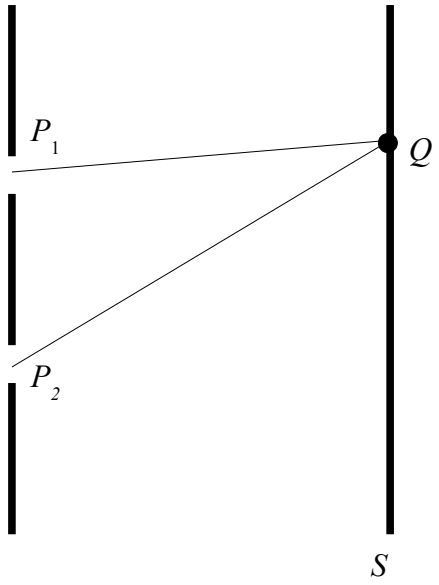

Figure 2.12: Double aperture experiment from an extended source.

2.4.3 Spatial Coherence Requirements

In recording the hologram, both reference and object beams must have well-defined wavefronts that are constant in time. The spatial coherence of a light field is a measure of the degree of phase correlation at two different points of space at a single time. This correlation is primarily dependent on the size of the source from which the light originated [40].

If a meaningful criterion is set for minimum spatial coherence, the van Cittert-Zernike theorem can be used to estimate the maximum spatial extent of a lightsource suitable for forming holograms. The van Cittert- Zernike theorem formally relates the degree of spatial coherence to the lateral extent of a source through a Fourier transform relationship. The theorem will just be stated here, for a further discussion see chapter 10 of Born and Wolf. For the case of an extended source containing mutually incoherent oscillators, but with a narrow spectral bandwidth $\Delta\upsilon$, the van Cittert-Zernike theorem can be expressed as follows [37]: *When a small source illuminates two closely spaced points located in a plane a long distance from the source, the degree of coherence between complex electric fields at two points is given by the magnitude of a normalised*

Fourier transform of the intensity distribution of the source.

Consider the geometry shown in fig. 2.13 where a small pinhole, *S*, located in the *x'y'* plane, allows only a small area of the source to pass to an *xy* plane a distance *R* away. The two positions P_1 and P_2 on the *xy* plane have coordinates (0, 0) and (*x*, *y*) respectively. Figure (2.13) describes a situation similar to that in fig. (2.12); equation (2.28) defining the complex degree of coherence $\gamma_{12}(\tau)$ applies. For the case of $\tau = 0$ and with the points P_1 and P_2 located as in fig. (b), $\gamma_{12}(0) \equiv \mu_s(x, y)$ can be written as

$$\mu_s(x,y)=\frac{\int_{-\infty}^{\infty} \boldsymbol{v}(0,0,t)\,\mathbf{v}^*(x,y,t)\,dt}{\left[\left(\int_{-\infty}^{\infty}\mathbf{v}(0,0,t)\,\mathbf{v}^*(0,0,t)\,dt\right)\left(\int_{-\infty}^{\infty}\mathbf{v}(x,y,t)\,\mathbf{v}^*(x,y,t)\,dt\right)\right]^{1/2}} \quad , (2.33)$$

where μ_s is the *complex degree of spatial* (*transverse*) *coherence* of the apertured source as measured in the *xy* plane.

By means of the van Cittert-Zernike Theorem the degree of spatial coherence is expressed as the magnitude of a normalised Fourier transform of the intensity distribution over the pinhole:

$$\left|\mu_s(x,y)\right|=\left|\frac{\int_{-\infty}^{\infty}\int_{-\infty}^{\infty} I(x',y')\exp[2\pi i(\xi x'+\eta y')]dx'dy'}{\int_{-\infty}^{\infty}\int_{-\infty}^{\infty} I(x',y')dx'dy'}\right| \quad , (2.34)$$

where $\xi = x/\lambda R$, $\eta = y/\lambda R$ and λ is the mean wavelength of the radiation emitted by the source. The validity of the theorem depends on the following assumptions:

1. The radiation from the source is quasi-monochromatic; i.e. λ is much greater than the deviation $\Delta\lambda$.
2. The separation *R* between the pinhole and the *xy* plane is much greater than the extent of the pinhole or the distance *r*.
3. The radiation inside the pinhole is spatially incoherent
4. The coherence length of the source radiation $c/\Delta f = \lambda^2/\Delta\lambda$ is much greater than the maximum difference in optical paths between either of the sampling

points and any point in the source. (Here f is the temporal frequency).
The assumptions are all satisfied with relative ease even when using soft X-rays from a synchrotron source using modest spectral filtering.

If the intensity of the source is assumed to be uniform over the circular pinhole of radius r_0, integration of equation (2.35) yields

$$|\mu_s| = \left| \frac{2J_1(\pi r_0 \theta / \bar{\lambda})}{\pi r_0 \theta / \bar{\lambda}} \right| \quad , (2.36)$$

where J_1 is a Bessel function of the first order. Figure (2.14) is a plot of $|\mu_s|$ versus $\pi r_0\theta/\lambda$. Figure 2.14 shows that $|\mu_s|$ decreases steadily from unity when $\pi r_0\theta/\lambda = 0$ to zero when $\pi r_0\theta/\lambda = 3.83$. A further increase in $\pi r_0\theta/\lambda$ re-introduces a small amount of coherence, but the degree of spatial coherence remains smaller than 0.14. The function $|\mu_s|$ decreases steadily from unity for $\pi r_0\theta/\lambda = 0$ to 0.88 when $\pi r_0\theta/\lambda = 1$. A departure of 12 percent or less from the maximum value of unity can be regarded as sufficiently close approximations to full coherence [40].

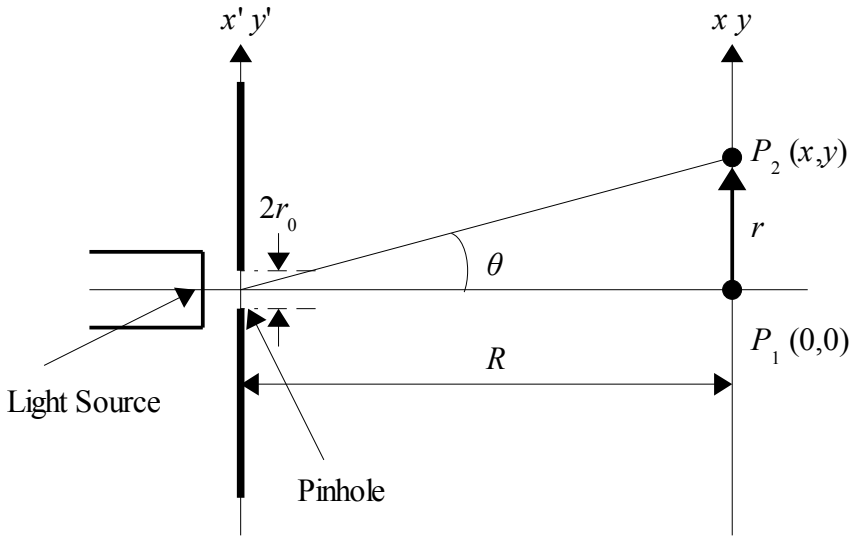

Figure 2.13: Geometry related to discussion of the spatial coherence of a light source.

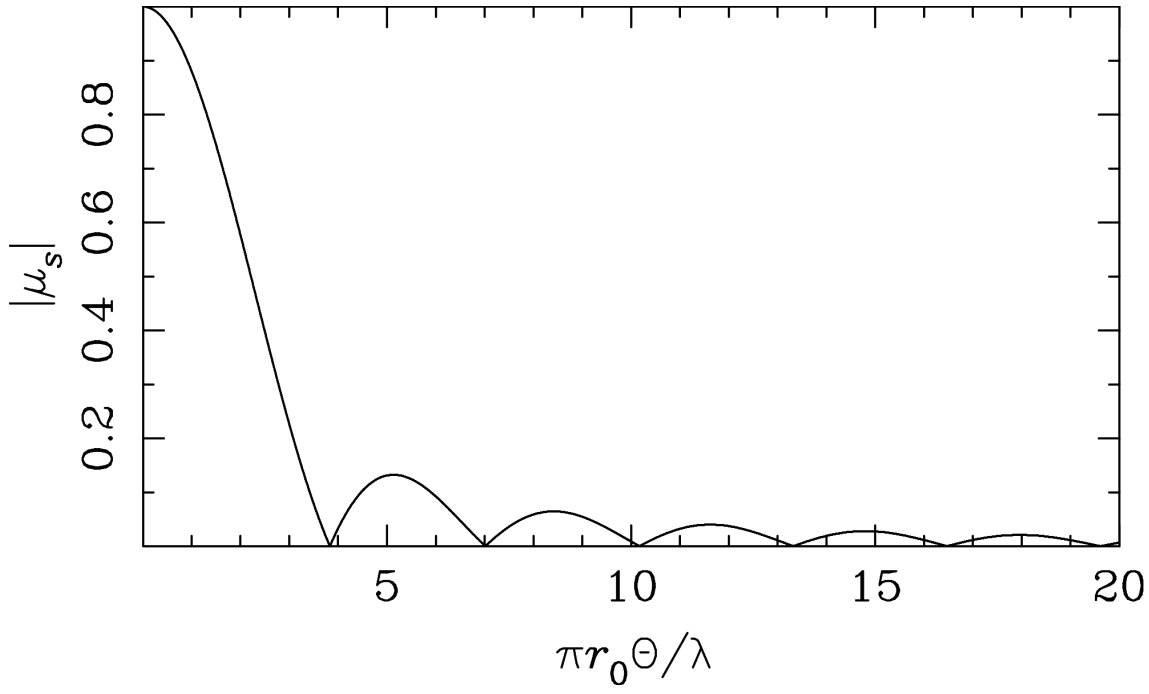

Figure 2.14: Degree of spatial coherence for a circular pinhole versus $\pi r_0 \theta / \lambda$.

Chapter 3

Commissioning of Beamline I07

3.1 Introduction

With the increasing availability of third-generation synchrotron facilities, surface X-ray diffraction has become an important tool for structural and morphological characterisation of surfaces and interfaces [1, 41, 42]. Because of the low scattering cross-section of X-rays, kinematical scattering theory applies and the interpretation of scattered X-rays is relatively straightforward. The major drawback of the low scattering cross-section is the weak scattering signal, which has been overcome by the brightness of the synchrotron radiation.

Initial analysis using surface X-ray diffraction emphasised the in-plane projected structure factor, but were typically less sensitive to the positions of the atoms perpendicular to the surface [43]; this was mainly dictated by the designs of the diffractometers and sample chambers that only allowed limited perpendicular momentum transfer. However, more recent diffractometers have extra degrees of freedom (on the detector) enabling a wide range of perpendicular momentum transfer to be reached and thus allowing atomic coordinates to be determined with high accuracy.

Beamline I07 at the Diamond Light Source is a high resolution X-ray diffraction beamline for investigating the structures of interfaces and surfaces under different environmental conditions. The beamline has a (2+3)-type diffractometer [44], which combines the ideal resolution behaviour of a *z*-axis (fixed angle of incidence) diffractometer [45] with the mechanical simplicity and range of a (2+2)-circle diffractometer.

As of February 2010, the beamline was operational but was in optimisation mode. The purpose of this chapter was to commission the diffractometer by comparing CTR scattering, from a Si bicrystal, obtained using the various types of rodscan and detectors. After a brief description of the beamline, diffractometer and methods of

obtaining data, a crystal truncation rod is presented for the various scan types and compared. Finally, any alignment issues of the diffractometer are examined.

3.2 Beamline I07

Beamline I07, at the Diamond Light Source, Didcot, UK, is a purpose built beamline for the study of interfaces and surfaces by X-ray diffraction. The X-ray source (fig. 3.1) has a U23 undulator capable of producing highly collimated and intense beams. After passing through the white beam slits, the beam enters a double-crystal silicon monochromator; two crystals with a common, horizontal axis of rotation. The monochromator tunes the X-ray energy and focuses the beam in the horizontal direction. The two mirrors after the monochromator remove unwanted harmonics and focusses the beam in the vertical and horizontal direction respectively.

A (2+3)-type diffractometer is mounted on the beamline. The (2+3)-type diffractometer combines the ideal resolution behaviour of a *z*-axis diffractometer with the mechanical simplicity of the (2+2)-circle diffractometer [44]. Vlieg shows in [44] that the *z*-axis and (2+2)-circle geometries can be made fully equivalent by an additional azimuthal degree of freedom of the detector. The (2+3)-type diffractometer (fig. 3.2) has five degrees of freedom: α and ω for the sample only and δ, γ and υ for the detector motion. The angle of incidence is set by α, the sample azimuth by ω. The direction of the outgoing wavevector is determined by angles δ and γ. The beamline control software performs all the necessary angle calculations to enable measurements to be taken at the desired points in reciprocal space [47].

The diffractometer can be equipped with several detectors. The two detectors used in this experiment are a Cyberstar scintillation detector and a PILATUS 100K detector. The Cyberstar scintillation detector is a point detector and has several advantages; it has good energy resolution, low dead time, can cope with high count rates [48] and does not require cooling. The PILATUS detector [49, 50] is a hybrid pixel array detector. A hybrid pixel detector is composed of a silicon sensor, which is a two-dimensional array of pn-diodes, connected to an array of readout channels designed with advanced CMOS technology. The advantages of hybrid pixel detectors can be summarized as: “zero noise” provided by energy threshold capability of the photon

counting electronics, a high dynamic range, allowing for simultaneous observation of weak scattering and high intensity diffracted peaks, high quantum efficiency and short readout times. The PILATUS area pixel detector operates in single-photon counting mode. The parameters of the PILATUS detector are shown in table 3.1.

There are a series of attenuators that are installed behind the samples and just in front of the detectors. These attenuators are controlled remotely by the beamline software. The beamline software can be configured to manipulate the attenuators automatically so that continuous scans can be made without having to pause for filter settings to be changed.

Samples are mounted on a hexapod that has several motor movements (fig. 3.3). Translational movements are along x, y and z while the rotations are given by r_x, r_y and r_z.

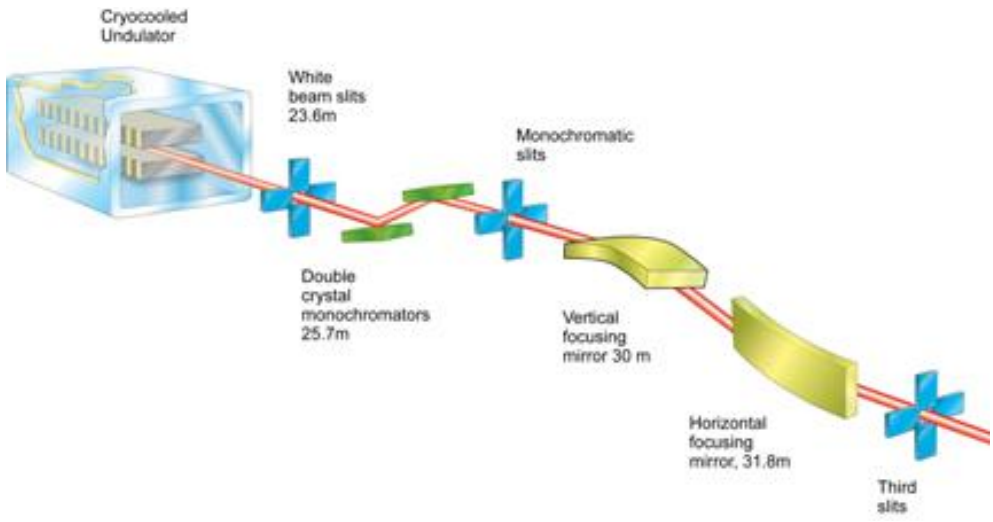

Figure 3.1: The X-ray source of beamline I07. The cryocooled undulator was installed during the summer of 2010 after the experiments had taken place. Before this a U23 undulator was in place, and was capable of producing energies up to 20 KeV. After [46].

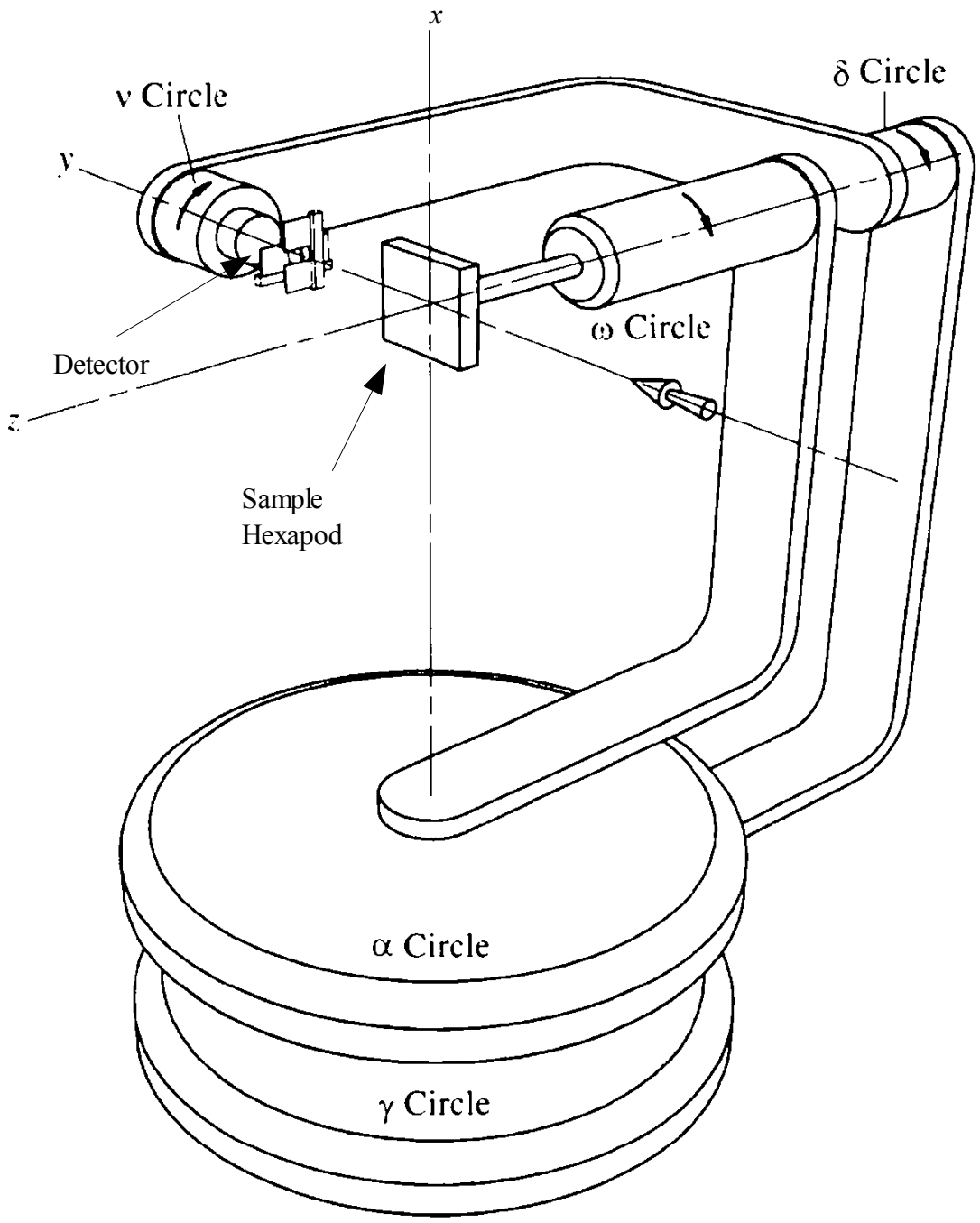

Figure 3.2: Schematic of a (2+3)-circle diffractometer. This has the same geometry as the (2+2)-type, but with the addition of a υ circle for the azimuth of the detector and slits. After [44].

Sensor	Reverse-biased silicon diode array
Active Area	83.8 mm x 33.5
Number of Pixels	94965
Pixel Size	0.172 mm x 0.172 mm
QE at (i) 8 KeV (ii) 15 KeV	(i) 99% (ii) 55%
Readout time	2.7 ms
Frame Rate	300 Hz
Energy Range	3-30 KeV
Dynamic Range	20 bit

Table 3.1: Parameters of the PILATUS 100K detector system [51]

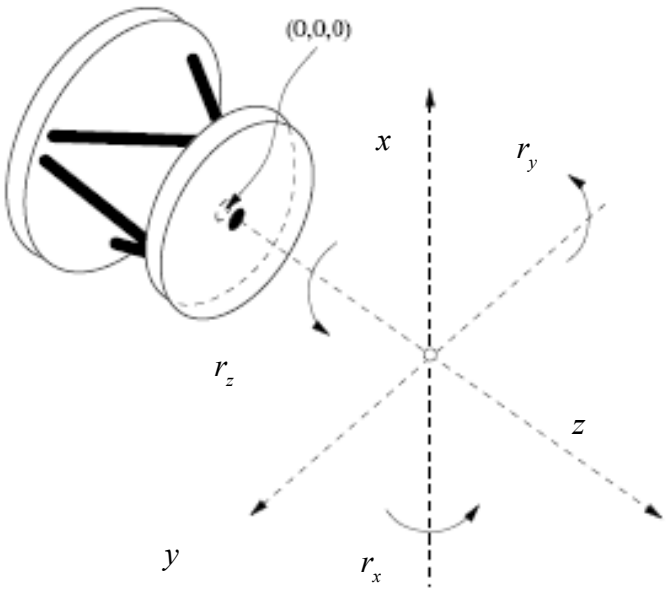

Figure 3.3: Motor movements of the hexapod. After [52].

3.3 Aligning the Diffractometer

In order to record a CTR we require concerted movement of at least three motor

movements (ω, δ and γ). The alignment procedure [52] involves positioning the entire diffractometer relative to the direct X-ray beam; zeroing the diffractometer movements; aligning the sample interface; and accurately obtaining the angles for the Bragg reflections used to calculate the orientation matrix. The use of the PILATUS detector makes the alignment process different and simpler (most notably in the diffractometer alignment and obtaining reflections of the orientation matrix) compared to using traditional point detectors. In order to prevent beam damage to the PILATUS detector all filters were in place.

3.3.1 Aligning the Detector

The first step in the alignment process was to align the detector. All angles were 0^{o}. The position of the direct beam on the detector was recorded and assigned the coordinates (x_1,y_1). The detector was rotated around its own axis, υ, by 180^{o} and the new position of the beam observed; which had coordinates (x_2,y_2). The centre of the υ rotation was at (x_1+x_2)/2, (y_1+y_2)/2. The values of δ and γ were changed until the direct beam was at the centre of rotation and δ and γ were zeroed.

The zero of υ was found by rotating γ so that the direct beam was close to one side of the area detector and the beam height recorded. The beam was moved to the other side of the detector. If the height remained constant, then this was the zero position of υ. If the height changed then υ was changed and the above process is repeated until the beam height was constant, at which point υ was zeroed.

3.3.2 X and Y Centering

The next procedure was to centre the sample in x and y so the direct beam passed through the centre of the sample. The sample used in this chapter is the same Si bicrystal studied in chapter 4. All diffractomer angles were 0^{o}. The beam was scanned as the hexapod moved in x and then y. The direct beam passed through the middle of the sample when the beam profile was at a minimum (fig. 3.4). The hexapod was moved to the x and y positions of the minimum. The process for aligning z is described in chapter 4.

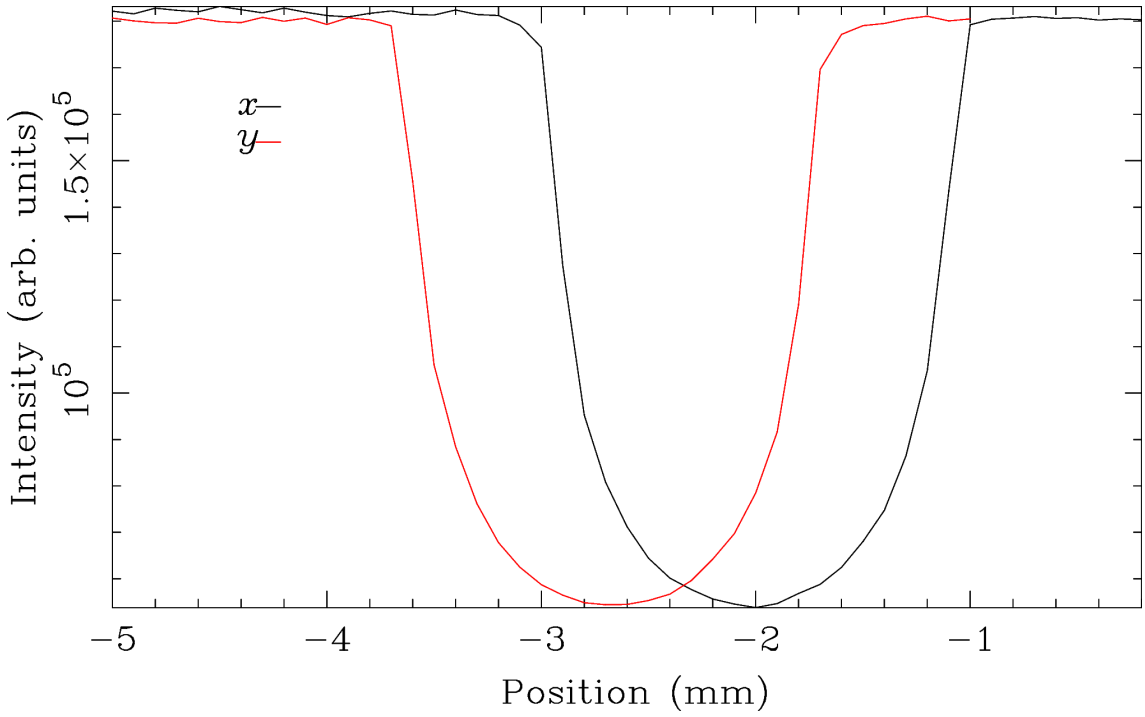

Figure 3.4: A scan across the direct beam profile for the position of the hexapod in *x* and *y*. Note that when the sample is centered in both *x* and *y* there is still 33% transmission through the sample at a beam energy of 22.65 KeV.

3.3.3 Sample Angular Alignment

The rotation of the sample in *x* and *y* (r_x and r_y respectively) was aligned by rotating either r_x or r_y for a given value of ω until a peak was found; ω was then rotated through ± 180° and the above process repeated (fig. 3.5). In each case the value of r_x and r_y for which the peak occurred were noted and the values of r_x and r_y were centred accordingly between these values.

3.3.4 Incoming Angle

Once all of the angles were aligned, the diffractometer was moved to some 2θ position; α was aligned simply by rotating it until a peak was measured (fig. 3.6).

3.3.5 Obtaining Reflections for the Orientation Matrix

Diffraction experiments require precise knowledge of the orientation of the crystallographic axes in the fixed frame of the diffractometer, in order to navigate reliably in reciprocal space [53]. This requires an orientation matrix, which is calculated from the motor positions for at least two well defined positions in reciprocal space [53]. Obtaining the diffractometer angles for Bragg reflections was relatively easy using the area detector. The beamline software controlling the diffractometer calculates the motor angles for a given Bragg Peak (*hkl*). The angles γ and δ are fixed but ω can be out by many degrees. The Bragg Peak was found by rotating ω until the Bragg peak was seen on the area detector. The position of the Bragg peak was found at the maximum intensity (fig. 3.7).

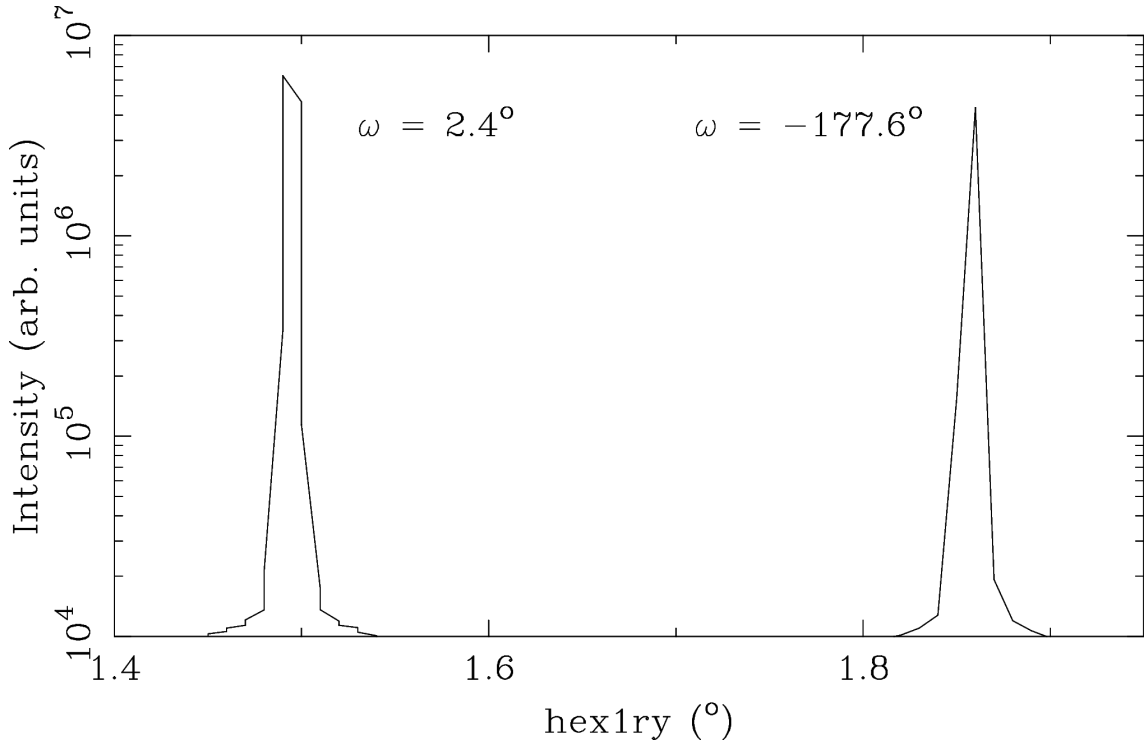

Figure 3.5: Sample angular alignment. The sample was rotated until a Bragg peak was located for a given ω value. ω was rotated through ± 180° and the process repeated until the peak was located. The hexapod was then centred.

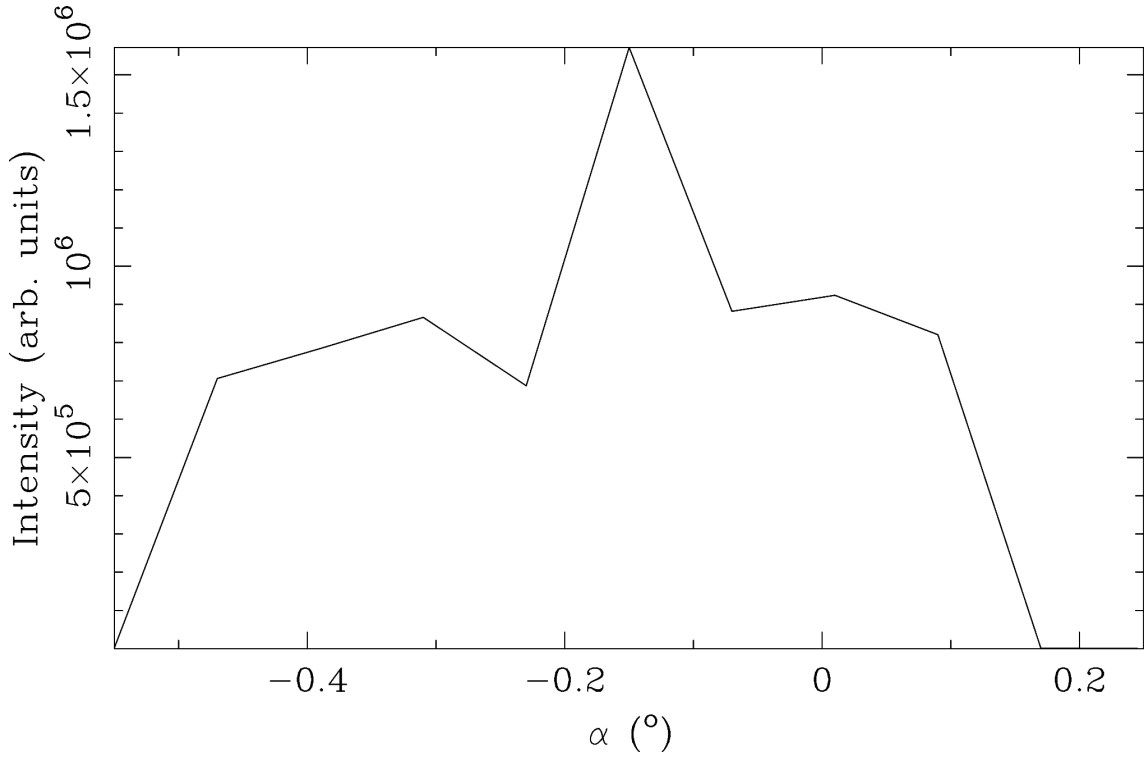

Figure 3.6: Aligning the incoming angle on a Bragg peak.

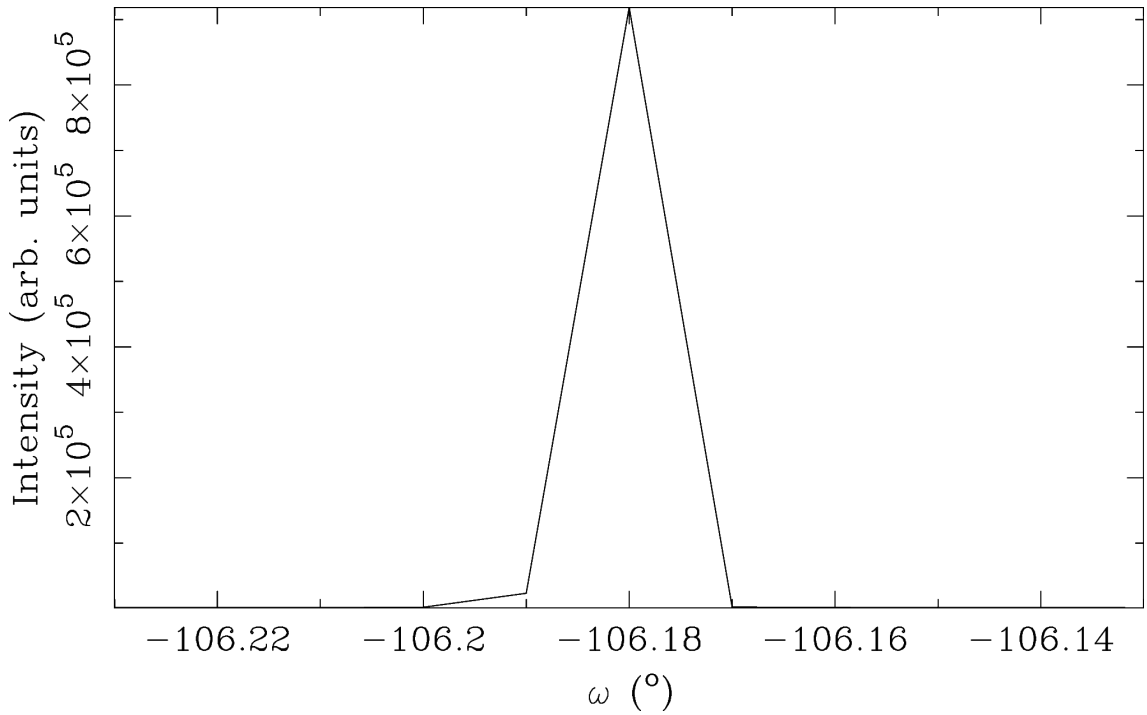

Figure 3.7: The sample was rotated until the Bragg peak was seen on the area detector. The position of the Bragg peak was found at the maximum intensity.

Once ω was optimised, it was often seen that the Bragg peak was no longer centred on the area detector. The angles α, δ and γ were scanned over a small range until the Bragg peak was centred. The experiments were performed in z-axis mode with a fixed angle of incidence of 0^{o}.

Once all the angles were aligned the Bragg peak can be added to a list of reflections that are used to obtain the reflection matrix. The procedure of obtaining the orientation matrix using the area detector is considerably faster than using the point detector because (i) no detector scans need to be recorded to ascertain the maximum of the Bragg peak and (ii) the large area detector makes it probable, using the first estimate for the angle settings, that the peak will be visible. By tracking the Bragg Peak as ω is rotated, the position of the Bragg peak can be established very rapidly.

3.4 Rocking and Constant Velocity Scans

The integrated intensity of a CTR is measured at a certain height along a rod (i.e. at a certain momentum transfer in the direction normal to the surface or interface). The integration is performed over a finite slice of the rod determined by the acceptance of the detector arrangement which depends on experimental parameters (see appendix section A2) [24]. The integrated intensity of the rod is measured in a scan, which starts away from the rod at the background level, going through the peak intensity of the rod and ending again on the other side of the background level. The background-subtracted, total sum of detected photons is then a measure of the integrated intensity [24]. The scan is performed by rotation of the crystal around an axis normal to the scattering plane with the detector fixed (fig. 3.8). This scan is known as an ω-scan. There are two types of this scan; the rocking scan, where the sample is rocked about its surface normal and for each ω the photons are counted for a specified time, and the constant velocity (c.v.) scan, where the sample rotates about its surface normal at a constant velocity. The potential benefits of the c.v. scan are that the scans are faster as there is no settling time of the diffractometer and it does not miss sharp peaks, however, one potential draw back is the peak shape may not be accurately captured.

The rocking and c.v. scans were performed by orientating the detector and sample to fulfil the (*hkl*) diffraction condition and then rotating the sample around its

surface normal in positive and negative ω values. During the rotation the intensity was measured by a scintillation detector. For each rocking scan, approximately 50-200 data points were measured for each l height. The number of data points was dependent on the range and increment of ω. In order to track the diffraction feature with the detector, the δ and γ motors of the detector arm and the sample rotation ω must move in a concerted manner as a function of l [53]. The integrated intensity was obtained using the program ANA [54].

First a scan was read into ANA, and either a Lorentzian or Gaussian line shape was fitted to the data. This gives a measure of the background at the left and right of the peak for each scan. The peak was integrated numerically to give the integrated intensity. ANA saved the integrated intensity and error for each value of l. When there was a clear peak in the data set the background is obtained easily. However, when the signal to noise ratio worsens, care was taken that the peak fitting obtained a good estimate of the background.

At values of l close to the Bragg peak care was taken when integrating the peak. As the sample rotated in ω the point detector measures both the CTR and the Bragg peak. The background in this case became curved, increasing as it approached the CTR. The background was incorrectly predicted when a Gaussian was fitted to it and the subsequent integrated intensity was incorrect. The solution was to delete the background points and integrate over just the peak. The error in this measurement was then just the square root of the intensity.

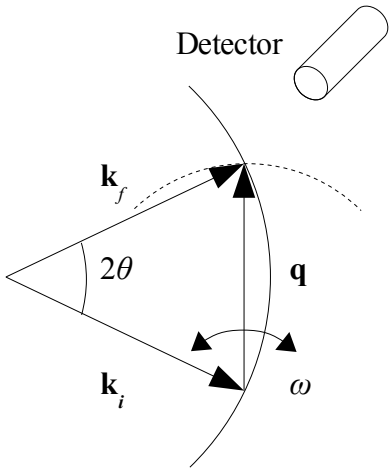

Figure 3.8: Rocking scan (ω-scan). The crystal was rotated about an axis normal to the scattering plane spanned by $\mathbf{k}_i$ and $\mathbf{k}_f$. Diffraction was obtained when $\mathbf{q}$ is intersecting the Ewald sphere and $\mathbf{q} = \mathbf{k}_f - \mathbf{k}_i$.

3.5. Stationary Scans

The stationary scan, so called because the sample does not need to be rotated about its surface normal, accepts the entire in-plane component of the rod, for a given height l, by use of the PILATUS detector. The integrated intensity is found by obtaining the signal S; accomplished by drawing a box that contains the entire CTR and then integrating over all the pixels in the region of interest (ROI) [53]. The background B is obtained in the same manner. The integrated intensity is obtained by subtracting the background from the signal:

$$I = S - B \quad , (3.1)$$

where B is scaled by N_s/N_b where N_s is the number of pixels in the the signal ROI and N_b is the number of pixels in the background ROI. This process is illustrated in fig. 3.9. An advantage of the area detector is that the size and positions of the ROI are user defined, and if an artifact is present that contributes to the signal, the ROI of the background can be appropriately placed on the artifact such that the integrated intensity is not affected.

Photon counting is a Poissonian process [55]. Whilst counting photons the

variance on an observed quantity of photons Q is the number of photons (var(Q) = Q). The standard deviation, σ(Q), is the square root of the variance. It follows for the integrated intensity that

$$\mathrm{var}(I) = S + B \text{ . (3.2)}$$

The relative error is the standard deviation of the integrated intensity divided by the integrated intensity, and is given by

$$R_{err} = \frac{\sigma(I)}{I} \text{ . (3.3)}$$

The relative error reduces to $S^{-½}$ when B equal to zero. It is clear that high values of S and low values of B give the smallest relative error.

3.5.1 Detector Slit Size

The slits immediately after the sample were fully open up to this point. The horizontal separation (x) was 17.935 mm and the vertical (y) 22 mm, when fully opened. The signal to noise ratio was investigated by varying the horizontal and vertical widths (fig. 3.10). The intensity of the CTR at (2.35,0,2.07) was measured for a counting time of 100 seconds. The signal to noise ratio (SNR) is derived from the signal and background, calculated in the manner presented in section 3.5, and is given by the ratio of the two. The SNR ratio of fig 3.10(a) is 3.669, (b) is 4.183, (c) is 4.083 and (d) is 3.933. Changing the widths of the detector slits has little effect on the SNR. There is always a signal measured outside of the slit region by the area detector; a result of scattering from the slits.

3.5.2 Beam Slit Size

Prior to this stage the slits in front of the sample were fully open. This can lead to an increase in the background noise from things like diffuse scattering; which can be

minimised by changing the distance between the beam slits. The diffractometer was moved to the CTR at (2.35,0,2.07). The intensity was measured for a slit gap of 200 μm and then every 2 μm until the slits were fully closed (fig. 3.11). The counting time was kept constant at 100 seconds for each scan. The background decreases steadily with decreasing slit size, the signal behaves similarly to about 30 μm at which point the signal is approximately constant until the slit distance is 20 μm at which point the signal falls to zero rapidly. The difference between the two is approximately constant as the slit size decreases, but there is a clear increase at 24 μm. The slit size is kept at 24 μm throughout the experiment as it gives the largest intensity.

3.6 Correction Factors

The structure factors, $|F_{hkl}|$, are derived from the integrated intensities by application of various correction factors. The correction factors are dependent on the diffractometer geometry and the scan type used [43, 44].

The integrated intensities of the rocking and c.v. scans, I_ω, and stationary scan, I_s, are given in their final forms below:

$$I_\omega = \frac{\Phi_0 r_e^2 A_0 \lambda^2 \Delta\gamma}{\omega_0 A_u^2} |F_{hkl}|^2 P L_\omega C_{rod} C_{area} C_{atten} \quad , (3.4)$$

$$I_s = \frac{\Phi_0 r_e^2 A_0 \lambda^2 T}{A_u^2} |F_{hkl}|^2 P L_s C_{area} C_{atten} \quad , (3.5)$$

where Φ_0 is the incident flux (photon s^{-1} mm^{-2}), ω_0 is the rotation speed, A_0 is the active surface area, A_u is the area of the unit cell, r_e is the classical electron radius, T is the total counting time, $\Delta\gamma$ is the angular acceptance of the detector, P is the polarisation factor, $L_{\omega(s)}$ is the Lorentz factor for the rocking (stationary) scan, C_{rod} is the correction for the rod interception, C_{area} is the area correction and C_{atten} is the absorption correction. The correction factors are discussed in more detail in the appendix (section A.2).

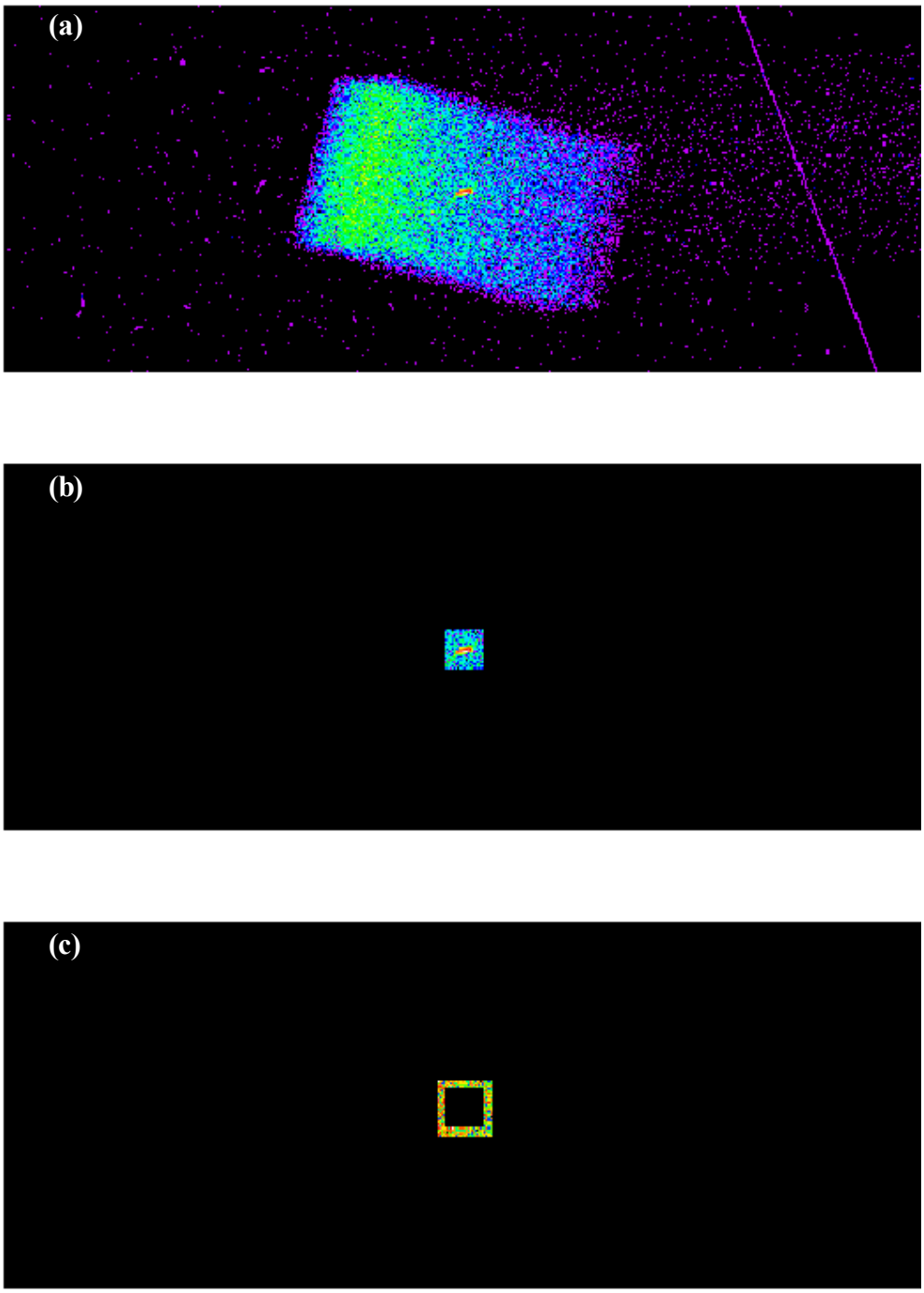

Figure 3.9: This figure illustrates how the integrated intensity is obtained from the area detector. (a) The CTR. (b) A region of interest that encapsulates the CTR is integrated giving the entire signal. (c) The background is then measured from a second ROI and subtracted from the signal.

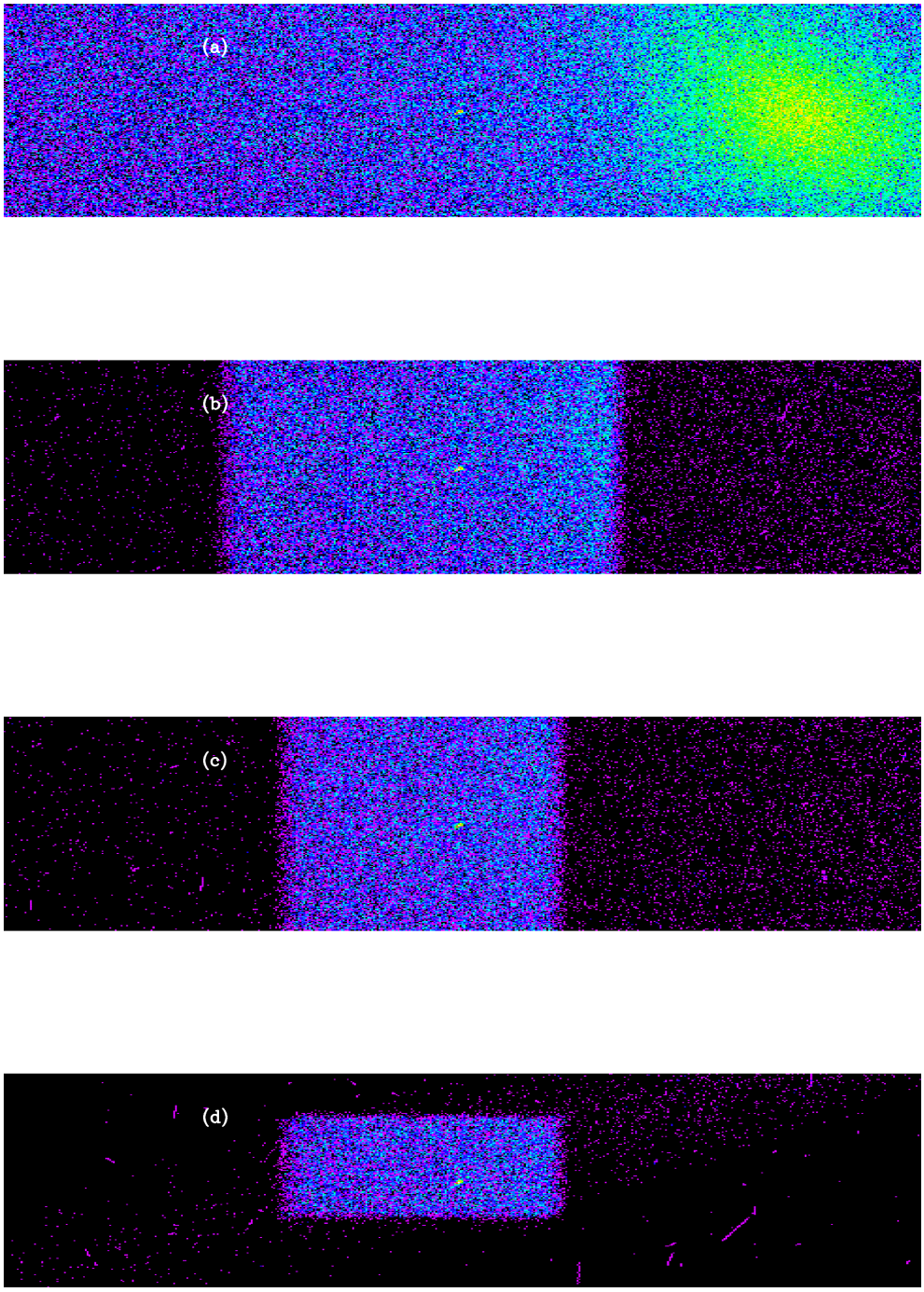

Figure 3.10: The signal of the CTR at (2.35,0,2.07) and the background is calculated for the various detector slit sizes: (a) x =17.935 mm, y = 22 mm, (b) x =5 mm, y = 22 mm, (c) x =3 mm, y = 22 mm and (d) x =3 mm, y = 3 mm.

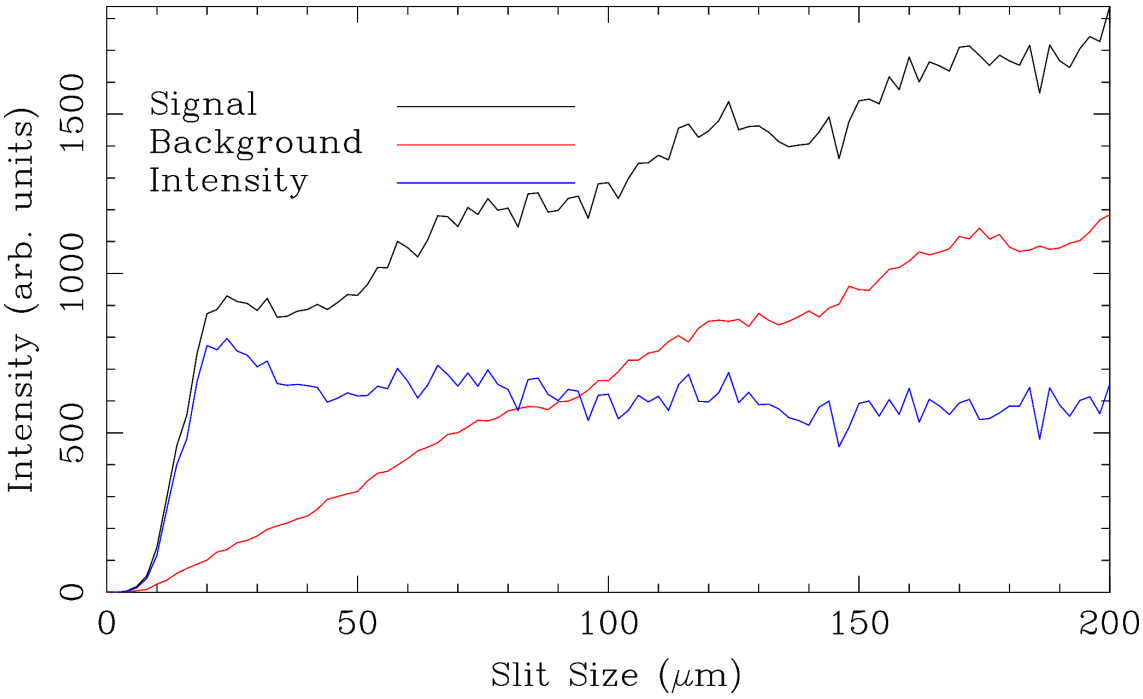

Figure 3.11: The difference between the measured signal and background as a function of the sample slit size.

3.7 Comparison of the Stationary and Rocking Scans

To compare the rocking and stationary rodscans two different comparisons of the rod along the $(22\bar{4})$ Bragg peak were performed. The first compared the signal to noise ratio (SNR) of the integrated intensities and structure factors obtained by the different scans under identical conditions.

Thirteen data points were measured along the rod. The rocking scan comprised of two parts; a background and a peak scan. The background scan scanned a range of ω 1° either side of the peak, whereas the peak scan had a range of 0.05° either side. A total of 92 data points were measured for each point along the rod.

The integrated intensities of the two modes are shown in fig. 3.12(a). The integrated intensity increases at l = -4.06 as the total counting time increased from 150 to 524 seconds. Between l = -4.12 to -4.16 there was a large increase in the integrated intensities for all modes. This is explained by viewing figs. 3.13 to 3.14. Figure 3.13 shows the images obtained by the stationary scan at different l along the rod. At l =

-4.12 an artifact is present and the passage across the CTR is shown from l = -4.14 to -4.18. The integrated intensity increases at l= -4.16 for the stationary mode, because the artifact cannot be distinguished from the rod in the box subtraction method. However, we can conclude that the intensity is anomalously large due to the artifact and this data point can be deleted accordingly.

Figure 3.14 shows the peak scans of the rocking mode. At l = -4.14 the peak of the rod is engulfed by that of the artifact and the subsequent integrated intensity is incorrect. At l = -4.16 the artifact and the rod can be distinguished and the integrated intensity is found by deleting the points associated with the artifact. However, this can only be done in confidence as we know the larger peak is spurious from the area detector. The scattering from the artifact is roughly ten times more intense than the rod.

The structure factors (fig. 3.12(b)) are found by applying the relevant correction factors and normalising for counting times. The discrepancies between the structure factors of the stationary scan, F_{hkl}^{S}, and the rocking scan, F_{hkl}^{ω}, are derived by calculating the R-factor:

$$R=\frac{\sum \left|F_{hkl}^{\omega}\right|-\left|F_{hkl}^{S}\right|}{\sum \left|F_{hkl}^{\omega}\right|} \quad , (3.6)$$

this is a measurement of the agreement between the two scan types and is expressed as a percentage. The obtained value of R 5.09% suggests excellent agreement between the rocking and stationary scans.

The statistics of each scan are shown in tables 3.2-3.3. The integrated intensities of the stationary mode are always approximately several orders of magnitude larger and the relative error stays below 5%. The intensity is much larger as the integrated intensities obtained by the rocking mode have already been normalised to the total number of counts Φ_0 by ANA. The relative error of the rocking scan increases from under 7% close to the Bragg peak to over 40% far from the Bragg Peak.

The statistical SNR is given by

$$SNR=\frac{I}{\sigma(I)} \quad . (3.7)$$

Table 3.4 shows the SNR for the scan types and is always largest for the stationary mode and is approximately 2.5-3 times larger close to the Bragg peak and greater than 6 times larger further from the peak. When the different modes have the same counting time; the stationary mode always has the largest signal, the smallest statistical error and the largest SNR even far away from the Bragg peak when the scattering from the CTR is weak.

The SNR of all the modes can be improved by increasing the counting time, t, and varies as a function of $\sqrt{t}$. For example if the counting time was increased fourfold the SNR would double. Generally the SNR is approximately 2.5 times larger for the stationary mode compared to the rocking mode, and for the two to be comparable, the counting time of the rocking mode would have to be increased a factor of 6.25. Assuming that a typical synchrotron experiment is allocated a beam time of 7 days and 50 points along each rod need to be measured, estimates on the total number of rods obtainable by each scan type can be made. If a counting time of 150 seconds is used on each point for the stationary mode, then an entire rod can be measured in 7500 seconds (2 hours and 5 minutes).

Taking the rocking mode to comprise of a background and peak scan, where the background and peak scans have the same characteristics mentioned earlier, and a total of 92 measurements taken; the total counting time at each point is t = (92*6.25 + 58) seconds (where the 58 seconds is the time taken to rock the sample); measurement of an entire rod takes approximately 8 hours and 47 minutes.

Assuming that the *entire* 7 days is spent working, then 80 rods can be measured with the stationary scan compared to 19 rods with the rocking scan Practically, the number of rods measured is less than this for all modes as things like sample preparation and the alignment procedure of the diffractometer have not been considered.

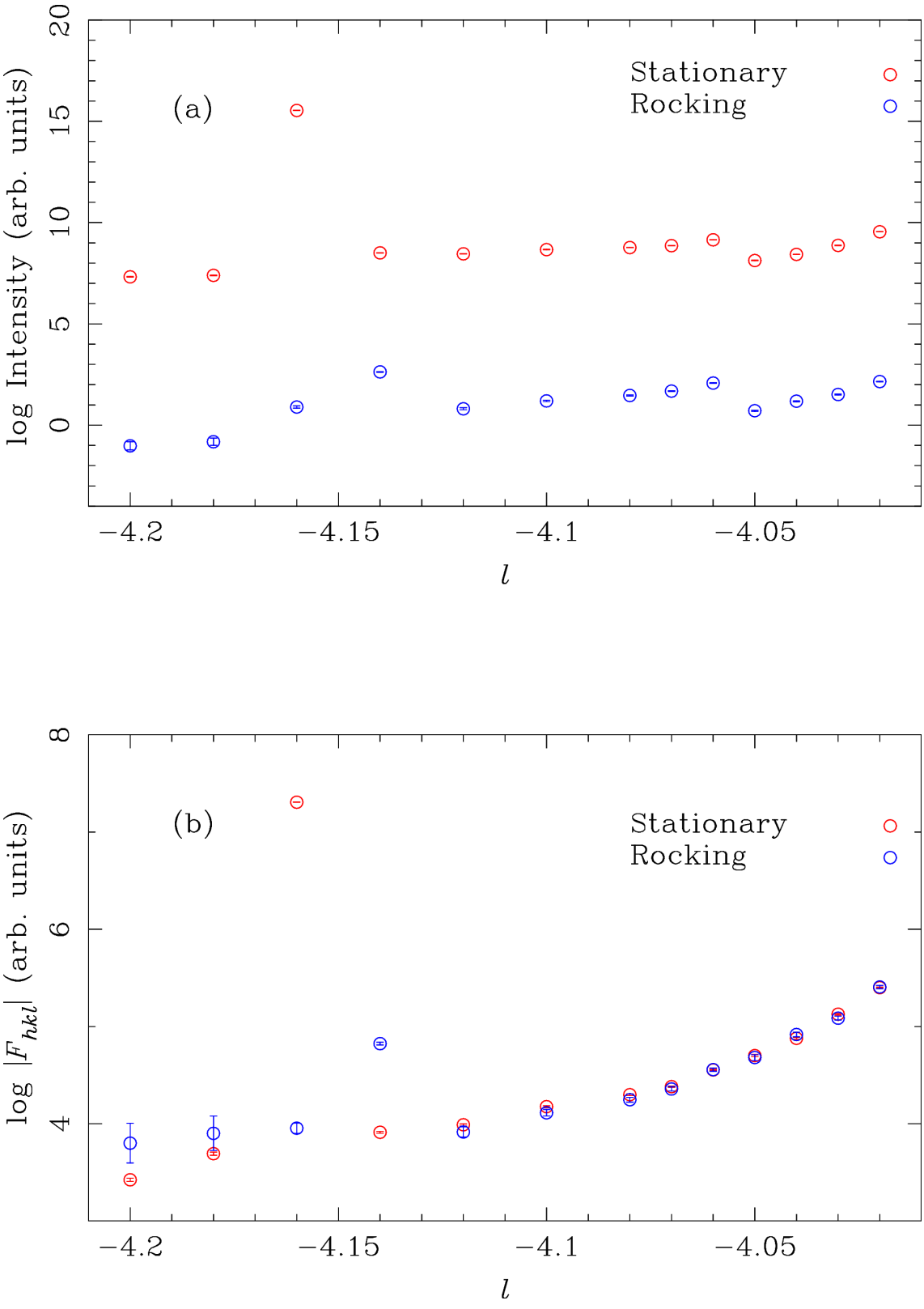

Figure 3.12: Comparison between the measured (a) integrated intensities and (b) structure factors for the stationary and rocking scans.

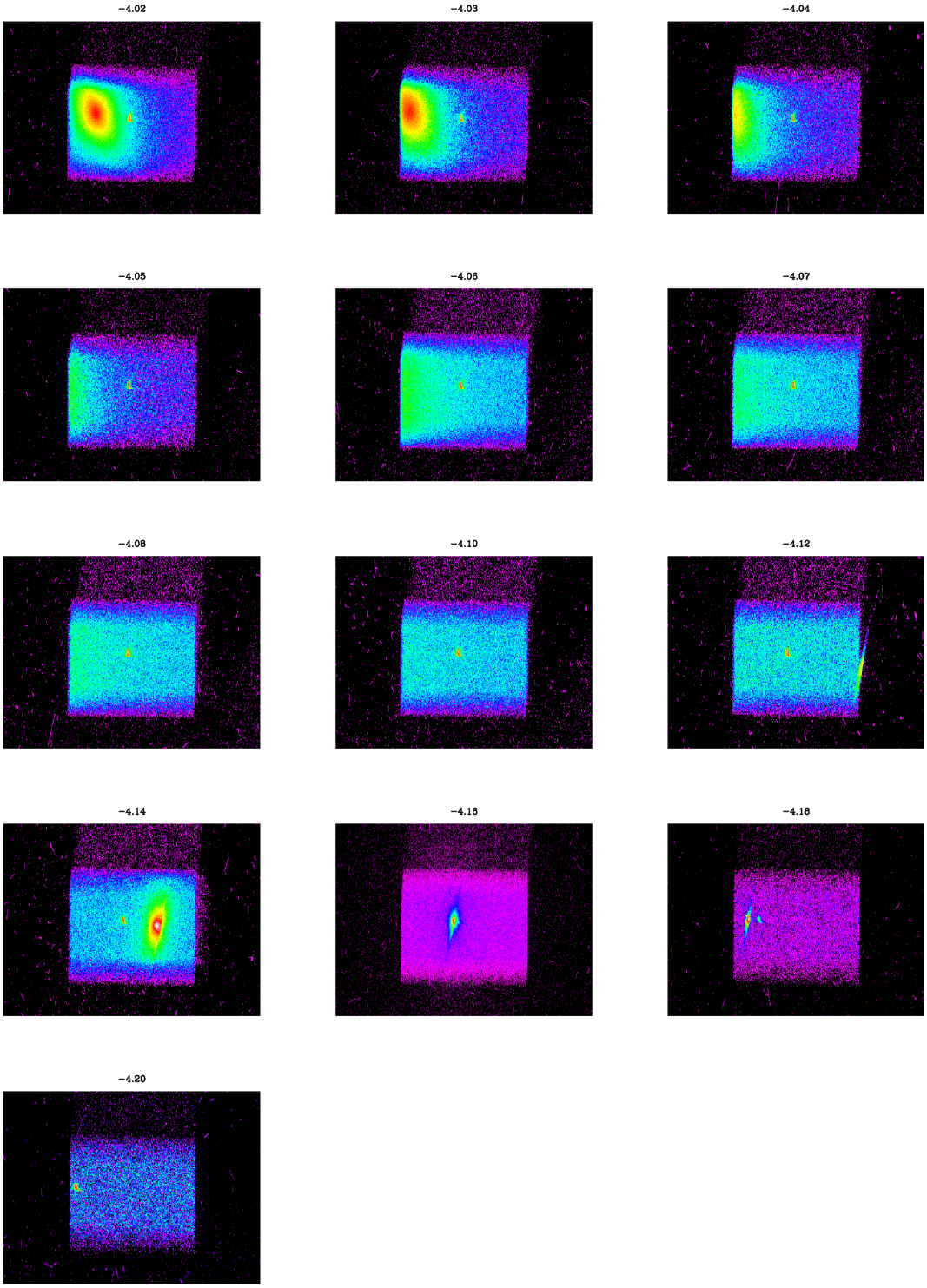

Figure 3.13. Images obtained by the area detector. The *l* values are displayed. Note the artifact moving across the detector for *l* = -4.12 to -4.18. An anomalously large signal is obtained if the artifact is not corrected for.

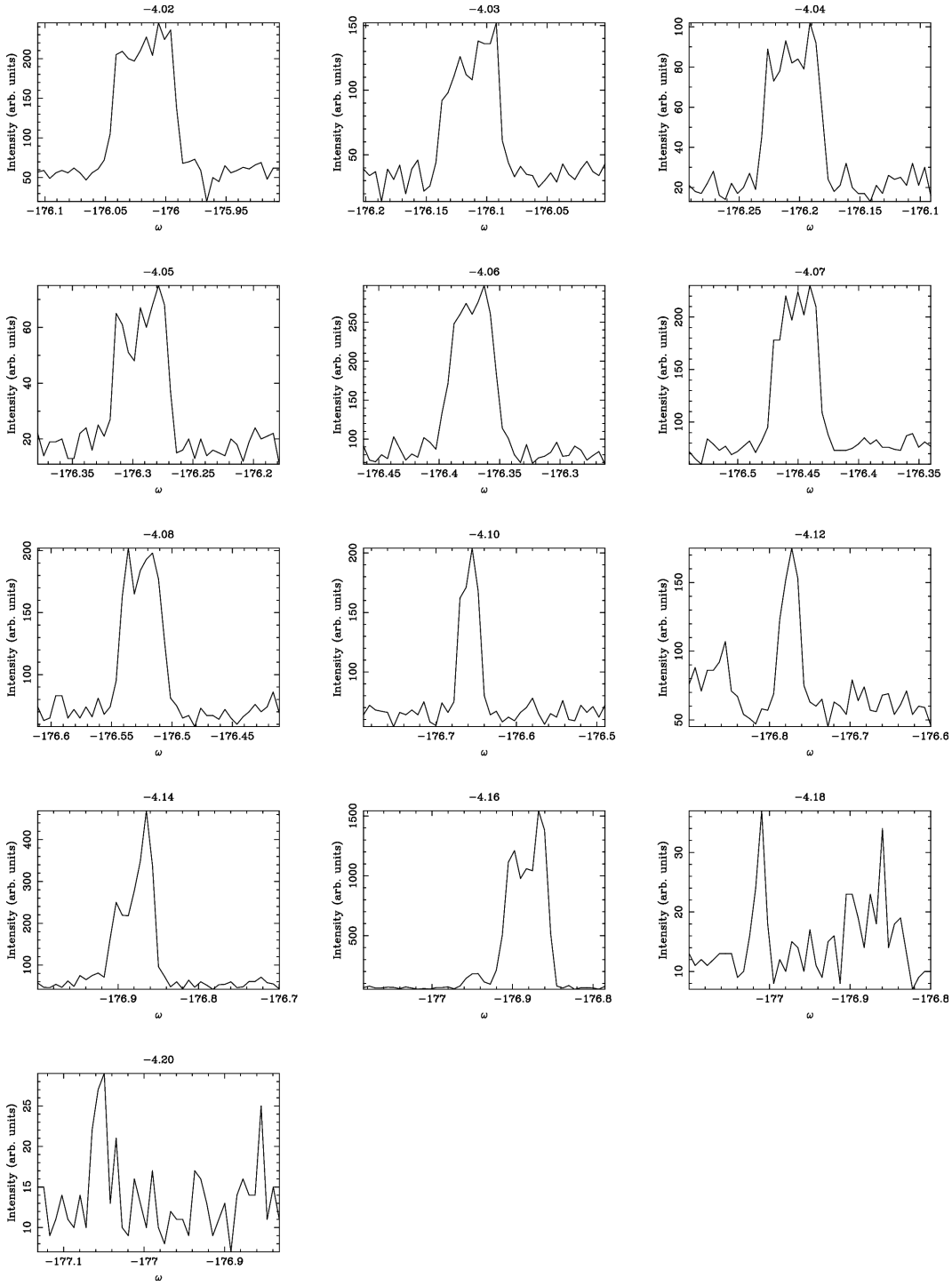

Figure 3.14: The peak scans of the rocking mode. The top hat shape of the curves indicates that the width is determined by the experimental resolution.

l	Time (s)	*S*	*B*	*I*	σ(*I*)	R_{err} (%)
-4.02	180	21597	7595.11	14001.88	170.86	1.22
-4.03	151	10208	3057.21	7150.78	115.17	1.61
-4.04	150	6766	2193.69	4572.31	94.66	2.07
-4.05	150	5134	1742.41	3391.59	82.92	2.45
-4.06	526	14438	5033.97	9404.02	139.54	1.48
-4.07	524	11126	4067.12	7058.88	123.26	1.75
-4.08	525	10519	4113.94	6405.06	120.97	1.89
-4.10	527	9594	3785.49	5808.51	115.67	1.99
-4.12	526	8147	3433.19	4713.82	107.61	2.28
-4.14	526	9067	4123.35	4943.65	114.85	2.32
-4.16	525	5640057	39378.52	5600678.48	2383.16	0.04
-4.18	151	2721	1101.40	1619.60	61.83	3.82
-4.20	150	2330	816.95	1513.05	56.10	3.71

Table 3.2: Statistics for integrated intensities obtained from area detector.

l	Time(s)	*I*	σ(*I*)	R_{err} (%)
-4.02	180	8.57	0.31	3.6
-4.03	151	4.54	0.21	4.6
-4.04	150	3.25	0.18	5.5
-4.05	150	2.03	0.14	6.9
-4.06	526	7.95	0.3	3.8
-4.07	524	5.36	0.27	5.0
-4.08	525	4.31	0.25	5.8
-4.10	527	3.31	0.26	7.9
-4.12	526	2.24	0.27	12.1
-4.14	526	13.86	0.44	3.2
-4.16	525	2.44	0.3	12.3
-4.18	151	0.44	0.18	40.9
-4.20	150	0.36	0.17	47.2

Table 3.3: Statistics for integrated intensities from ω scan.

l	Area	*ω*
-4.02	81.87	27.65
-4.03	62.18	21.62
-4.04	48.13	18.06
-4.05	40.87	14.5
-4.06	67.17	26.5
-4.07	57.39	19.85
-4.08	52.93	17.24
-4.10	50.08	12.73
-4.12	43.65	8.30
-4.18	26.13	2.44
-4.20	27.02	1.71

Table 3.4: Comparison of the SNR for the scan types.

In the second comparison the entire rod was measured with both scan types and the structure factors compared. The rod was measured from l = -4.21 to -3.75; 43 points were measured with the stationary mode compared to 26 with the rocking mode. The counting time was kept at 120 seconds for each point in the stationary mode. The rocking scans comprised of a background and peak scan and the counting time at each point varied between 0.5 and 2 seconds depending on the SNR.

The integrated intensities and structure factors are shown in figs. 3.15 (a) and (b) and those obtained with the rocking mode have been normalised for time. The stationary mode intensities are much larger than those obtained by the rocking mode; typically 1000 times larger; the R factor is 11.32% for the structure factors. This shows that the structure factors obtained by the two different modes are comparable. The statistical error associated with each point along the rod is smaller for the stationary mode. This is especially notable further from the Bragg peak where the error associated with the rocking mode is very large.

3.7.1 Alignment issues

Statistically, the stationary mode has the smallest relative error and largest SNR. However, due to misalignment issues with the diffractometer, the rod moves off the area detector at large distances away from the Bragg peak (i.e. as γ tends to 0^o). A direct result of this is that the stationary mode can not be left unattended for long periods of time or the user runs the risk of only measuring background. This is illustrated in fig. 3.13. For values of l less than -4.16 the rod rapidly moves off centre and to the left of the detector, hence the scans were terminated at l = -4.21.

This appears to be a fairly common problem and was observed for several rods, such as the (202) rod (fig. 3.16). The scan was terminated at l = 1.61 to stop the rod moving off the detector. The diffractometer was realigned by rotating ω until the rod was centred and a discrepancy in ω of 0.28^o was found. A new orientation matrix was calculated from this point and the scan continued (fig. 3.17) upon which the rod stayed centred. Later investigation of the specular alignment at the (0,12,0) Bragg Peak found α to be out by 0.042^o. There appears to be a misalignment between the sample and detector arms that causes the diffractometer to gradually lose steps in α and ω; leading to the CTR moving off the detector.

This misalignment can be overcome by recalculating the orientation matrix at the point where the rod slips off the detector. At this point the matrix is optimised at the ends of the rod but realignment needs to be performed close to the Bragg peak. Unfortunately this can be time consuming especially if this has to be done for every rod.

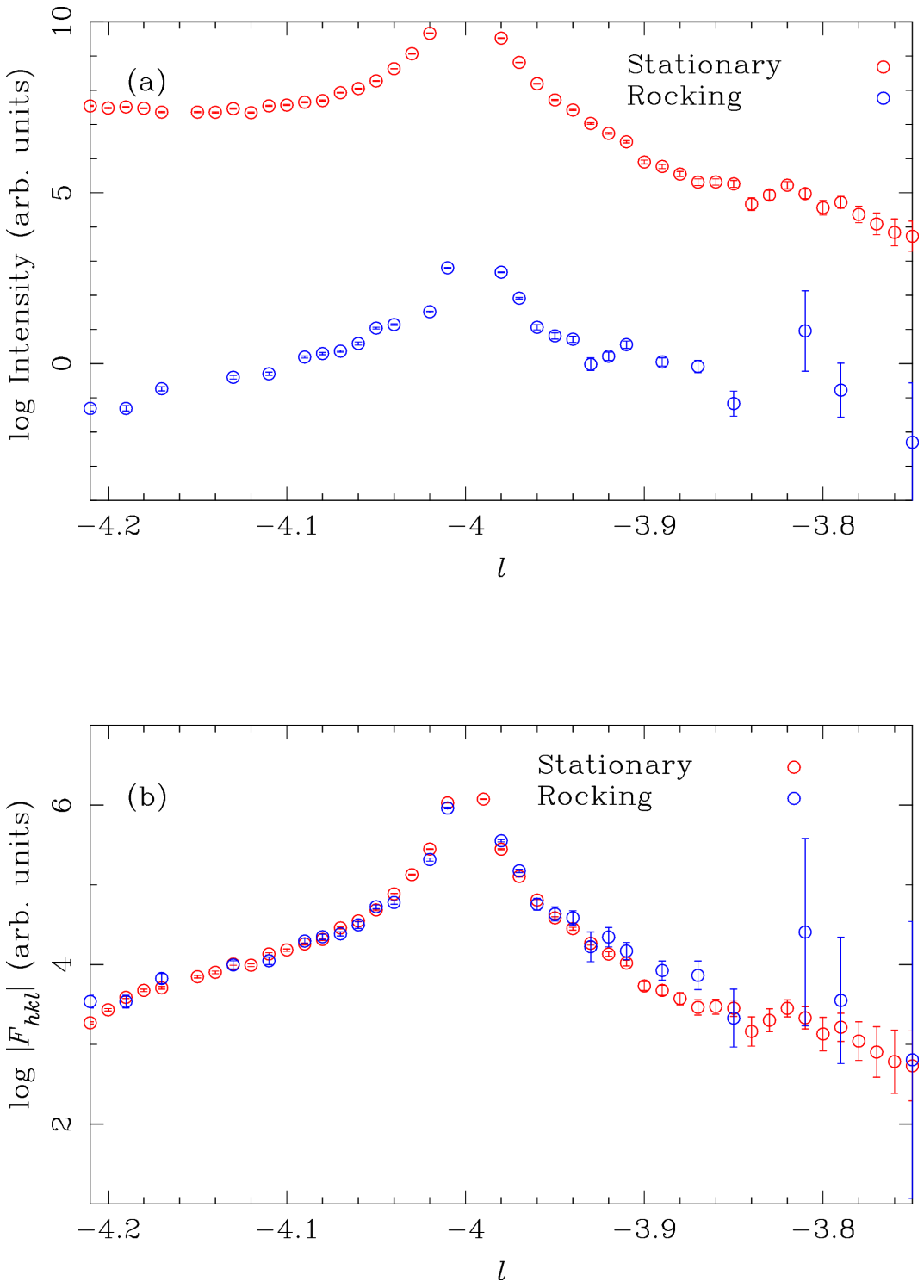

Figure 3.15: Comparison between the measured (a) integrated intensities and (b) structure factors for the stationary and rocking scans.

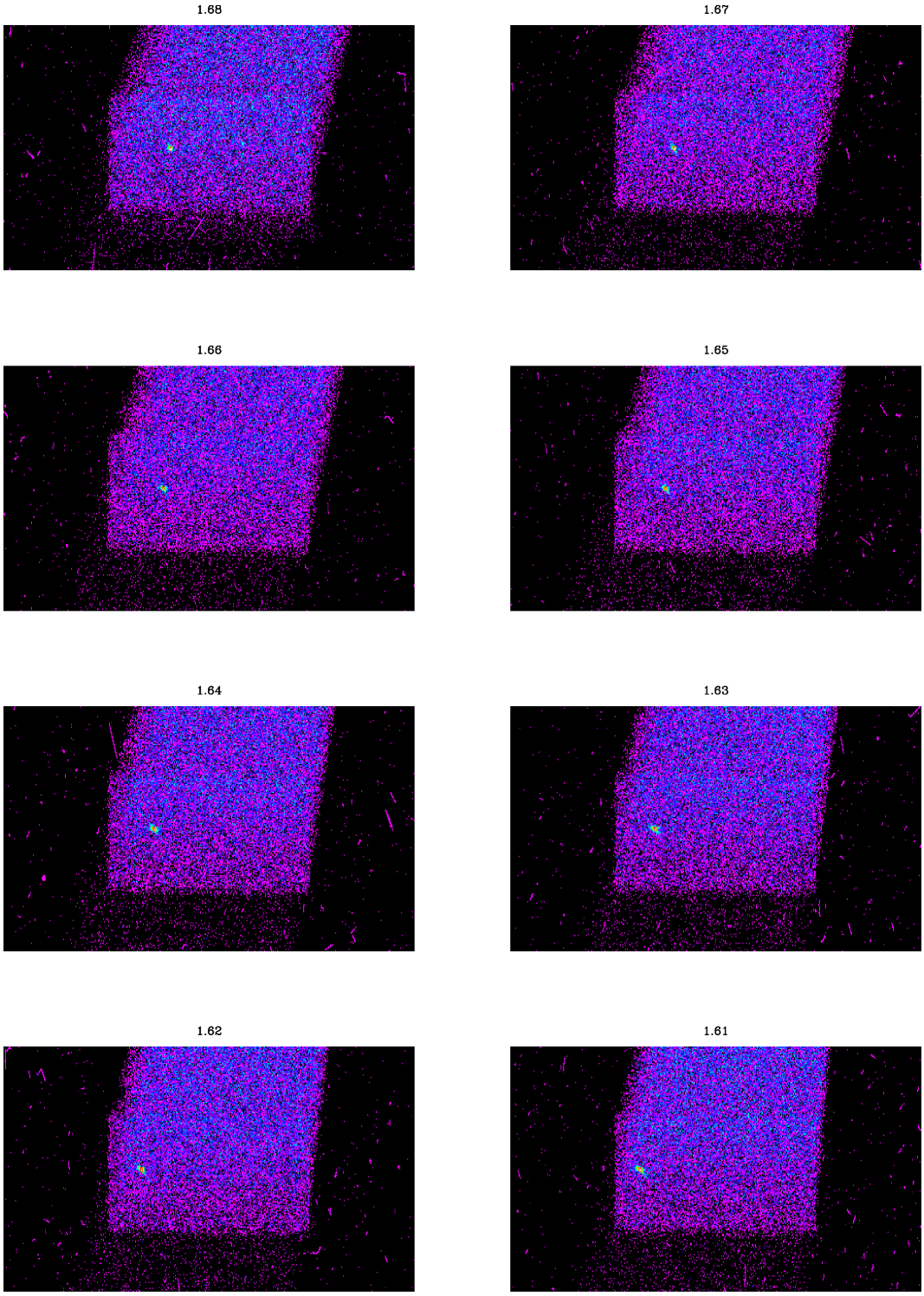

Figure 3.16: The misalignment of the diffractometer results in the rod moving across the area detector. The *l* position along the rod are displayed.

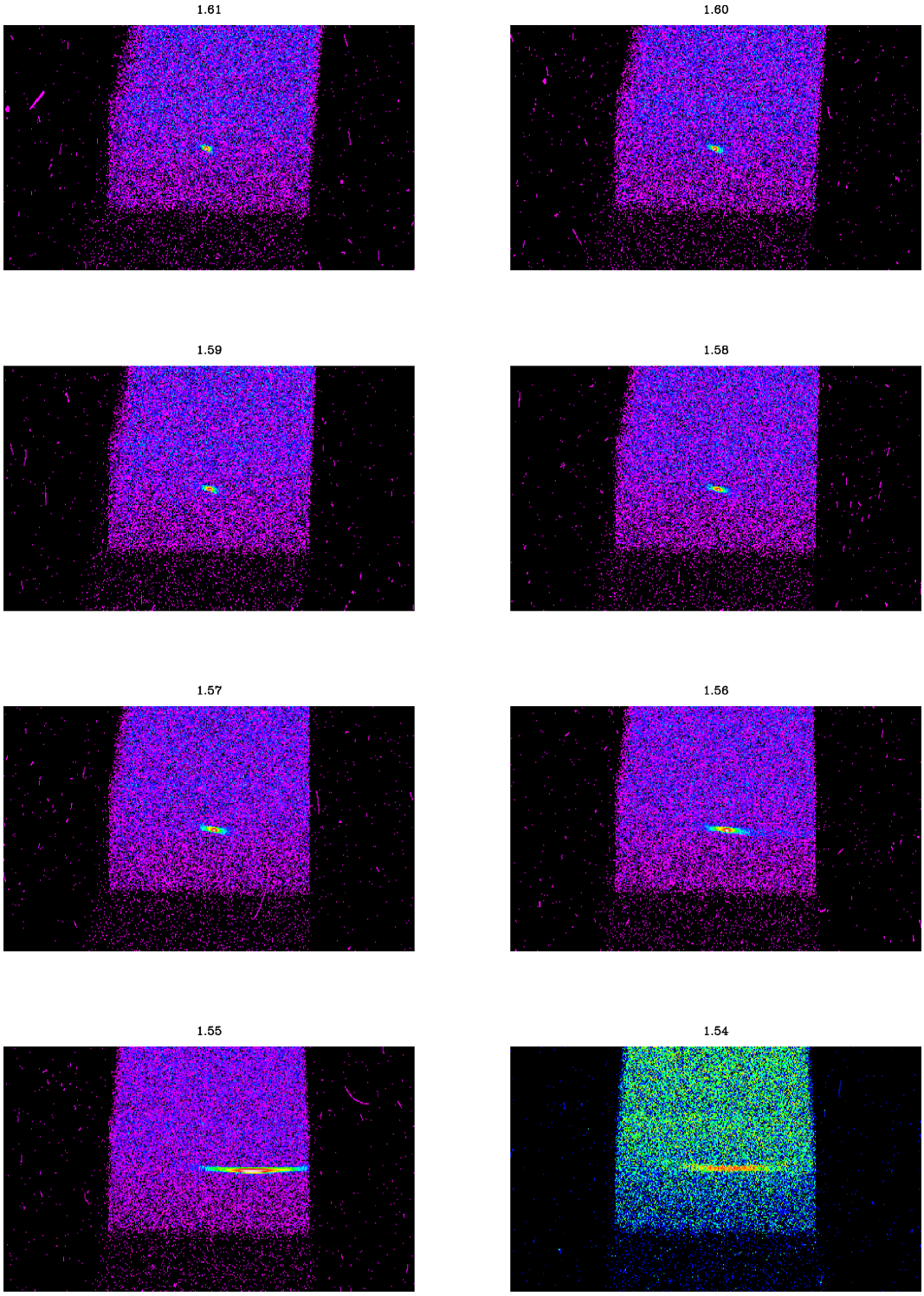

Figure 3.17: The continuation of the scan along the CTR once the diffractometer has been realigned. The *l* position along the rod are displayed. The rod is now approximately centred. The rod is extended as *l* tends to zero as a larger range in *l* is sampled close to the foot of the CTR than at higher *l* (see fig. A.2.2. in the appendix).

3.7.2 Comparison of the Rocking and Constant Velocity Scans

Alignment issues of the diffractometer prevent large regions of certain rods being measured by the stationary mode. The reason behind the misalignments appear to be as a result of the α and ω motors losing steps further along the rod.

The effect these misalignments had on the rocking and c.v. modes was investigated. The diffractometer was moved back to the $(22\bar{4})$ Bragg peak and two things studied; if the peak moved off the point detector for $l < -4.21$ and, if not, the statistics of the two modes when both scans had background and peak scans over the same ω range and time.

The range of the background scan was 3^{o} and the rocking scan had a counting time of 1 second per point and data taken every 0.06^{o}, whereas the c.v. scan had a rotational velocity was $0.0357^{o}sec^{-1}$ and data taken every 0.0075^{o}. The total counting time of the background scan was 150 and 84 seconds for the rocking and c.v. modes respectively. The peak scan had a range of 0.3^{o}, and the rocking scan had a counting time of 1 second per point and data measured every 0.0075^{o} , whereas the c.v. scan had a rotational velocity of $0.0044^{o}sec^{-1}$ and data taken every 0.0008^{o}. The total time of peak scan was 64 seconds for both modes.

The merged background and peak scans of the rocking and c.v. modes are shown in figs. 3.19 and 3.20 respectively. The scans were from l = -4.01 to -4.31. In both modes the CTR is located in the middle of the background scan. Unlike the stationary mode, it appears that there is no danger of the CTR moving out of the detector range due to peak always being located within the wide range of the background scan.

The CTR is measured for values of $l < -4.21$; the integrated intensities and structure factors of the two modes are shown in figs. 3.21(a) and (b) respectively. The integrated intensity of the rocking mode is always larger than that of c.v. mode and a comparison of the two shown in table 3.5. It is seen that the SNR and R_{err} are similar for the different scan types. The SNR is generally higher for the c.v. scan apart from when the signal is very weak (i.e. l = -4.21, -4.26) at which point it is difficult to distinguish from the background. The peaks at l = -4.16 and -4.36 are very strong but are a result of artifacts.

The R-factor between the different modes was 6.13%, indicating that the two

modes give consistent measurements provided they are over the same range and total counting time.

The accuracy of ω was investigated during the c.v. scans. The value of ω reported by the beamline software was compared directly with the diffractometer reading of ω. Typically there was a discrepancy of approximately 0.01^{o} when the rotational velocity was $0.0357^{o}sec^{-1}$ and 0.001^{o} when the velocity was $0.0044^{o}sec^{-1}$; the discrepancy is larger for larger velocities. The rotational speed of this technique therefore limits accuracy in ω.

l	I		$\sigma(I)$		R_{err} (%)		SNR	
	ω	c.v.	ω	c.v.	ω	c.v.	ω	c.v.
-4.01	38.71	7.01	0.66	0.09	1.71	1.28	58.65	77.89
-4.06	1.77	0.30	0.14	0.02	7.91	6.67	12.64	15
-4.11	0.64	0.16	0.09	0.01	14.06	6.25	7.11	16
-4.16	13.96	2.68	0.32	0.05	2.29	1.87	43.62	53.60
-4.21	0.32	0.18	0.06	0.09	18.75	50	5.33	2
-4.26	0.30	0.04	0.06	0.01	20	25	5.00	4
-4.31	558.62	54.69	2.05	0.21	0.37	0.38	272.49	260.43
-4.36	0.71	0.15	0.1	0.01	14.1	6.67	7.10	15

Table 3.5: Statistics for the integrated intensities for the rocking and c.v. modes.

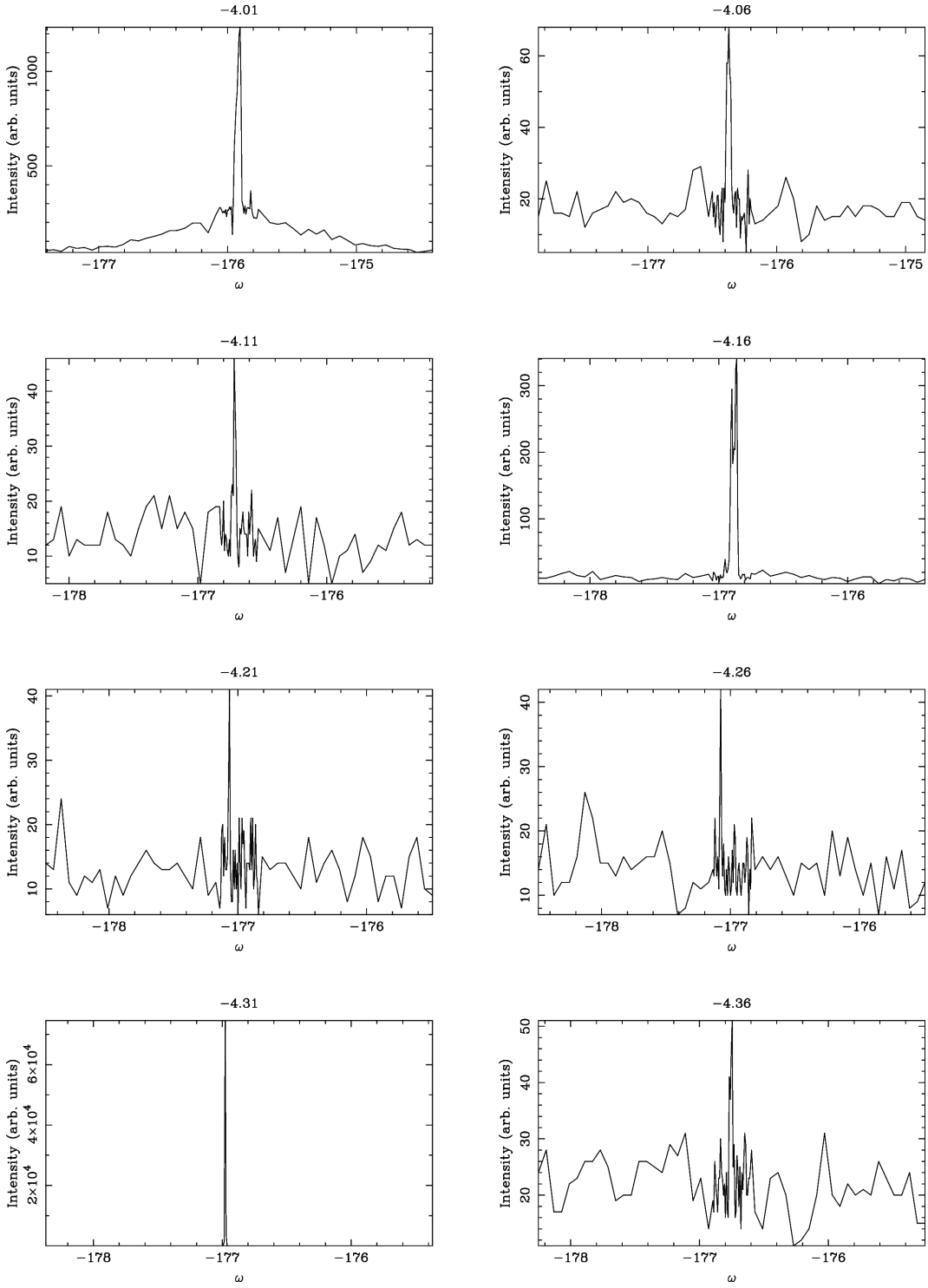

Figure 3.19: The merged peak and background scans for the rocking scan.

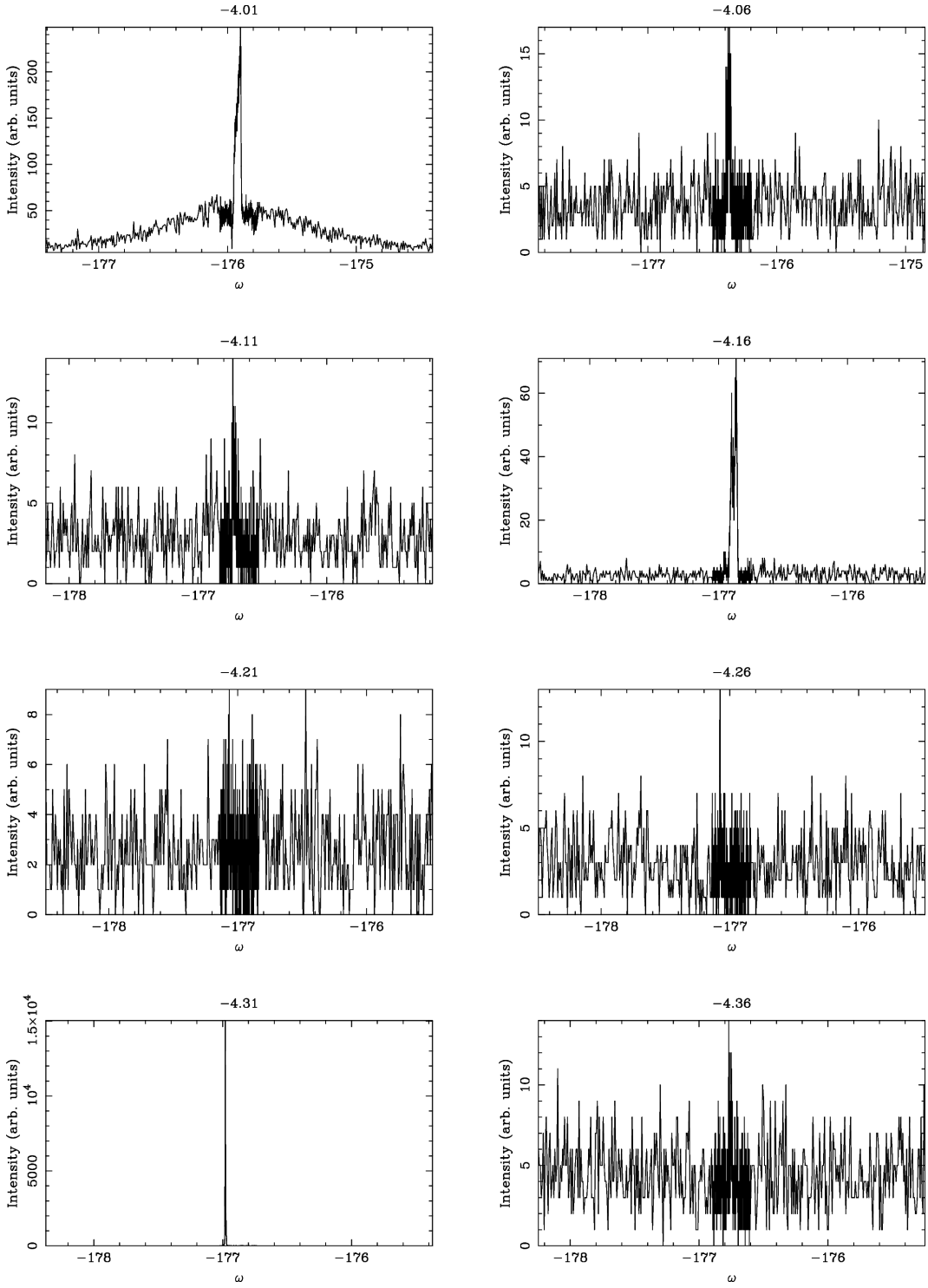

Figure 3.20: The merged peak and background scans for the c.v. scan.

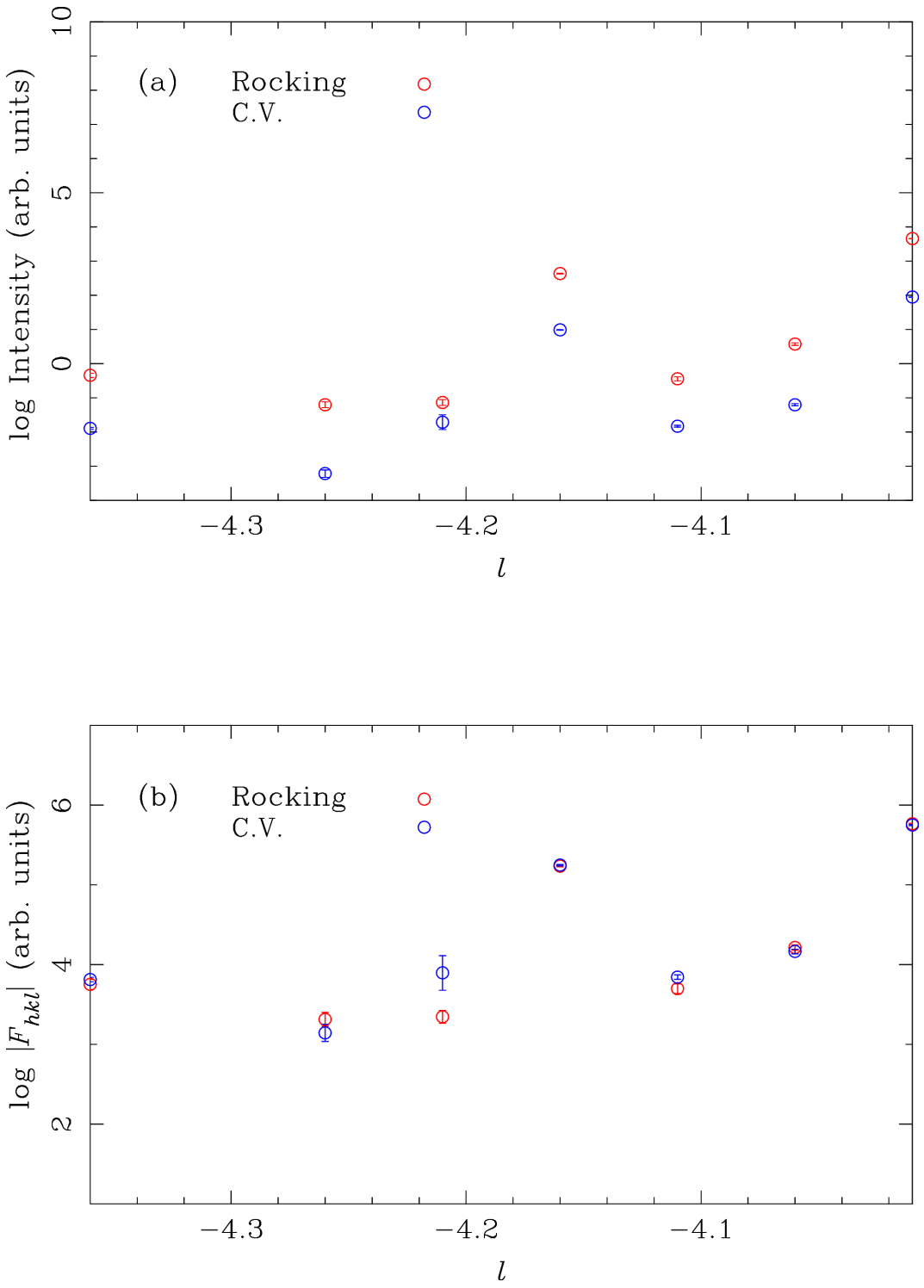

Figure 3.21: Comparison of (a) the integrated intensities obtained by the rocking and c.v. modes and (b) the structure factors.

3.8 Conclusions

The integrated intensity and structure factors of several CTRs measured by stationary, rocking and constant velocity scans have been compared using a (2+3)-type diffractometer in *z*-axis mode. The differences between the structure factors are almost within the their respective statistical errors which validates all three measuring modes for crystallographic purposes.

The use of an area detector instead of a point detector in CTR measurements greatly increases the reliability and the data acquisition rate by almost an order of magnitude. This offers users the possibility of investigating more complex systems within the restricted beam time available to synchrotron users.

There are also several other advantages of using the area detector to obtain CTRs; (i) it has the smallest statistical error, (ii) fewer correction factors need to be calculated to obtain the structure factor, (iii) there is no need for sample rotation along each point of the CTR as the full extent of the signal is where the rod intersects the Ewald sphere and is measured in a single image thereby improving the counting statistics; the diffractometer only needs to move to the calculated angles and the entire image is captured, (iv) the background is obtained in the same scan as the signal, (v) there is no dark current contributing to the background and, perhaps most importantly, (vi) artifacts that contribute to the scattering signal can easily be recognised and accounted for and then subsequently removed from the data set.

However, the intensities of the stationary scans are strongly dependent on misalignments, such as a poorly determined orientation matrix or diffractometer motors losing steps. The misalignments can cause the CTR to move off the area detector altogether, and as a result of this it is therefore impractical to leave an automated scan along the rod left unattended, for fear of losing the rod. This can be overcome by obtaining new orientation matrices but this can be time consuming and a nuisance to the user. The misalignments do not appear to affect the rocking and c.v. modes due to the wide range of the background scan, although the possibility that other geometries affect these type of scans can not be ruled out. Although the SNR is poorer for these scans, the structure factors obtained are comparable to that of the stationary mode, albeit with a larger statistical error. For these reasons both the rocking and c.v. modes are also viable

approaches to measuring CTRs even though there is the option of using the stationary mode.

Finally, only the statistical errors have been considered thus far. The systematic error is typically 5-15% [24, 42, 53, 54, 56, 57] and is estimated by averaging symmetry-equivalent reflections. The systematic errors were not determined in this experiment and as a result of this, the error was set to 10% for all data points if the error was less than this. Once this step is taken practically all differences between the rocking and stationary structure factors fall within the respective experimental error bars.

Chapter 4

X-ray Bicrystal Truncation Rod Study of a Si Σ13 Symmetric Tilt Grain Boundary

4.1 Introduction

Polycrystalline semiconductors are used extensively in modern technology, such as resistors, transistors, capacitors, diodes and solar cells. Grain boundaries in these materials affect their physical and electrical characteristics greatly [3].

As a result of this grain boundaries have been studied extensively, both experimentally and theoretically. Experimentally grain boundaries are measured using high resolution transmission electron microscopy (HRTEM) [11, 58, 59]. However, the resolution required to measure the boundaries is very difficult to obtain and the results are often difficult to interpret. Theoretical studies are complicated by the fact that for a given angle there are multiple interface structures that can exist [2]. The only way to distinguish between the boundaries is to compare grain boundary energy of the structures. However, since experimental observations have shown different grain boundaries can exist for a given angle there is more than energetics to predicting the correct grain boundary.

In this chapter, X-ray bicrystal truncation rod (BCTR) scattering, from a Si Σ13 interface is presented. CTR scattering is commonly used to determine the atomic arrangement at surfaces where interference between the Bragg rod scattering due to the truncated bulk crystal and the relaxed or reconstructed surface layers gives sensitivity on the atomic scale. Unlike surface X-ray diffraction, the bicrystallography of the interface gives rise to two, overlapping CTRs, one from each crystal. The interface is buried and the large penetration of X-rays into matter is exploited, allowing the study of interfaces which are otherwise inaccessible by other standard surface science techniques.

The experimental and simulated X-ray scattering from a grain boundary is highly dependent on the atomic positions. Several possible grain boundary structures are presented and modelled in preparation for X-ray scattering simulations. To ensure the atoms are in their equilibrium positions their strain energy is minimised. In the first part of this chapter, the Keating energy is discussed, and a model is developed to minimise the Keating energy of the grain boundaries. The Keating energies of the relaxed grain boundaries are then compared with other minimisation techniques.

In the second half of the chapter, a model for the scattering from the grain boundary interface is presented and the simulated scattering from the grain boundaries is compared with experimental data and used to discriminate between the grain boundaries.

4.2 Limitations of Current Techniques

The study of grain boundaries has been the subject of many experimental and theoretical studies. There are several experimental methods for characterising the grain boundary; the most common of which is HRTEM [60]. The principle of any interface observation is to observe both crystals, either side of the grain boundary. If this can be achieved, an interpretable two-dimensional projection of a three-dimensional crystal can be obtained. However, the projection is vary rarely easy to interpret directly and a comparison with simulated images is often necessary (fig. 4.1). The main limitation of this technique is that HRTEM is a two-dimensional technique and as a result of this the grain boundary is averaged over the sample thickness; there is always a reduction of one-dimension in the available information and only two-dimensional projections can be obtained. There are also other limitations including the attenuation of the electron beam and radiation damage to the sample. As the electron beam is weakly penetrating, if the grain boundary is buried, then the sample has to be thinned to the extent that it is effectively destroyed to access it.

Another approach is to predict the structure of the grain boundary theoretically. However, these studies are complicated by the fact that for a given tilt angle several possible grain boundary structures can exist physically. This has been shown in [59] where the authors have observed several possible grain boundaries for various tilt angles

in both Si and Ge bicrystals. The lowest energy structures can be calculated using various techniques, including the tight-binding model and the Tersoff potential. Often it is found that several of the grain boundary structures are close in energy and that the energy of the grain boundary depends on the calculation method used (e.g. first principles versus analytic potential calculations) [2, 59]. Therefore it has been suggested that the energetics of the grain boundary is not the complete story in correctly predicting the grain boundary structure [2, 59].

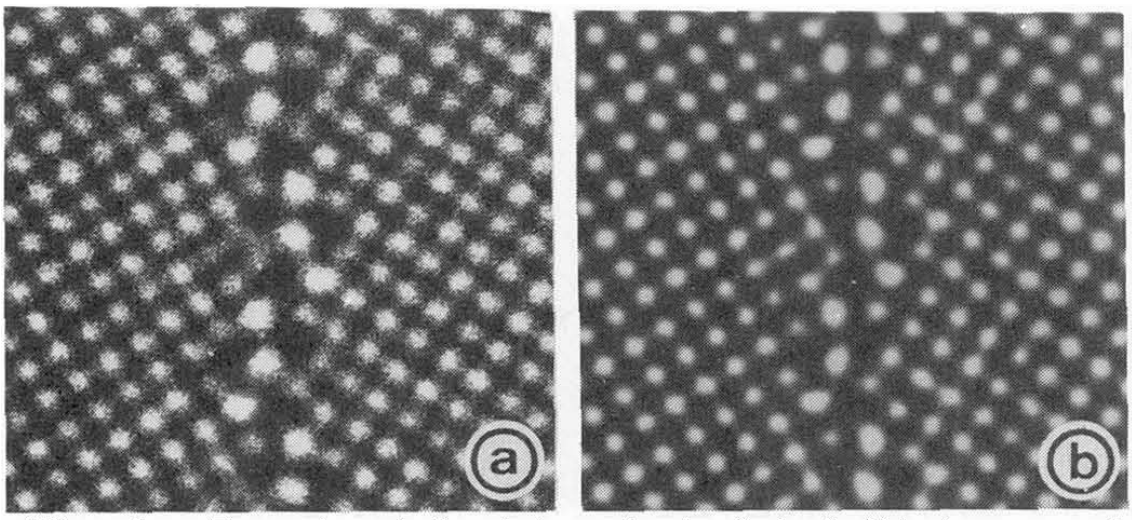

Figure 4.1: Comparison between (a) the experimental and (b) simulated images of a Ge Σ13 (510) grain boundary. The experimental image is obtained with HRTEM. After [59]

4.3 The Si Bicrystal Sample

The silicon bicrystal used in the experimental studies presented in this thesis was grown by the Czochralski method [61]. In this approach, single crystals are grown by slowly and very slightly dipping a small, crystallographically aligned seed crystal into a molten pool of the same material. The seed is slowly withdrawn from the molten pool whereby the liquid material crystallizes at the seed. This process is shown in fig. 4.2. In order to grow a bicrystal by the Czochralski method two seed crystals are used. Bicrystals are formed when two identical lattices are joined together such that their orientations differ by a rotation angle θ, known as the tilt angle. The growth of the

bicrystal is initiated from two seed crystals, and θ is determined by the orientations of these seeds [62]. This is illustrated in fig. 4.3. Bicrystals are then formed in the same manner as the single crystal above.

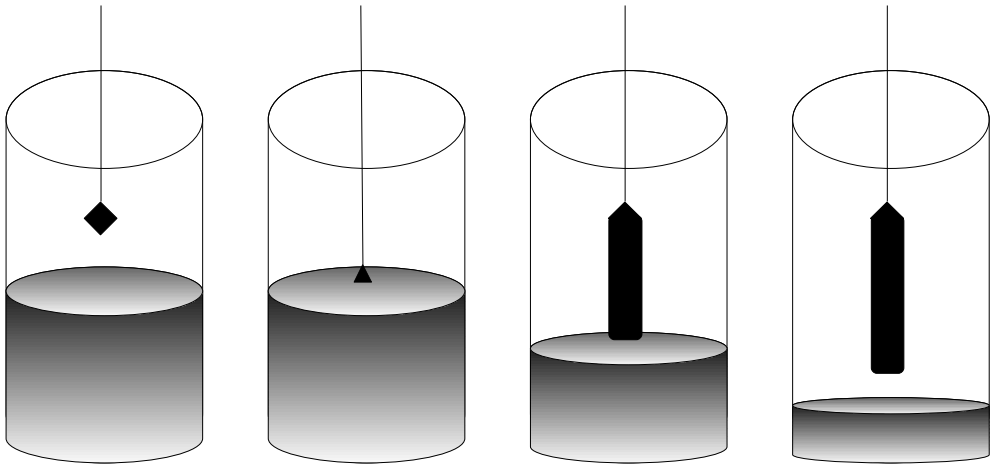

Figure 4.2: The Czochralski method. This figure illustrates the different stages of growth form left to right. The first step illustrates the introduction of the seed crystal, the second illustrates the seed being dipped into the molten pool, the third the pulling of the crystals and the final stage the fully formed crystal.

There are two important factors that affect the growth of the bicrystal; the distance between the seeds and the withdrawal speed [62, 63]. The distance between the two seeds is critical; for too small distances the crystals grow together too quickly and for too large distances the crystals take too long to grow together and polycrystals are obtained. The optimum distance between the two seeds is typically a few mm [62, 63]. The choice of the withdrawal speed is just as important. When the two single crystals come together to form a bicrystal, the nucleation must be precisely controlled such that the growth of the bicrystal starts only at one spot [62]. Typical speeds are of the order of mm/min [62, 63].

For the Si Σ13 bicrystal (the notation is described in section 2.3.2), the [001] axes of the seeds are parallel and used as the growth directions. For Σ13 the disorientation results from a rotation about the common [001] axis. The angle of rotation is 22.6^{o} and the boundary is (501). The bicrystal in this study is a cylinder (fig.

4.4) of diameter 1.8 mm and was cut from the boule using a diamond core drill.

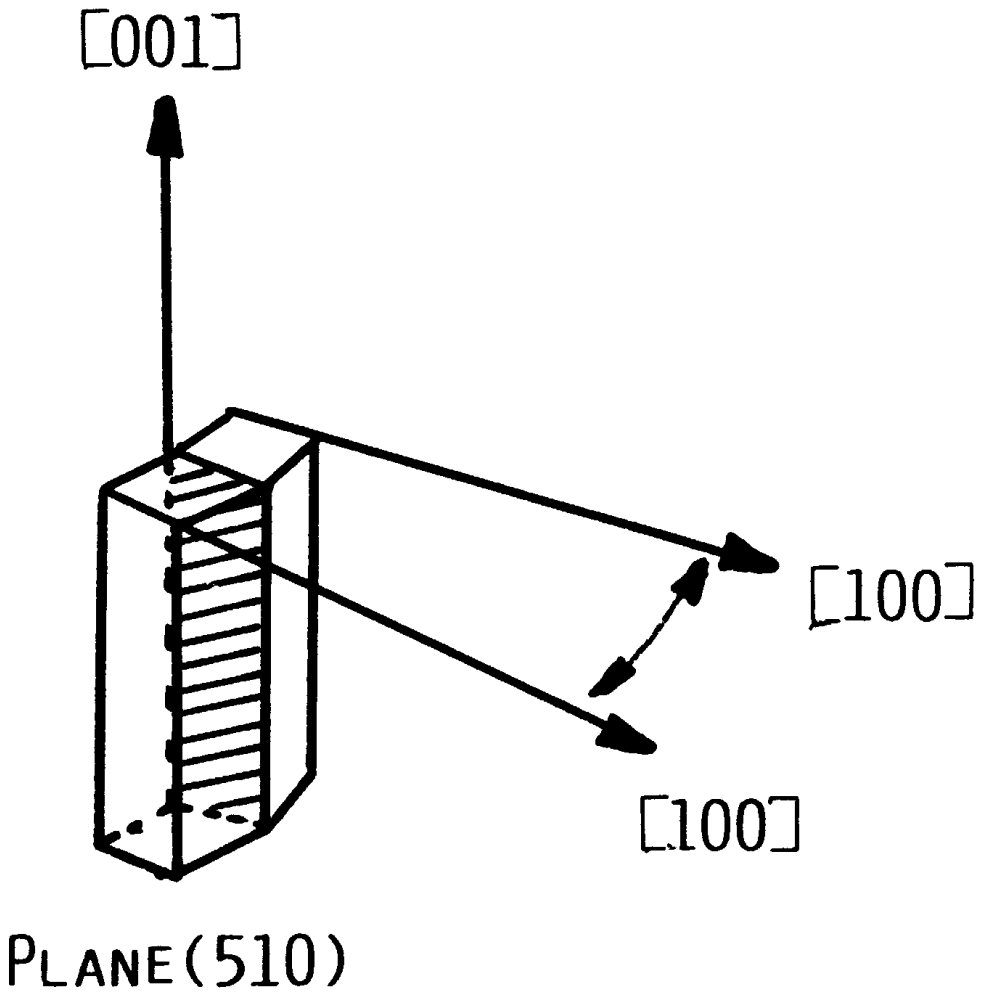

Figure 4.3: The angle of rotation between the two seeds for the Σ13(510) bicrystal, after [63]. The tilt angle between the two seeds is 22.6°.

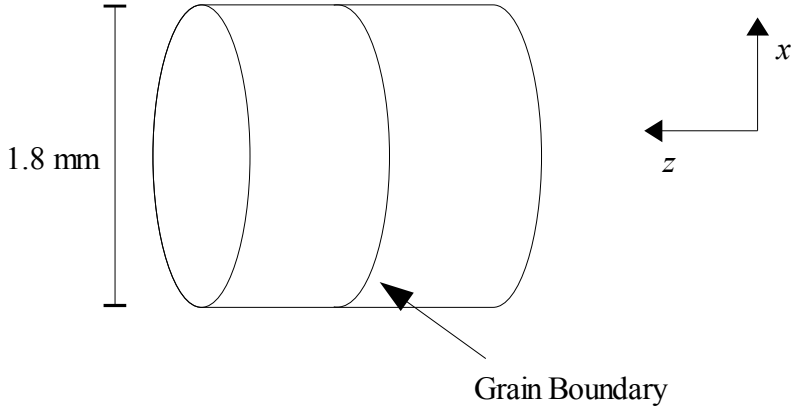

Figure 4.4: Schematic illustration of the Si bicrystal sample geometry. The *y* direction is out of the plane of the paper.

4.4 Keating Energy

The elastic strain (V) of a crystal is subject to various physical requirements and these may be divided into two classes: the general conditions, such as rotational and displacement invariance, and those imposed by the symmetry of the crystal structure [64]. The requirement that the energy be invariant under an arbitrary displacement of the lattice as a whole ensures that V can depend only on the *differences* between nuclear positions,

$$V = V(\mathbf{x}_k - \mathbf{x}_l) = V(\mathbf{x}_{kl}) \quad , (4.1)$$

where $\mathbf{x}_{kl} = \mathbf{x}_k - \mathbf{x}_l$ and where $\mathbf{x}_k$ is the position of the kth nucleus after deformation [64]. But V must also be invariant under a rotational transformation. The $\mathbf{x}_{kl}$ are not invariant under such a transformation; they transform as vectors. The only invariants which can be formed from the $\mathbf{x}_{kl}$ are the scalar products between them and functions of such products, which leads to

$$V(\lambda_{klmn}) = V(\mathbf{x}_{kl} \cdot \mathbf{x}_{mn} - \mathbf{X}_{kl} \cdot \mathbf{X}_{mn}) \quad , (4.2)$$

where $\mathbf{X}_k$ is the position of the kth nucleus prior to deformation. The final term in

equation (4.2) is included such that the strain is "zero" when the deformation is removed.

The Keating energy could be described as a sum over a large number of λ_{klmn}. However, only 3*N*-6 invariants are necessary to specify an arrangement of *N* points in three-dimensional space, and this is much smaller than the number of λ_{klmn} defined by equation (4.2). Keating concludes that only six scalars (fig. 4.5) are required for each lattice point to determine the strain energy of a bulk crystal provided the strain energy is dependent on nuclear positions only.

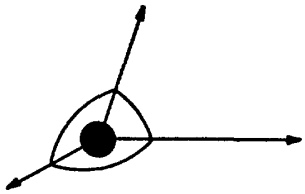

Figure 4.5: A lattice point with its six scalars. Three scalars give distances to the neighbouring atoms and the remaining three the angles between them. Image from [64].

Consider a diatomic structure with an *A* atom at the lattice point and a *B* atom within the unit cell, Keating defined $\mathbf{x}_1(l)$, $\mathbf{x}_2(l)$ and $\mathbf{x}_3(l)$ as the position vectors of the *B* atoms in neighbouring unit cells relative to the *A* atom of the unit cell (l) and $\mathbf{x}_4(l)$ as the position vector of atom *B* in (l) with respect to the *A* atom there. This gives ten scalar products $\mathbf{x}_m(l).\mathbf{x}_n(l)$ (m,n =1,2,3,4) per unit cell.

The basic unit cell of the diamond structure is a rhombohedron with two atoms (1 and 0 of fig. 4.6) on its major axis, which is directed along the [111] direction. Each *B* atom represented by an open circle is bonded to four *A* atoms represented by a filled circle. For instance atom 0 is bonded to atoms 1, 2, 3 and 4. This gives rise to ten scalar products. The strain energy in equation (4.2) is now given as

$$V=\frac{1}{2}\sum_{l}\left[\frac{\alpha}{4a^2}\sum_{i=1}^{4}(x_{0i}^2(l)-3a^2)^2+\frac{\beta}{2a^2}\sum_{i,j>i}^{4}(\boldsymbol{x}_{0i}(l)\cdot\boldsymbol{x}_{0j}(l)+a^2)^2\right] \quad , (4.3)$$

where *V* is summed over all the primitive unit cells. The Keating parameters α, the

central first-neighbour constant, and β, the noncentral second-neighbour constant, describe pure bond stretching and bond bending with some stretching component respectively [65] The parameters α and β for Si (in 10^3 dyn/cm) are 51.51 and 4.70 respectively [65]. The factors $3a^2$ and a^2 are the bulk equilibrium value of the scalar products in equation (4.3). This ensures that the strain is at a minimum for the undistorted lattice.

4.4.1 Minimisation Method

The Keating energy is found by finding the relaxed positions of the atoms in the bicrystal and interface. This is done by using multidimensional minimisation algorithms from the gnu scientific library [66].

The Fletcher-Reeves conjugate gradient algorithm is used. The conjugate gradient algorithm proceeds as a succession of line minimizations. The sequence of search directions is used to build up an approximation to the curvature of the function in the neighbourhood of the minimum. An initial search direction p is chosen using the gradient, and line minimization is carried out in that direction. The accuracy of the line minimization is specified by the parameter *tol* (which is specified to be 0.1). The minimum along this line occurs when the function gradient g and the search direction p are orthogonal. The line minimization terminates when $\mathbf{p}.\mathbf{g} < tol\ |\mathbf{p}|\ |\mathbf{g}|$. The search direction is updated using the Fletcher-Reeves formula $p' = g' - \beta g$ where $\beta = -g'^2/g^2$, and the line minimization is then repeated for the new search direction. The stopping criterion used is $g < 10^{-3}$. This gives a relaxed structure without an unduly long computational time.

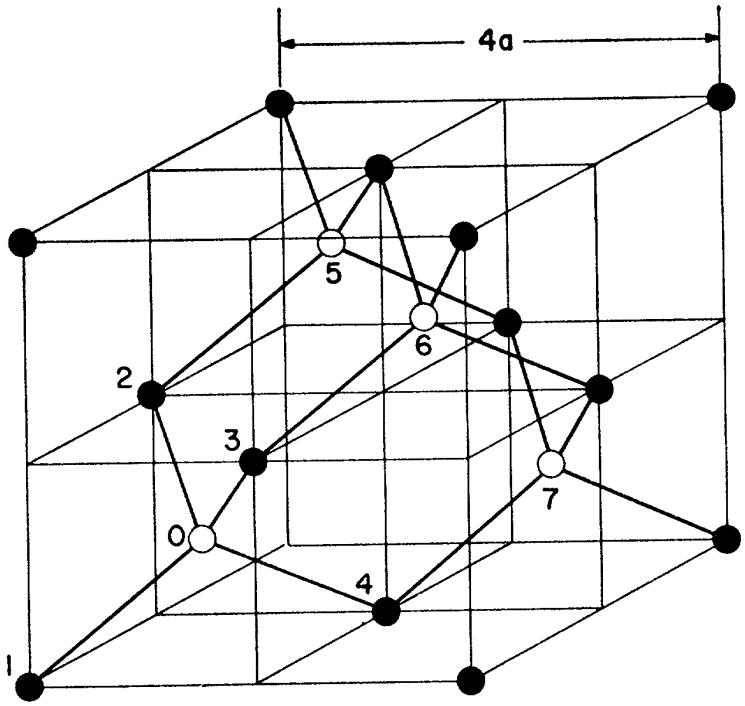

Figure 4.6: The crystal model. The open and filled circles represent the atoms on the two different sublattices. The length of the unit cell is 4*a*. Image from [64].

4.5 Interface Structure

In section 4.2 there was a discussion on the fact that theoretical studies were complicated by the fact that several possible grain boundaries exist that are fully bonded and four-fold coordinated for a given tilt angle. Several such possible structures for the Si Σ13 symmetric tilt grain boundary are presented by Morris et al. [2] and are shown in fig. 4.7. Several of the structures have been observed experimentally and a high resolution image of structure (a) is shown in fig. 4.8; this led Morris et al., to suggest that the energetics alone is not enough for predicting the structure of the grain boundary.

For the Σ13 {501} symmetric tilt boundaries, the repeat distance along the boundary is ½ √26 a_0, where a_0 is the cubic lattice constant. The boundary contains a number of dislocations, with a total Burgers vector of **b**=[100]. The individual dislocations that occur are either **b**= ½ [110] and **b** = ½ [1$\bar{1}$0] pairs of edge dislocations or **b** = ½ [101] and **b** = ½ [10$\bar{1}$] 45° mixed dislocation pairs. Structure (e) and (f) are grain boundaries made up solely of edge dislocations, and are characterised, in

projection, by a set of fivefold and threefold rings sharing a vertex. The mixed dislocation core structures (structures (g) and (h)) also appear as a set of fivefold and threefold rings, but sharing an edge [2]. The dislocation types are illustrated in fig. 4.9, and all of the grain boundaries can be constructed from the three structural units. For example structures (g) and (h) have straight arrangements of CACA and AACC respectively.

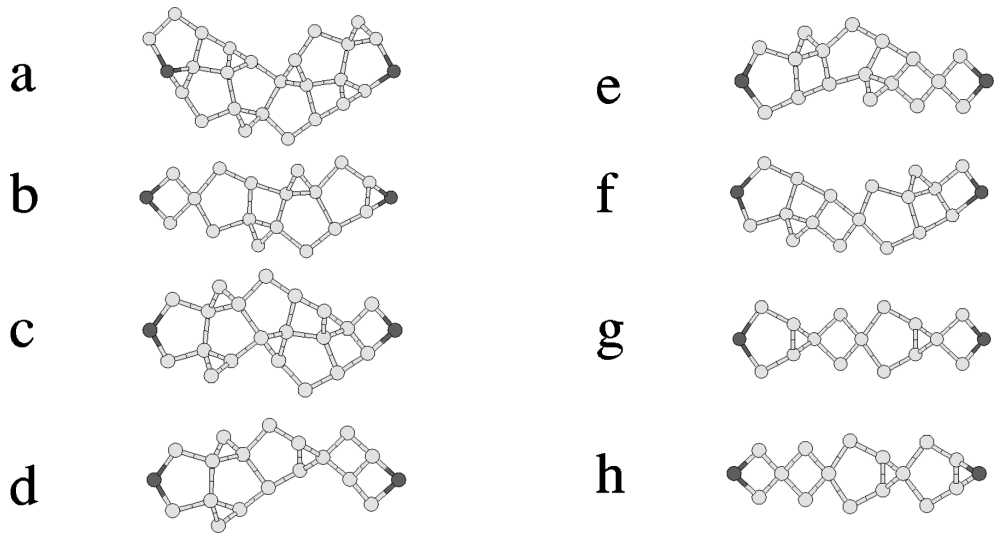

Figure 4.7: Eight possible structures for the {501} symmetric tilt boundary. The structures are shown in order of increasing grain boundary energy. Image taken from [2].

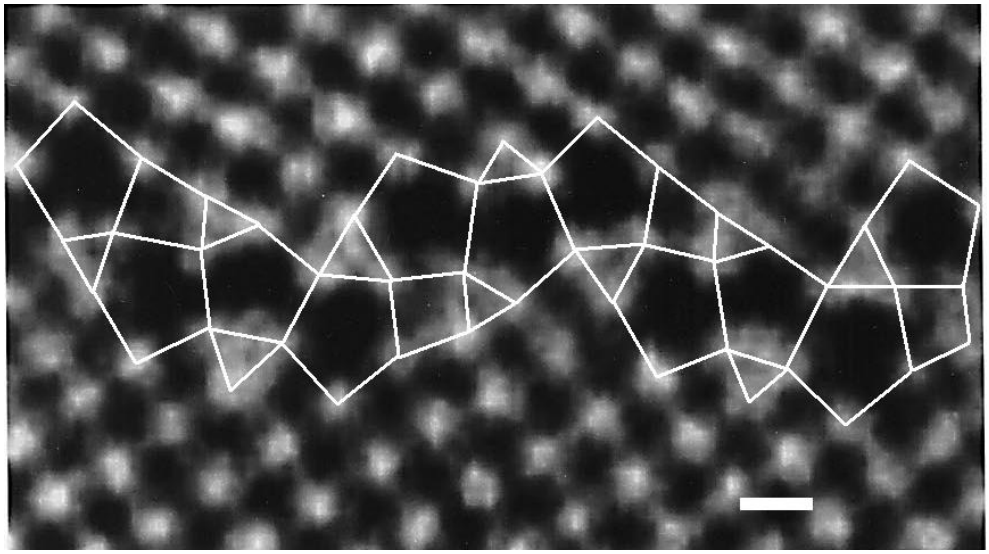

Figure 4.8: Z-contrast image of the Si Σ13 symmetric tilt grain boundary from Chrisholm et al. [58]. This is structure (a) from fig. 4.7. The scale bar is 0.2 nm and the bonds have been drawn on for illustrative purposes.

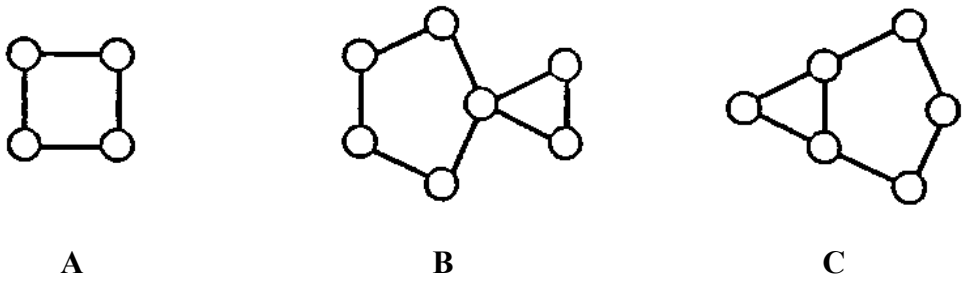

Figure 4.9: The structural units that make up the grain boundary structures. From left to right: a perfect crystal (unit A), pure edge dislocation (unit B) and a mixed dislocation (unit C). After [67].

4.5.1 Coincidence Site Lattice of the Σ13 Tilt Boundary

The structure of the Σ13 tilt boundary is two-dimensionally periodic within the interface. Its unit cell is determined by the coincidence site lattice (CSL).

The method for generating the CSL for the Σ13 grain boundary is taken from

Sagalowicz and Clark [30]. Firstly a colour is assigned to each crystal; in this instance the top crystal is black and the bottom crystal red. A common origin for the crystals is defined and then the bottom crystal is then rotated 22.6° with respect to the top crystal. The two lattices are considered infinite in extent and are then allowed to interpenetrate creating the dichromatic pattern seen in fig. 2.4. The resultant CSL have their own space group, which is related to that of the original FCC Bravais lattices, but has lost some of the FCC symmetry elements. This CSL forms the Σ13 unit cell. It contains 26 standard Si diamond unit cells. The Σ13 unit cell has dimensions of $a_1 = ½ \sqrt{26}\ a_0$, $a_2 = a_0$ and $a_3 = ½ \sqrt{26}\ a_0$.

4.6 Keating Energy Minimisation

The structures were then fully relaxed using the Keating minimisation. This was done using by firstly creating the two Si crystals in the manner mentioned above. The boundary plane was then inserted in such a way that only atoms belonging to the top crystal are on one side of it and atoms from the bottom crystal the other side. This gives the unrelaxed structure of the boundary. Finally an interfacial expansion is introduced between the crystals to accommodate the grain boundary. The interfacial expansion was typically 2-7 Å. Each Si crystal contained four Σ13 unit cells (two horizontal and two vertical) (fig. 4.10). This meant that the interface structure would repeat itself twice along the grain boundary. The atomic coordinates of the interface atoms were then entered manually. To ensure correct bonding the bonds between the atoms in the bulk Si crystals and the interface were also entered thus giving the unrelaxed structure of the bicrystal. Periodic boundary conditions are applied to the structure in the x and y directions creating an array of the Si Σ13 bicrystal. The structures then underwent the Keating minimisation process mentioned above. The structures were relaxed after approximately a few thousand iterations (fig. 4.11). Relaxation occurs when the Keating energy does not change after subsequent iterations. Due to the relatively small numbers of atoms (< 500) it took approximately 30 minutes to minimise each structure using a 2.4 GHz computer.

The relaxed structures can be seen in fig. 4.12, the structural properties in table 4.1 and the Keating parameters in table 4.2. The number of atoms in each relaxed

structure range from 428 to 444 atoms. The Keating energy is found to be similar across all of the structures, with the lowest energy structure having an energy approximately 10% smaller than the highest energy structure. Figure 4.12 shows the structures on a temperature scale. The hot (red) atoms have the most strain and the cool (blue) atoms have the least. The temperature scale is not absolute and varies from structure to structure. Figure 4.12 shows that the strain is localised at the interface and the bulk Si is in its equilibrium position within either the first or second layer of the bulk. The structures are all fully four bonded and are physically realistic as the individual fivefold, fourfold and threefold rings that make up each structure are not planar and actually spiral along the tilt axis.

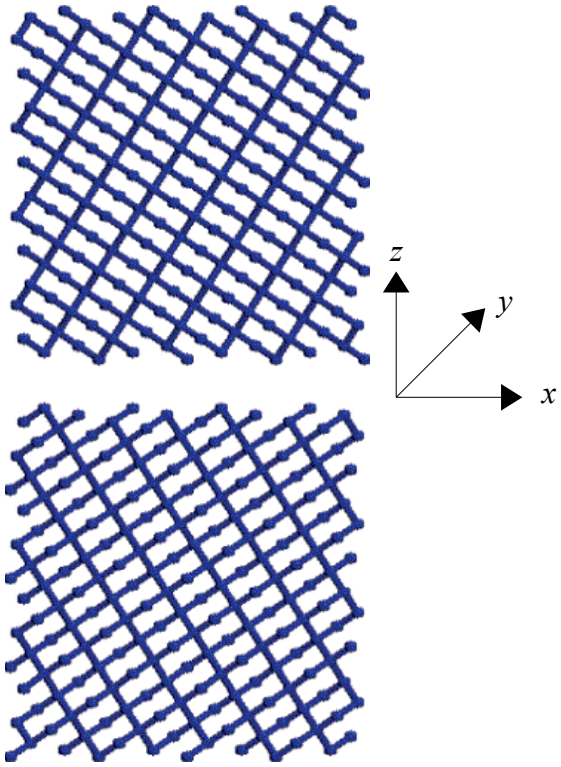

Figure 4.10: The generated Si bicrystal. Each crystal contains four Σ13 unit cells.

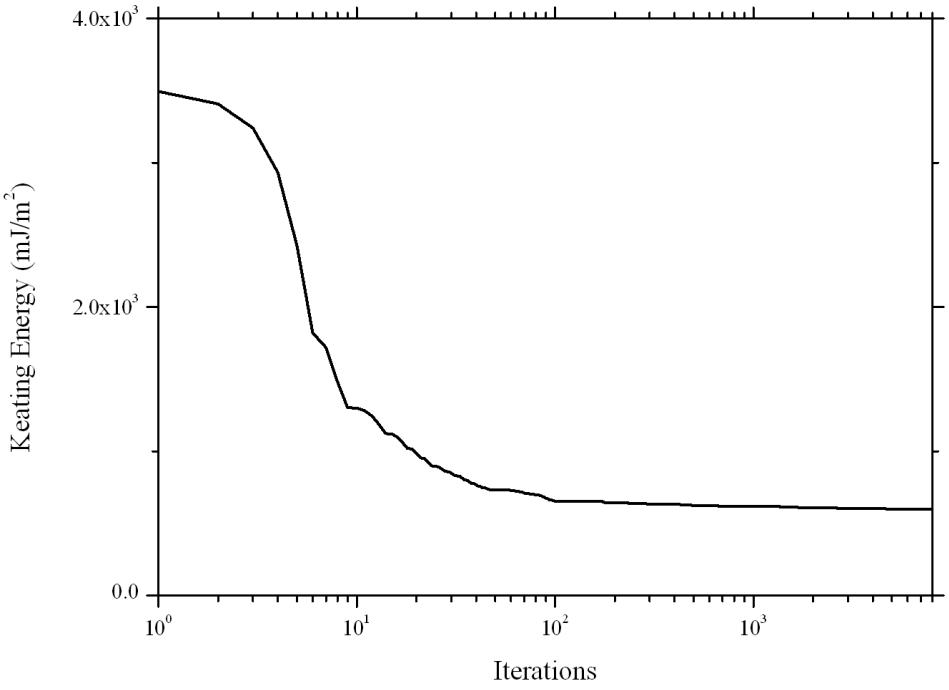

Figure 4.11: Change in Keating energy during the minimisation procedure of the bicrystal and interface.

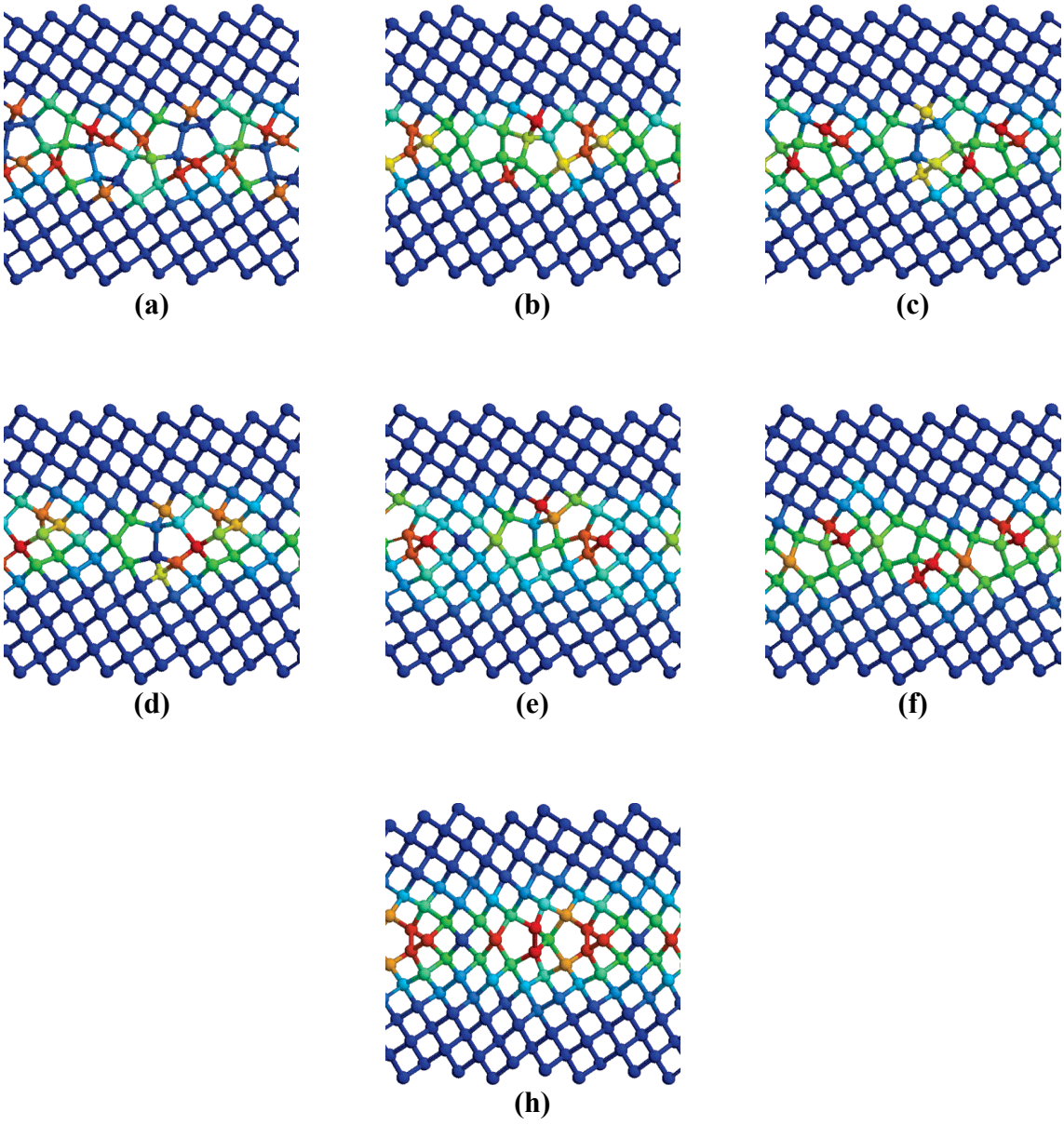

Figure 4.12: The possible Σ13 interface structures. The structures are fully four-coordinated and fully relaxed according to the Keating model. The atoms are colour coded to indicate each atoms contribution to the Keating energy with high energy atoms appearing hotter.

Structure	Number of Atoms	Offset in x	Offset in y	Offset in z
a	444	0.03600	-0.62490	0.13600
b	436	0.01250	-1.15050	0.09500
c	428	0.01330	-0.98700	0.05602
d	428	0.00700	-0.94200	0.05370
e	432	-0.01140	-1.05050	0.07280
f	428	0.03290	-1.05750	0.05420
h	432	-0.00065	-1.13500	0.07111

Table 4.1: The structural properties of the various grain boundaries. The number of atoms for each structure is given. The offsets given are the rigid body translations between the top and bottom crystals, and are in fractions of the generated bicrystals (units of Å).

Structure	Bending	Stretching	Keating
a	577.82	18.97	596.79
b	529.09	17.63	546.72
c	582.03	21.19	603.21
d	568.66	24.37	593.02
e	526.29	28.39	554.68
f	570.41	30.71	601.12
h	549.04	27.65	576.69

Table 4.2: The Keating energies of the grain boundaries, in units of mJ/m^2. The bending and stretching components are shown to illustrate the relative weighting of each to the Keating energy.

The Keating parameters in table 4.2 are shown graphically in fig. 4.13. The bending parameter appears to vary weakly with the grain boundary structure, whereas the stretching term generally increases as the grain boundary energy increases. A comparison of our Keating energy and the grain boundary energies obtained by Morris et al. is shown in fig. 4.14. It is seen that the Keating values follow very similarly to the Tersoff ones. This is unsurprising because the Keating energy is similar to the Tersoff

potential in the fact that the Tersoff potential is also comprised of bond-bending and stretching components. The Keating energy of all the structures are within 10% of each other. This tells us that Keating energy depends only weakly on the structure of the grain boundary when compared to the tight-binding (TB) and *ab-initio* energies which show considerable differences. The TB and *ab-initio* simulations found structure (a) to be the lowest energy grain boundary and structure (h) to be the highest energy structure. Interestingly, structure (a) has the most dislocation cores whereas the grain boundaries that are structurally similar to the bulk, with a minimal number of dislocation cores, are all high energy. This is clearly not the case with the Keating model, which has structure (b) as the lowest energy and structure (c) as the highest energy. There is a complete lack of correlation between the classical potentials and the first-principle calculations. This suggests that the dislocation cores are probably not modelled very well with the classical potentials due to excessive bond bending and stretching.

Another problem with calculating the grain boundary energies is that energies are dependent on the calculation method used. Two groups of authors [2, 59] obtained different energy ordering of structures (d) and (e) using different versions of the Tersoff potential.

However, the energy of the structure in this scope of work is not crucial. As mentioned earlier several of the structures exist physically, for example Kim et al., [11] have obtained high resolution images of the Si Σ13 grain boundary that has structure (d). Therefore there is more than energetics to correctly predicting the grain boundary structure. The above shows that the grain boundary energies are very similar to each other when calculated using the analytical potentials unlike when the energies are calculated from first principles. The grain boundary structure is unknown and is to be found by simulating scattering from the grain boundary interface and comparing it with experimental scattering. The simulated scattering is dependent on the atomic coordinates of the interface, therefore in this approach the most important thing is the position of the relaxed atoms. Morris et al., report that for the various methods used to find the energy, the position of the relaxed atoms remain the same even though the energies differed.

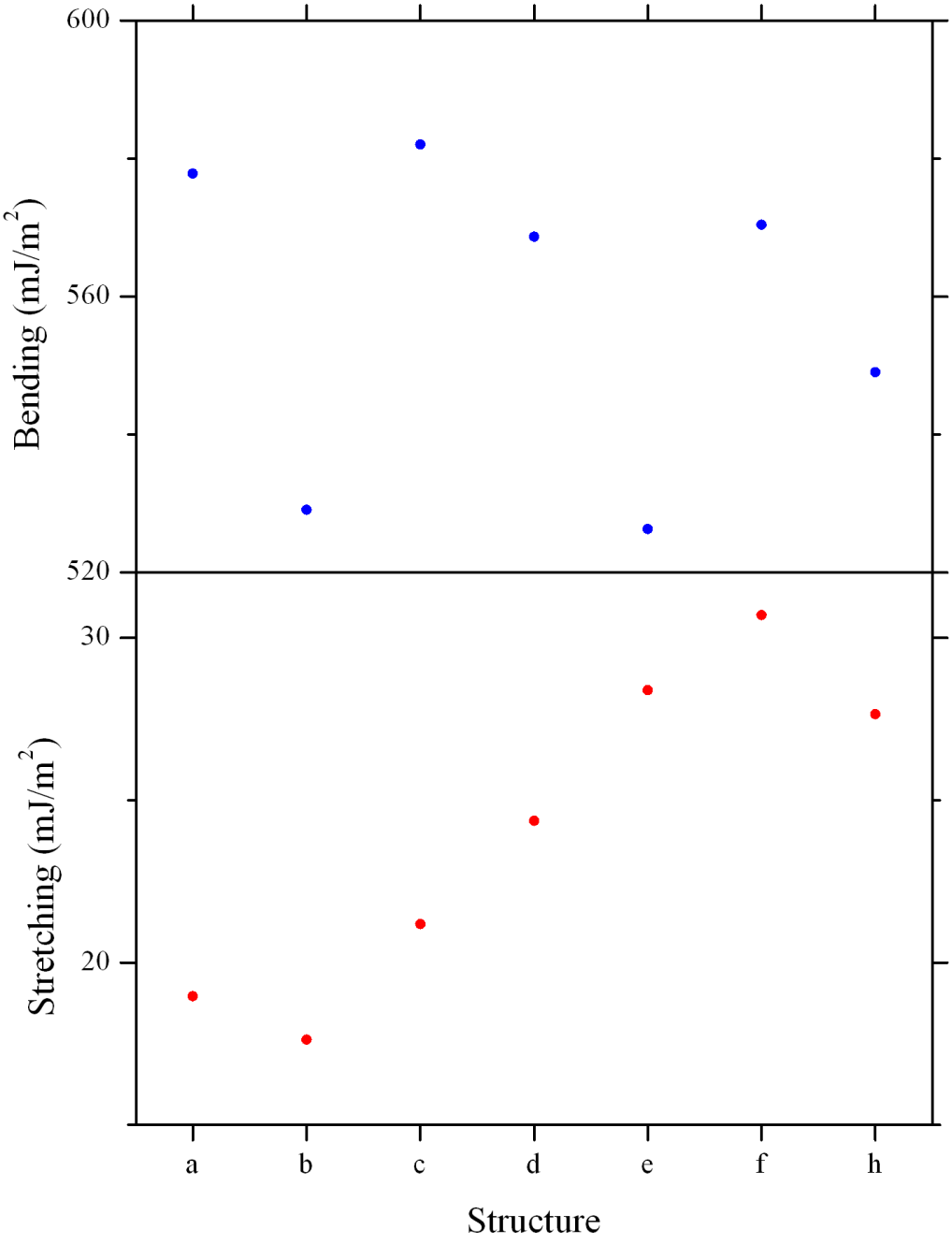

Figure 4.13: The bending and stretching components of the Keating minimised structures.

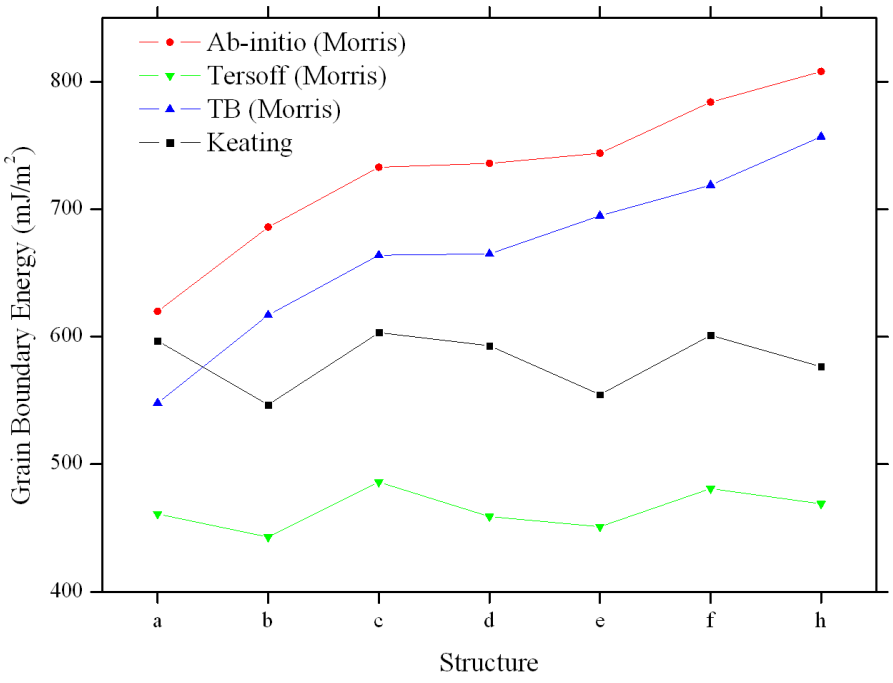

Figure 4.14: Grain boundary energies for the different structures identified in fig. 4.7. The Tersoff, tight binding and ab-initio are taken from [2]

4.7 The Si Σ13 Unit Cell

To simulate X-ray scattering we start with the relaxed structures of the grain boundary interfaces. As the Si Σ13 unit cell is used in the Keating minimization for convenience it is used in the simulated scattering process.

As well as changing the real space coordinates the Si Σ13 unit cell also changes the reciprocal space indices. It is important that the Σ13 Miller indices are used instead of those associated with the standard diamond unit cell. The relationship between the Σ13 Miller indices (H, K, L) and the standard ones are given by the following transformations:

$$\begin{pmatrix} H \\ K \\ L \end{pmatrix} = \begin{pmatrix} 1 & 0 & -5 \\ 0 & 1 & 0 \\ 5 & 0 & 1 \end{pmatrix} \begin{pmatrix} h \\ k \\ l \end{pmatrix} \quad , (4.4)$$

$$\begin{pmatrix} h \\ k \\ l \end{pmatrix} = \frac{1}{26} \begin{pmatrix} 1 & 0 & 5 \\ 0 & 26 & 0 \\ -5 & 0 & 1 \end{pmatrix} \begin{pmatrix} H \\ K \\ L \end{pmatrix} \quad . (4.5)$$

In the following discussion the term unit cell refers to the Σ13 CSL.

4.7.1 Measured Rods

The interface structure was probed using X-ray crystal truncation rod (CTR) scattering. CTR scattering is a surface and interface structural tool with atomic sensitivity.

The X-ray diffraction experiments were performed on the (2+3)-type diffractometer at the I07 beamline at the Diamond Light Source described in chapter 3. The wavelength λ = 0.7276 Å was chosen because the X-ray beam penetrates the sample at this high energy but the quantum efficiency of the detector is also high. The experimental procedure is described in more detail in the previous chapter. However, before the experiment can begin we first need to ensure that we are scattering off the interface. Because the lattices of the upper and lower crystal are rotated 22.6^{o} with respect to the [001] direction the reciprocal lattices and the CTRs of the two are easily distinguishable. This is shown in fig. 4.15 for the K = 0 plane for the Σ13 unit cell. The coordinate system was set to that of the top crystal. Firstly, the diffractometer was rotated to the calculated angles for the (080) Bragg peak. The sample was moved out of the beam by moving the hexapod in the z-direction. The sample was then gradually moved across the beam and the peak measured using the area detector. Attenuators were placed in front of the detector so that the Bragg peak did not saturate and damage the detector. The measured intensity was zero when the sample was out of the beam and increased several orders of magnitude when the beam passed through the top crystal. When the beam moved off the top crystal and into the interface the intensity decreased and fell off to zero when the beam was on the bottom crystal.

To convert from the rods in one crystal to the same rods in the other a transform has to be applied. The transformation to calculate the Miller indices of the bottom crystal in terms of the coordinate system of the top crystal is given by

$$\begin{pmatrix} h_{top} \\ l_{top} \end{pmatrix} = \frac{1}{13} \begin{pmatrix} 12 & -5 \\ 5 & 12 \end{pmatrix} \begin{pmatrix} h_{bottom} \\ l_{bottom} \end{pmatrix} \quad , (4.6)$$

where k has been excluded as it is the same for both crystals. The process was then repeated with the (20-2) Bragg peak of the bottom crystal. The intensity increased as the beam moved onto the bottom crystal and then decreased to zero when the beam moved onto the top crystal. The position of the interface was found where the intensities crossed over (fig. 4.16). The position this occurs was recorded and the hexapod was moved to this position.

The rods were obtained by measuring the scattering perpendicular to the interface along the CTRs that extend from the Bragg peaks because of the truncation of the crystals at the interface. The intensity distribution along the rod depends on the detailed atomic structure of the interface. The rods were obtained by moving off a Bragg peak in the [501] direction. The BCTRs contain contributions from the top and bottom crystals as well as the interface. The transmission geometry used ensured that all three were illuminated by the X-ray beam at the same time.

The experimental data was collected by measuring the integrated intensities obtained by stationary and ω-scans and then applying the the relevant correction factors. The attenuation of the beam through the sample is taken into account by applying the absorption correction (see appendix A.2.6). The following eight rods were measured; (-8,0,*L*), (-16,0,*L*), (-4,1,*L*), (16,-1,*L*), (22,2,*L*), (18,3,*L*), (32,4,*L*) and (18,5,*L*). The (-8,0,*L*), (-16,0,*L*), (-4,1,*L*) and (22,2,*L*) rods were measured using the stationary mode and the remainder by ω-scans.

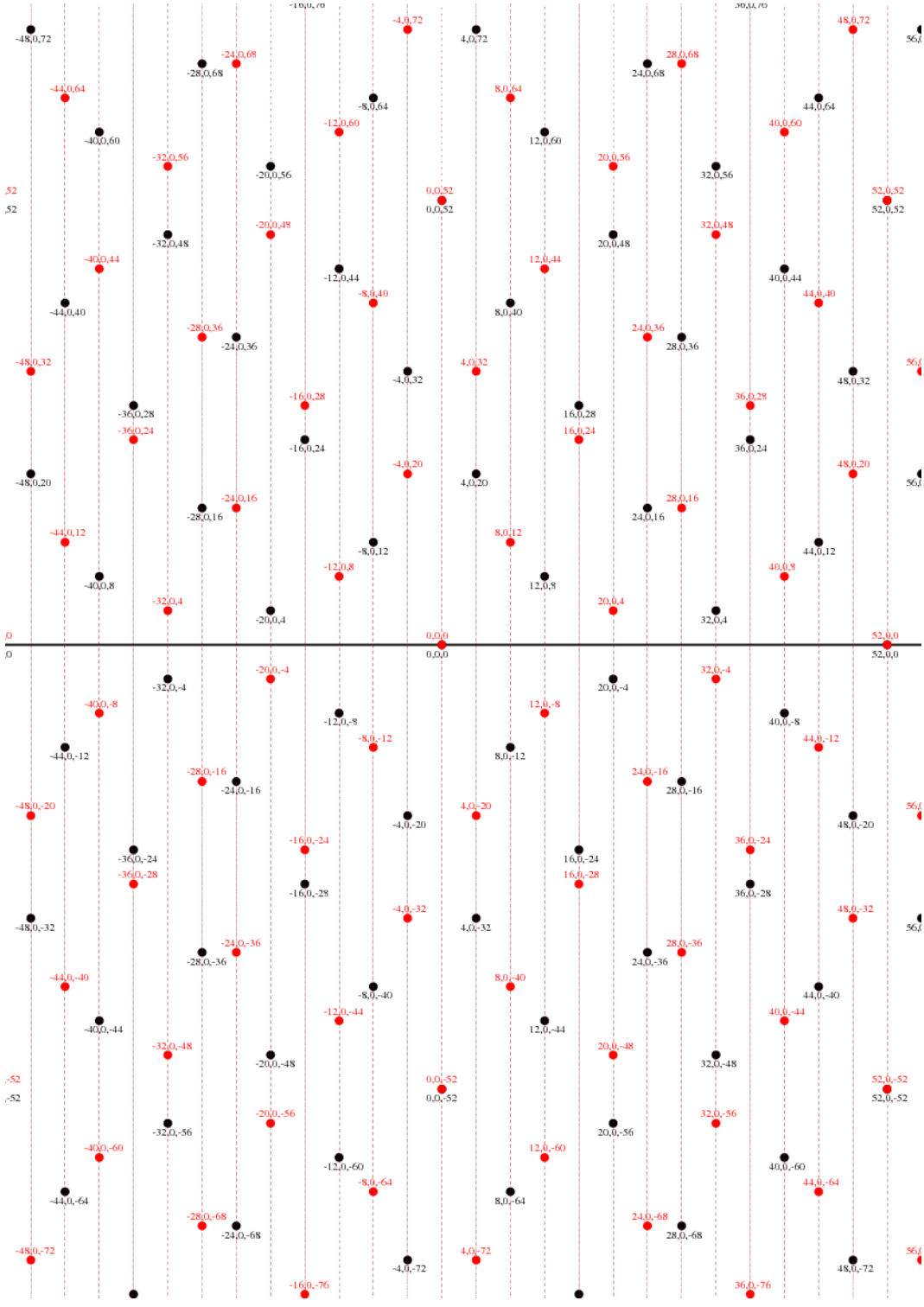

Figure 4.15: The reciprocal lattice of the bicrystal in the *K*=0 plane (see appendix section A.3 for different *K* planes). The black circles belong to the reciprocal lattice of the top crystal and the red circles the reciprocal lattice of the bottom crystal.

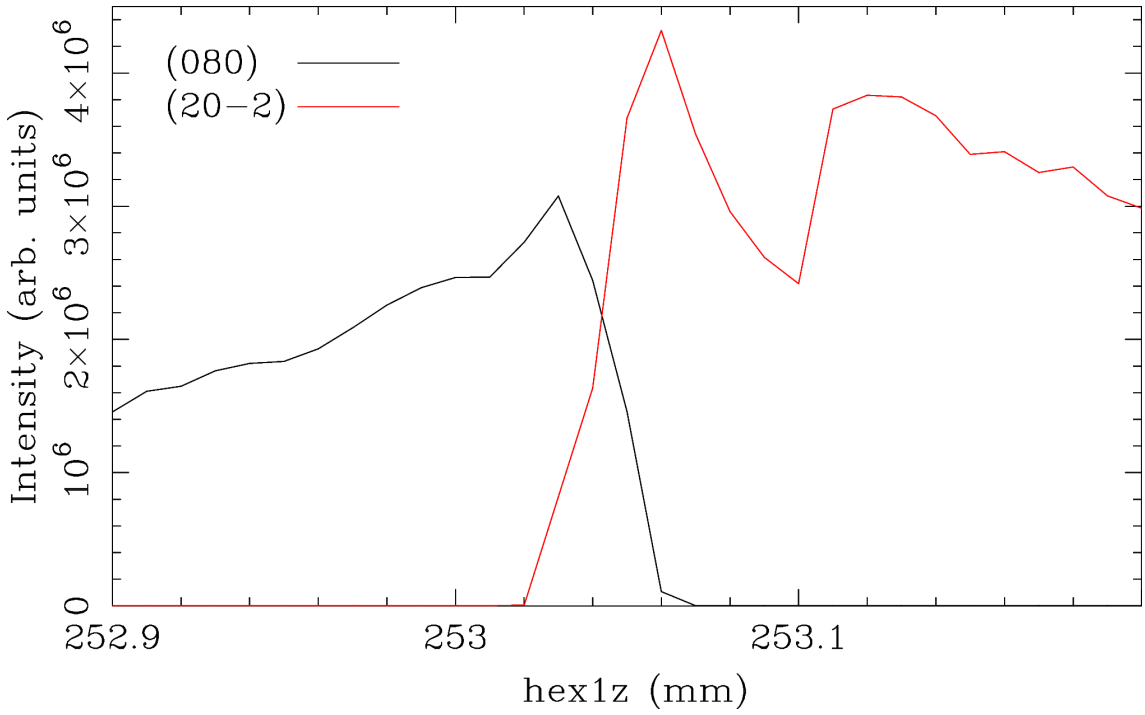

Figure 4.16: Locating the interface: the integrated intensities of the (080) Bragg peak of the top crystal and the (20-2) Bragg peak of the bottom crystal. The hexapod was moved in *z* until the beam moved onto either crystal. The interface position was found where the intensities crossed.

4.8 Simulated Scattering

In deriving the scattering from the proposed interface structures it is convenient to calculate the contributions from the top and bottom crystals and the interface structure separately before adding them together (the three separate regions are schematically illustrated in fig. 4.17). Thus there are three "unit cells" to consider. The convention used here is that the lattice parameters $\mathbf{a}_1$ and $\mathbf{a}_2$ of the interface unit cell are lying in the interface plane and that $\mathbf{a}_3$ is pointing outwards [68]. The miller index L is along the out-of-plane direction.

Assuming perfect crystalline order in the top and bottom crystals, the scattering from these crystals can be reduced to a one-dimensional sum over all layers [69]. Using the kinematical approximation the scattering from the ideal bottom crystal, starting at (x, y, z)=(0, 0, 0), is given by:

$$f_{bottom} = \sum_{z=0}^{-\infty} F_{bottom}\, e^{2\pi i l z} \quad (4.7)$$

where F_{bottom} is the structure factor of the unit cell for the bottom crystal. Expanding the sum gives

$$1 + e^{-2\pi i l} + e^{-4\pi i l} + .. + e^{-\infty \pi i l} = \frac{1}{1 - e^{-2\pi i l}} \quad . (4.8)$$

By substituting equation 4.8 into equation 4.7 the following is obtained

$$f_{bottom} = F_{bottom} \frac{1}{1 - e^{-2\pi i l}} = F_{bottom} \frac{e^{\pi i l}}{2i \sin(\pi l)} \quad . (4.9)$$

The first part of equation 4.9 is the standard form of the crystal truncation rod [26] and the denominator takes into account that the crystal is truncated at the interface. By using the relation $e^{i\theta} = \cos(i\theta) + i\sin(i\theta)$ equation 4.9 now rewritten as

$$f_{bottom} = F_{bottom} \frac{\cos(\pi l) + i \sin(\pi l)}{2i \sin(\pi l)} = \frac{F_{bottom}}{2} \left(1 - \frac{i \cos(\pi l)}{\sin(\pi l)} \right) \quad . (4.10)$$

In a similar derivation the scattering from the top crystal, starting at (0, 0, 0), is given by

$$f_{top} = \frac{F_{top}}{2} \left(1 + \frac{i \cos(\pi l)}{\sin(\pi l)} \right) \quad , (4.11)$$

where F_{top} is the structure factor of the unit cell for the top crystal, which may be related to that of the bottom crystal by symmetry.

In this instance, the scattering from the interface can be written as

$$f_{interface} = \sum_{j} f_j e^{2\pi i (Hx_j + Ky_j + Lz_j)} \quad , (4.12)$$

where f_j is the atomic form factor of the j^{th} atom, (HKL) the Miller Indices and $(xyz)_j$ the position of the j^{th} atom in fractional coordinates.

The total scattering is given by the coherent sum of all three contributions:

$$f_{total} = f_{top} e^{i\mathbf{q}.\mathbf{d}} + f_{bottom} + f_{interface} \quad , (4.13)$$

The interference between the contributions from the two crystals, which depends sensitively on the interface separation, **d**, arises here [69] . Figure 4.18 shows that as the interface expansion between the crystals increases there is an increase in the number of oscillations in the total scattering. This is a result of a phase difference being introduced due to normal shift of the upper crystal lattice with respect to the bottom one. It is important to note that these terms can only be added together coherently provided the intensity is properly integrated [70]. The coordinates of the interface and bulk atoms need to defined with respect to a common origin and it is important to define the bulk unit cells starting directly above and below the interface unit cell. The interface can be chosen to extend arbitrarily deep into both crystals provided the layers directly above and below the interface form the bulk unit cells. When the atoms in the extended interface layer are kept at their bulk positions the calculated scattering will remain unchanged [68].

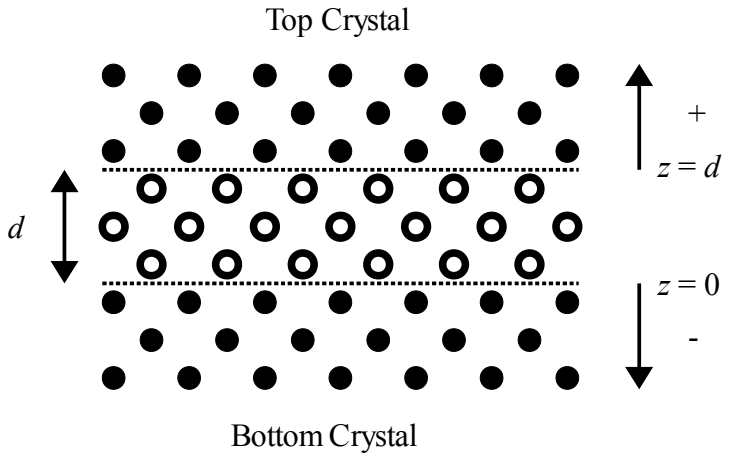

Figure 4.17: Schematic of the interface layer between two crystals. The top crystal extends to infinity and the bottom crystal to minus infinity. The crystals are separated by a distance *d*.

The next step is to simulate the scattering from the Keating minimised relaxed structures. As mentioned earlier, the relaxed structures consist of a top and bottom bulk crystal and the interface structure. The top and bottom crystals contain four unit cells each. This entire structure is considered the interface for the sake of the simulated scattering and the scattering is described by equation 4.12. The next stage is to introduce another top and bottom crystal. The top crystal begins at the layer directly above where the interface terminates and the bottom crystal directly below. The scattering from the top crystal is given by equation 4.11 and the bottom crystal by equation 4.12. The total structure can be seen in fig. 4.19 and the individual scattering components in fig. 4.20. Upon comparison with fig. 4.18 it can be seen from fig. 4.20 that the interface contributes significantly to the total scattering; as the rod changes significantly due to the grain boundary structures. Figure 4.20 shows that the interface term oscillates considerably but the total scattering does not. This occurs because the majority of the interface described earlier is bulk like. As a result of this the phase of the interface cancels with that of the scattering of the top and bottom crystal leading to a total scattering that does not oscillate.

The bicrystal breaks the 3*m* symmetry of the diamond cubic structure. The bicrystal itself can be considered to be produced from the single crystals by a series of operations, each of which involves a loss of symmetry (dissymmetrization) [30, 70]. The scattering is calculated as an average of two domains with opposite direction of symmetry. In one domain the structure spirals inwards along the tilt axis and in the other outwards. This is illustrated in fig. 4.21 which shows the (22,2,*L*) and (22,-2,*L*) rods compared with the data. These domains are energetically equivalent but give very different rods. The (22,2,*L*) rod is a good fit of the data close to the Bragg peak but is relatively poor further up the rod, whilst the opposite is true for the (22,-2,*L*) rod. It is seen that averaging the two rods gives a much better fit of the data, implying that the two domains occur in the interface.

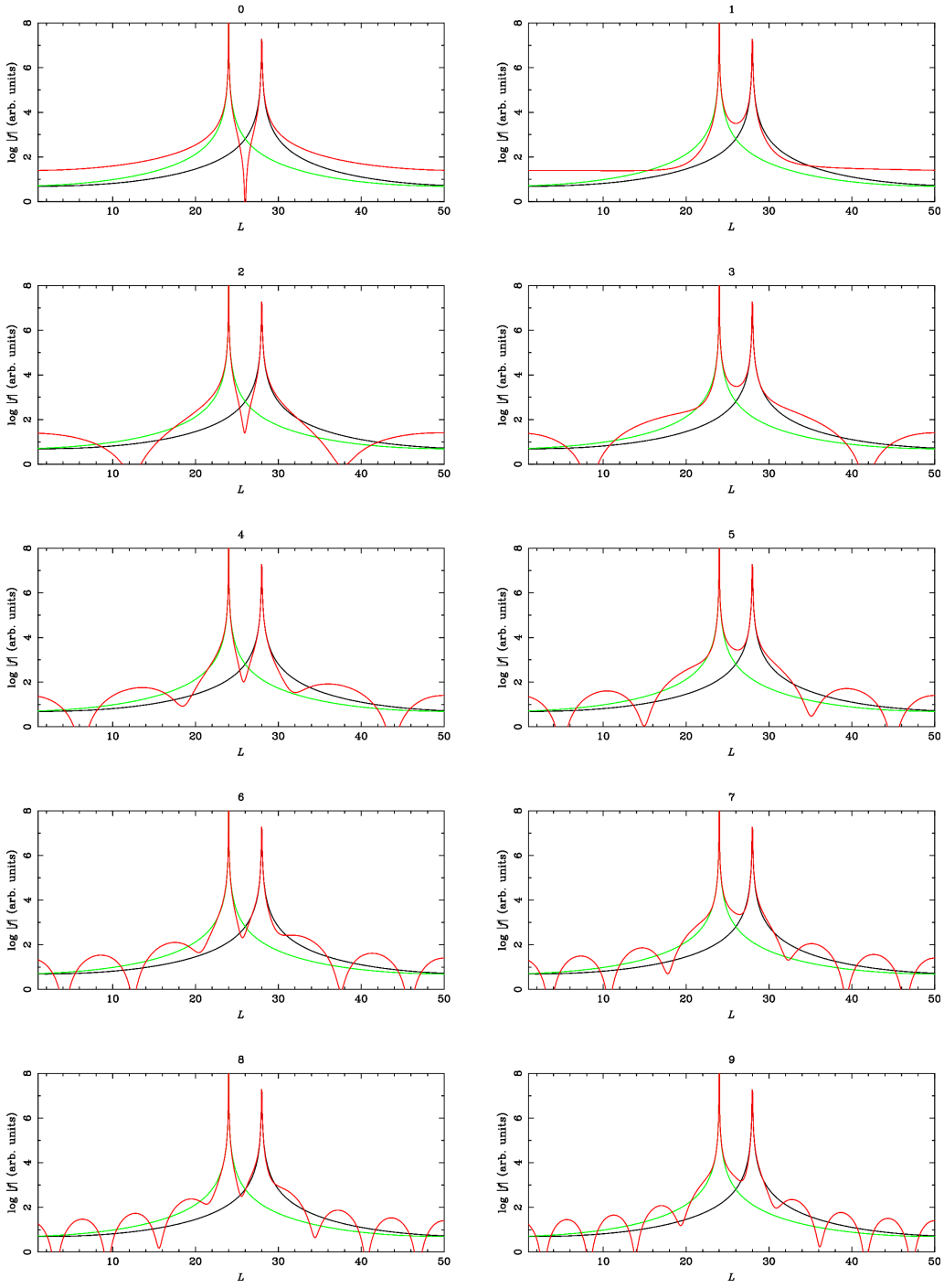

Figure 4.18: The effect of the separation between crystals on the total scattering of the (-16,0,*L*) rod. The total scattering is the red line, the contribution from the top crystal the green and the bottom crystal the black. The title of each graph is the separation between the crystals as a percentage of one of the bulk crystals.

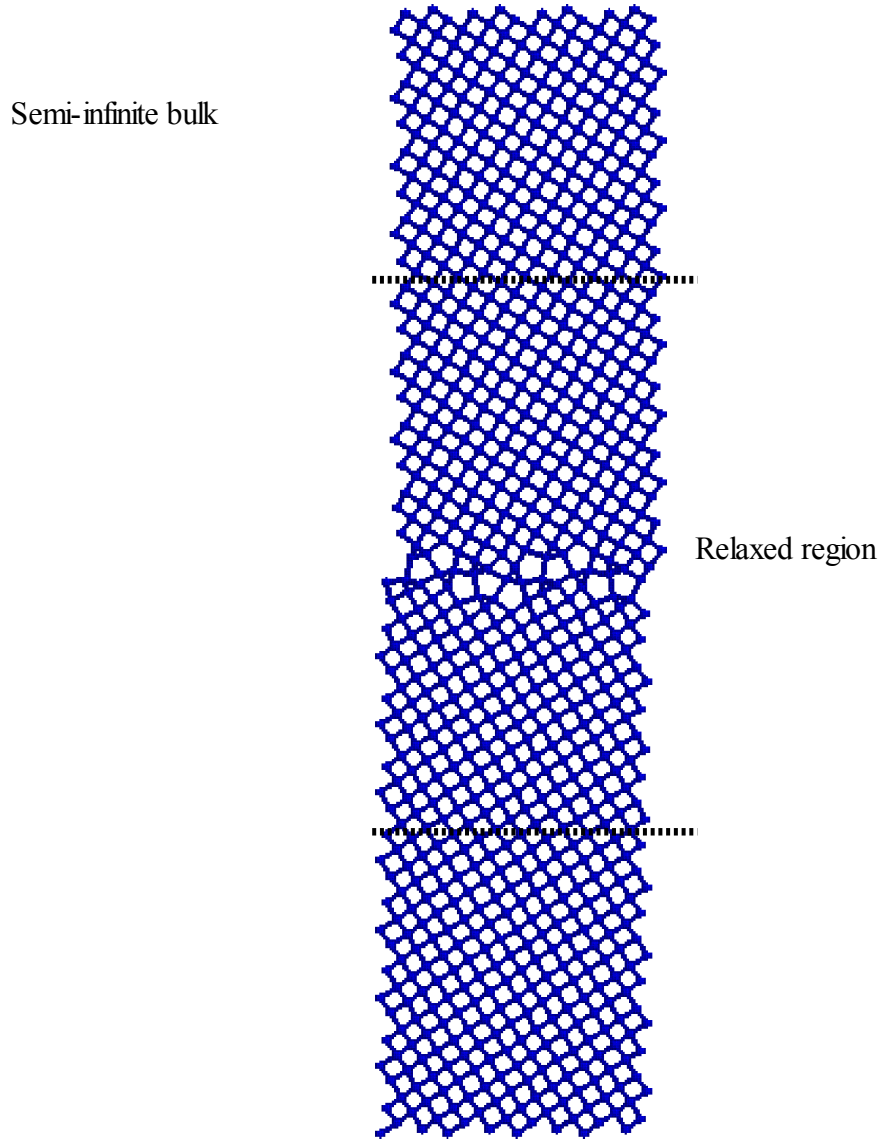

Figure 4.19: The total structure comprises of three distinct regions; two bulk like Si crystals separated by the grain boundary interface.

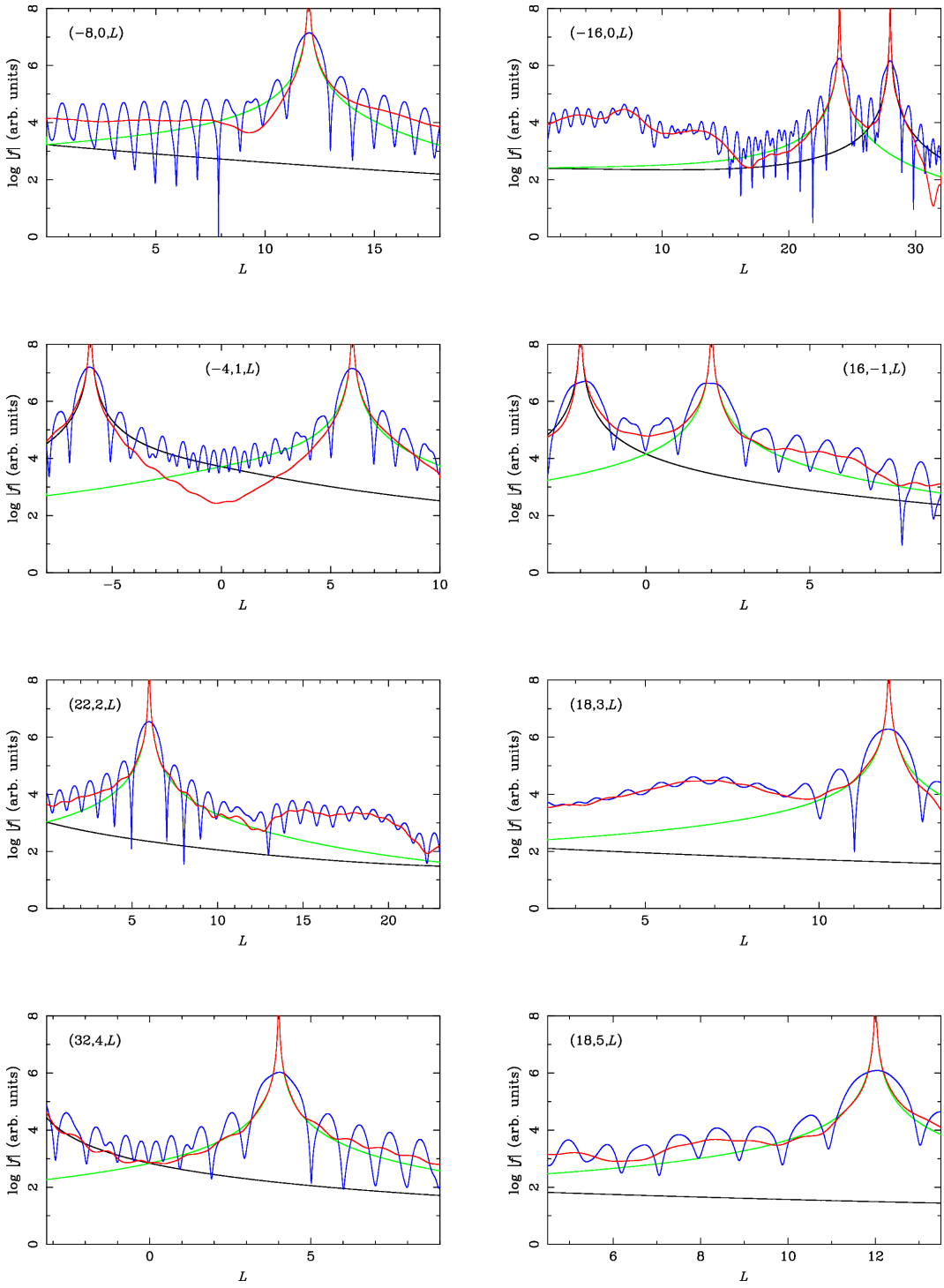

Figure 4.20: Contribution of the scattering from the top crystal (green line), bottom crystal (black), interface (blue) to the total scattering (red) from a relaxed structure (a).

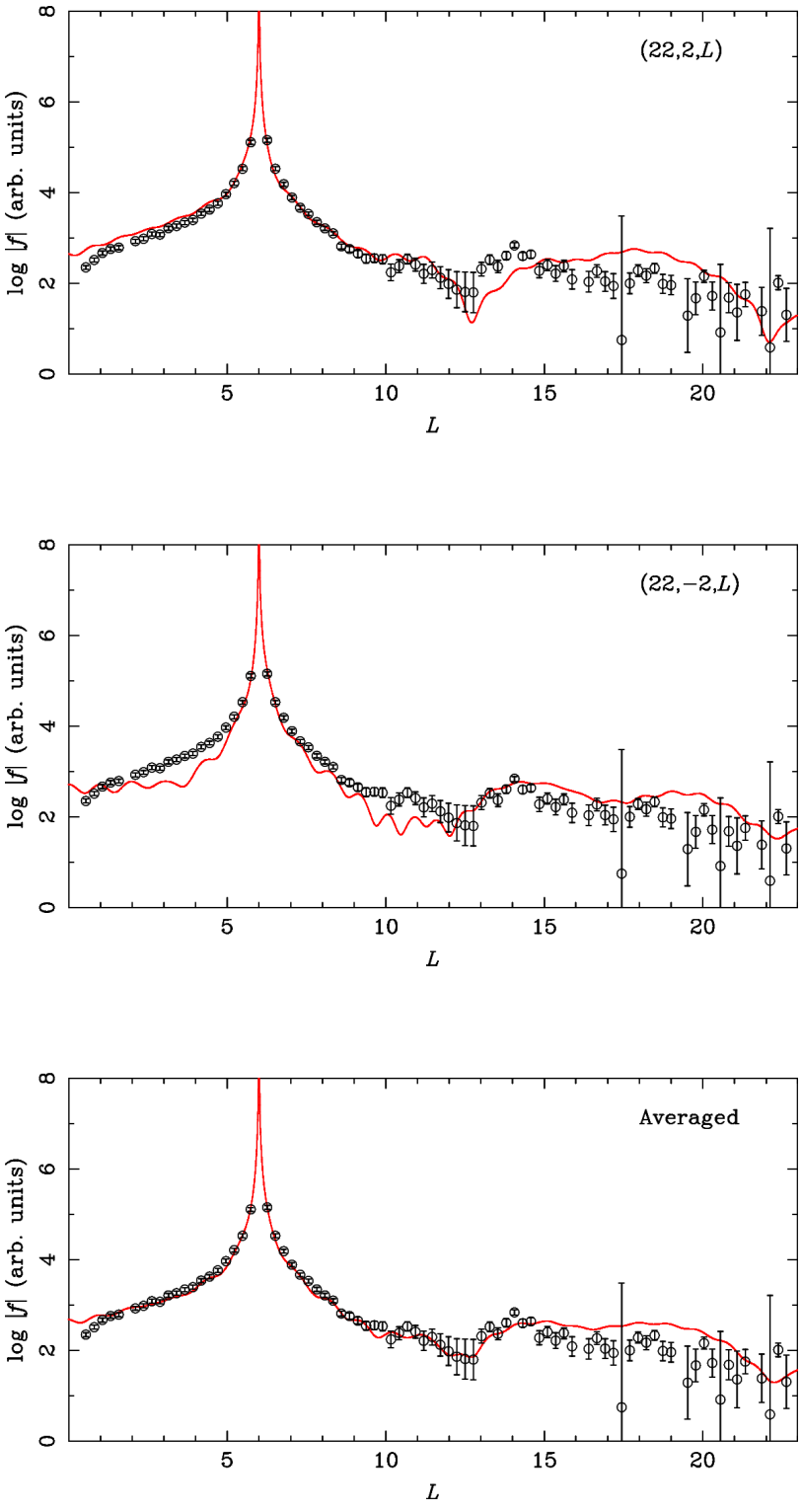

Figure 4.21: The total scattering for the (22,2,*L*) rod, (22,-2,*L*) rod and the average of the two compared with the measured data.

4.9 Comparison with Data

The measured rods compared with the simulated scattering from the various relaxed grain boundary structures can be seen in figs. 4.22 to 4.24. Straight away it can be seen that the different relaxed grain boundaries all have varying successes at predicting the rods. For example, there is excellent agreement between structure (a) and the (-16,0,L) rod, but poor agreement with structure (b) and several sharp minima between L = 0 and L = 20 are now present. These differences have arisen from the interference between the waves scattered by the different regions of the bicrystal which is dependent on the atomic coordinates of the grain boundary and can be seen by comparing the rods from structures (c), (d) and (f). The interface expansions for these structures are all very similar, yet the simulated scattering is very different for all the rods. This is most noticeable in between the Bragg peaks for the (-4,1,L) rod. This is as a result of the scattering from the interface and bulk having a similar magnitude but different phases for the various grain boundaries.

The simulated scattering from all the grain boundaries gives good fits for most rods apart from the (-8,0,L), (-16,0,L) and (22,2,L) rods. The goodness of fit can be explained as the range of L is relatively small and the rods are not far away from the Bragg peaks. As expected, the graphs show that the scattering from the grain boundary has no effect on regions very close to the Bragg peak simply because the intensity of the Bragg peaks are much greater. As we move further away from the Bragg peaks the difference between the scattering and the data set becomes much more pronounced as the scattering from the grain boundary has similar or greater magnitude than the scattering from the top and bottom crystal (this is illustrated in fig. 4.20).

Qualitatively it is seen that structure (a) gives the best fit of the rods overall. The χ^2 for the proposed structures (see appendix, section A.4) is given in table 4.3. Structure (a) has the best agreement with χ^2 = 1.43 whereas the χ^2 for the remaining structures varies between 4.98 to 7.79. The difference in the χ^2 demonstrates the sensitivity of the simulated scattering to the atomic position of the interface structures and the distance between the Si crystals. Hence there is a clear argument that structure (a) is the interface structure. The χ^2 of each individual rod for structure (a) is given in table 4.4. Only one rod has a χ^2 greater than 2; the value of 3.96 for the (18,3,L) rod can be explained by the

discrepancies between the model and measured results close to the Bragg peak. This rod was obtained using an ω-scan and close to the Bragg peak we were unable to separate the peak from the background. As a result of this data points close to the peak have an intensity greater than that of the simulated scattering.

Structure	χ^2
(a)	1.43
(b)	5.03
(c)	4.98
(d)	6.75
(e)	7.42
(f)	7.79
(h)	7.14

Table 4.3: A list of χ^2 for each structure.

Rod	χ^2
(-8,0,*L*)	1.95
(-16,0,*L)*	1.5
(-4,1,*L*)	1.46
(16,-1,*L*)	1.3
(22,2,*L*)	0.87
(18,3,*L*)	3.96
(32,4,*L*)	0.91
(18,5,*L*)	1.16

Table 4.4: χ^2 of each rod for structure (a).

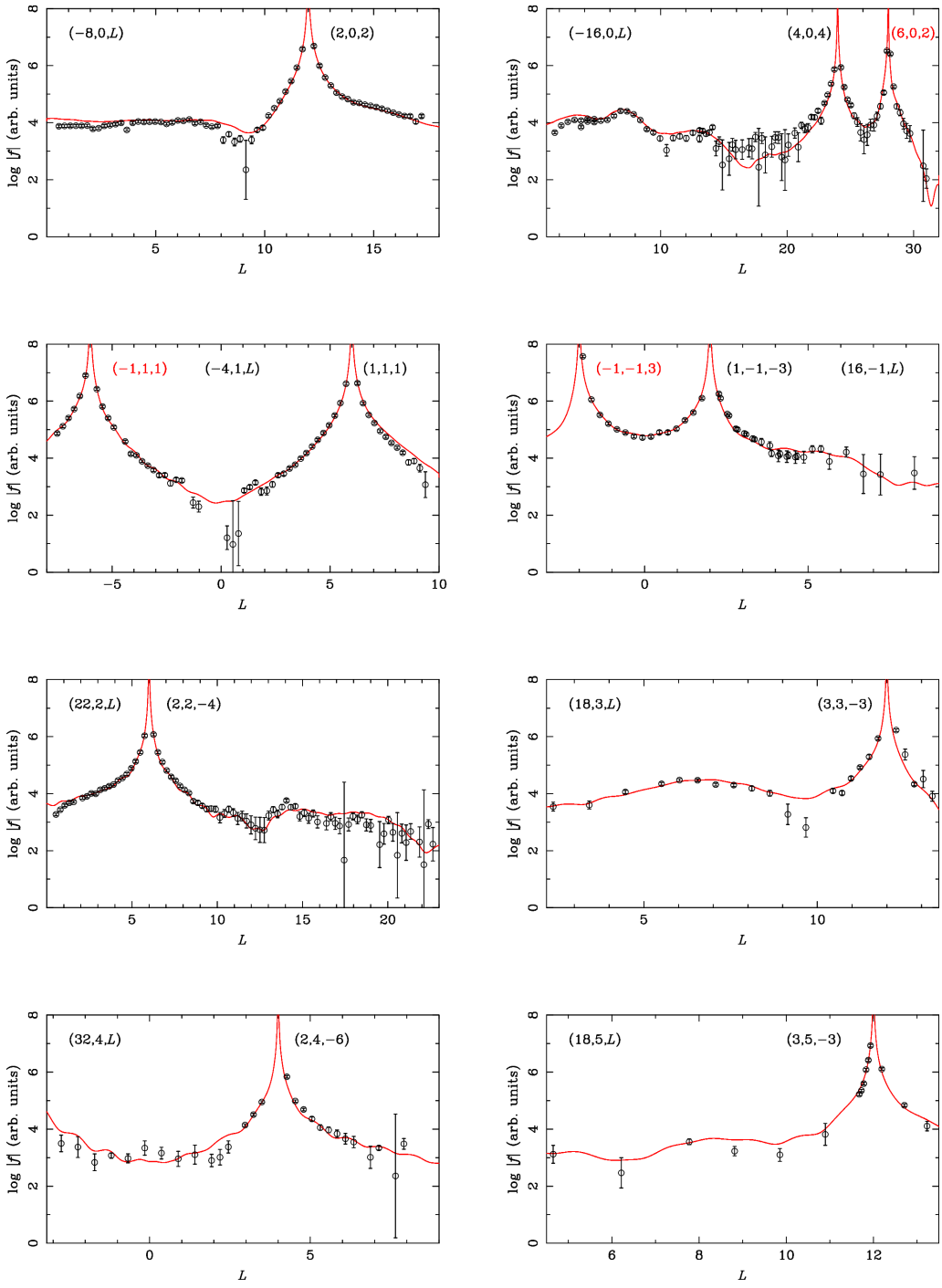

Figure 4.22: Comparison of the measured BCTRs (circles) with the simulated scattering (red line) from structure (a). The Bragg peaks associated with standard diamond unit cell are labelled for clarity; black from the top crystal and red from the bottom crystal.

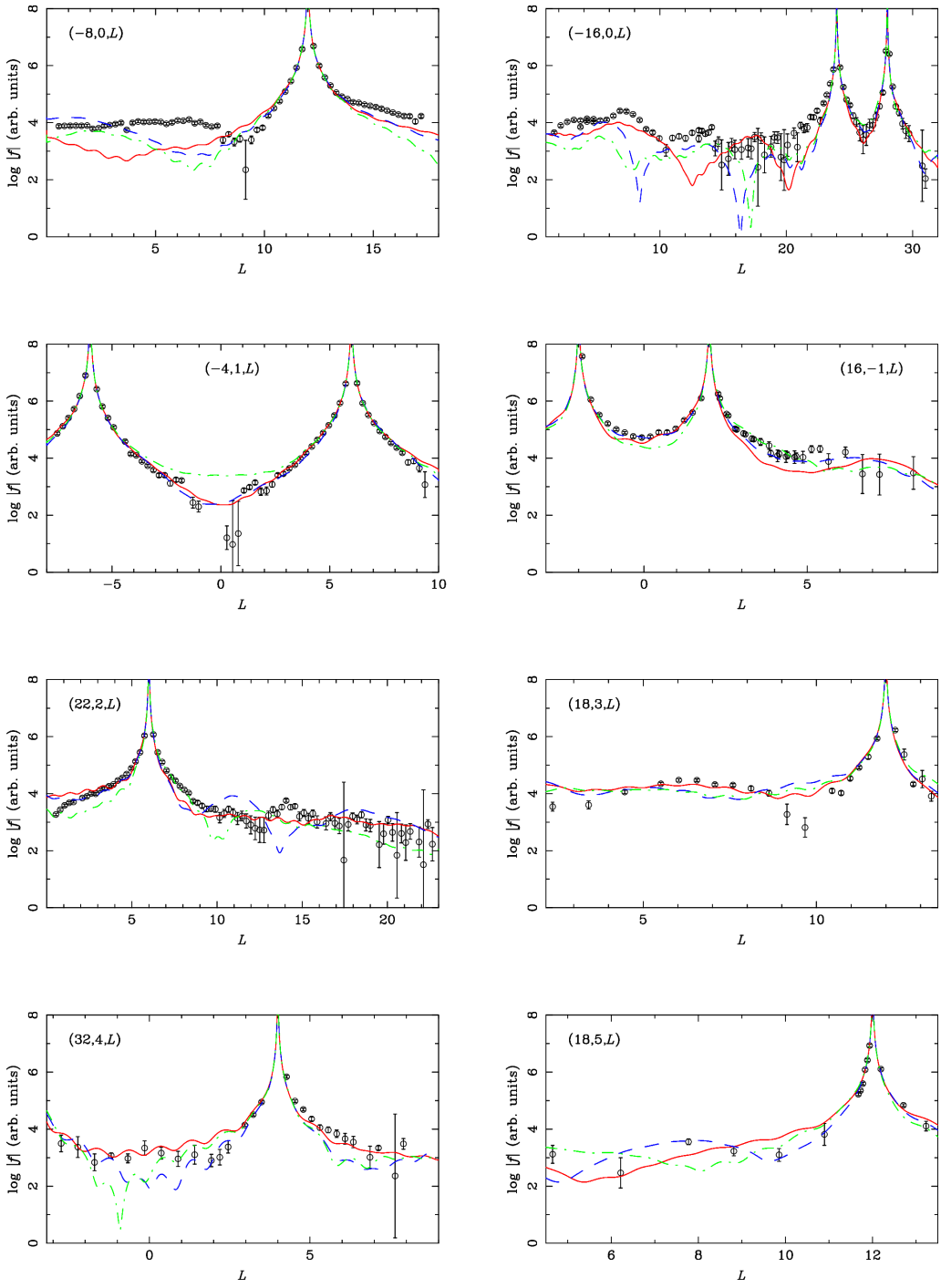

Figure 4.23: Comparison of the measured Bicrystal truncation rods with the simulated scattering from structures (b) (red solid line), (c) (blue dashed line) and (d) (green dot-dashed line).

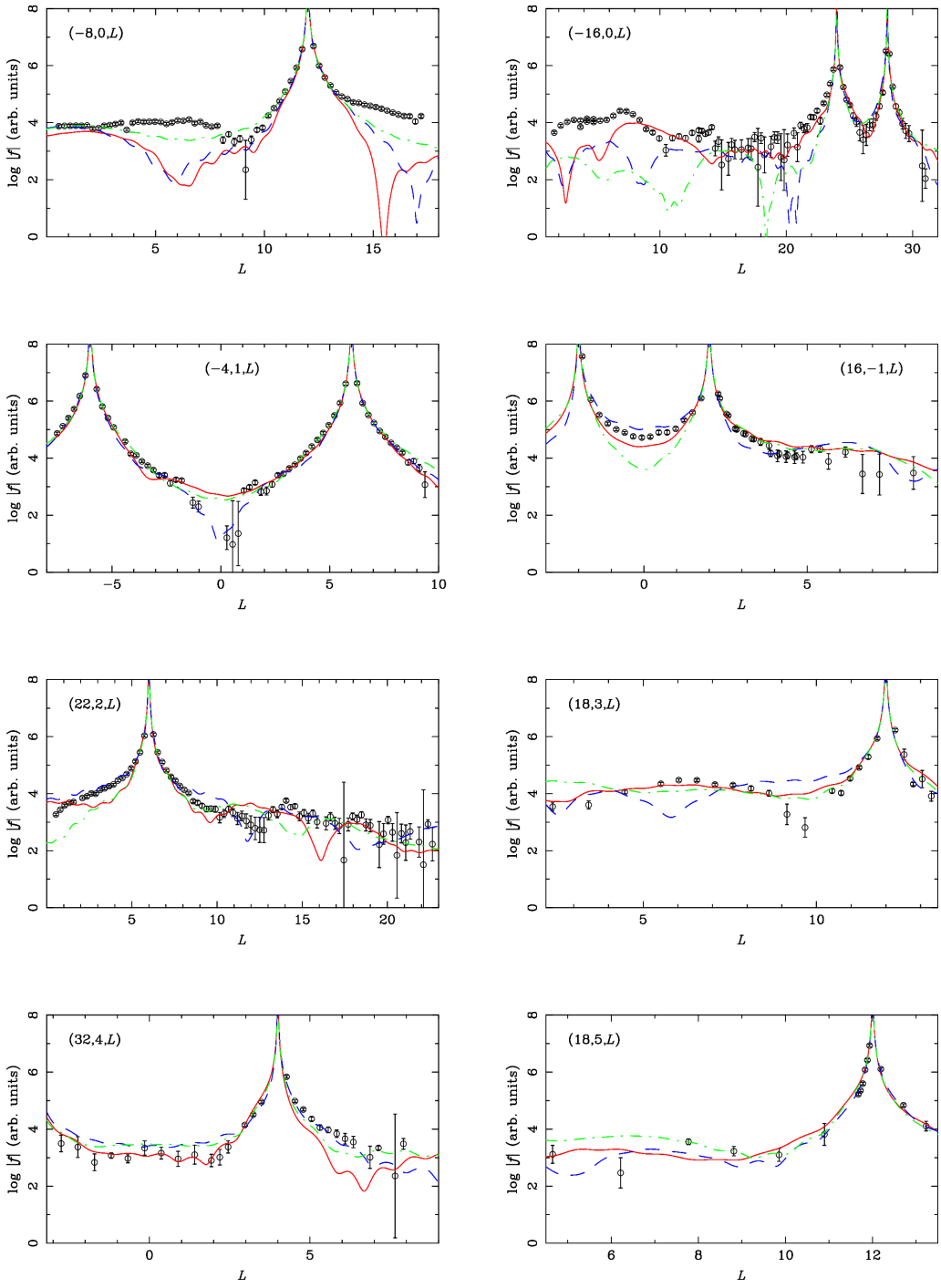

Figure 4.24: Comparison of the measured Bicrystal truncation rods with the simulated scattering from structures (e) (red solid line), (f) (blue dashed line) and (h) (green dot-dashed line).

4.10 Sensitivity to the Interface Expansion

So far the simulated BCTRs have been calculated for relaxed structures. The interface expansion is found from this as no constraints have been applied. In order to determine if the Keating minimisation found the correct interface expansion the simulated scattering for various expansions was investigated. After structure (a) has been relaxed, the layer of atoms that are connected to the grain boundary are moved in [001] and fixed in space. The atoms are moved up if they belong to the top crystal and down if they belong to the bottom. The net result is that there is an increase in the distance between the crystals from the relaxed position. The total deviations from the relaxed positions are; 0.1Å, 0.2Å and 0.5Å. For example, for an expansion of 0.1Å the atoms of the top crystal are moved up by 0.05Å and those of the bottom down by 0.05Å. Once these layers are fixed in space, the interface undergoes the Keating minimisation. This is a very quick process as the relaxed structure is used as the starting point. The rigid body translations and Keating energies for the different deviations are shown in table 4.5. The Keating energies all increase as the expansion increases; there is little difference in the bending component with expansion but a marked difference in the stretching component. The stretching component drastically increases with expansion and exceeds the bending term for 0.5Å.

The simulated BCTRs are shown in figs. 4.25 to 4.27. The overall χ^2 for the 0.1Å is 1.995, 2.294 for the 0.2Å and 3.948 for the 0.5Å datasets compared with 1.43 for the relaxed structure. The goodness of fit decreases as the deviation from the relaxed position increases. The scattering from the interface changes significantly for the (16,-1,*L*), (18,3,*L*), (32,4,*L*) and (18,5,*L*) rods as a result of the change in atomic coordinates; leading to poorer fits away from the Bragg peak. The interference between the crystals becomes more pronounced close to the Bragg peak as the phase changes with distance; this is observed between the peaks for the (-16,0,*L*) rod. The minimum between the peaks is to the right of the dataset at 0.2Å and to the left at 0.5Å. This demonstrates the sensitivity of our model to both the distance between the crystals, even for fractional Å changes, and the atomic coordinates of the interface. The relaxed structure gives the best fit of the data, meaning that provided the atoms and correct bonding is given the Keating minimisation finds the correct expansion.

Distance	Offset in *x*	Offset in *y*	Offset in *z*	Bending	Stretching	Keating
Relaxed	0.036	-0.623	0.136	577.82	18.97	596.79
0.1Å	0.034	-0.634	0.136	583.23	97.28	674.39
0.2Å	0.034	-0.634	0.137	572.28	166.96	739.23
0.5Å	0.034	-1.023	0.146	602.97	648.86	1251.82

Table 4.5: The rigid body translations (as a fraction of the generated bicrystal – units of Å) and Keating energies (in mJ/m^2) of structure a when the distance (001) between the crystals in increased from the relaxed position. The relaxed structure has been included for comparison.

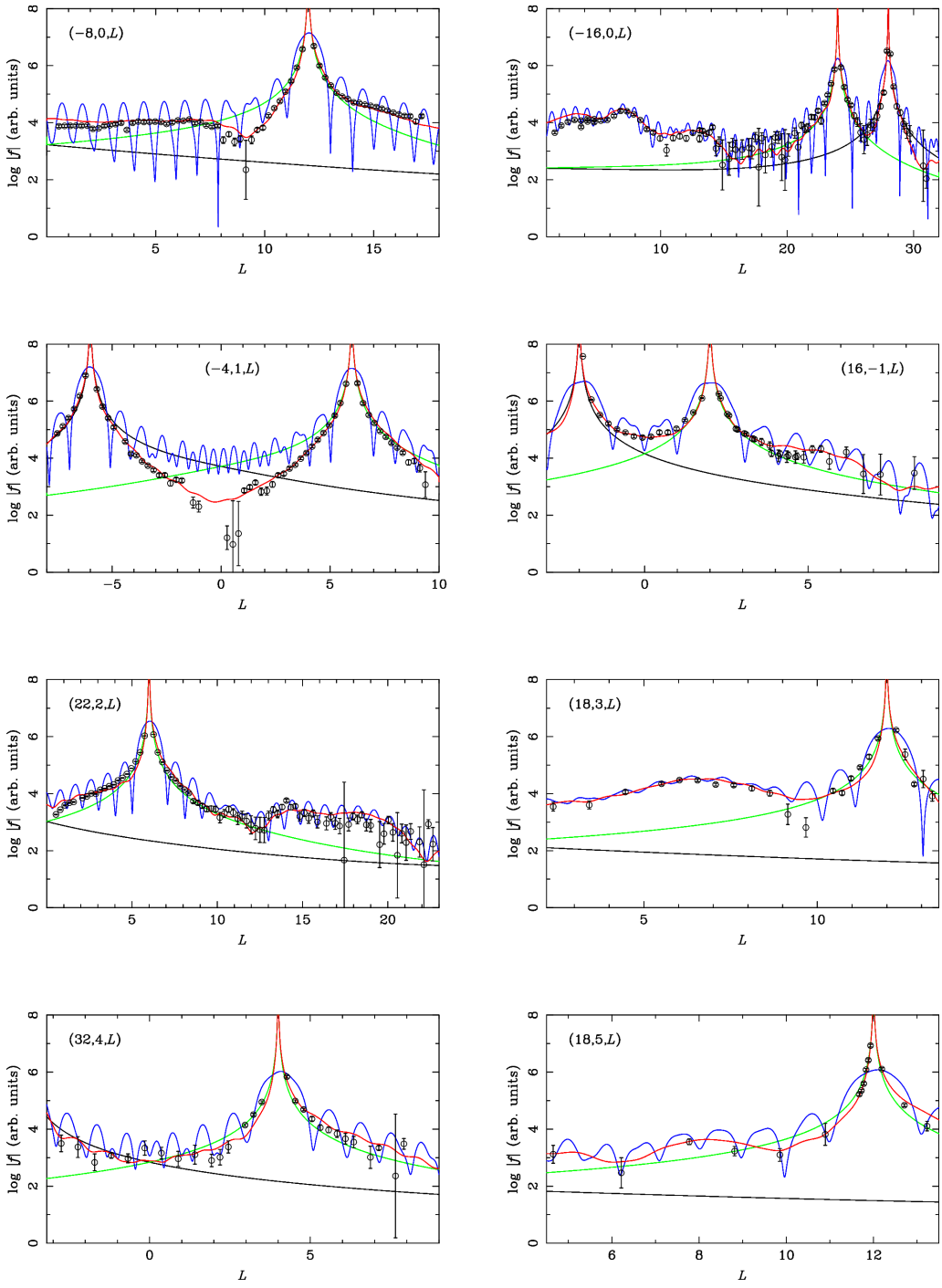

Figure 4.25: The simulated BCTRs obtained when the interface expansion is increased by 0.1Å from the relaxed position.

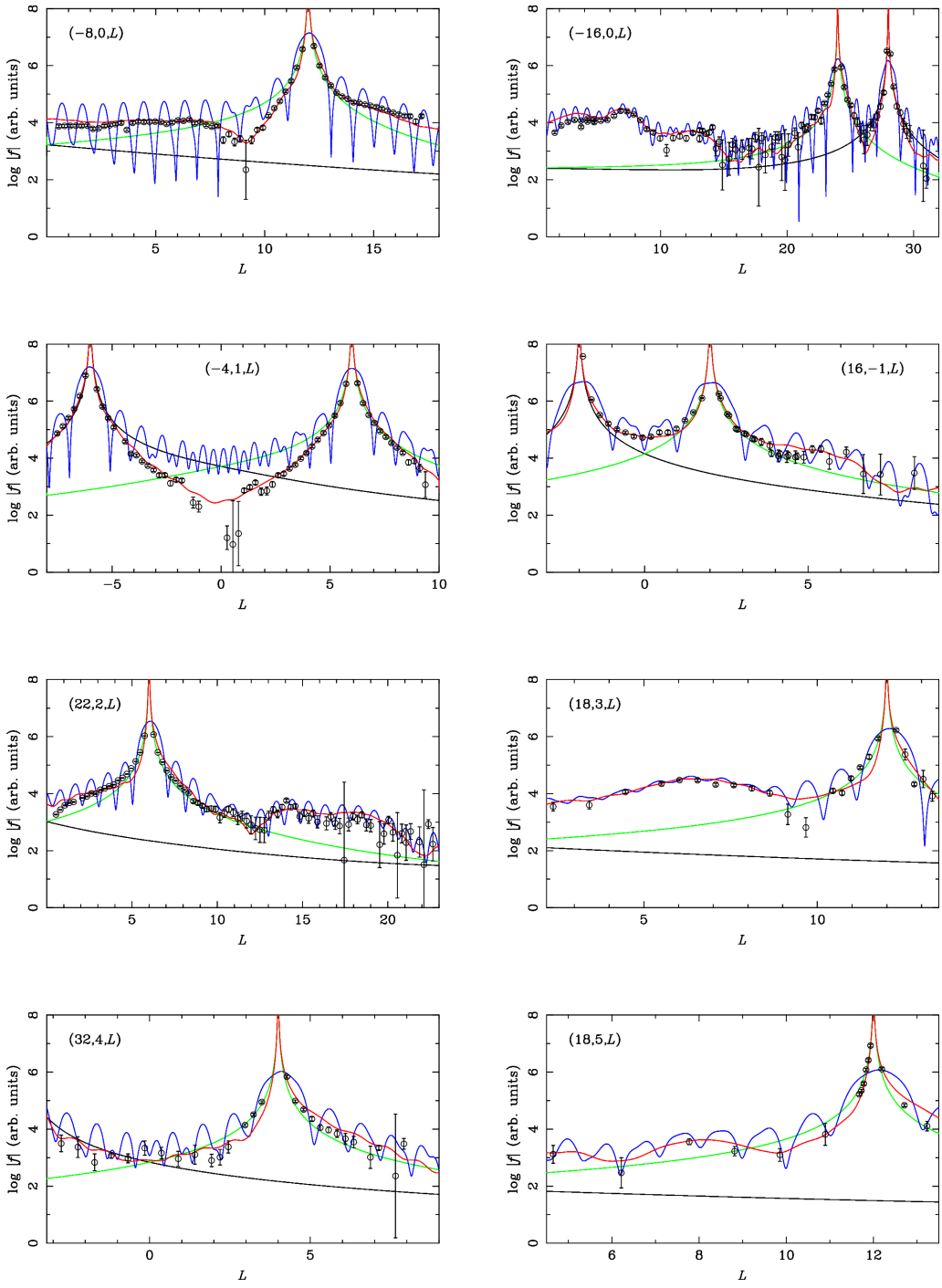

Figure 4.26: The simulated BCTRs obtained when the interface expansion is increased by 0.2Å from the relaxed position.

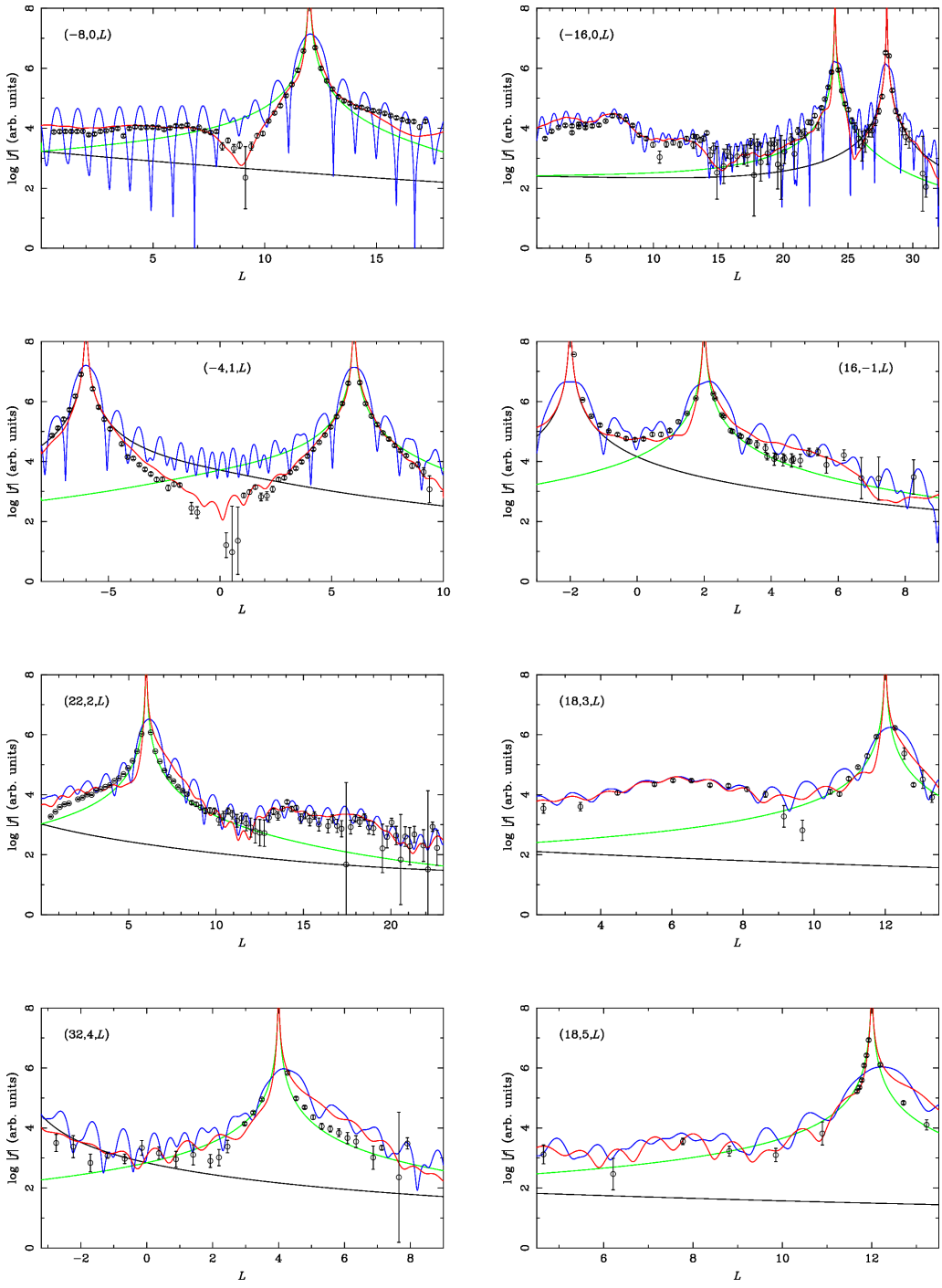

Figure 4.27: The simulated BCTRs obtained when the interface expansion is increased by 0.5Å from the relaxed position.

4.11 In-Plane Scans

The in-plane reflections were measured using the constant velocity mode. The reflections along (*H*, 3, 0), shown in fig. 4.28, measure only background in the majority of cases, but peaks are observed for *H* = -6, 2, 4, 6, 8, 14, 16, 18, 20 and 22. However, some of the scans (*H* = -6, 2, 22) have two peaks. The extra peaks are due to artifacts in the interface, most likely precipitates, as repeats of these scans off the interface measured only background (fig. 4.29). Upon observation with the area detector (fig. 4.30), the scattering is neither a result of a Bragg peak nor is it rod-like, as in the geometry used the rod would appear as an extended streak (fig. 4.31), but, due to the sharpness of the peaks and pattern, it is crystallographically aligned with the grain boundary.

Attempts were made to estimate the precipitate material by considering the *d*-spacing. The spacing between planes, *d*, is perpendicular to the set of *hkl* planes, and is calculated from Bragg's law:

$$d = \frac{\lambda}{2\sin(\theta)} \quad . (4.17)$$

The spacings in table 4.6 are presented in the order they were found rather than for some physically important characteristic. The *d*-spacings were compared to the powder diffraction files (PDFs) [71] and correspond to a theoretically obtained SiO diffraction pattern which is consistent with the precipitate material in [11, 30]. We were unable to fully determine the precipitate material as we have not obtained all the *d*-spacings; the *d*-spacings in the PDFs are systematically ordered in terms of their intensity beginning with the most intense peak; as this information is lost to us it makes the searching routine far more difficult.

(*H*, *K*)	2θ	*d* (Å)
-6, 1	11.88	3.52
-6, 3	24.93	1.69
2, 3	23.39	1.79
22, 3	41.22	1.03
12, 4	36.23	1.17

Table 4.6: The position in reciprocal space, 2θ angles and subsequent value of *d* for the double peaks.

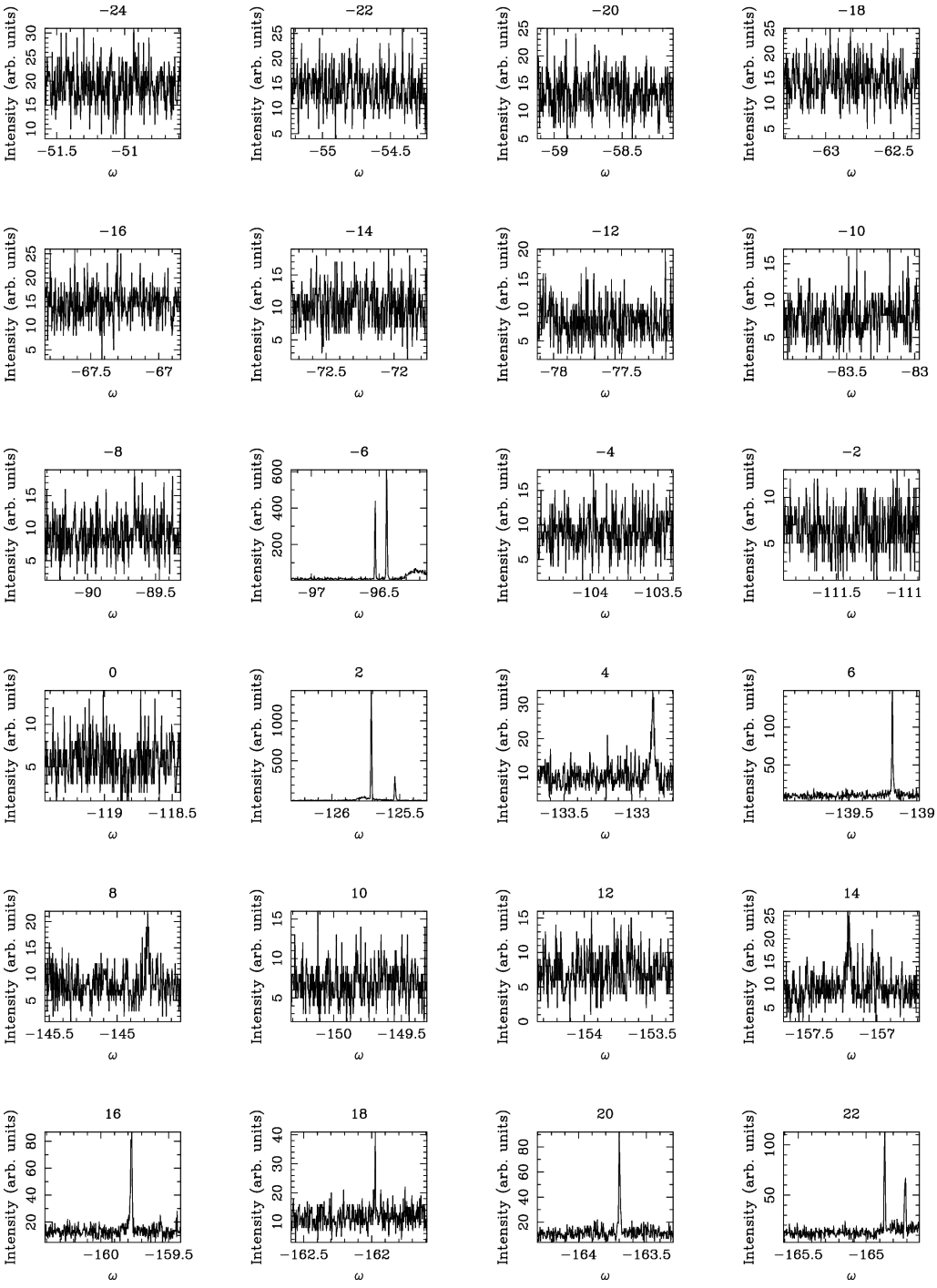

Figure 4.28: The constant velocity scans along (*H*30), where *H* is given in the figures. Double peaks are present at *H* = -6, 2 and 22.

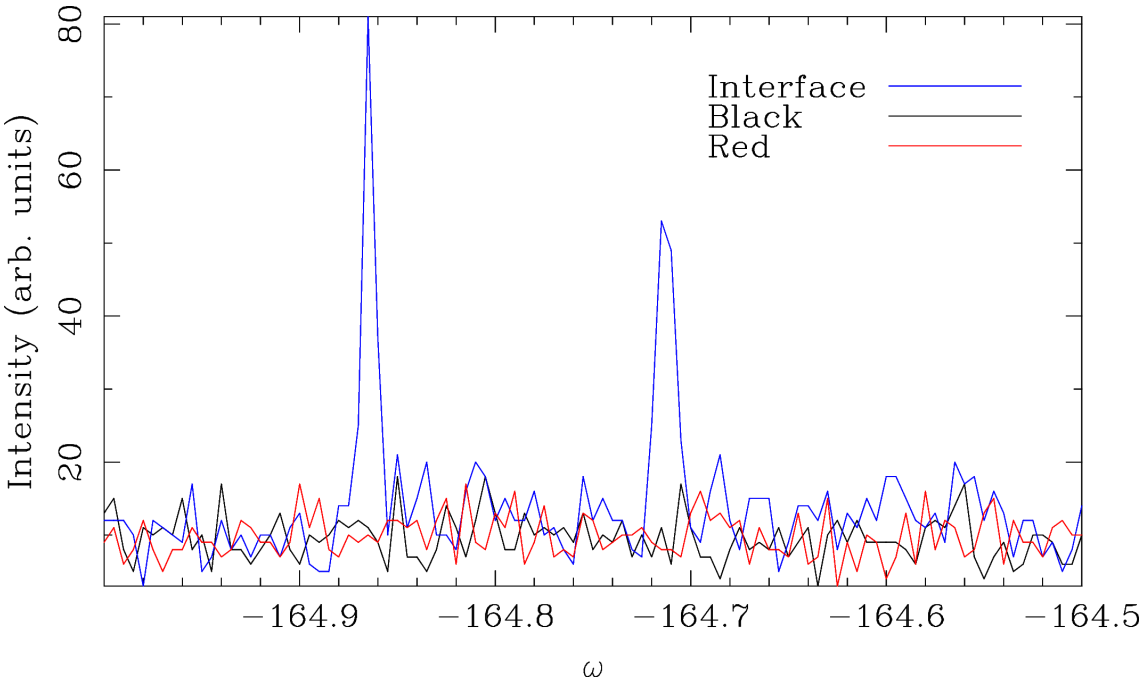

Figure 4.29: Comparison of the constant velocity scan at (22,3,0) when the scan is at the interface and for the top (black) and bottom (red) crystals. The two peaks are only seen at the interface.

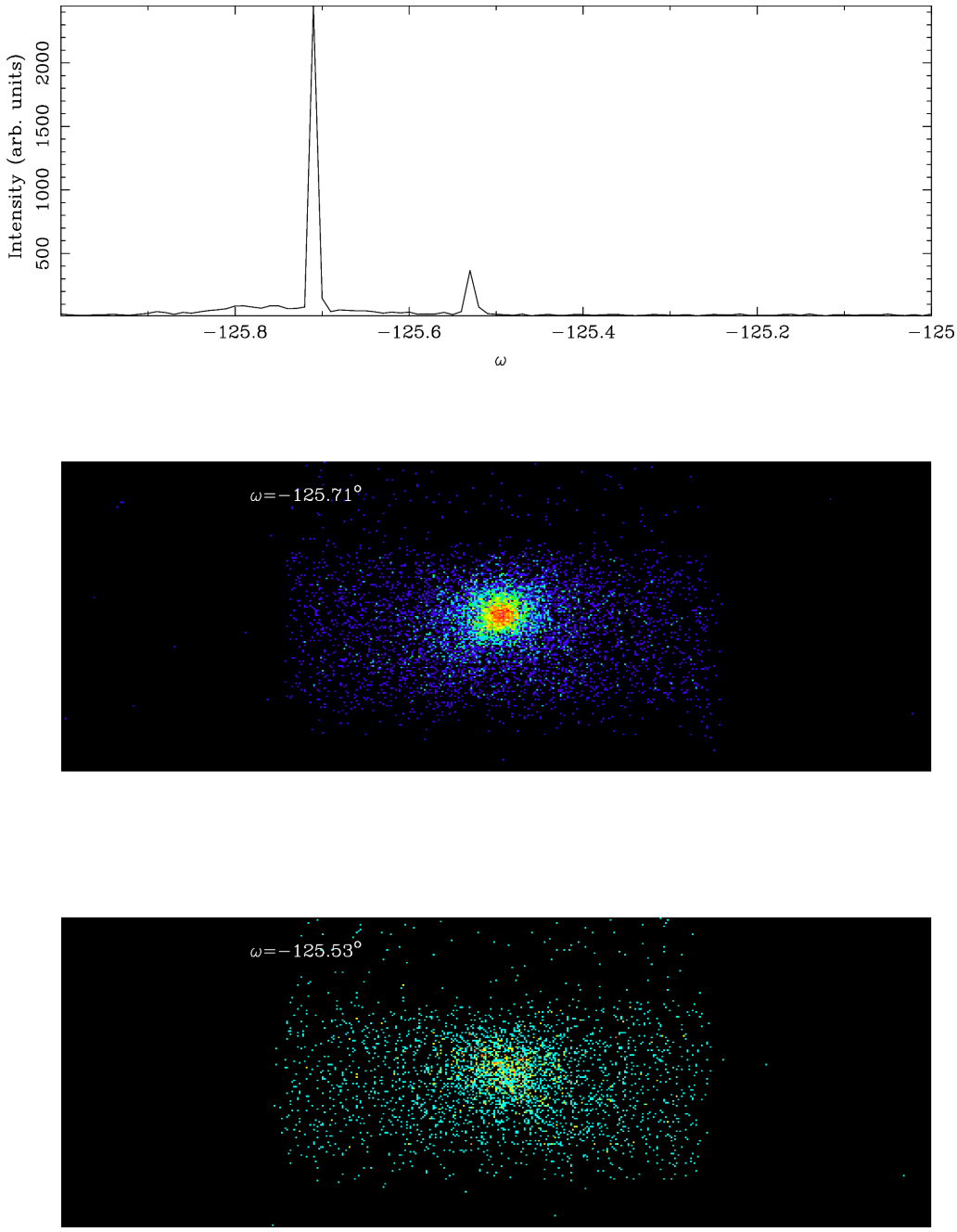

Figure 4.30: A repeat measurement of the (22,3,0) in-plane scan. This time the stationary scan was used and ω was rotated. The area detector images correspond to the peaks in the ω scan.

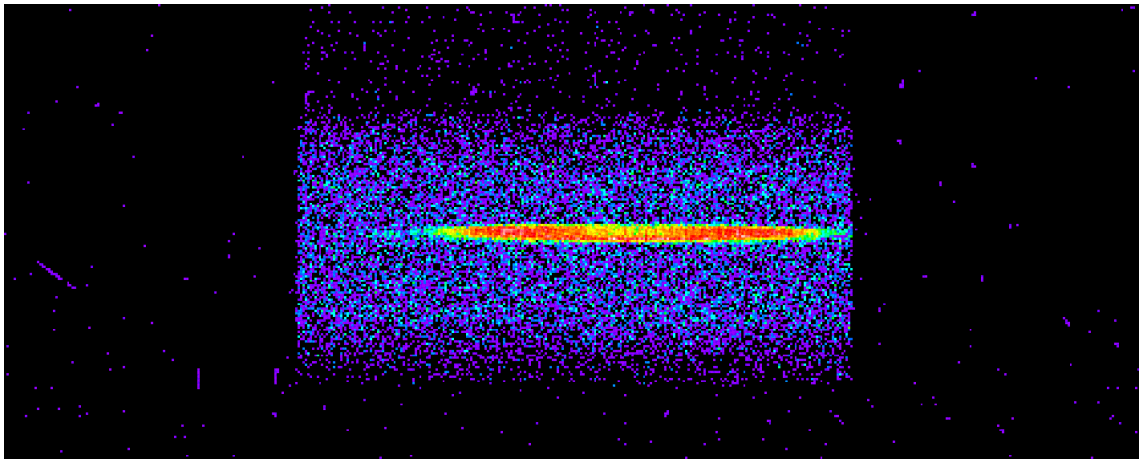

Figure 4.31: Rod measured by the in-plane scan.

4.12 Conclusions

Bicrystal truncation rods have been measured from a Si Σ13 symmetric tilt grain boundary. It is found that the BCTR data yields both information about the rigid body translation between the two crystals and the atomic structure of the grain boundary interface.

The grain boundary structure is found by simulating scattering from various interfaces. The relaxed interfaces were found by minimising the Keating energy. The Keating minimisation does not correctly predict the high and low energy structures obtained by Morris et al., who used the TB and ab-initio approach. However, since both structure (a) and (d) have been observed experimentally, the energetics of the grain boundaries do not provide enough information to correctly predict the interface structure. Morris et al., showed that the energy of structure (a) is approximately 20% less than that of structure (d). The simulated scattering is dependent on the atomic structure of the grain boundary and for this scope of work the more important result of the Keating minimisation is the relaxed atomic positions of the grain boundaries.

The simulated scattering is different for each grain boundary structure. As a result of this we are able to discriminate between potential grain boundaries based on the goodness of fit between the experimental rods and the predicted ones. We have found that the scattering from structure (a) clearly gives the best fit of the data. Our results agree with the interface observed by the high resolution z-contrast image

obtained by Chrisholm et al. [58], and it is the lowest energy structure found by Morris et al. [2]. Therefore BCTR scattering is a viable alternative to the study of interfaces compared to traditional methods. Our technique is non-destructive as the large penetration of X-rays into matter is exploited, the modelled grain boundaries are three-dimensional, and the measured rods are sensitive to the interface structure. This approach to the study of bicrystal grain boundaries therefore overcomes the traditional problems associated with determining the structures.

This approach can be extended to grain boundaries of different materials. For example the grain boundary energies found by Morris et al., for Ge are incredibly similar and as a result of this many of these structures have been observed experimentally [59], making predictions of the grain boundary very difficult. If our approach is used we can model the boundary, simulate scattering and discriminate based on goodness of fit.

Chapter 5

Design and Commissioning of a Holography Endstation at Beamline I06.

5.1 Introduction

Lensless high resolution imaging by X-ray Fourier transform holography (FTH) using soft X-rays was first proposed by McNulty et al., in 1992 [72], with the ultimate aim to obtain 10-20 nm resolution in three dimensions of biological samples. The technique has recently been used to study magnetic multilayers containing cobalt [20, 21], where the resonant magnetic X-ray scattering (RMXS) is a result of the 2*p*-3*d* transition in transition metals. Therefore, tuneable energies provide element specificity and the contrast in magnetic images is provided using X-ray circular dichroism.

Beamline I06 is a soft X-ray nanoscience beamline with circularly polarised X-rays and fulfils the above requirements to study magnetic samples using FTH. This chapter details a series of experiments performed on the branchline of beamline of I06 at the Diamond Light Source. The chapter is divided into two parts. In the first half, the suitability of the branchline is considered along with sample preparation. A holography chamber was built and commissioned. The second half of the chapter presents some preliminary results and some data analysis considerations. The chapter finishes with a new method of creating well defined masks, which could possibly overcome the current resolution limits of this technique.

5.2 Previous Studies: Introducing the Mask-Sample Design

Lensless FTH has been used to image magnetic nanostructures with soft X-rays by using an integrated mask-sample design [20, 21]. The mask-sample is fabricated by the use of a Si_3N_4 membrane on a Si support frame. On one side of the membrane a

thick gold film is grown and on the other side a magnetic multilayer is grown. This gold film needs to be opaque to X-rays at the *L*-edge of transition metals. The mask-sample is illuminated in transmission geometry and a CCD detector positioned down-stream from the sample to record the hologram. A focused ion beam (FIB) is used to cut a circular aperture out of the gold film and down to the Si_3N_4 membrane. This is the object aperture and defines the beam through the sample. The X-rays undergo RMXS and these form the object wave. Next to the object aperture a smaller circular pinhole is drilled all the way through the mask-sample. This smaller pinhole is the reference hole and the X-rays that pass through this are the reference waves. The light scattered from the object and reference interfere upon detection in the far-field to form a hologram (fig. 5.1).

The in-plane reference and object holes conveniently define a lensless Fourier transform geometry. The object image can be easily separated and retrieved by a single Fourier transform of the hologram. This entire process is shown conceptually in fig. 5.2. In fig. 5.2 (a) a simulated mask-sample design is illuminated by a coherent light source and (b) shows the subsequent far-field hologram. The reconstructed image shown in fig. 5.2 (c) is obtained by a single Fourier transform on the hologram. The bright intense area in the centre contains the autocorrelations of the reference and object. The cross-correlations of the object and reference are shown on opposite sides of the central structure. The images only differ by their orientation, otherwise they are identical and contain exactly the same information about the object. Detailed information about the object is extracted at this point.

5.2.1 Limitations of the Mask-Sample Design

The limitations of the mask-sample approach are illustrated by simulated scattering in fig. 5.2. The real space image in fig. 5.2 (c) is formed where the reference convolutes the object. The mask-sample in fig. 5.2 (a) is 2000 x 2000 pixels. The features on the object have a diameter of 13 pixels and the reference hole has a diameter of 13 pixels. The features on the reconstructed image are visible but have a reasonably poor resolution. The resolution of the mask-sample design is limited by the size of the reference hole and is illustrated by further simulations in fig. 5.3. In fig. 5.3 (a) the

reference hole has a diameter of 19 pixels and in 5.3 (b) the reference hole has a diameter of 3 pixels. The features of the object in 5.3 (a) can only be faintly observed, whilst in 5.3 (b) the features are very sharp.

Currently the reference holes produced by the FIB are greater than 60 nm in size. This is for two reasons: firstly, the resolution of the FIB is approximately 50 nm and secondly drift in the FIB. Both these factors make it difficult to make a small, well defined reference hole and ultimately limit the size of the reference hole. The resolution of the reconstructed images can, in theory, be improved by applying phase retrieval algorithms.

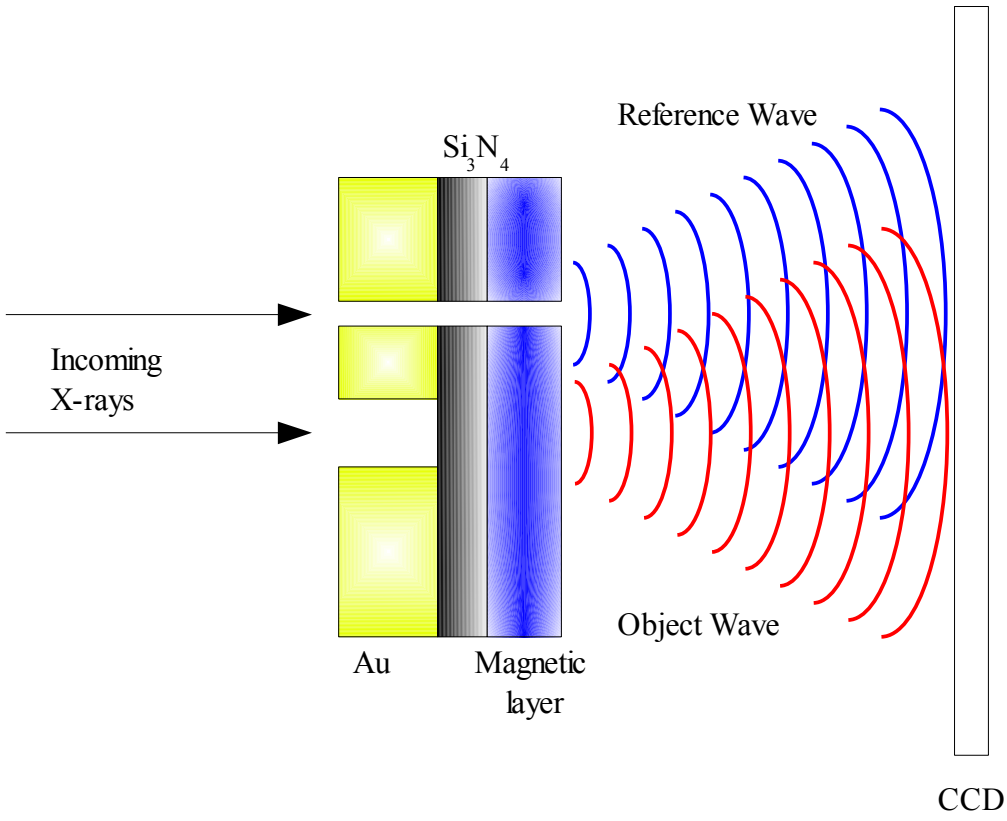

Figure 5.1: Transmission geometry used in lensless FTH. The object and reference waves are defined by the mask and the resultant hologram recorded on the CCD.

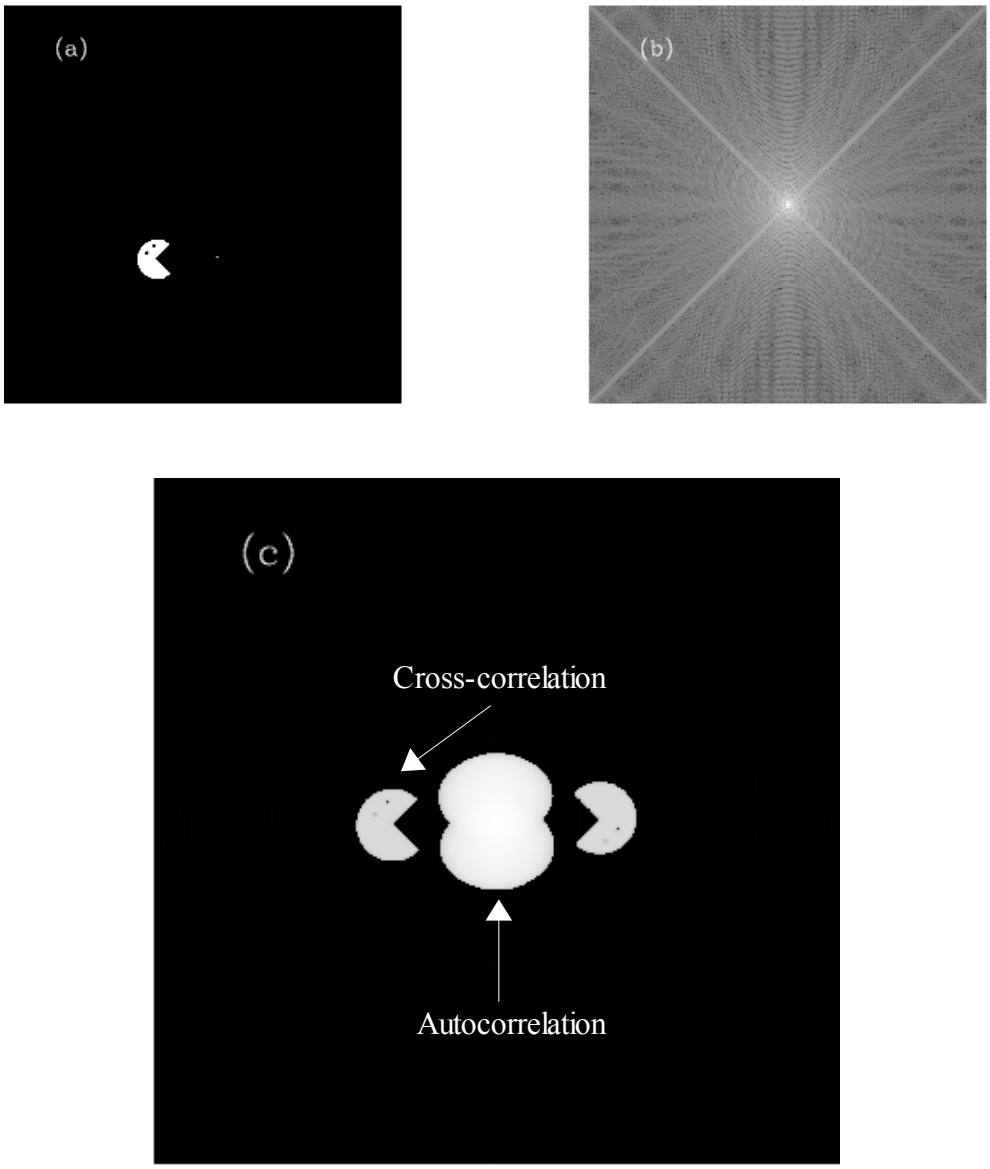

Figure 5.2: The principle of lensless Fourier transform holography demonstrated with a simulated sample and scattering. (a) The object and the reference hole is illuminated with coherent light. (b) The hologram recorded in the far field. (c) The reconstructed image is a Fourier transform of the hologram.

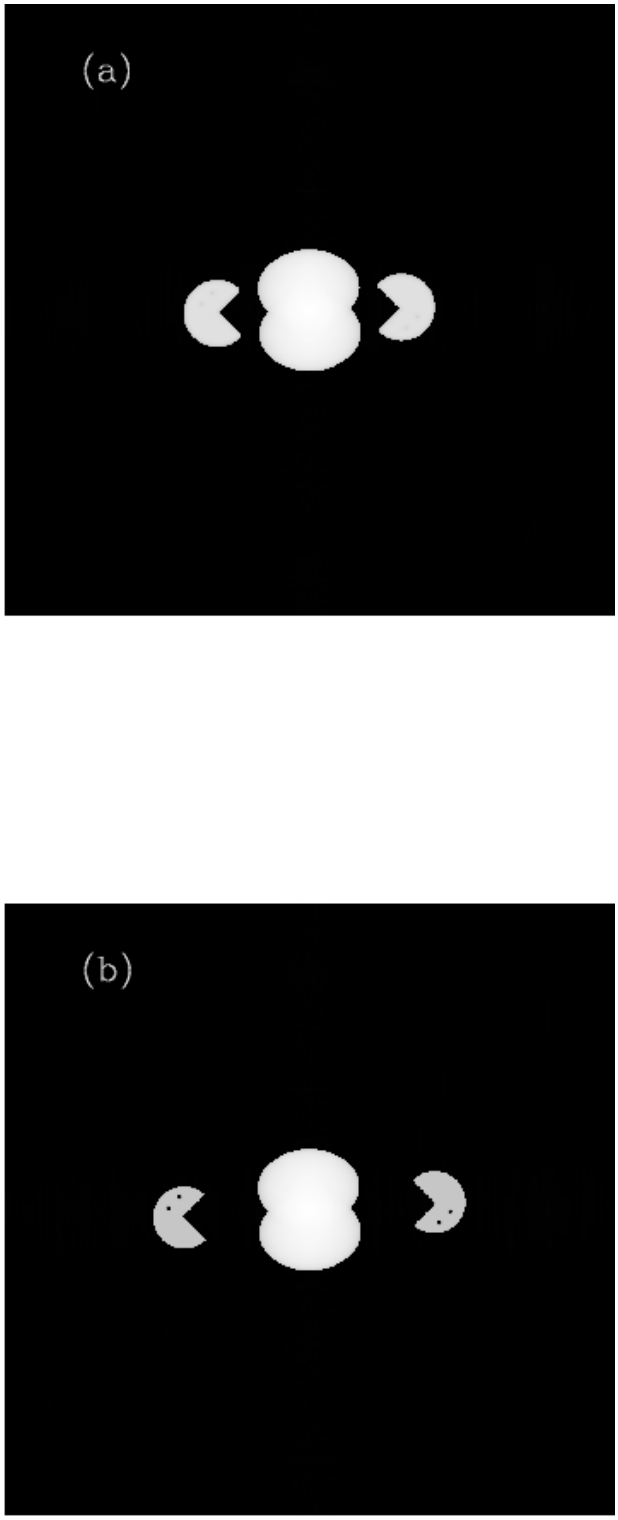

Figure 5.3: Reconstructed images from simulations using various sized reference holes: (a) a reference hole of diameter 19 pixels and (b) a reference hole of 3 pixels.

5.3 Beamline I06

Beamline I06 of the Diamond light source, delivers circularly polarised, soft X-rays to a photoemssion electron microscope and branchline. The design of the beamline is shown in fig. 5.4. The branchline, the parameters of which are displayed in table 5.1, has a beam height of 1415 mm and a user end station can be attached onto it; allowing a wide range of experiments to be performed. The measurements detailed in this chapter were performed on the branchline, using a custom made "holography" chamber (which is discussed in more detail in section 5.7)

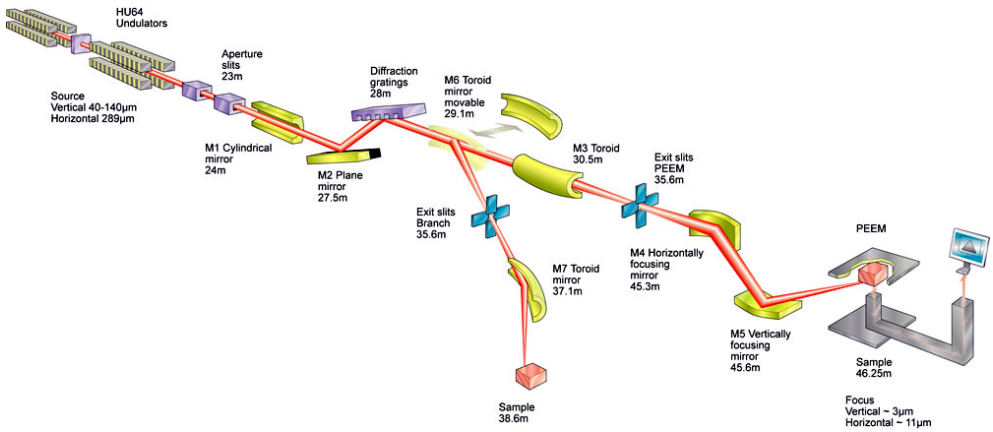

Figure 5.4: The X-ray source of beamline I06. The M6 toroid mirror is moveable and the beam is supplied to the branchline when the mirror is in the path of the beam. After [73].

Spot size (μm)	200 (H) x 20 (V)
Energy range (first circular harmonic)(eV)	106-1300
Resolving power ($\Delta E/E$)	10^{-4} @ 400 eV

Table 5.1: Branchline Parameters.

5.3.1 Transverse Coherence Length of Beamline I06

In order to separate the cross-correlation and autocorrelation terms in equation

2.26 the object and reference holes in the transmission mask need a separation of d, given by the following [74]

$$d > \frac{3}{2} d_o + d_r \quad , (5.1)$$

where d_o is the diameter of the object and d_r is the diameter of the reference. However, in order to preserve the relative phase between the object and reference the following needs to be true

$$\xi > (d + d_o + d_r) \quad , (5.2)$$

where ξ is the transverse coherence length of the X-ray beam. In previous studies d_o [20, 21] is 1-1.5 μm and d_r is approximately 100 nm which gives d as approximately 2.35 μm. The transverse coherence length therefore needs to exceed 3.95 μm.

The transverse coherence properties of the branchline, and hence the ability to perform holography experiments, was investigated by measuring the diffraction pattern from a single pinhole. Fraunhofer diffraction of partially spatially coherent light by slit and circular apertures has been treated in detail [75-85]. To obtain the far-field irradiance distribution we make use of Schell's theorem [86], which states that the irradiance distribution in the Fraunhofer diffraction pattern of a quasi-monochromatic spatially stationary aperture distribution is proportional to the Fourier transform of the product of the aperture autocorrelation function and the normalised aperture mutual intensity function. The diffraction from a circular pinhole in the far-field irradiated with partially coherent light is given by [83-85, 87]:

$$I(\theta) = I_0 \int_0^2 Y(\rho) C(\rho) J_0(ka\theta\rho) \rho \, d\rho \quad , (5.3)$$

where I_0 is the intensity at the centre of the Airy disk, $Y(\rho)$ is the mutual coherence function, $C(\rho)$ is the autocorrelation function of the aperture, J_0 is a Bessel function of order zero, k is the mean wavenumber and a is the radius of the circular pinhole. The

variables θ and ρ, the normalised distance between two points over the aperture, are defined in fig. 5.5. $Y(\rho)$ is a measure of the coherence of the source at the aperture and is given by

$$Y(\rho)=\frac{2J_1(\rho\alpha)}{\rho\alpha} \quad , (5.4)$$

where J_1 is a Bessel function of the first order and α is a measure of the transverse coherence (i.e. the number of correlation intervals contained in the aperture radius and is given in multiples of the aperture radius) and adjusting this varies the coherence at the aperture. A value of α equal to zero corresponds to perfect coherent illumination and when α is infinite incoherent illumination is obtained, all other values correspond to partial coherence. Equation 5.4 is almost identical to the degree of spatial coherence, $|\mu_s|$, defined by equation 2.36. The measure of coherence satisfies the condition $|\mu_s|$ = 0.88, which is the maximum departure from unity for which the source can be considered fully coherent [40, 88]. $C(\rho)$ for a uniformly illuminated circular aperture is given by

$$\begin{aligned} C(\rho)=&[\pi(1-\beta+\beta^2/3)]^{-1}\left[2(1-\beta+\beta^2/3)L-\beta(2-\beta)L\rho^2\right.\\ &\left.-(1-3\beta+5\beta^2/3)\rho\epsilon+\beta(1-\beta/9)\rho^3\epsilon/2-\beta^2\rho^5\epsilon/40\right] \end{aligned} \quad , (5.5)$$

where $L = \cos^{-1}(\rho/2)$, $\epsilon = (1- \rho^2/4)^{1/2}$ and β is the apodization filter parameter. The autocorrelation function for various β is plotted in fig. 5.6 (a) and simulated diffraction from a circular pinhole for various α in fig. 5.6 (b). The simulations are performed by integration of equation 5.3. It is seen from the simulations that as the spatial coherence decreases (i.e. α increases) the central area broadens, the central intensity decreases, the dips between the bright fringes gradually disappear and the simulated diffraction pattern approaches the form of incoherent limit.

The coherence length was determined by comparing experimental diffraction from a circular pinhole with simulated data. Both α and β were varied until there was sufficient agreement with the experimental data.

The diffraction patterns were measured using the transmission geometry

illustrated in fig. 5.7. Circular apertures, with diameters of 10 and 20 μm, were irradiated by a partially coherent, quasi-monochromatic circular source with a mean wavelength of 18.2 Å. The aperture was a distance 1m away from an optical, out of vacuum CCD. The diffraction patterns were recorded by the use of an in vacuum YAG crystal which fluoresced in the presence of X-rays and this fluorescence was recorded. The exposure time of the CCD for the diffraction patterns ranged from 60-180 seconds. The patterns were background subtracted by taking the difference between the CCD images with the beam on and off for the same exposure time. A typical diffraction pattern for a 20 μm aperture is shown in fig. 5.8; it is seen that up to 13 fringes are visible. The intensity distributions are found by taking a radial average of the diffraction patterns.

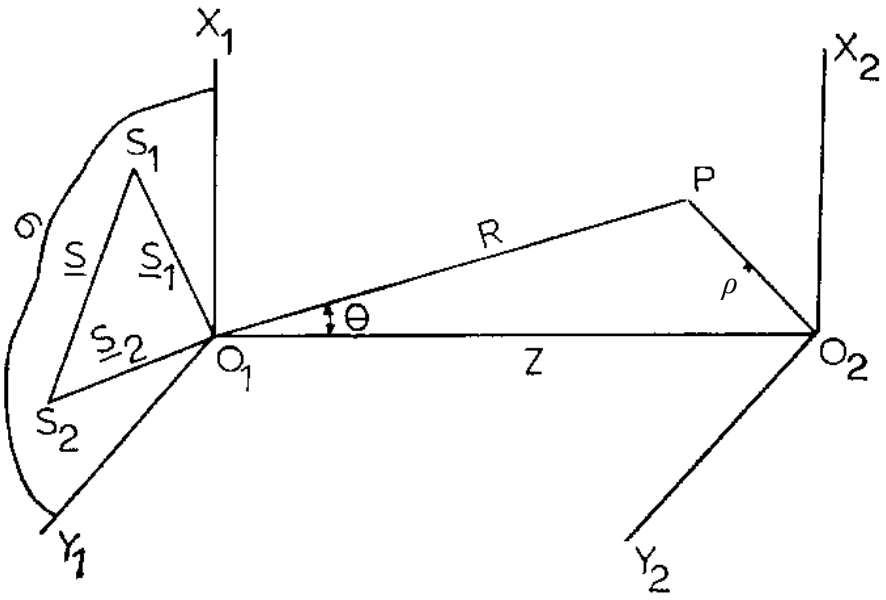

Figure 5.5: The coordinate system of the partially coherent diffraction from a circular aperture. S_1 and S_2 are different points on the aperture. O_1 defines the coordinate system of the aperture and O_2 that of the far-field diffraction pattern. After [84].

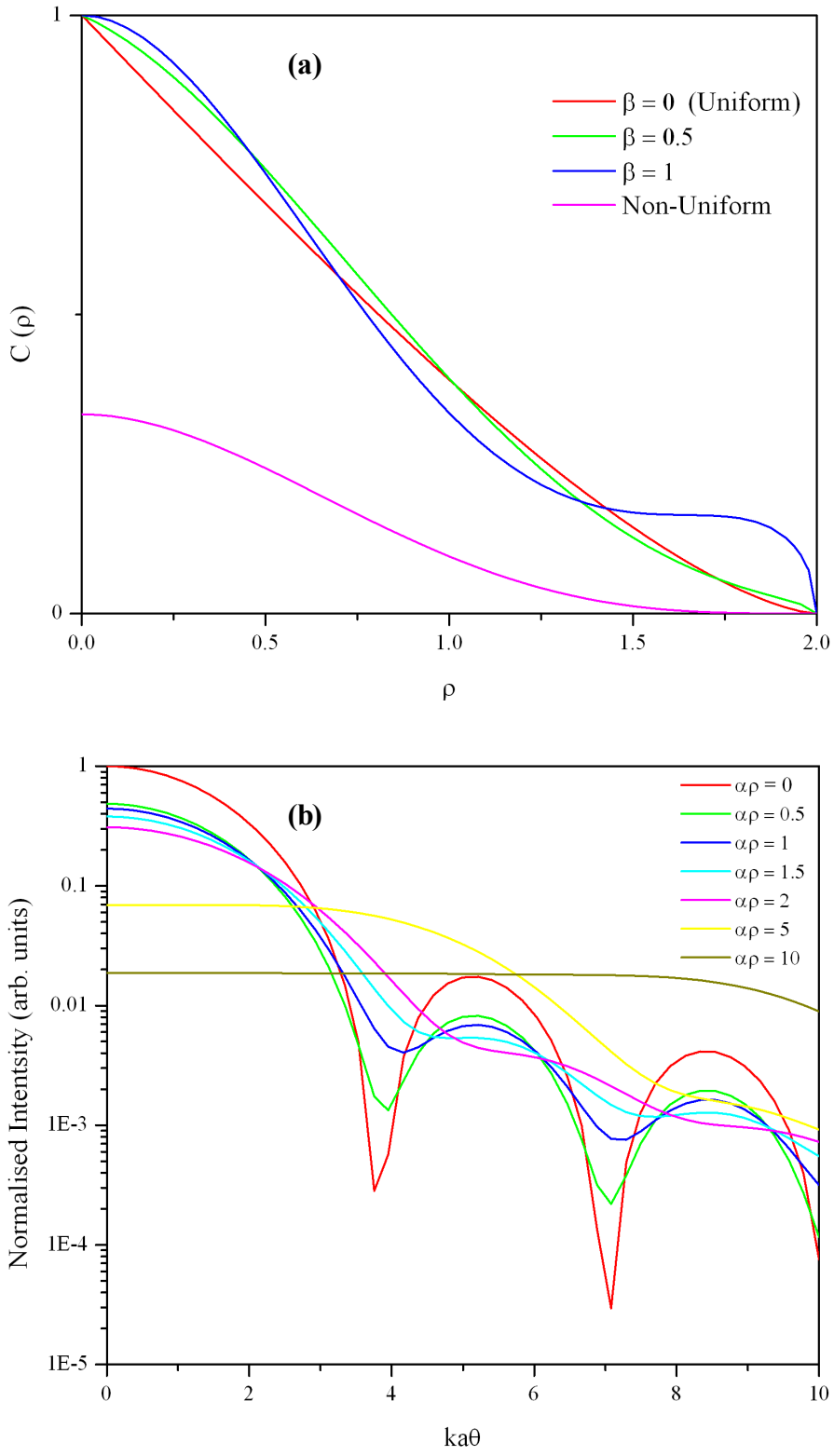

Figure 5.6: (a) The autocorrelation function for various values of β. (b) Simulated diffraction patterns for various $\alpha\rho$.

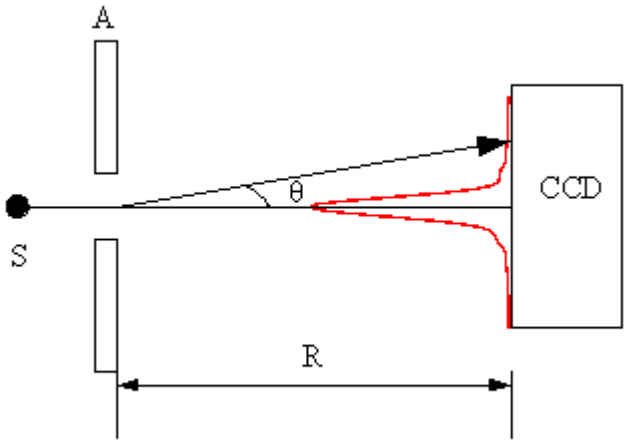

Figure 5.7: Schematic experimental set-up.

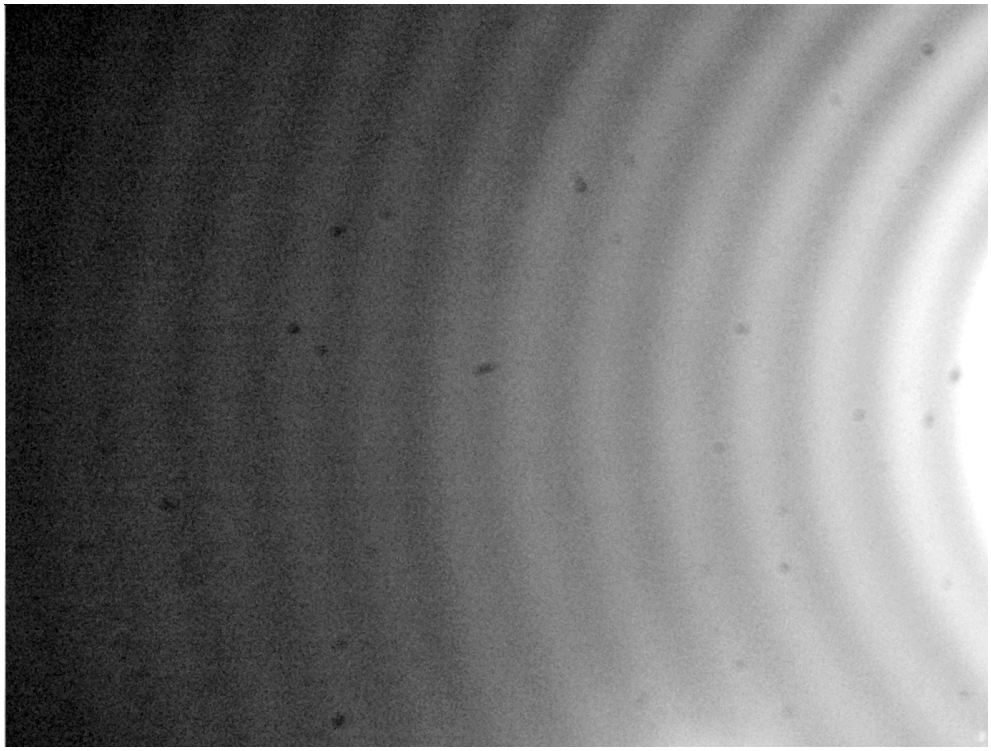

Figure 5.8: Diffraction pattern from a 20 μm circular pinhole displayed on a logarithmic scale.

The coherence length was obtained by finding the best fit between the experimental diffraction patterns and the patterns calculated by equation 5.3. The values of α and β were varied and equation 5.3 was integrated numerically. The best fits

obtained occurred when $\beta = 0$. The value of α obtained was 1.1 for the 10 μm (fig. 5.9) and 2.2 for 20 μm (fig. 5.10) apertures. It is observed that the calculated patterns fit the experimental patterns reasonably well. These values indicate that the coherence length of the beam is approximately 9 μm.

The measured coherence length is greater than the required 3.95 μm. As a result of this it is possible to perform holography experiments on the branchline of I06.

5.4 Sample Considerations

As the branchline of I06 has the potential to perform a holography experiment, thoughts can now turn to the creation of the samples and the integrated mask-sample design. The creation of the mask-sample is taken from [21] but will also be discussed here.

5.4.1 Sample Holder

The Si_3N_4 membranes are very fragile, and any excess pressure on the Si wafer can cause the membrane to break. Therefore, in order to minimize this an “all in one” sample holder was developed. The Si_3N_4 membranes were placed in the recess of the sample holder and then held in place with silver adhesive. A SEM image of this can be seen in fig. 5.11. Although this meant the sample holders were one time use only, it meant there was no tension across the surface of the Si wafer, which is not true when the samples are clamped.

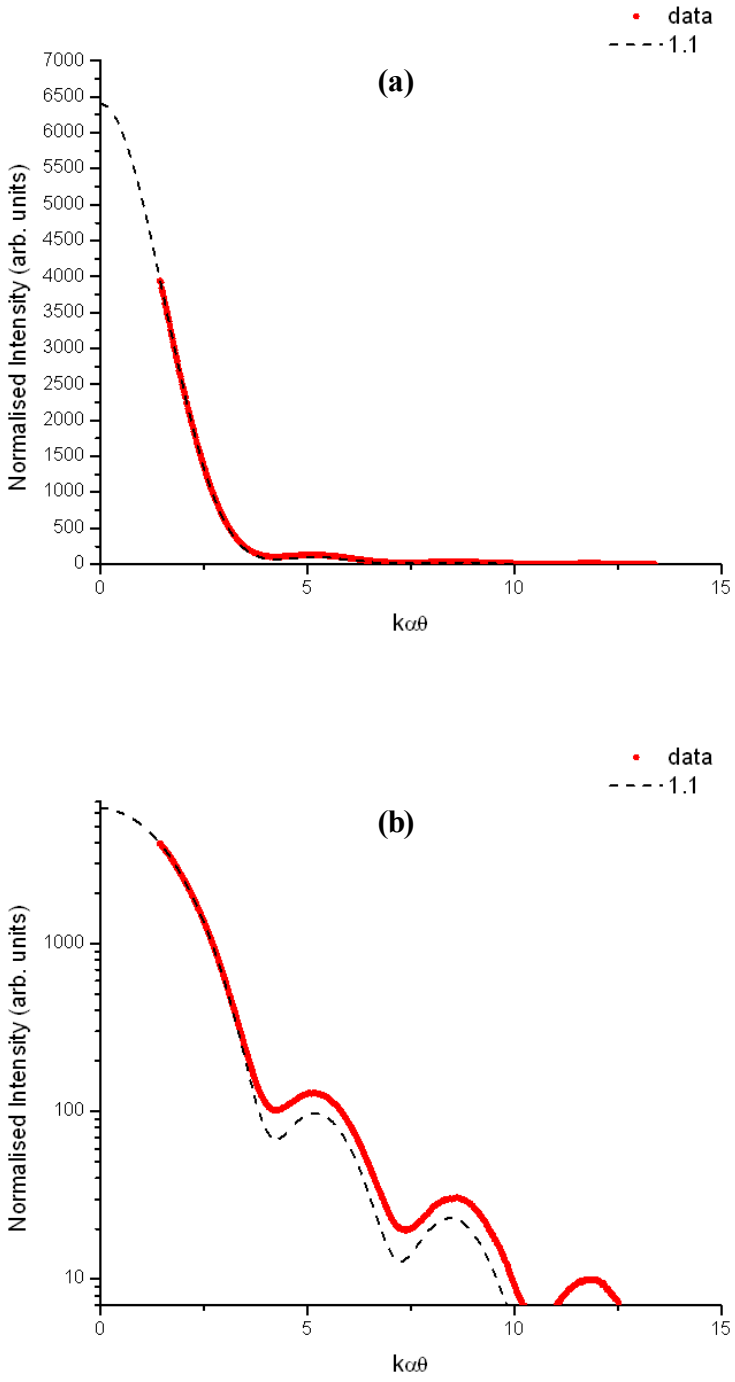

Figure 5.9: Comparison between experimental data and simulation (β = 0, α = 1.1) for the 10 μm circular pinhole. (a) Linear plot. (b) Log plot.

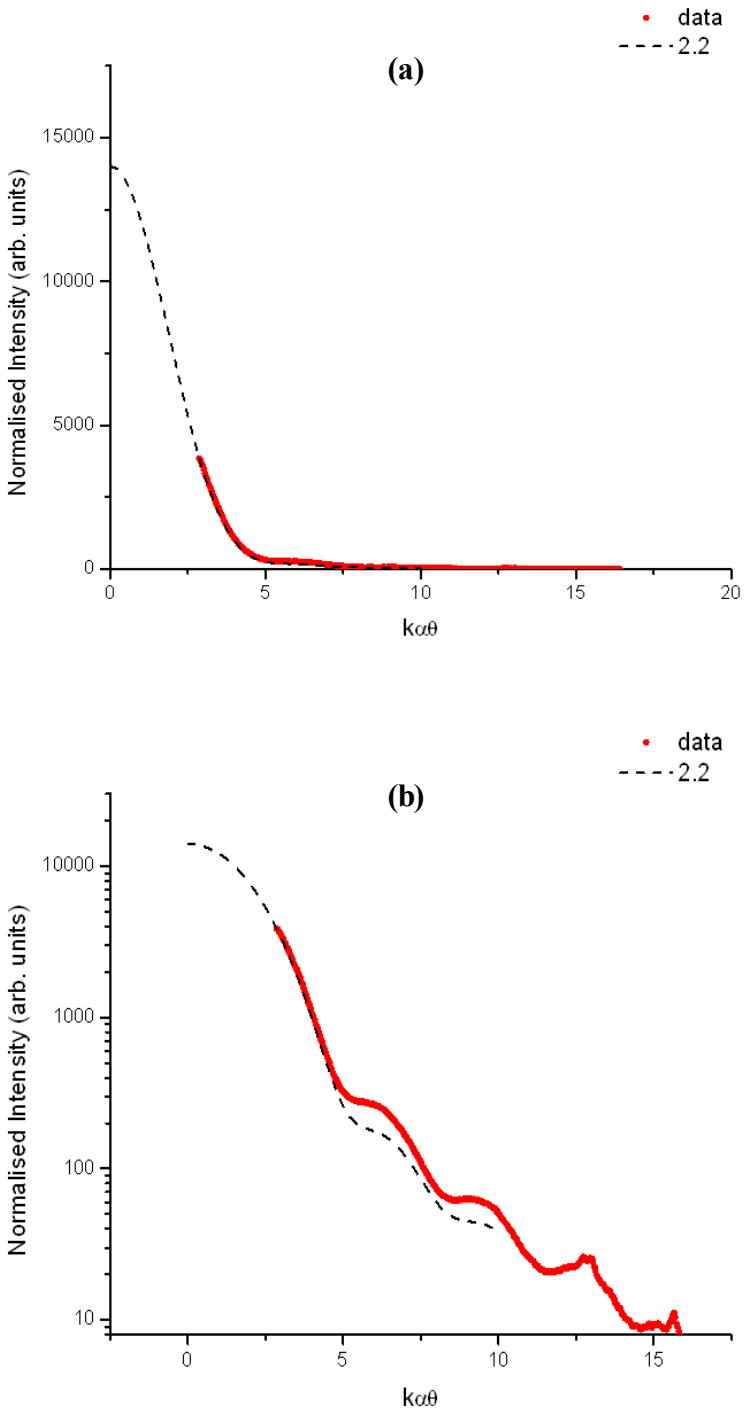

Figure 5.10: Comparison between experimental data and simulation ($\beta = 0$, $\alpha = 2.2$) for the 20 μm circular pinhole. (a) Linear plot. (b) Log plot.

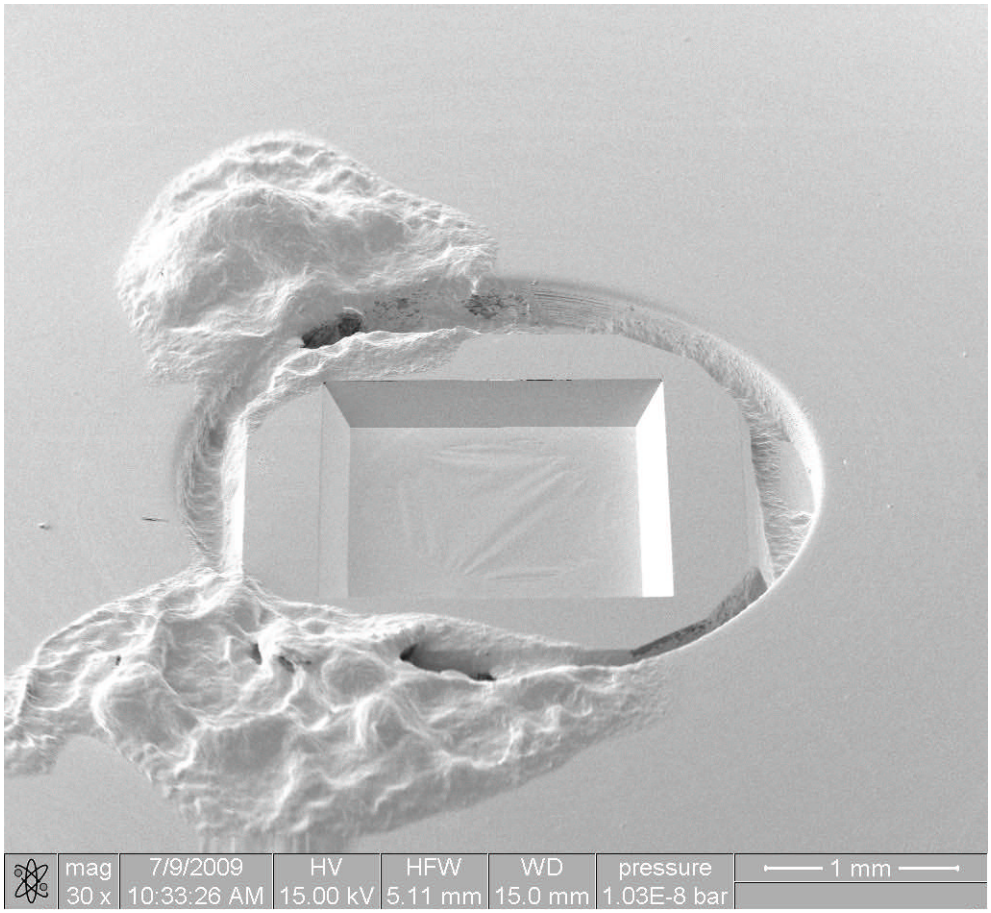

Figure 5.11: SEM image of a Si_3N_4 membrane stuck to the sample holder with silver adhesive. The membrane rests in a recess and then stuck in place.

As the membranes were stuck to the sample holder, it meant that the sample stages in the ultra-high vacuum (UHV) coater, FIB and holography chamber had to be custom made. In the middle of the recess there was a square hole of dimensions 1mm x 1mm. The position of the hole corresponded to the exact dimensions of the Si_3N_4 membrane. The hole had several purposes:

1. It allowed for evaporation of both the Au mask and the magnetic layer. In the UHV coater the top of the membrane was positioned to be directly over the Au evaporator. When the Au evaporation had finished the sample stage could be rotated through 180^o and the magnetic layer deposited on the underside of the membrane. This would save days of time as the UHV chamber wouldn't have to be vented, pumped down and baked every time a magnetic layer was required.

2. When milling the sample holder would be bolted onto the FIB's sample stage. When finished milling, the sample holder could be removed from the sample stage, rotated through 180^{o} degrees and the underside of the membrane seen.
3. Finally, it meant that the sample holder could be used in the holography chamber. The X-rays could pass through both the membrane and the hole, allowing transmission geometry.

5.4.2 Silicon Nitride Membranes

The Si_3N_4 membranes were purchased from Silson Ltd. The membranes are 100 nm thick and have a size of 1 mm x 1 mm. The membranes are supported by a Si wafer that is 200 μm thick.

These membranes are vital to the holography experiment as transmission of X-rays at the Fe L_3 edge is approximately 75% [89]. They also form the basis of the integrated mask-sample design. The Au layer is grown on one side of the membrane and the magnetic layer on the other side. The FIB is then used to create the mask-sample.

5.4.3 Sample Preparation

The fundamental requirement of the mask is that it is opaque to soft X-rays. Gold was chosen as it acts as an excellent attenuator to soft X-rays and it mills far more readily than most materials. A gold mask 1200 nm thick was evaporated onto a Si_3N_4 membrane using an UHV coater. The thickness of the mask was measured by a crystal thickness monitor. The Au was evaporated onto the Si_3N_4 at a pressure of approximately $1x10^{-10}$ mbar. The Au was placed inside a ceramic crucible which was heated by resistive heating by applying a current to a tungsten filament and the temperature set by selecting a particular current value. The deposition rates of the Au evaporator taken over 10 minutes can be seen in table 5.2.

I (A)	Deposition Rate ($Ås^{-1}$)
4.61	0.01
4.78	0.01
5.04	0.03
5.22	0.06
5.39	0.11
5.56	0.20
5.82	0.41
6.00	0.64
6.17	0.90
6.34	1.46

Table 5.2: Deposition rates of Au for various currents.

Once the Au mask was grown, the sample holder was rotated through 180^{o} and the underside of the membrane faced two evaporators containing Fe and Gd. If the Fe and Gd are coevaporated at the right ratio, the resultant film will have random worm domains of approximately 100 nm in size when it is magnetized out of plane. The films should have the following ratio $Gd_{0.17}Fe_{0.83}$ and be 40 nm thick [90-92]. The films were then capped by a 10 nm thick layer of Ag to prevent oxidation.

5.4.4 The Focussed Ion Beam Microscope

The University of Leicester has the commercially available Quanta 3D dual beam system from FEI. Dual beam systems have both a scanning electron microscope (SEM) and FIB (fig. 5.12). The ion-source used is a liquid metal ion source, which provides the brightest and most focussed beam of all commercially available ion sources [93]. Ga ions are extracted from the reservoir by field emission and the typical emission current is approximately 2 μA. The ions are then accelerated to 30 kV and focussed on the sample. The beam current and diameter is controlled by a series of beam defining apertures.

The size and shape of the beam intensity on the sample determines the basic resolution and milling precision. Generally the smaller the beam diameter, the better the

resolution and milling precision. The ultimate resolution is limited by the sputtering and therefore ultimately is signal dependent. Secondary electrons are generated by interaction of the ion beam with the sample surface and this can obtain high resolution images. The sputtering action (fig. 5.13) of Ga ions enables precise machining of samples.

The sample stage has a eucentric point. This is the region where the electron and ion beams cross. At this point the electron beam field of view is the same area being milled by the ion beam. This allows for non-destructive imaging using the SEM and milling using the FIB.

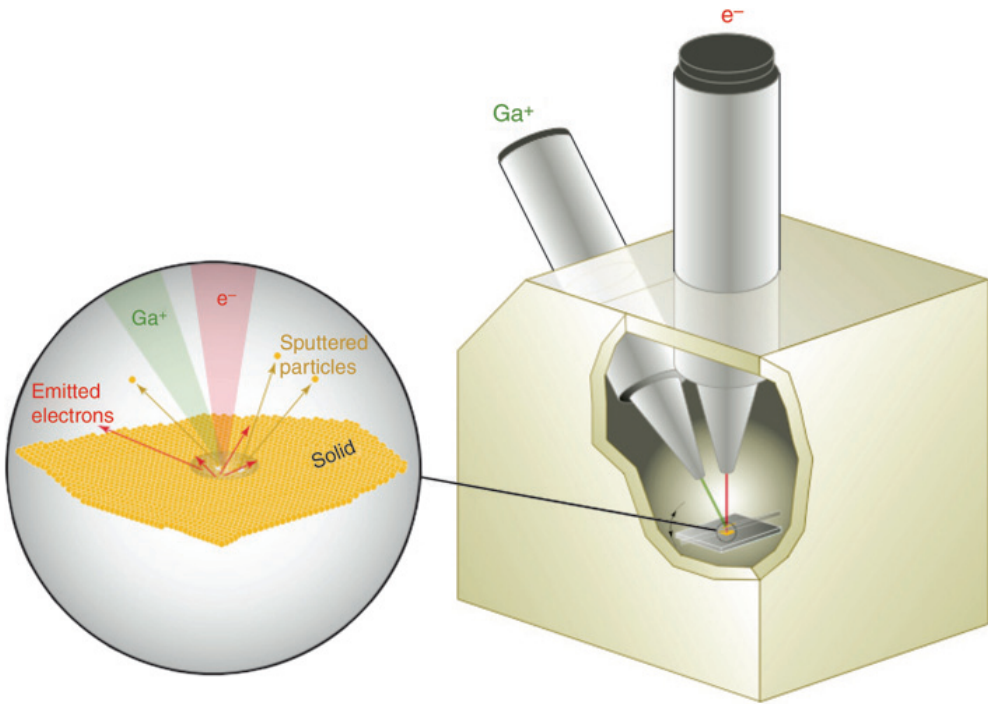

Figure 5.12: Schematic of a dual-beam FIB-SEM instrument. The expanded view shows the interaction of the ions and electrons with the surface. After [93].

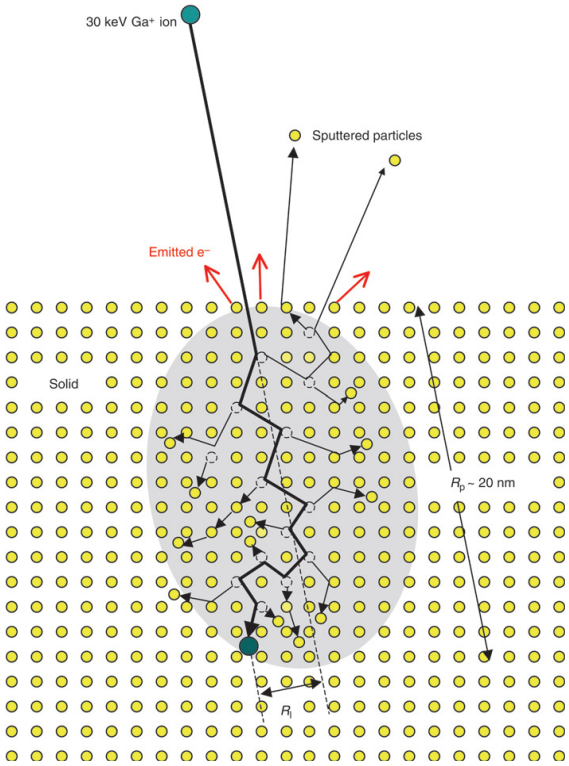

Figure 5.13: Schematic illustration of a collision cascade generated by a 30 keV Ga ion incident on a crystal lattice, showing the damage created in the collision cascade volume, and the projected range R_p and lateral range R_l of the implanted ion. When the ion beam impinges on the surface it loses kinetic energy as a result of interactions with the surface atoms. Ion kinetic energy and momentum are transferred to the solid through both inelastic and elastic interactions. In inelastic interactions, ion energy is lost to the electrons in the sample and results in ionization and the emission of electrons and electromagnetic radiation from the sample. In elastic interactions ion energy is transferred as translational energy to screened target atoms and can result in damage (displacement of sample atoms from their initial sites) and sputtering from the sample surface. After [93].

The sputtering described earlier can be utilised to create specific patterns by creating a path that describes the pattern. The path is described by a 4096 x 4096 matrix. The parameters for each x and y along the path includes the amount of time the beam spends on each pixel (dwell time) and the overlap between adjacent pixels. These parameters create a path which is repeatedly milled for the duration of the milling time.

The milling time is calculated by the FIB software based on the material to be milled, the milling depth and path size. The path is generated by using the FIB software by drawing simple geometric shapes.

The beam diameter varies with beam current. At 30 kV the smallest beam currents are 1 and 10 pA at which point the beam diameter is approximately 10 nm. The milling is faster for increased beam currents but this also increases the destructiveness of the beam, making it difficult to create well defined reference and object holes. The quality of the beam focus and astigmatism also has significant effect, as a well focussed, circular beam mills more precisely than an unfocussed beam.

5.4.5 Object holes

The object hole determines the field of view in holography and it is created by removing the Au mask from the Si_3N_4 membrane and leaving the magnetic layer intact.

The established method to do this is to use the Si_3N_4 membrane as contrast as it appears much darker than the Au and mills away approximately 10 times slower than the Au [21]. This allows for selective milling of the Au.

To preserve the relative phase, the object was never larger than 2 μm. The objects were milled with a beam current of 10 pA. The majority of the Au was removed within 200-300 seconds. However, a major experimental concern is the presence of stubborn grains which were almost endemic in places. This is attributable to the thickness of the Au. The Au masks were designed to be thick to prevent any transmission through them at the Fe L_3 edge and our masks are typically 200-500 nm thicker than previously used [20, 21]. As of yet the only way to remove the stubborn grains is to mill smaller 100 to 400 nm circles over the grains until they eventually disappear (fig. 5.14). The beam current was set to 1 pA during this procedure to reduce the beam damage. This method is used because it prevents any excess milling of the nitride membrane which could damage the magnetic layer below it.

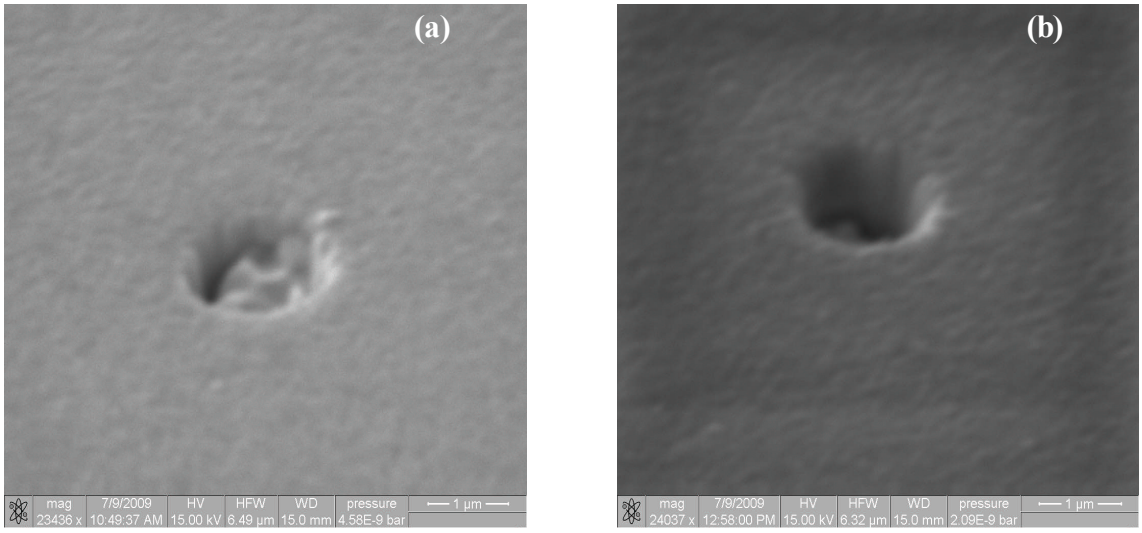

Figure 5.14: (a) Stubborn grains present in the object hole after 200 seconds of milling. (b) Removal of stubborn grains by continuously milling small circles.

5.4.6 Reference Holes

The reference holes have to be clearly defined as they limit the resolution of lensless FTH. The reference hole ensures that the phase is encoded in the hologram and an image is formed where the reference convolutes the object in real space. Therefore small, clearly defined reference holes are desirable. The reference needs to go all the way through the mask and sample.

In order to meet the above requirements the beam needs to be superbly focused. This is obtained in the following steps

1. Set the filter mode from “live” to “average”. This averages the image over several images.
2. Set the beam current to 1 or 10 pA.
3. Get a good contrast/brightness ratio.
4. Zoom in on the sample surface as far as the FIB can (this is approximately x1.5 million magnification).
5. The ion beam will automatically mill material away.
6. Zoom out slightly and focus on the milled region remembering to correct any astigmatism of the beam.

7. Repeat this process until desired focus is obtained.

Step 6 is particularly important as the reference holes will only be circular if they are free from stigmatic aberrations; the circles give a measure of the astigmatism of the beam. When astigmatism is present the circle becomes elliptic, and the eccentricity depends on the level of astigmatism.

The reference holes are created in single steps. It is difficult to tell if all material has been removed and the only definitive way to determine this is to look at the underside of the sample. However, it can be very difficult to locate the reference hole in this manner, especially if the holes were below the resolution limit of the FIB and if the capping layer is very smooth. This was the case with our samples and the reference holes simply could not be located/observed. The only current method for ensuring the reference has gone all the way through the sample is just to continue to raster the beam over it. Drift poses two significant problems, the first is that it may enlarge the reference and finally, and more problematically, it may just cause the sputtered Au to be moved from one region to another. The drift was quite significant; in some cases the sample would move tens of nm in the space of a few minutes. This meant that the milling of the reference holes were limited to small milling times (<60 seconds). When drift was present a higher beam current was used to ensure faster milling.

5.5 Holography Chamber.

As the branchline of I06 has sufficient coherence for lensless FTH, a diffraction chamber was designed to carry out such an experiment. The final design comprised of two 6-inch six way crosses (figs. 5.15 and 5.16 (a)). The first cross was bolted onto the branchline and connected to the second cross. Two linear drives were connected onto the first cross on opposite flanges. Each linear drive had a two axis *x*-*y* manipulator, along with micrometers so the positions could be recorded. The pinholes were attached to one linear drive. The following circular pinhole diameters were available; 50, 20 and 10 μm. Each pinhole was separated from the next by 4 mm in *x*. The samples were attached to a custom built “dog-leg” that was attached to the other linear drive. This ensured that when both the pinholes and sample were fully wound in, the sample rested 6.7 mm behind the pinhole in the centre of the cross (fig. 5.16 (b)). At this distance from

the sample the pinhole does not add to the coherence of the beam; instead it is used to reduce the intensity of the beam illuminating the sample.

On the second cross, another linear drive, with only vertical movement, was attached. A photodiode was attached on this linear drive. The photodiode was used for absolute intensity measurements. When the full beam was incident on the photodiode, a current of a few mA is generated. When only part of the beam is on the diode this current can be a few pA. In order to measure this smaller signal a current amplifier was used and the gain typically $1x10^{9}$ or $1x10^{10}$. A beamstop was attached to the bottom of the photodiode, however, it was not used for the duration of the experiment. Behind the photodiode was a YAG crystal that converted the soft X-rays into visible light. An external, out of vacuum CCD was mounted onto the work station and recorded the visible light. The CCD was 12 bit, had 1376 x 1040 pixels and the pixel size was 15.9 μm.

The beam at the branchline was 1415 mm off the ground. An aluminium plate was made that would bolt onto the existing workstation. This plate formed the base of the chamber. The chamber was supported on the plate by the manufacture of four aluminium supports comprised of two bases and two tops. The bases went under the flanges connecting the first cross to the branchline and under the flange connected to the fluorescent screen. Half the flange would rest in the base. Once the bases were in place the tops were bolted on, securing the chamber.

The branchline was under vacuum and the chamber had to be small enough so that it could achieve high vacuum just by being pumped down by the existing pumps. The pressure inside the chamber was approximately $1x10^{-6}$ mbar after 10 minutes of being pumped down. The chamber also allowed for quick changing of samples. The beam was prevented from reaching the chamber by closing the beam shutter. The ion pump was closed and the branchline valved off. The linear drive holding the sample, would be removed from the chamber. The sample would be replaced, and the linear drive reattached. The valve was reopened, pumping the chamber down. Once at sufficiently low pressure the ion pump would be turned on and the shutter reopened. The process of valving off the branchline to having beam again, after practice, took only 10 minutes.

Each six-way cross had a viewpoint on it. This allowed one to observe the

pinholes, samples and diode being wound in and out. During the experiment the viewpoints were covered in foil, the lights turned off and the chamber covered with opaque sheets. This effectively reduced ambient light levels to zero.

5.5.1 Alignment Process

The beam passed through the centre of the chamber. Pinhole and sample alignment were obtained by scanning both through the beam and measuring the current of the photodiode. Once the pinholes were aligned, the photodiode was wound out of the beam and the visible light recorded by the CCD. The sample was found by setting the beam energy to 1000 eV which greatly increased the transmission through the mask-sample; this transmission was recorded by the CCD. The corners of the Si_3N_4 membrane were located by moving the sample through the beam and their coordinates recorded (fig. 5.17). The sample was then centred on these coordinates and the photodiode was wound in. The sample was moved in very small steps until a maximum signal was recorded on the photodiode, this increase in signal was attributed to an increase in transmission where the object was.

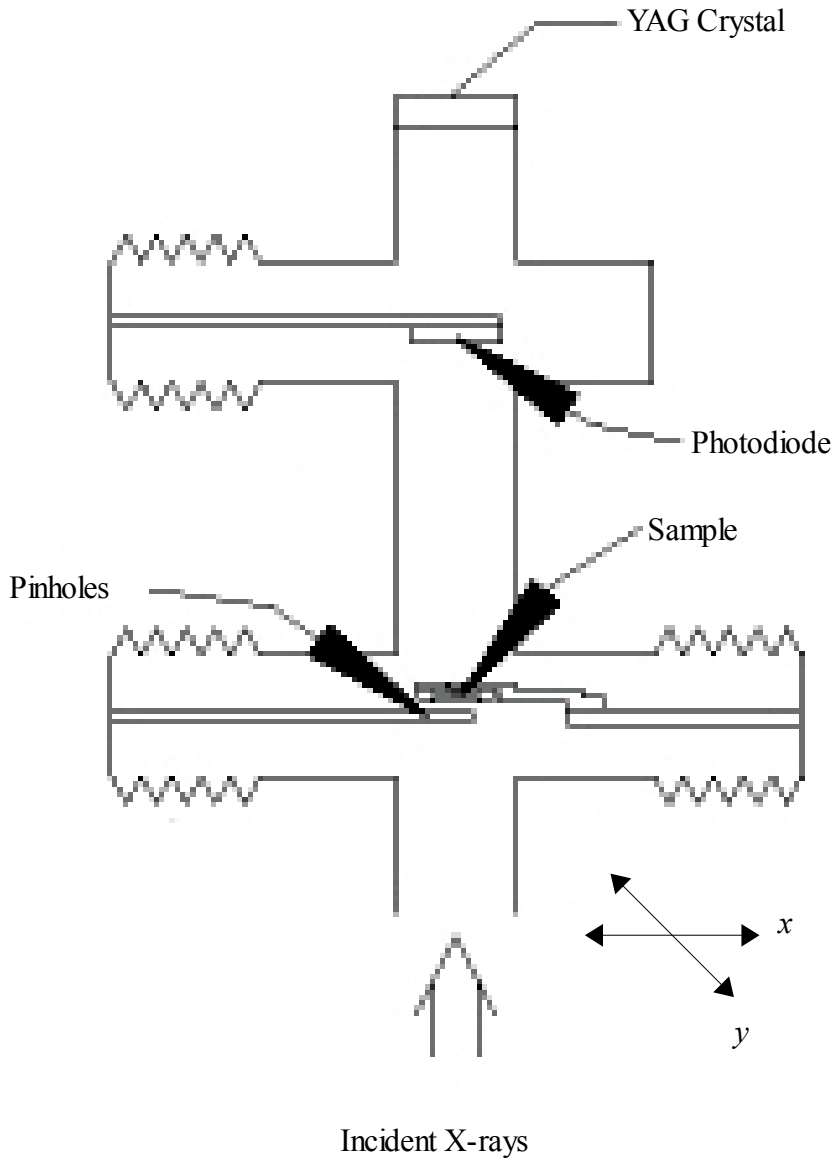

Figure 5.15: Schematic layout of the holography chamber. The *z*-direction goes straight through the chamber. The X-rays would pass through the pinhole and sample and detected by the diode.

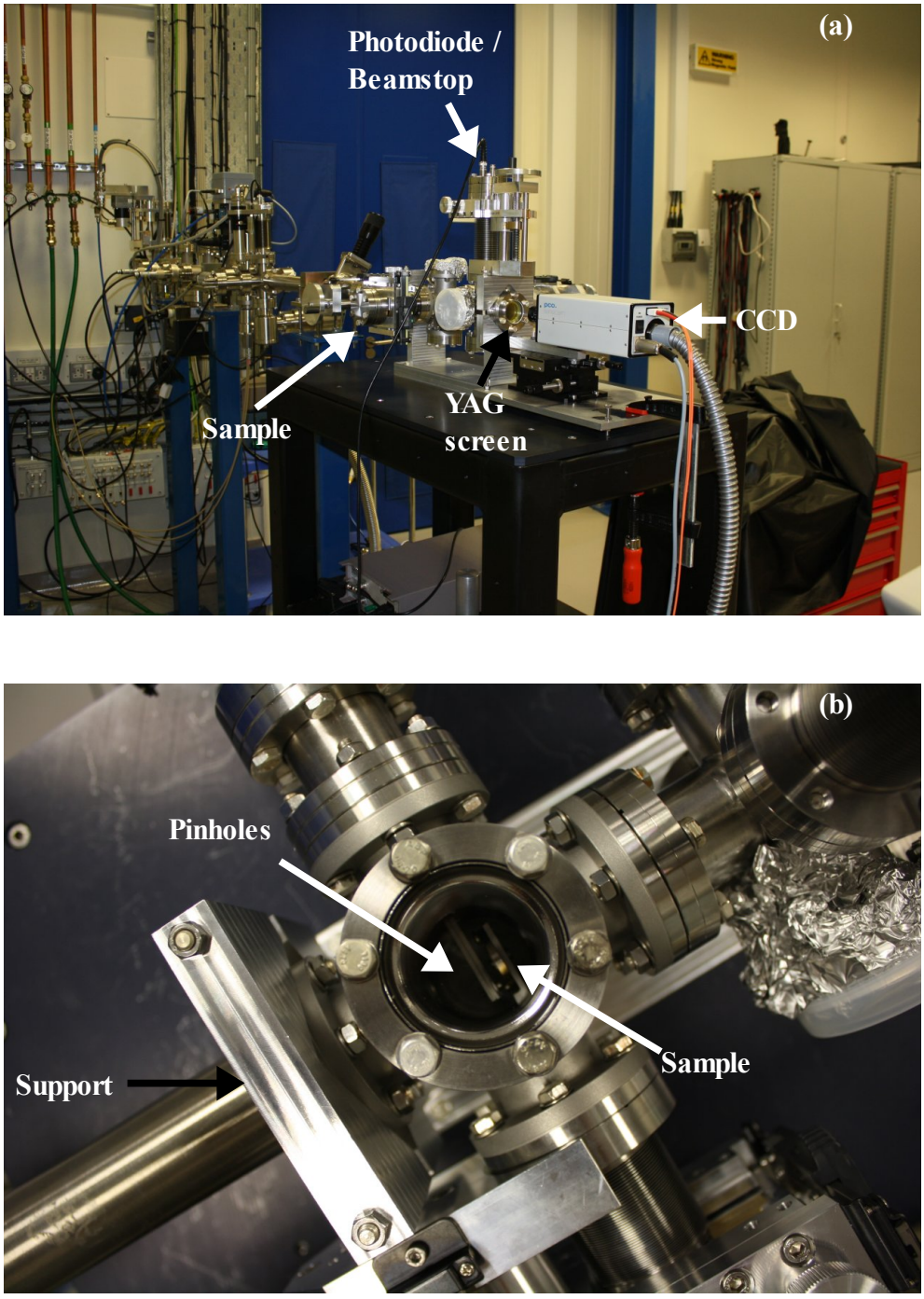

Figure 5.16: (a) Photograph illustrating the holography chamber. (b) Viewpoint of first six-way cross showing the sample resting behind the pinholes.

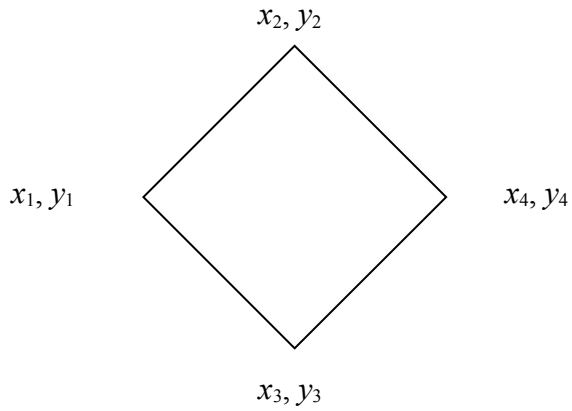

Figure 5.17: Si_3N_4 membrane as seen by the CCD at 1000 eV. The coordinates of the corners were recorded. This gave a clear boundary in which the sample was present.

5.5.2 Sampling Considerations

This section covers the resolution and the field of view (FOV) of the holographic reconstruction both of which are dependent on several key parameters of the chamber; such as the sample-detector distance and the size and number of pixels in the CCD [94-97].

5.5.2.1 Resolution

The maximum diffraction angle, θ (fig. 5.18), that can be recorded by a detector is given by

$$\sin\frac{\theta}{2}\approx\frac{\theta}{2}=\frac{\lambda}{2d} \quad , (5.6)$$

which leads to

$$\theta=\frac{\lambda}{d} \quad , (5.7)$$

where d is the resolution. Considering the distance, z, from the sample to the detector we get

$$\tan\frac{\theta}{2}\approx\frac{\theta}{2}=\frac{x}{2z} \quad , (5.8)$$

giving

$$\theta=\frac{x}{z} \quad , (5.9)$$

where x is half the detector length. Combining equations (5.7) and (5.8) the following is obtained

$$d=\frac{\lambda z}{x}=\frac{\lambda z}{N\Delta x} \quad , (5.10)$$

where N is the number of pixels in the CCD and Δx is the pixel width. In our setup λ = 1.8 nm, z = 180 mm, N = 1376 in the horizontal direction 1040 in the vertical, and Δx = 15.9 μm. This gives a maximum observable resolution of 14.8 nm in the horizontal and 19.5 nm in the vertical.

5.5.2.2 Oversampling Ratio

In order to use phase retrieval algorithms successfully we first need to consider oversampling. Sampling the diffraction pattern more finely than the Nyquist frequency (the inverse of the size of the diffracting object) corresponds to surrounding the sample with a no density region [97]. Provided the no density region is bigger than that of the sample, sufficient information is recorded so that the phase can be retrieved from the oversampled diffraction pattern [94]. In order to determine the oversampling it is useful to introduce the concept of an oversampling ratio [95] which is given by

$$\sigma = \frac{total\ number\ of\ pixels}{unknown\ valued\ pixel\ number} \quad . (5.11)$$

This ratio has to exceed 2 in 1D in order to successfully retrieve the phase [95, 96]. The oversampling ratio in 1D is given by [96]

$$\sigma_{1D} = \frac{dN}{2a} \quad , (5.12)$$

where a is the size of the object. Experimentally the size of a was 1 to 1.5 μm. Taking the largest value of a the oversampling ratio in 1D was found to be 6.79. The ratio for 2D is just the product of the oversampling in the vertical and horizontal which gives us a 2D oversampling ratio of 46.12. This ratio is more than sufficient for us to use phase retrieval algorithms.

5.5.2.3 Field of View

The field of view is calculated from [97]

$$FOV = \frac{\lambda z}{\Delta x} \quad . (5.13)$$

Using the parameters mentioned earlier, the field of view is 20.4 μm. The object size must be no larger than FOV / σ_{1D}. This condition is met provided the object does not exceed 3 μm [97].

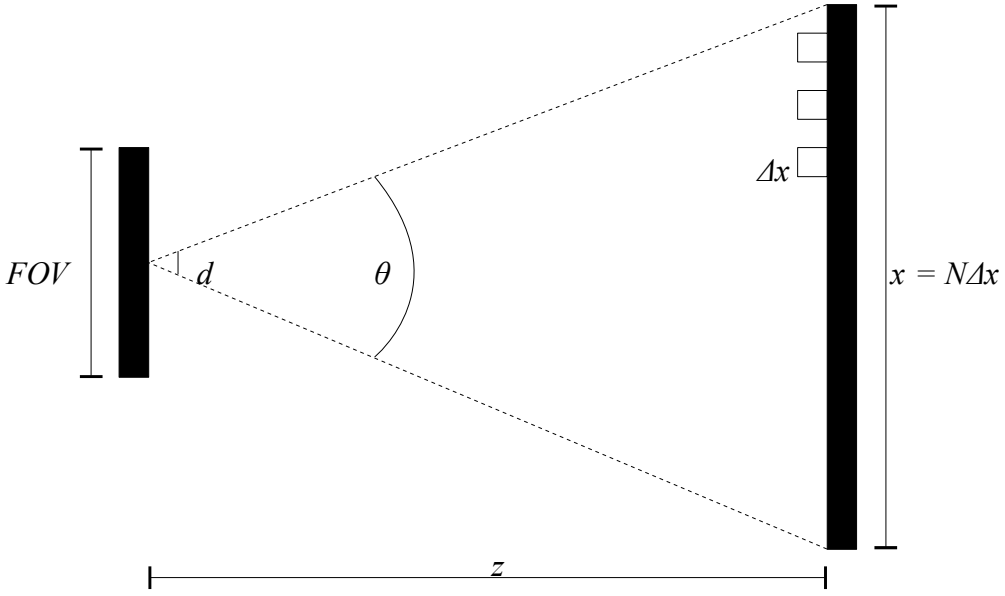

Figure 5.18: Diffraction geometry. A sample of size, *a*, has *d* resolvable elements and is located a distance *z* away from a detector. The detector is of width *x* and contains *N* pixels of size *Δx*. After [97].

5.6 Fourier Transform Holography

Eight nanostructured masks were created using the FIB. Each mask had a different sample. However, only one mask-sample was successful (illustrated in fig. 5.19) and this was used to commission the experiment. The high failure rate can be attributed to the thickness of the gold. Although the mask is opaque to X-rays it becomes incredibly difficult to mill through gold this thick. It was exceptionally difficult to remove all the stubborn grains and to create well defined reference holes. Drift of the samples in the microscope meant that we were unable to mill through all the layers; in the majority of cases the gold was simply moved from one region to another when milling.

The Au mask was 1.2 μm thick and the transmission of X-rays through the Au mask was $9x10^{-10}$ of the incident 707 eV (1.75 nm) photons. The reference holes are approximately 100 nm in diameter and the object has a diameter of 1.2 μm.

The holograms were recorded for the following exposure times: 1, 10, 100, 1000 and 3600 seconds. The high exposure times were used as an attempt to measure the

weak signal lost due to the noise level of the CCD. The hour exposure time was the largest permitted by the CCD software. The light transmitted through the Au mask was also a source of noise.

The hologram from the gold mask with the $Gd_{0.17}Fe_{0.83}$ layer can be seen in fig. 5.20 (a). The pixels at the centre of the diffraction pattern have the highest intensities and have saturated the CCD. These pixels correspond to the Airy disk from the object. The interference fringes across the hologram are periodic and have a spacing of 1.03 μm^{-1}.The speckles have a mean size of 5.07 μm^{-1}**.**

The reconstructed images are obtained by performing a simple two-dimensional Fourier transform on the recorded holograms. The reconstructed image is shown in fig. 5.20 (b). The reconstruction shows several things: (i) the autocorrelation of the object with itself, (ii) the cross-correlation of the reference and object waves, these form the reconstructed image and (iii) noise in the form of concentric rings around the autocorrelation. The cross-correlations are identical to one another, the only difference is that they have been rotated through 180^o. The features in the object are structural rather than magnetic because there was no difference between the left and right circularly polarized light and the features we observe in the object appeared for beam energies off resonance (the energy range was 400-3600 eV). The reconstructions also show that X-rays could only pass through one reference holes. The features in the reconstruction are residual islands of Au which are a direct result of the non uniformity in the milling process.

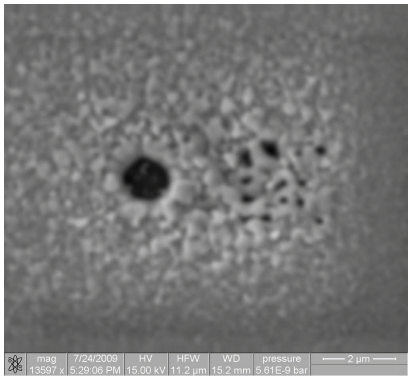

Figure 5.19: A FIB image of the object with an uniformly redundant array of reference holes. The X-ray beam could only pass through one of the references.

The features in the reconstructed images were compared with SEM images of the mask to see if they were real or not and to determine the resolution of the reconstructions. The comparisons may be seen in fig. 5.21. There is an excellent agreement between the two images and all features observable in the reconstruction are real. Secondly, the reconstruction has a higher resolution than the SEM. The smallest features in the SEM image are approximately 60 nm in size and appear blurry, whilst these features appear sharp in the image reconstruction. Therefore the resolution obtained with our experimental set up is less than 60 nm.

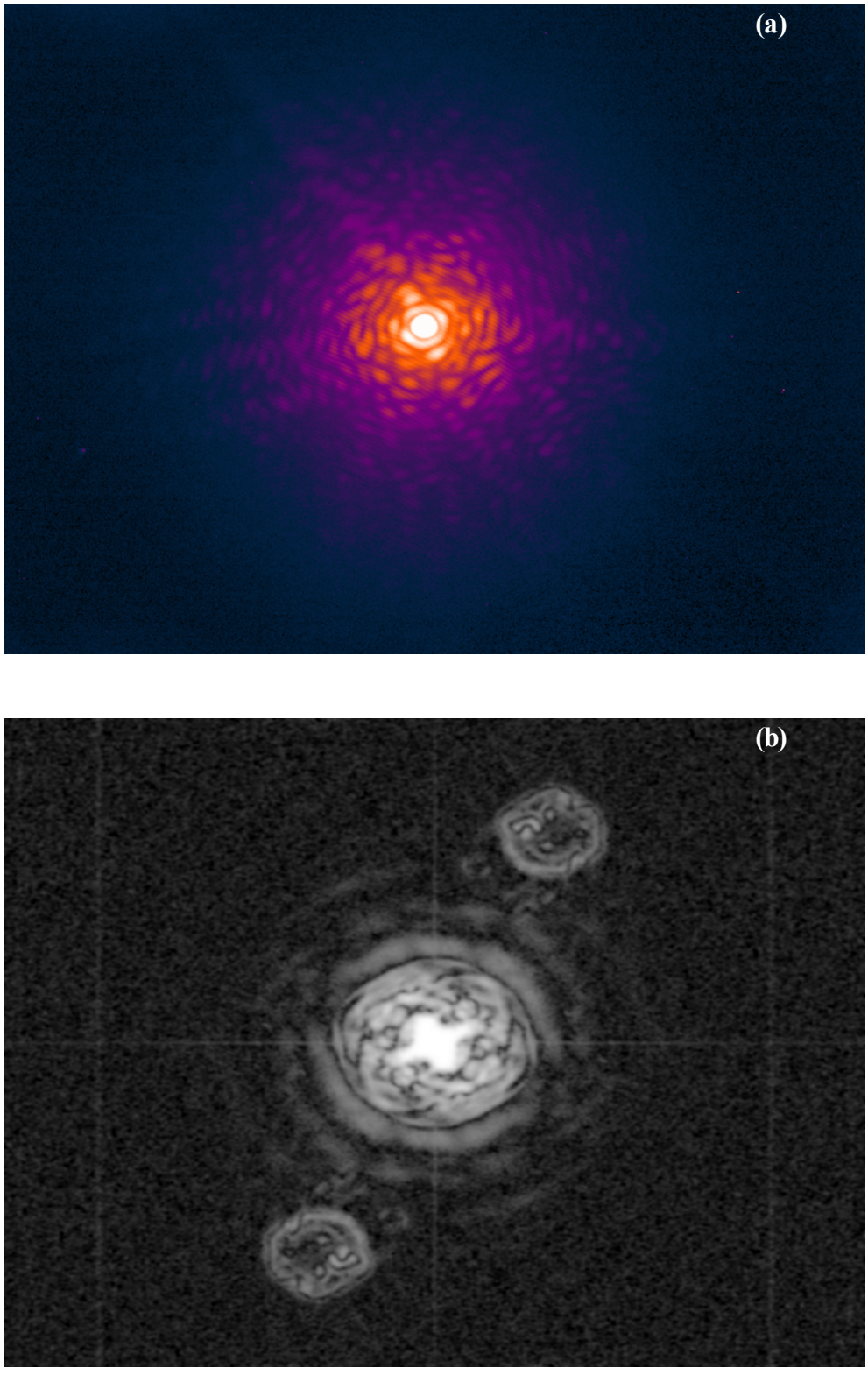

Figure 5.20: (a) Hologram obtained for a 3600 second exposure time. (b) Resultant reconstruction.

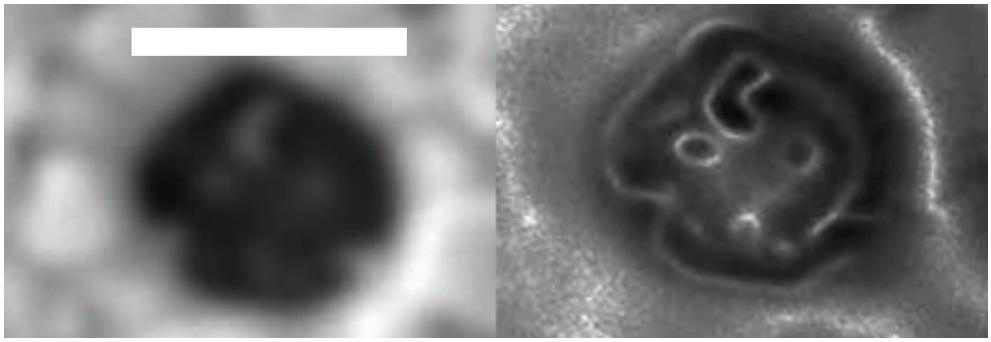

Figure 5.21: Comparison with the SEM image of the object (left image) and the cross-correlation reconstruction (the right); the colour of this image has been inverted. The scale bar on the SEM image is 1.2 μm. The smallest features in the object are approaching the resolution limit of the SEM as they are smaller than 100 nm.

5.7 Phase Retrieval

The following section details our attempt at applying phase retrieval algorithms to the holographic data. The aim was to use the reconstructed image as a tight support in iterative phase retrieval. As will be demonstrated later, a tight support leads to higher resolution reconstructions. The reconstruction was also used as the input for such algorithms so the algorithms started closer to the real solution. Subsequent iterations of the algorithm should have improved the image resolution.

Ultimately, such attempts were unsuccessful as large regions of the hologram are missing due to high noise levels. In the subsequent section the sources of noise are discussed as well as the attempts made to reduce them. Finally the ability of the phase retrieval algorithm to handle noisy data is considered and applied to our data.

5.7.1 CCD Noise and its Effect on the Reconstruction

The holograms were recorded using an out of vacuum CCD. There were two sources of noise; the readout noise of the CCD and the contribution of hot pixels.

The readout noise represents the random noise of the CCD that is measured under totally dark conditions and includes all noise sources (such as dark current) that

are independent of signal level [98]. For example dark noise is intrinsic to all semiconductors and occurs through the thermal generation of minority carriers. The readout noise therefore sets a lower limit on the exposure times for which the images are recorded. This is demonstrated in fig. 5.22 which shows the intensity profile of the simulated hologram from fig. 5.2 (b) and various readout noise. The only observable signal is that which exceeds the readout noise. Figures 5.22 (b) to (f) show the effect of noise in the simulated diffraction pattern, as a function of the maximum intensity, on the resultant reconstruction. As the noise level increases the amount of weak signal lost increases and this has significant degradation on the reconstructions. Firstly, it becomes increasingly difficult to see the smaller features of the object, which disappear completely for 1% noise, and secondly the boundary of the cross-correlations begins to blur and disappears for 10% noise. The increase in noise gives rise to concentric circles around the central autocorrelation. The radii of the rings increases with increasing noise.

Weaker signal was measured by increasing the exposure time. The experimental readout noise for the differing exposure times can be seen in fig. 5.23. Typically the background is between 45 to 55 counts and increases along the CCD from left to right; a direct result of a light leak from an unknown source (fig. 5.23 (f)). This light leak was invisible to the human eye and was present in all background scans, increasing in intensity and size as the exposure time increased. The maximum intensity of the light leak is 120 counts for a 3600 second exposure time. Precautions were taken to remove this leak, such as turning off the ion pump and foiling off the viewpoints. However, we were unable to remove the light leak. Due to the CCD being sensitive to a broad energy spectrum, it appears the light source was outside the visible spectrum.

The following exposure times were used: 1, 10, 100, 1000 and 3600 seconds. The larger exposure times ensured that the weak signal exceeded the background noise. This illustrates the problems associated with using a non-cooled CCD; the noise can be removed from the hologram by subtraction of dark images but the weak signal is still lost. Unlike the PILATUS detector used in the previous chapters, CCDs have no energy resolution and any light source will contribute to the measured signal again leading to a reduced observable signal.

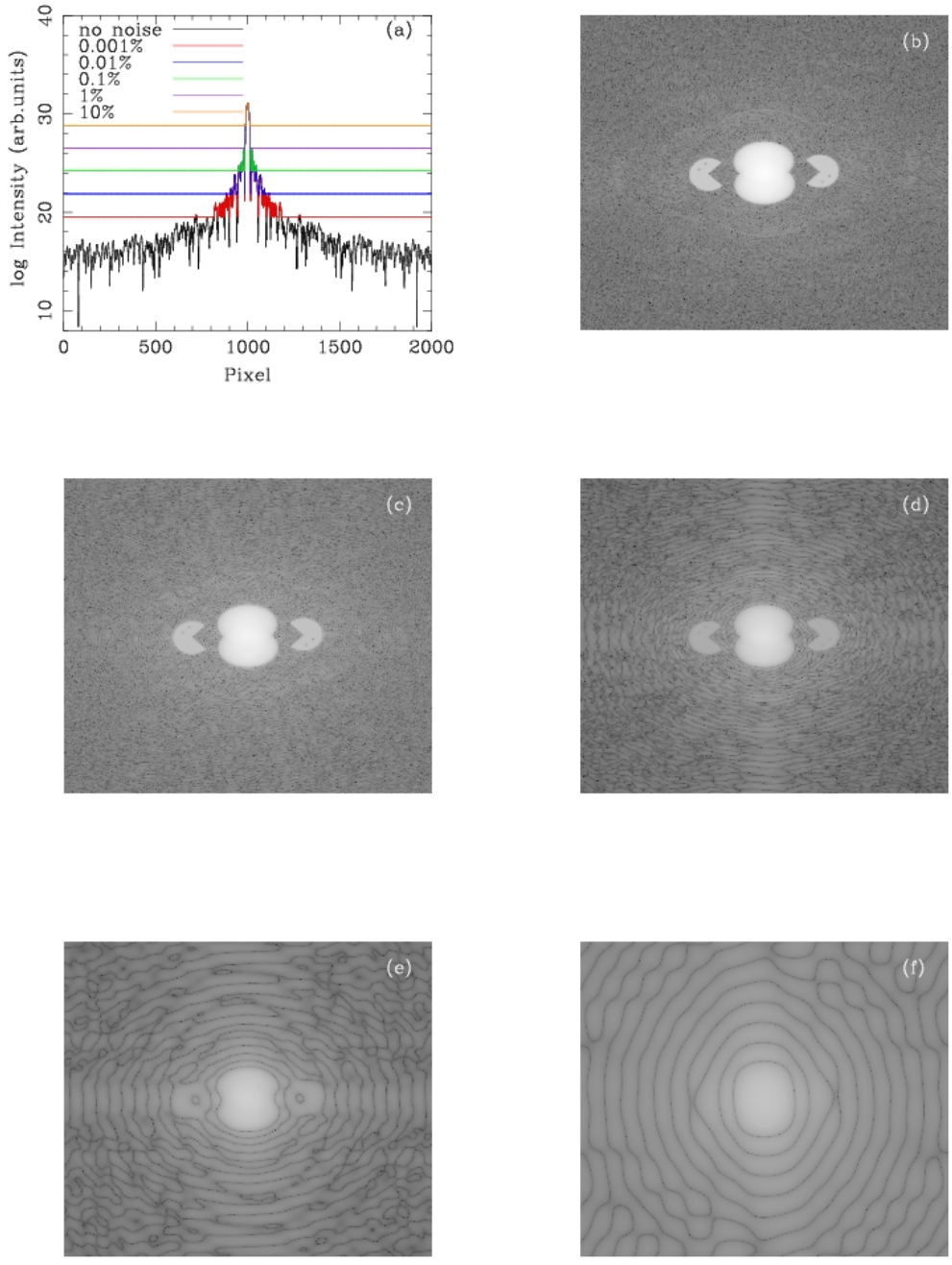

Figure 5.22: (a) Simulated diffraction patterns with varying background levels to illustrate the lost scattering. The reconstructions have the following constant background levels, taken as a function of the maximum intensity of the hologram: (b) 0.001%, (c) 0.01%, (d) 0.1%, (e) 1% and (f) 10%.

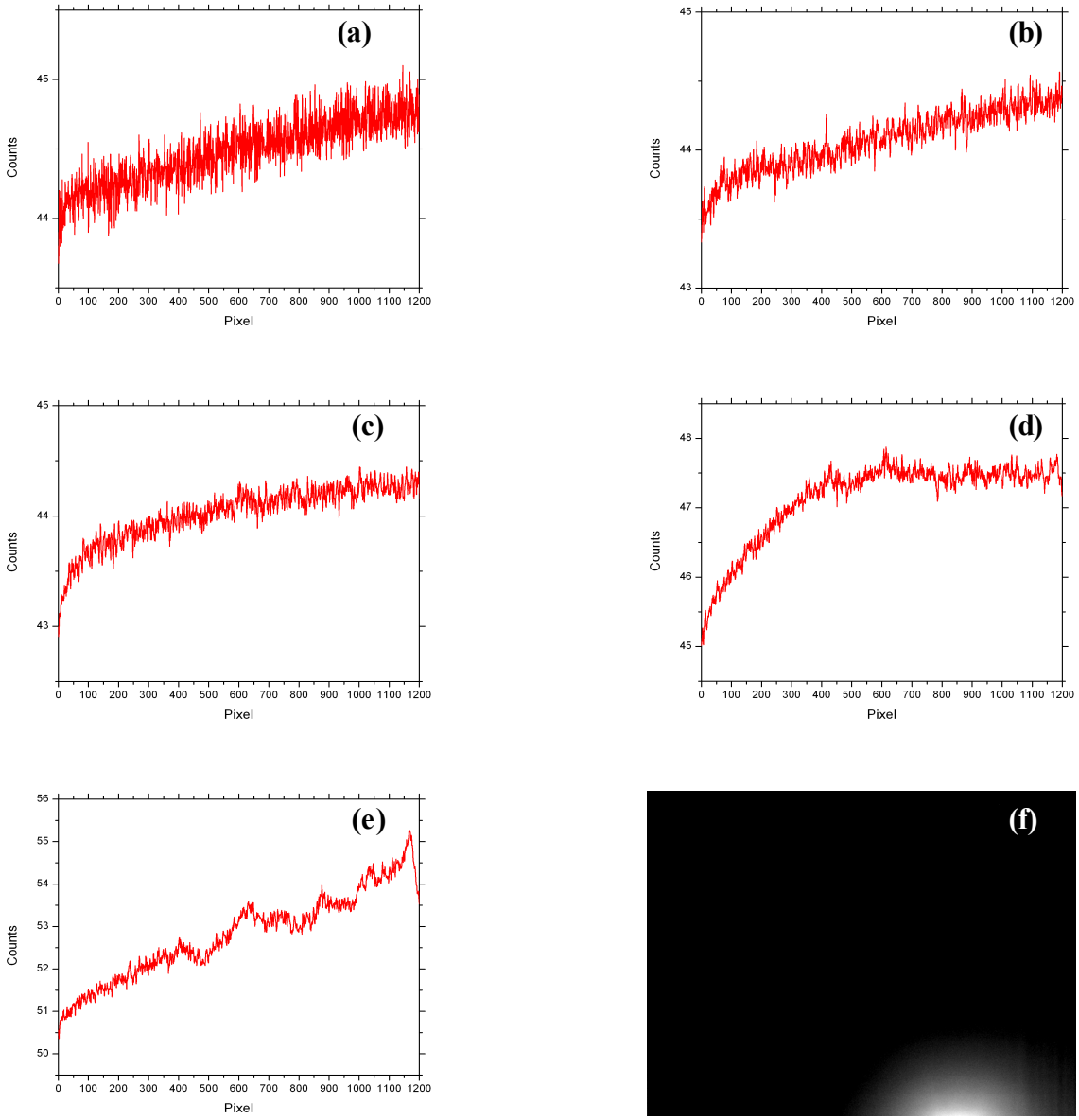

Figure 5.23: The measured CCD readout noise for (a) 1, (b) 10, (c) 100, (d) 1000 and (e) 3600 second exposure times. (f) The light leak for 3600 seconds.

The second source of noise arises from so-called "hot" pixels. These appear as the exposure time increases. It is seen that although they appear at random locations across the CCD their position always remains fixed. These pixels are much brighter than the surrounding area. These pixels are a result of charge leakages within the CCD sensor chip [98]**.** Although these pixels are always present they are not visible for lower exposure times because their contribution to the noise level does not exceed the general readout noise. The hot pixels have significant degradation on the reconstruction, as

shown in fig. 5.24. The simulated diffraction pattern has hot and "cold" pixels (where cold pixels are less bright than the surrounding area) and the reconstruction contains no information about the object.

The hot pixels were found by convoluting the dark images with the following matrix:

$$\begin{pmatrix} -1 & -1 & -1 \\ -1 & 8 & -1 \\ -1 & -1 & -1 \end{pmatrix} \quad . (5.14)$$

This would find pixels with an intensity greater (or less) than its 8 neighbouring pixels. The number and behaviour of the hot pixels can be seen in figs. 5.25 and 5.26. Figure 5.25 shows pixel histograms for 3600 second backgrounds and reveals a surprisingly large numbers of hot pixels with intensities greater than 100 counts. Figure 5.26 shows the behaviour of some select hot pixels as a function of exposure time. The error bars represent the rms error between various background scans. The graph shows that the intensity of the hot pixels behave linearly with time between exceeding the background and saturation. The rms error for each pixel is very small, showing that the position and behaviour of the hot pixels are very consistent. This is verified by table 5.3 which shows the mean number of hot pixels and the standard deviation.

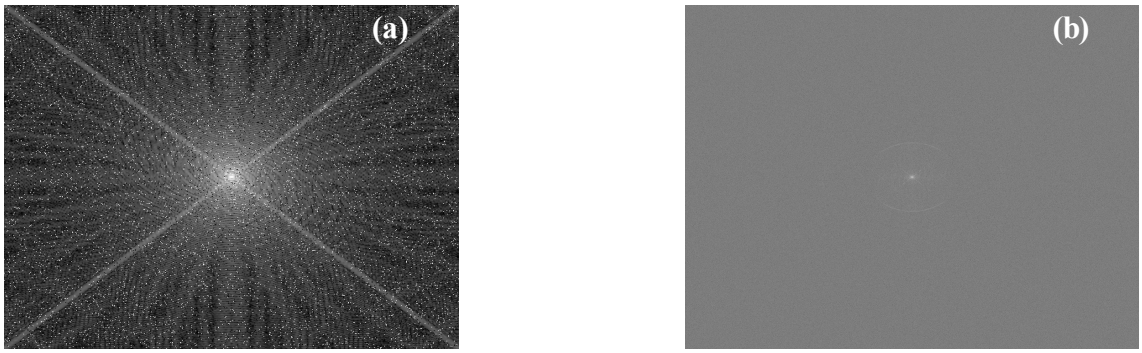

Figure 5.24: (a) Simulated diffraction pattern with random noise added to simulate the bright pixels. (b) The resultant reconstruction.

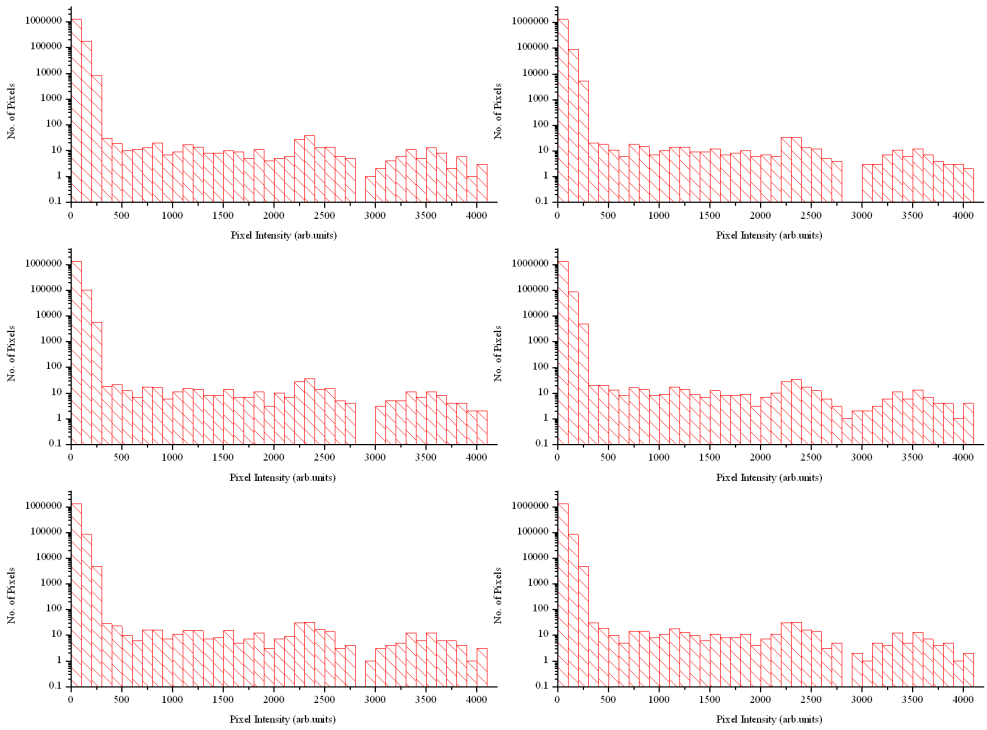

Figure 5.25: Histogram of pixel counts for a 3600 second background.

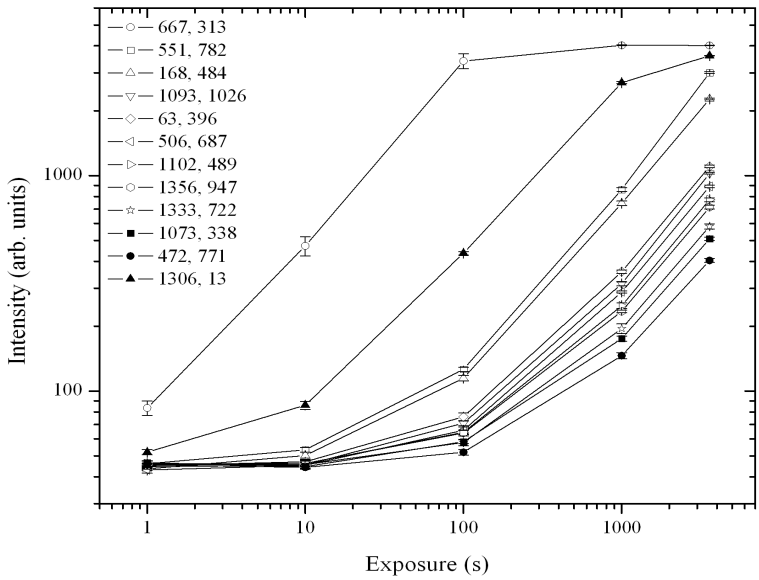

Figure 5.26: Behaviour of selected bright pixels as a function of exposure time. The error bars represent the rms error between various background scans.

Exposure Time (seconds)	Mean number of hot pixels	Standard Deviation
1	0	0
10	5.4	1.14
100	45.17	1.94
1000	341.67	6.19
3600	429.33	5.92

Table 5.3: Number of bright pixels for each background image

The hot pixels are corrected for by replacing them with the average of their 8 neighbours. If one of the neighbours is also a hot pixel (which has a low probability) it is replaced by the average of the remaining non-hot pixels. This is a quick procedure and leads to minimal blurring.

5.7.2 Airy Disk Reconstruction

A typical hologram and its reconstruction is shown in fig. 5.20 and the typical background is approximately 40 to 50 counts. The reconstruction has concentric rings of noise surrounding the autocorrelation; the intensity of which comparable to that of the cross correlations. The rings are present even when the hologram is background subtracted and result from the saturation of the Airy disk. This saturation is presented in fig. 5.27 (f), which shows a line profile through the centre of measured holograms. The CCD has a poor dynamical range and a meaningful signal can only be measured provided it is greater than 40-50 counts and less than 4095 counts. The background is approximately 1% of the maximum signal and this has significant degradation on the reconstruction (fig. 5.22 (e)).

The effect of saturation is demonstrated in simulations by varying the height and shape of the Airy disk. Firstly the Airy disk was set to a constant value (fig. 5.28 (a)), to mimic the experimental data, and finally to zero (fig. 5.28 (c)), mimicking the effect of a (e.g.) lead beamstop used to mask the centre of the detector. In both simulations the rings are present and the cross correlations have poor contrast with the noise (figs. 5.28 (b) and (d)).

Holograms measured with the same conditions but different exposure times are presented in figs. 5.27 (a) to (e). As exposure time increases more of the weak signal is measured, but, from 100 seconds onwards, the Airy disks saturates and is completely saturated for 3600 seconds. This leads to charge overflowing, since a CCD pixel behaves like a bucket [98]. Once the pixel has filled up with charges generated by the incoming photons, the charge will overflow into neighbouring pixels. This lead to the Airy disk and the neighbouring speckles becoming indistinguishable as both saturate for 3600 second exposure (figs. 5.27 (e) and (f)).

The reconstructed images are more detailed with increasing exposure time, however, the noise increases with increasing saturation of the Airy disk (fig. 5.29).

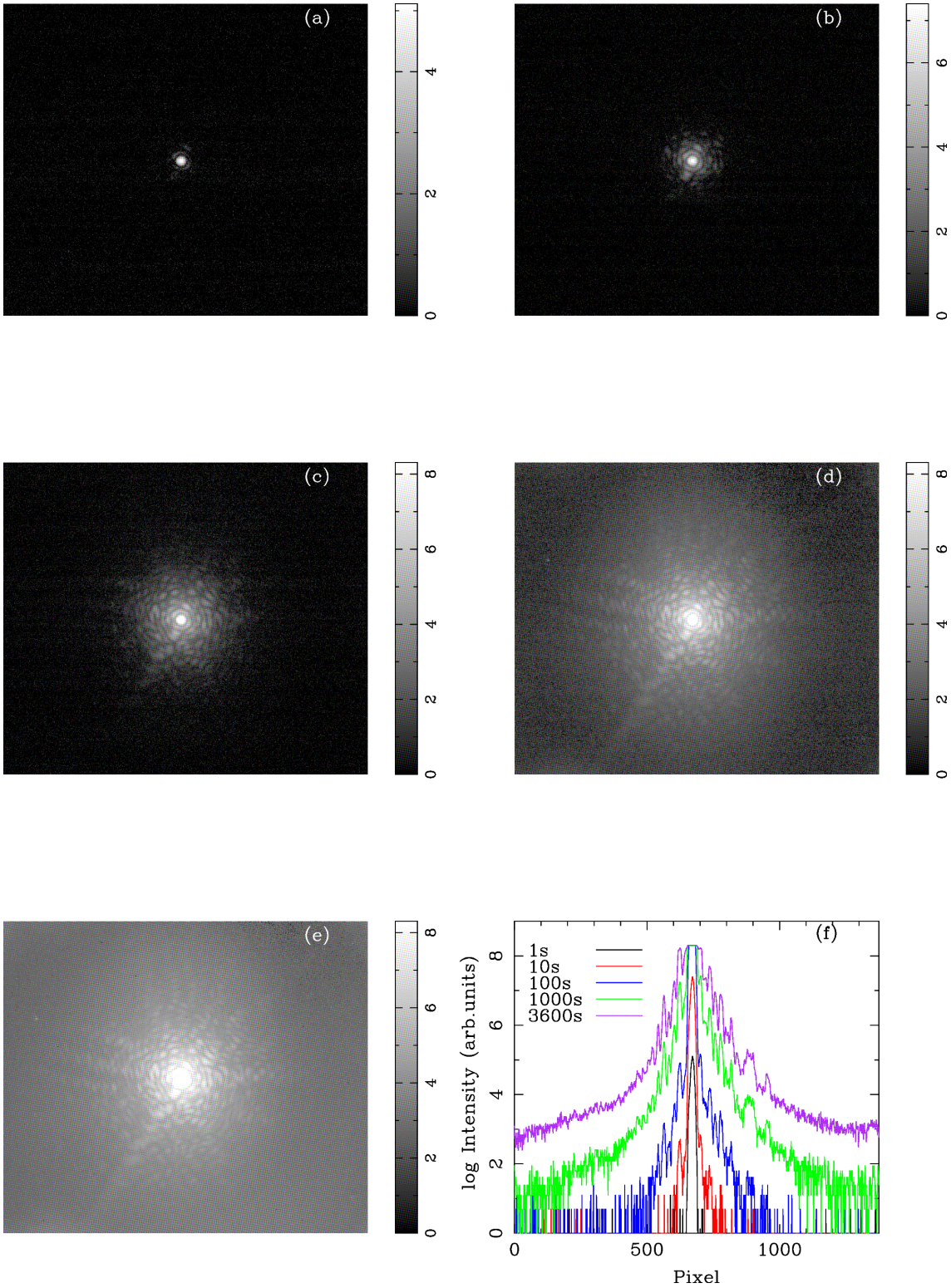

Figure 5.27: Measured holograms for exposure times of: (a) 1 s, (b) 10 s, (c) 100 s, (d) 1000 s and (e) 3600 s. The horizontal line profiles through the middle of the holograms is shown in (f).

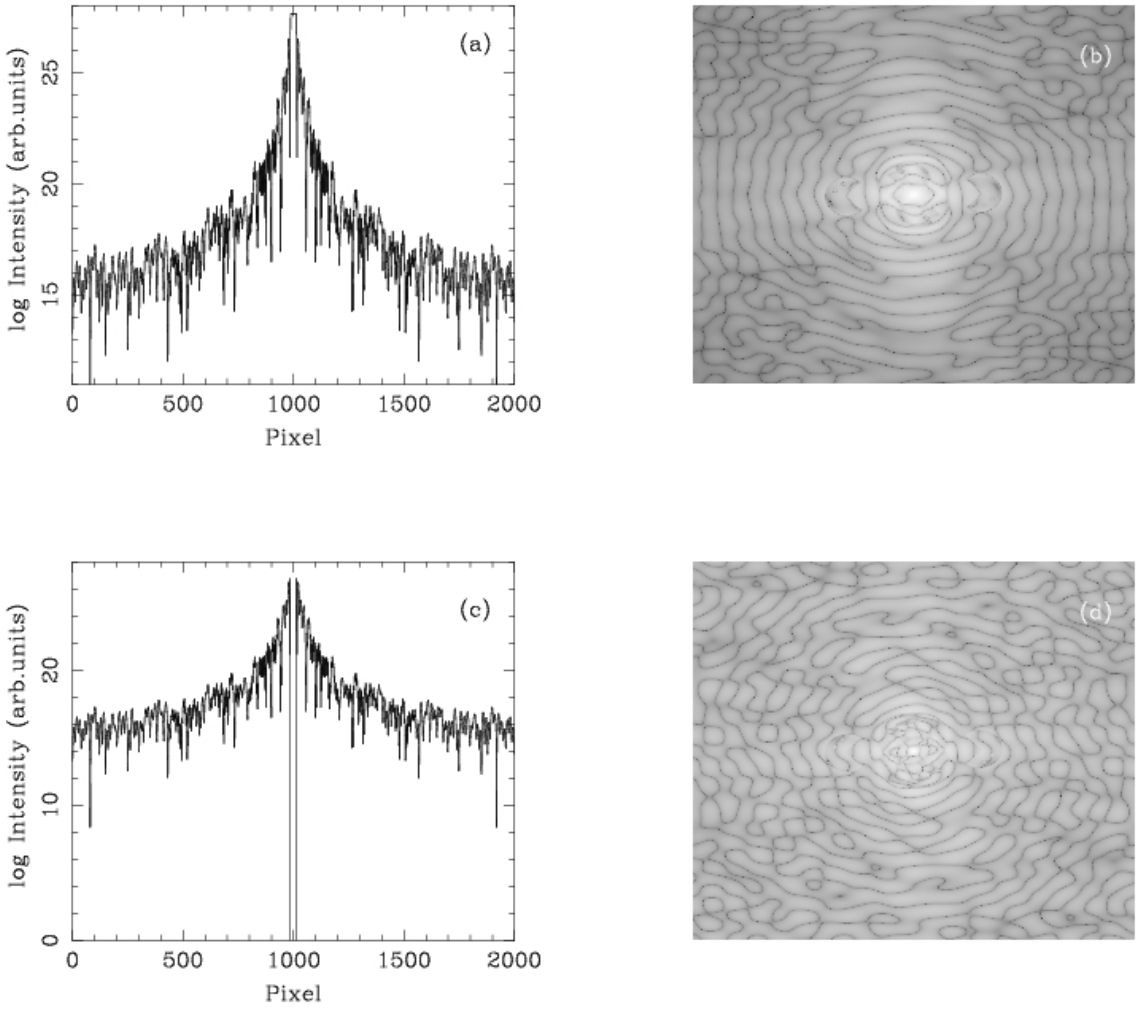

Figure 5.28: (a) Line profile of a hologram with the central peak set to a constant value and (b) the corresponding reconstruction. (c) Line profile of a hologram with the central peak set to zero and (d) the corresponding reconstruction.

The measured holograms were subjected to a threshold, to remove the saturated pixels and were normalised to exposure time (fig. 5.30 (a)). The saturated pixels removed from the 3600 second exposure were replaced by those from the 1000 second exposure, those pixels removed from the 1000 second exposure replaced by those from the 100 second exposure and so on. The resulting patched hologram (fig. 5.30 (b)) has no saturation (fig. 5.30 (c)) and enough weak signal is recorded to allow detailed reconstructions (fig. 5.30 (d)). The rings are absent and the cross-correlations have improved contrast with the background. However, patching the hologram generates noise across the reconstruction.

This approach again demonstrates the need for a low noise, and preferably, a high dynamic range CCD. The cross-correlations are present for exposure times of 10 s and there is very little noise in the reconstructions. However, the weak scattering, and subsequently the detail of the reconstructed object, is lost in the background noise. If the readout noise is reduced to zero, then detailed reconstructions can be obtained for low exposure times and none of the pixels saturate. Random sources of noise could be removed altogether by taking multiple images and then stacking them. If the CCD has poor readout noise but a high dynamical range, detailed reconstructions can be obtained by simply increasing the exposure time, but now the Airy disk is not saturated.

5.7.3 Phase Retrieval Algorithms

We start with Feinup's [99] improvement of the Gerchberg-Saxton algorithm, which retrieves the phase of a measured diffraction pattern, by a series of iterations between real and Fourier space and the application of constraints, from a single intensity measurement of the Fourier modulus of the object $|F|$. This algorithm, known as the error-reduction algorithm, has four steps (illustrated in fig. 5.31):

1. Take the modulus of the diffraction pattern and apply a random phase. Then perform an inverse Fourier transform.
2. This gives an estimate of the real space object. Apply real space constraints.
3. This gives a new estimate of the object. Perform a Fourier transform.
4. This gives a new Fourier space image with a new phase which is closer to the true phase then the starting phase. Replace the estimate of the modulus with the experimentally measured modulus and repeat.

The error-reduction algorithm can be applied to a wide range of problems in which partial constraints (in the form of measured data or information *a priori*) are known in the two domains. One simply transforms between the domains, satisfies the constraints before returning to the other domain.

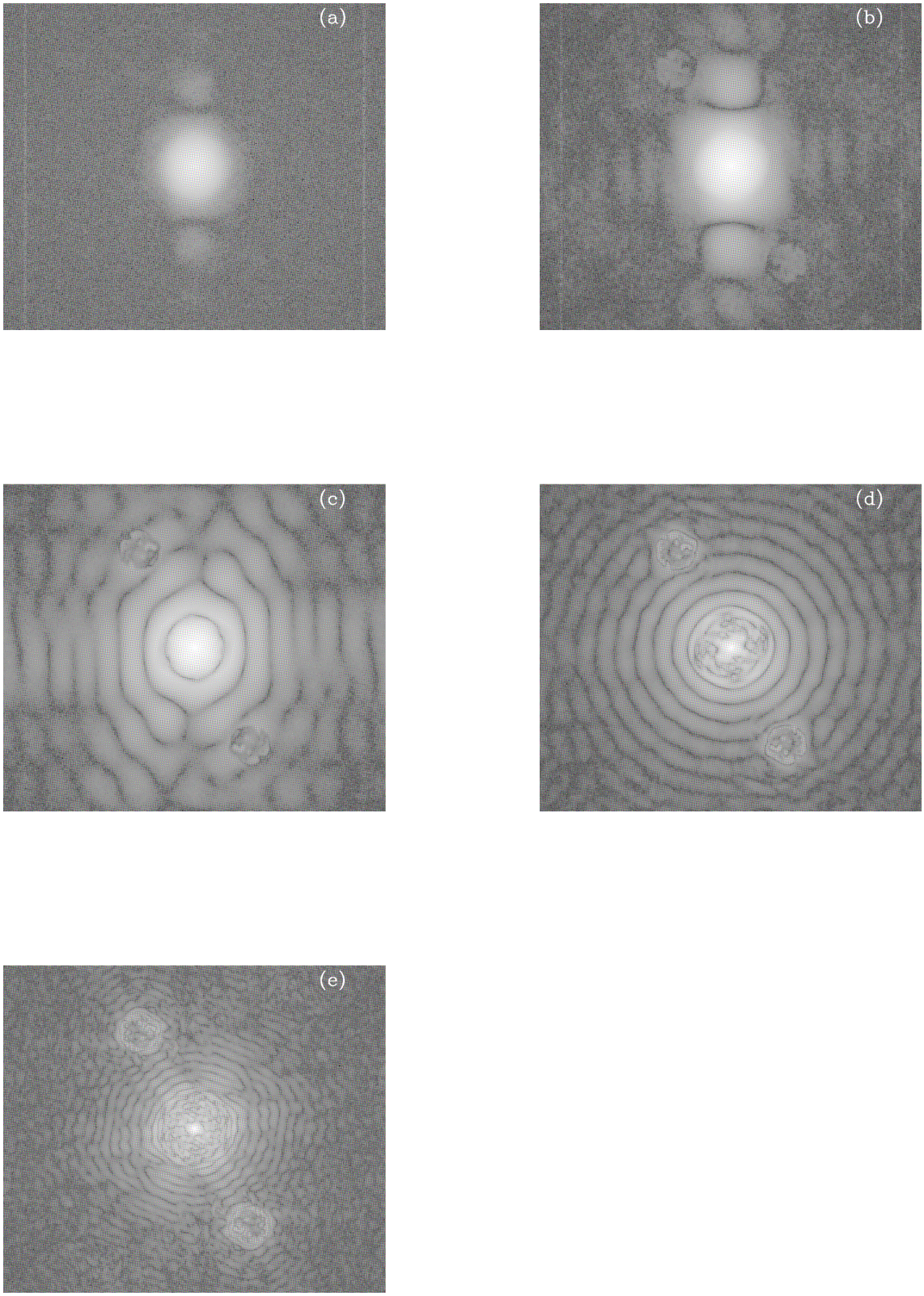

Figure 5.29: Reconstructions corresponding to diffraction patterns illustrated in fig. 5.27.

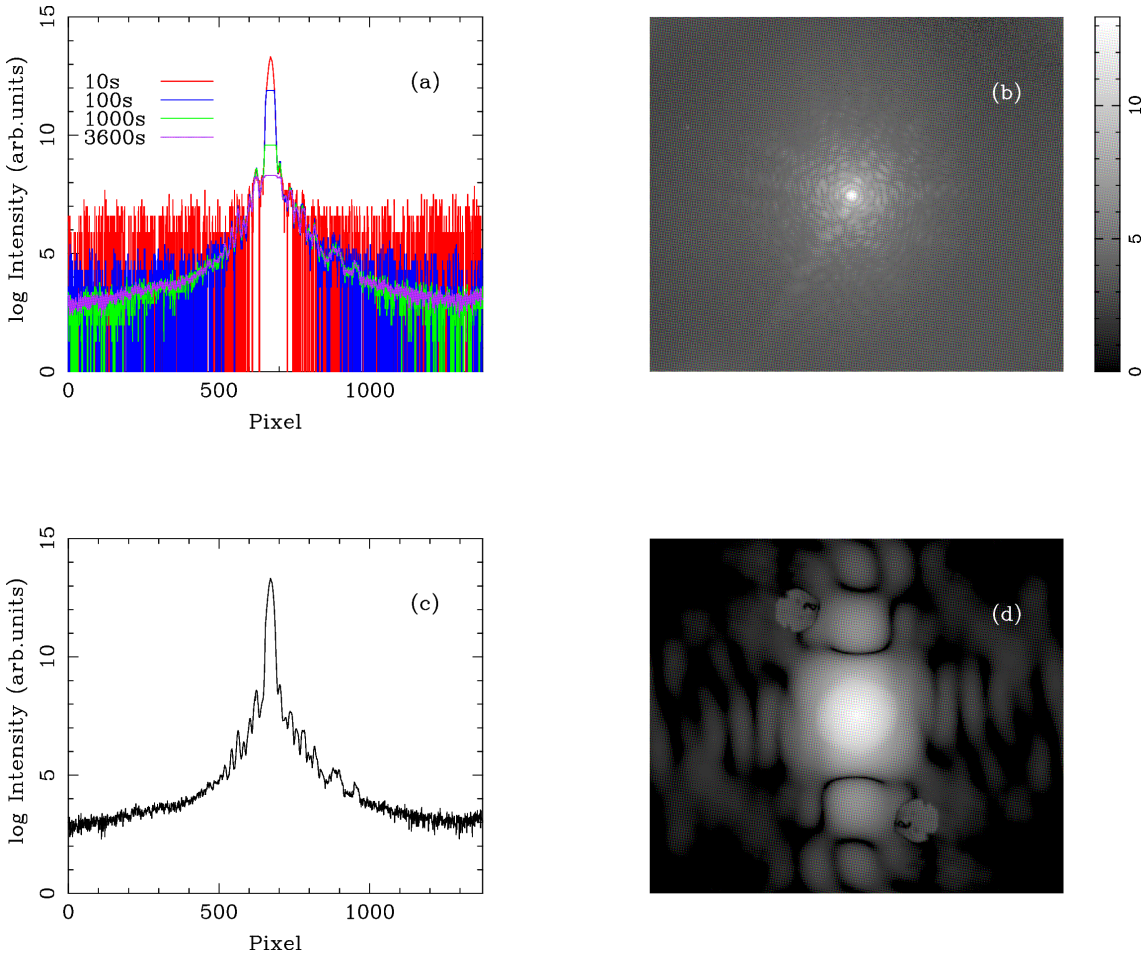

Figure 5.30: (a) Line profiles normalised to 3600 seconds. (b) Hologram combined from the various exposure times. (c) Line profile of the combined hologram. (d) The reconstruction of (b). This image has been contrast enhanced to remove the majority of weak noise.

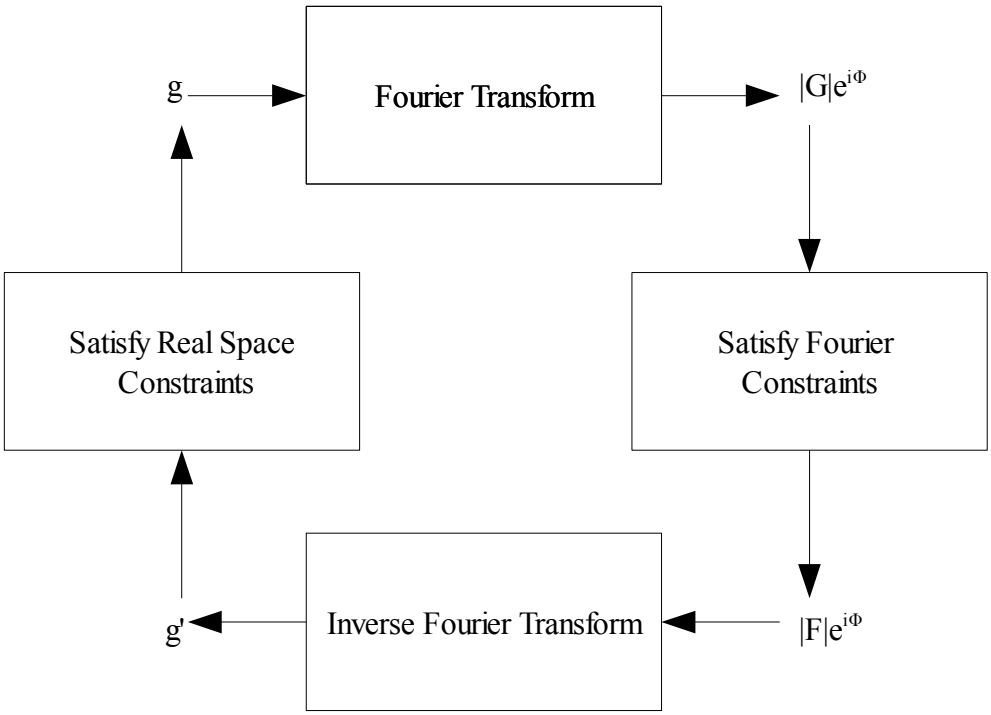

Figure 5.31: Block diagram of the error-reduction algorithm.

In the error-reduction algorithm the constraint in real space is given by

$$g_{k+1}=\begin{cases} g_k' & x\neq\gamma \\ 0 & x=\gamma \end{cases} \quad , (5.15)$$

where γ is the set of points for which $g'_k(x)$ violates the object-domain constraints . The iterations continue until the computed Fourier transform satisfies the Fourier-domain constraints or the computed image satisfies the object-domain constraints. The convergence of the algorithm can be monitored by computing the mean squared error, which for a single intensity measurement is given by $E_{ok}^2=\sum_{x=\gamma}[g'_k(x)]^2$. The normalised root mean squared (nrms) error is given by

$$E_{ok}=\frac{\sum_{x=\gamma}[g'_k(x)]^2}{\sum_{x}[g'_k(x)]^2} \quad . (5.16)$$

However, this algorithm has slow convergence. To overcome this Feinup introduced the hybrid input-output algorithm (HIO) [99], which differs from the error-reduction algorithm in the object domain. Now the input $g(x)$ is no longer the best estimate of the object, but rather the driving function for the next output $g'(x)$. The input $g(x)$ does not necessarily satisfy the object domain constraints and therefore allows for different versions of the input function. The next input g_{k+1} differs from that of the error-reduction algorithm and is a combination of the previous input g_k and output g_k' so that

$$g_{k+1}=\begin{cases} g_k' & x\neq\gamma \\ g_k-\beta g_k' & x=\gamma \end{cases}, \quad (5.16)$$

where β is a feedback parameter and is defined by Feinup to be equal to 0.9.

Phase retrieval algorithms can be applied to holography by considering the mask sample design shown in fig. 5.32 (a); in this instance the reference hole is larger than the features in the object. We are therefore unable to observe these features in the reconstructed cross-correlations (fig. 5.32(c)). However, the support mask can be conveniently obtained from the low resolution hologram by using the method developed by Marchesini et al., [100]. The object must fit within the cross-correlations and so the first estimate of the support is obtained by contouring and thresholding the cross-correlations for a given intensity level. The support is zero everywhere outside of the cross-correlations. Phase retrieval algorithms are then applied, where the initial step is to apply a random phase to the measured Fourier modulus. The support mask and reconstructions after 100 iterations of both the error reduction and HIO algorithm are shown in fig. 5.33. After a few iterations of both, one of the cross-correlations begins to fade and eventually disappears, overcoming the twin-image problem associated with holography, whilst the resolution of the remaining cross-correlation improves and the object is recognisable. The convergence of the algorithms can be made faster, simply by discarding one of the cross-correlations in the support mask.

The slow convergence of the error-reduction algorithm can be drastically improved by utilising the shrink wrap algorithm [100]. This algorithm is identical to the error reduction and HIO algorithms apart from one crucial difference; the support mask is continuously updated. After n iterations of either the error-reduction or HIO

algorithm, the real space image is convolved with a Gaussian, with σ = 3 pixels, and then thresholded above a certain intensity level. The convolution smooths out the noise in the real space image creating a well defined boundary of the support. After another n iterations, the real space image is again subject to a convolution, however σ is decreased by 1%, creating a sharper support mask. This process is repeated until a suitable level of convergence has been obtained.

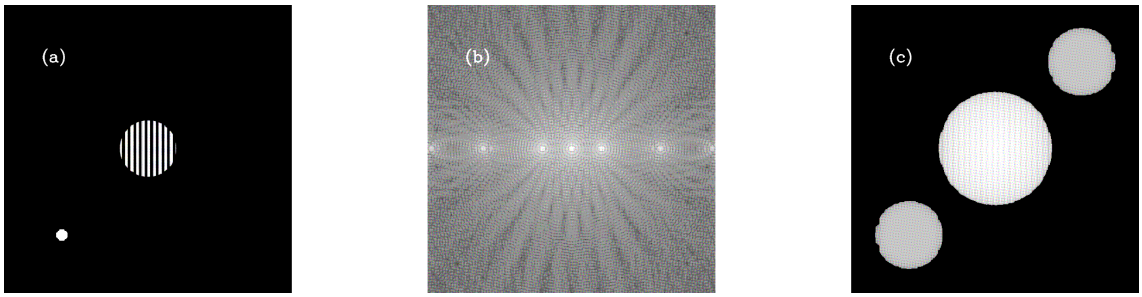

Figure 5.32: (a) The object and very large reference hole. (b) The simulated hologram. (c) The resultant reconstruction. The light and dark features in the object are unobservable due to the large reference hole.

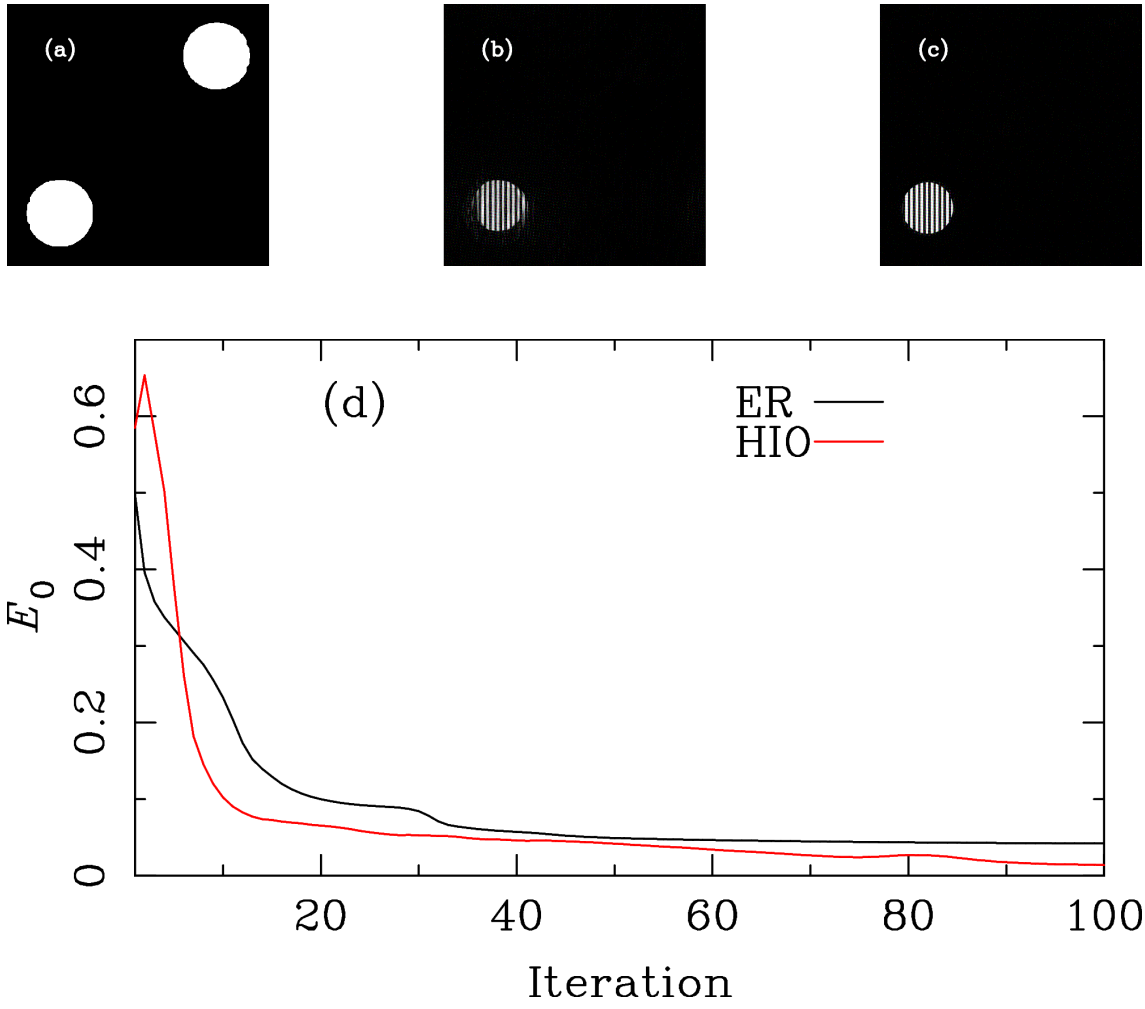

Figure 5.33: (a) The support mask obtained by thresholding the cross-correlations. (b) The reconstruction after 100 iterations of the error-reduction algorithm. (c) The reconstruction after 100 iterations of the HIO algorithm. (d) A comparison of the convergence of the error reduction and HIO algorithms. The HIO algorithm converges much faster than the error reduction and, bar the first two iterations, improves with each iteration. This diagram illustrates the problem with slow convergence of the error-reduction algorithm, which has stagnated in a local minimum after approximately 50 iterations

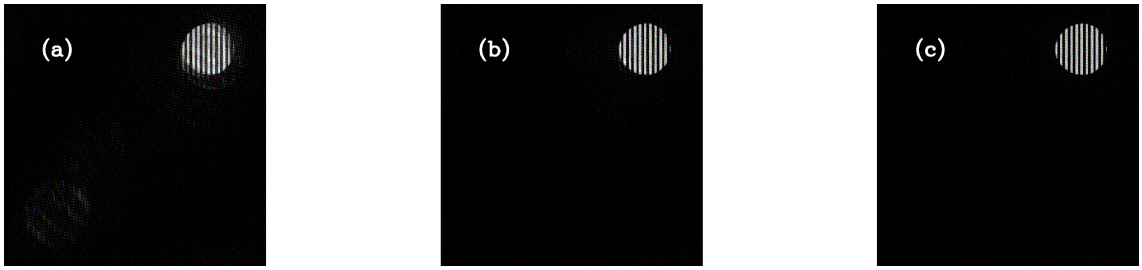

Figure 5.34: The combination of the shrink wrap and error reduction algorithms. The support is updated every 20 iterations by convolving and thresholding the real space image. The real space images are shown for (a) 20, (b) 40 and (c) 60 iterations of the error reduction algorithm.

Thus far the discussion on phase retrieval has only considered noise free data, which, in the case of our data, is physically unrealistic. Simulations were performed on noisy data, where the constant readout noise of the Fourier modulus is given as a percentage of the maximum intensity of the Airy disk (fig. 5.35). For relatively low noise levels, the reconstructed object after 100 iterations of the HIO algorithm is instantly recognisable. For intermediate noise levels the reconstructed object is recognisable but there is slight blurring of the light and dark features and for high noise only the envelope of the support is observed.

The size of the support mask is crucial for the phase retrieval algorithm's ability to handle noisy data. So far the support is obtained from the cross-correlations that, for the example of a large reference hole, gives us a loose support mask. If we tighten the support mask by increasing amounts, eventually using the object as the support mask, the HIO algorithm will obtain a recognisable object even in the presence of high noise levels in the Fourier modulus (fig. 5.36). The shrink wrap algorithm is superior to the HIO algorithm when a loose support is used [100] because it always improves upon the support (fig. 5.37). The noise level at which the algorithm fails [100] occurs when the noise in real space becomes larger than the threshold used to update the support. The optimum threshold setting depends on the noise level and reconstruction is only available in parts of the object where the contrast is above the noise [100].

Using this knowledge, we then apply the HIO and shrink wrap algorithms to our data. The support masks, shown in fig. 5.38, are different for the two algorithms. The

support mask for the HIO algorithm is obtained directly from thresholding one of the cross-correlations whilst a loose support that envelopes the cross-correlation is used for the shrink wrap. As our data is noisy, if a tight support mask is employed with the shrink wrap algorithm, updating the support mask after *n* iterations becomes problematic; if the threshold level is too low then the support mask will grow in size as it begins to engulf the surrounding noise, if the threshold level is too high then the support mask shrinks rapidly and severely truncates the object within several updates of the support. The cross over between these levels is very small and it is very difficult to accurately determine, hence, a loose support is used that is continuously updated.

The masks were obtained after the data had been background subtracted, the hot pixels removed and the saturated pixels patched. The real space images obtained from the HIO algorithm and the shrink wrap algorithm are shown in figs. 5.39 and 5.40 respectively. In both cases the quality of the reconstructed object is relatively poor and only the envelope of the object is observed. After 1000 iterations of the shrink wrap algorithm, the support closely resembles that used in the HIO algorithm, which indicates some level of success. However, the small features in the object are unobservable as they become engulfed in the noise, of which there are two sources: the readout noise and the patching of the saturated pixels. The simulations show that provided a tight support is used, the phase retrieval algorithms are fairly robust even in the presence of high readout noise, suggesting the failure arises from the patching of the saturated pixels. Unfortunately, the patching is a necessity as the data is even noisier if the pixels are left saturated.

It is here that a different approach of replacing the saturated pixels is taken [97]. As before the data is background subtracted, the hot pixels removed and the saturated pixels patched. The new approach diverges after the first iteration of the algorithm; the amplitude of $|G|$ is matched to that of $|F|$ where the intensity is *known* i.e. outside of the saturated region where the speckles are. The region where saturation occurs in the measured diffraction pattern is then replaced by the scaled region of the estimated diffraction pattern. This region is replaced after each iteration, thereby gradually improving on the initial estimate. The resulting real space images obtained using the HIO and shrink wrap algorithms are shown in figs. 5.41 and 5.42 respectively. After 20 iterations of the HIO algorithm the reconstruction is still noisy and details of the object

are unobserved; this is unsurprising as the patched regions of the measured diffraction pattern is still incorrect. At 100 iterations the estimate of the saturated regions have improved drastically allowing the features in the object to be faintly observed and after 1000 iterations the reconstructions are far less noisy and not only are the features seen with improved resolution and contrast but also more features are observed. A similar observation is made with the shrink wrap algorithm; not only does the support tend to the size and shape of the cross-correlation but also after 1000 iterations some features of the object are faintly observed.

We can draw several conclusions when applying phase retrieval algorithms to noisy holograms. Firstly, the cross-correlations define a convenient support mask as the real space object must be contained in them and after only a few iterations one of the cross-correlations disappears removing the twin-image problem associated with holography. In the case of noisy data it is better to use the HIO algorithm, due to either excessive growth or shrinking of the support mask using the shrink wrap algorithm. Finally, the estimated diffraction pattern can be utilised to replace any missing regions of the measured diffraction pattern allowing phase retrieval to be applied to incomplete data sets. Alternatively, one could overcome the majority of problems, by using a low noise, high dynamic range CCD.

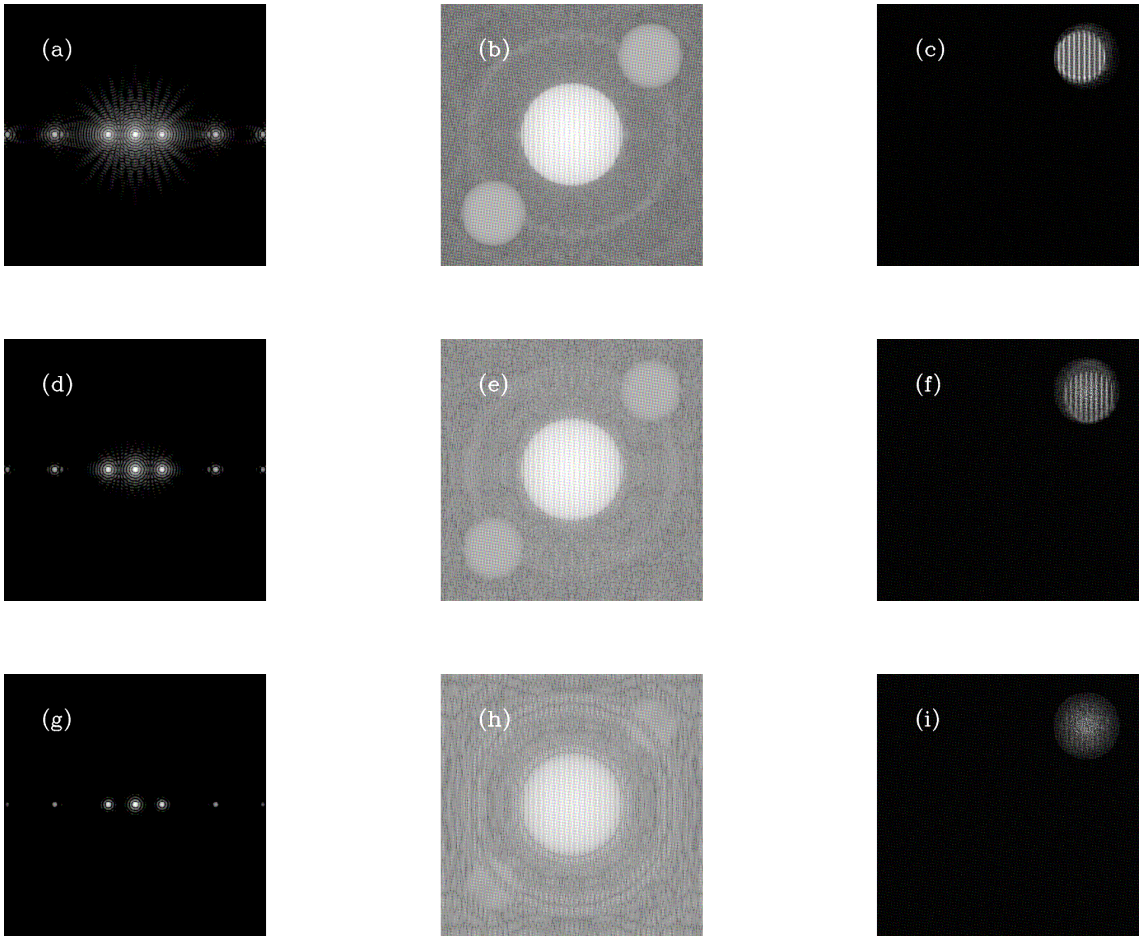

Figure 5.35: The effect a constant readout noise has on the simulated hologram displayed in fig. 5.32. The support structure is identical to that in fig. 5.33 (a) apart from the bottom left cross-correlation has been removed. Figures (a), (b) and (c) show the hologram, reconstruction and the reconstruction after 100 iterations of the HIO algorithm respectively, for a readout noise of 0.001% the maximum intensity of the Airy disk. Figures (d) to (f) and (g) to (i) show the same but for 0.01% and 0.1% readout noise respectively.

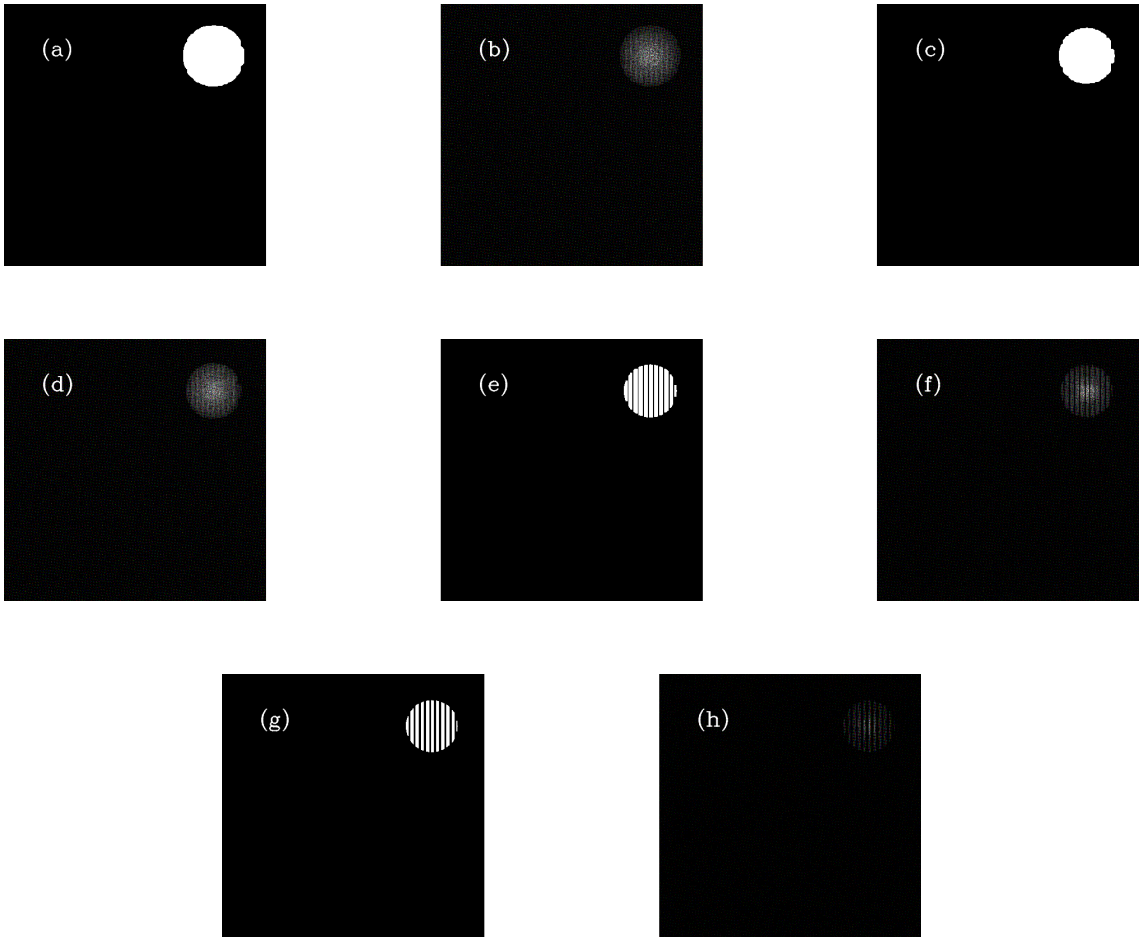

Figure 5.36: The tightening of the support mask and subsequent reconstructions after 100 iterations of the HIO algorithm for noisy a Fourier modulus (compare with figs. 5.35(g) to (i)). The reconstructions improve in quality as the support mask is tightened until eventually the object (g) is used as the support mask.

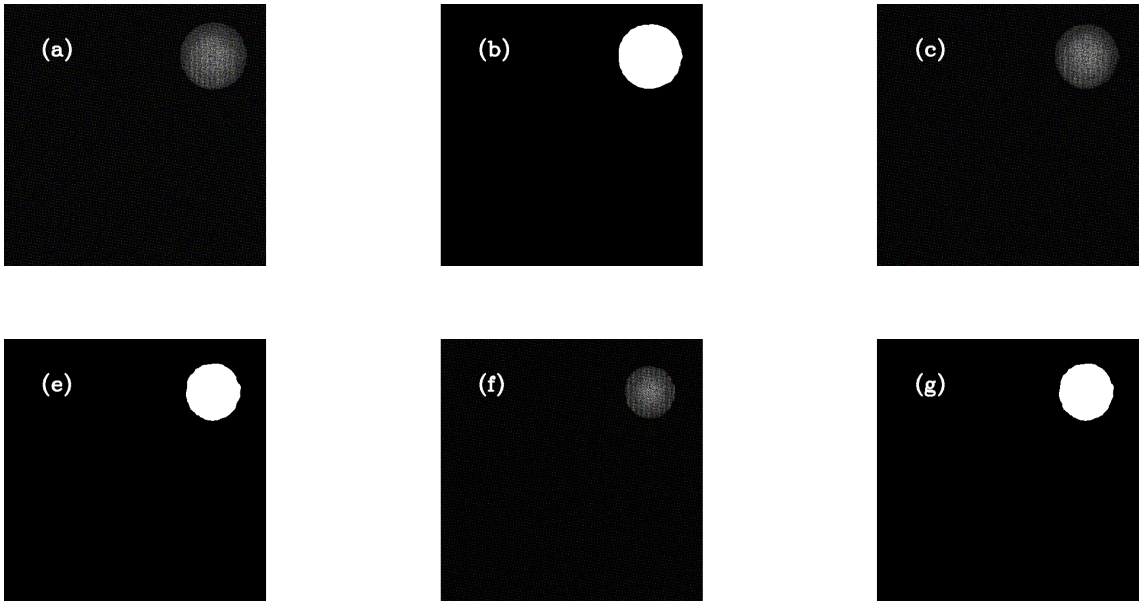

Figure 5.37: Image reconstruction using the shrink wrap algorithm. After every 20 iterations the support mask is obtained by thresholding the object at 25% it maximum intensity. The reconstruction and mask are shown after 20 ((a) and (b)), 60 ((c) and (d)) and 100 iterations ((e) and (f)). The algorithm is terminated after 100 iterations because the support mask is continually updated; after 100 iterations the support mask has shrunk to such an extent that it begins to truncate the object.

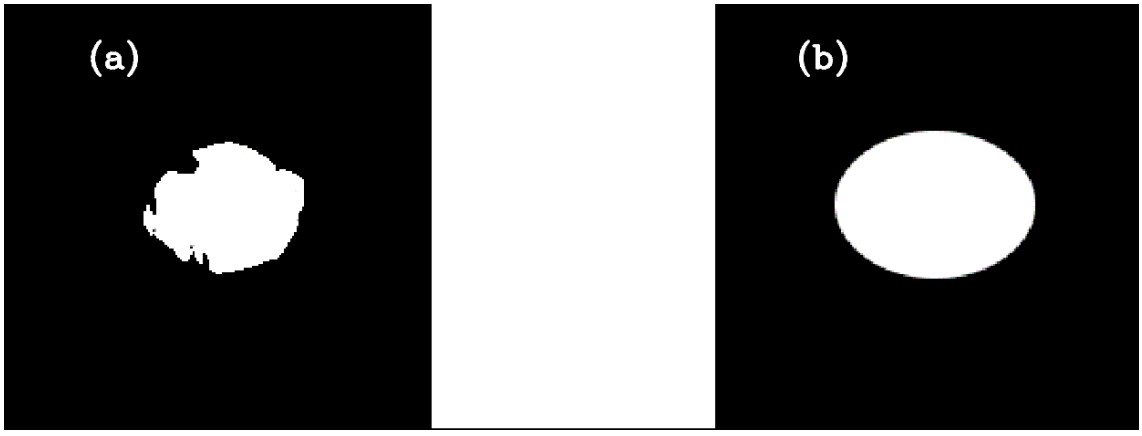

Figure 5.38: The support masks used in (a) the HIO algorithm and (b) as the initial support in the shrink wrap algorithm.

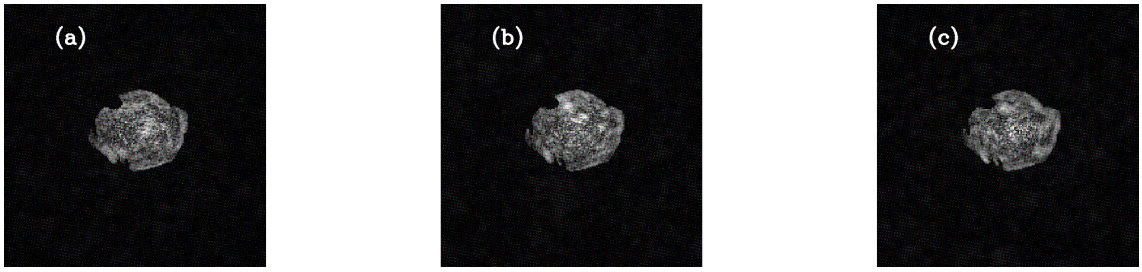

Figure 5.39: The real space image obtained after (a) 20, (b) 100 and (c) 1000 iterations of the HIO algorithm.

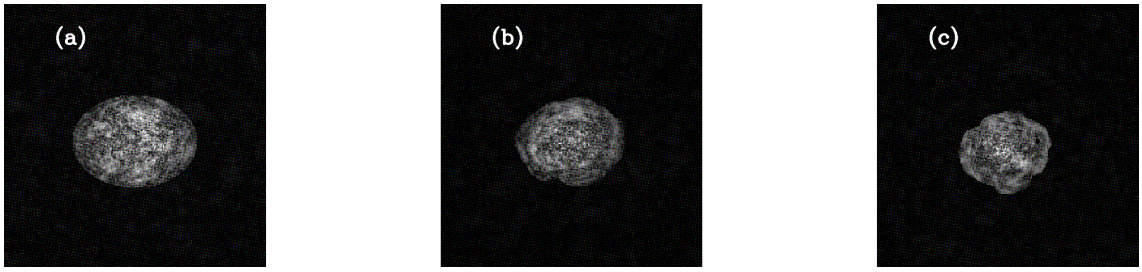

Figure 5.40: The shrink wrap algorithm, with a 15% threshold level, after (a) 20, (b) 100 and (c) 1000 iterations.

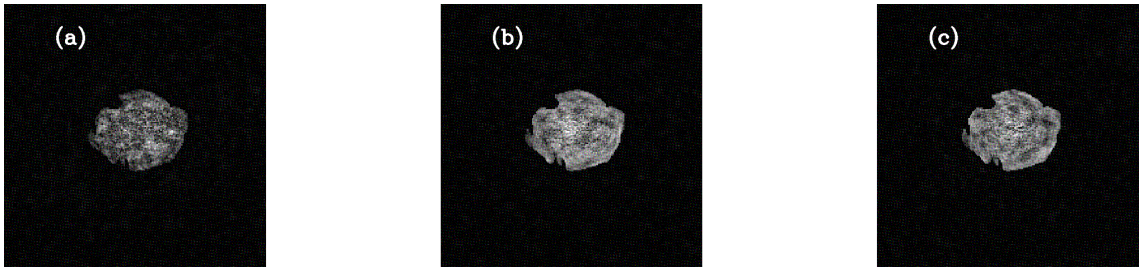

Figure 5.41: The real space image after (a) 20, (b) 100 and (c) 1000 iterations of the HIO algorithm where the saturated regions of the measured diffraction pattern are replaced by the scaled regions of the estimated diffraction pattern.

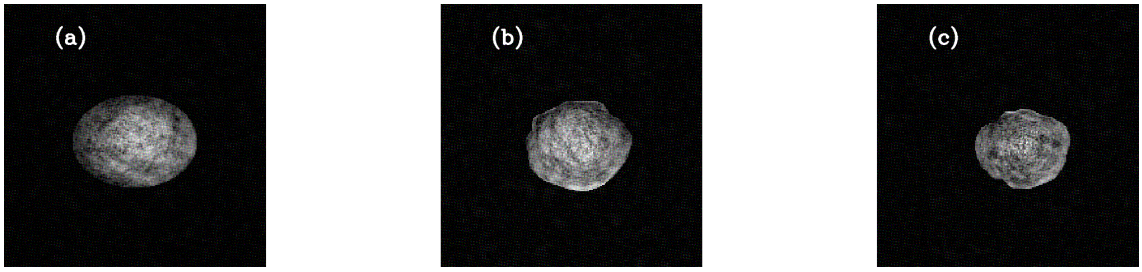

Figure 5.42: The shrink wrap algorithm, with a 25% threshold level, after (a) 20, (b) 100 and (c) 1000 iterations, where the saturated regions of the measured diffraction pattern are replaced by the scaled regions of the estimated diffraction pattern.

5.8 Design of Apparatus to Improve Reference Hole Milling

Thus far the presented holograms have all been limited by the readout noise of the CCD. However, this can be overcome by using a cooled CCD with a high dynamic range. A more pressing issue is the high failure rate of the mask-sample. In this work, 8 mask-samples were grown in the same manner and the masks had the same thickness. The reference holes had a diameter of 100 nm and were created using the method presented in [21]; the depth was set to 1.2 μm and the ion beam was rastered over each reference hole 20 times. This method is highly inconsistent and resulted in only one mask-sample being successful. Even in the successful mask-sample, the X-ray beam could only pass through one reference hole (fig. 5.19).

Here a more elegant method of creating well defined, circular reference holes is presented. A new, sample stage for the FIB was designed and is shown in fig. 5.43. The new sample stage had a base and a copper plate sandwiched between two insulating PEEK layers. A BNC connector was bolted onto the back of the base and one of the PEEK layers went on the base. There is a recess in the PEEK layers that the connector and the copper plate will slide into. An electrical connection is made between the plate and the cable by a conducting silver adhesive. The next insulating PEEK layer goes on top of the plate, and the sample holder is bolted on, holding everything together. A BNC cable was attached to the connector and this was attached to a feed through plate on the inside of the FIB. A BNC Connector went through the middle of the plate and on the outside of the plate another BNC cable was connected from this to a gain amplifier

which in turn was connected to a multimeter.

The top PEEK layer had a hole in it corresponding to the Si_3N_4 window. When the Ga ions mill all the way through the mask-sample they impinge on the copper plate and generate a very small current. This current was enhanced by the gain amplifier and gives a measurable signal on the multimeter.

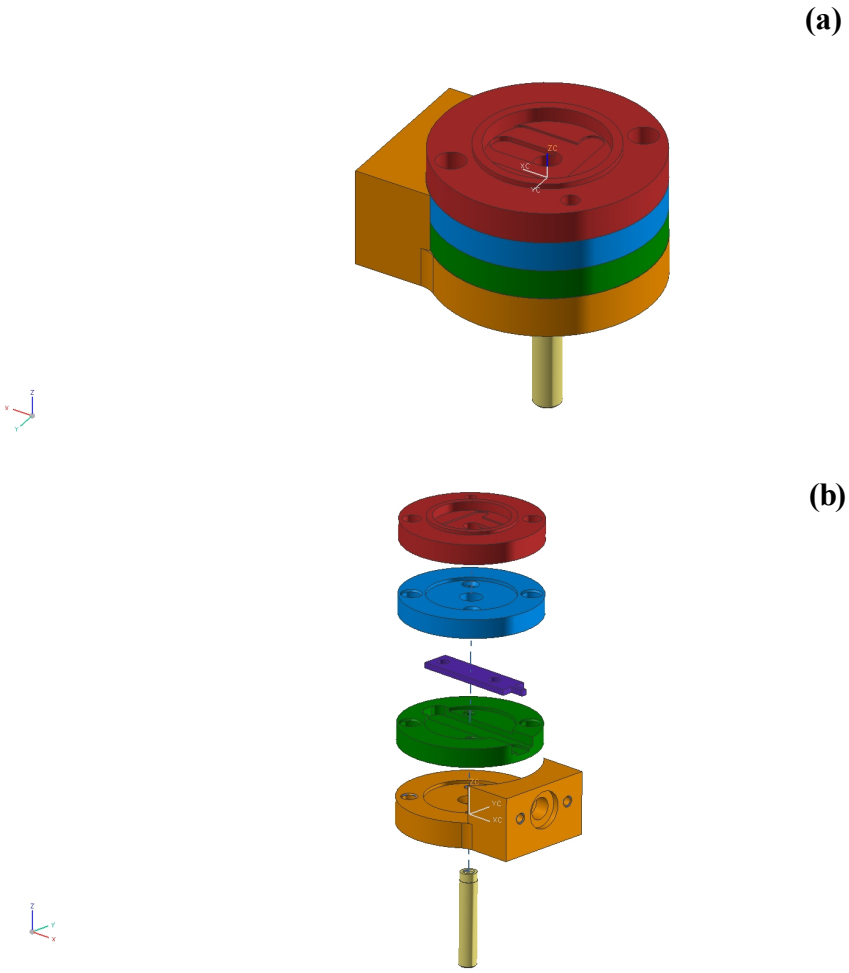

Figure 5.43: (a) The assembled stage. (b) Exploded cross section of the sample holder showing the order in which it is put together. From top to bottom: sample holder, PEEK layer, copper collection plate, PEEK layer and the base.

The gain was $1x10^9$,when the ion beam milled through the mask-sample, there was an observable signal of a few mV. When the beam first breaks through there is a sharp increase in the measured signal that continues to increase whilst the beam is still

breaking through. The detector allowed us to determine when all of the material had been removed because the signal would plateau. The size of the signal depended on the beam current and the size of the reference hole (fig. 5.44). The beam current used for the different references were as follows: 0.1 nA for the 5 and 2 μm references, 50 pA for the 1μm and 30 pA for the 500, 200 and 100 nm reference holes. The measured signal increases as the reference hole diameter increases and is easily distinguishable from the background signal even for the 100 nm reference. The reference holes are shown in fig. 5.45. Figure 5.45(a) shows the top of the Au film and 5.45(b) the underside of the Ag capping layer. The reference holes are circular and of a similar size either side of the mask-sample. The sample holder allows the user to explicitly know when they have removed all the material allowing the creation of well defined reference holes.

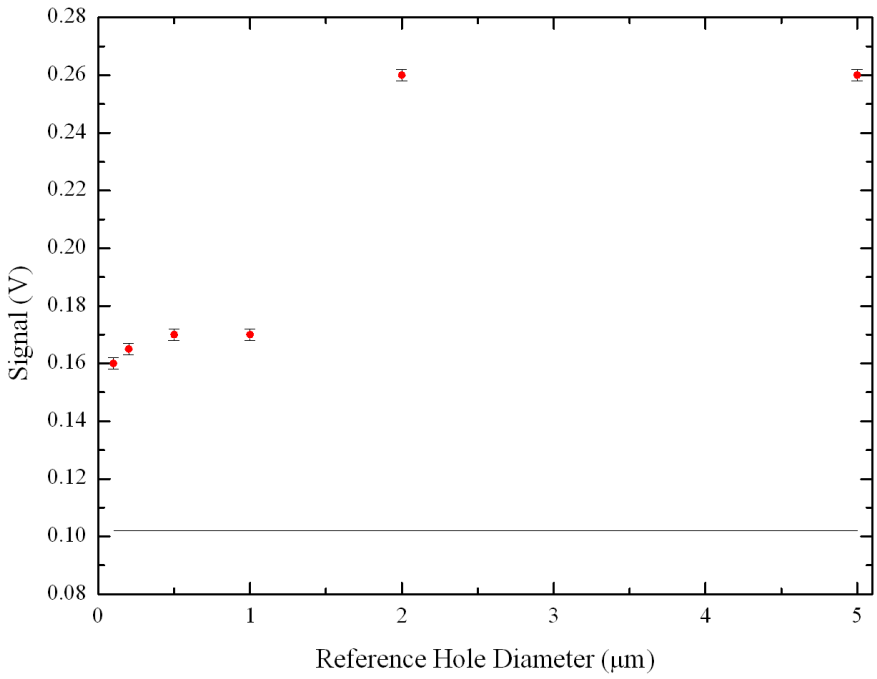

Figure 5.44: The observed signal for the various diameters of reference hole. The black line represents the constant background of the multimeter.

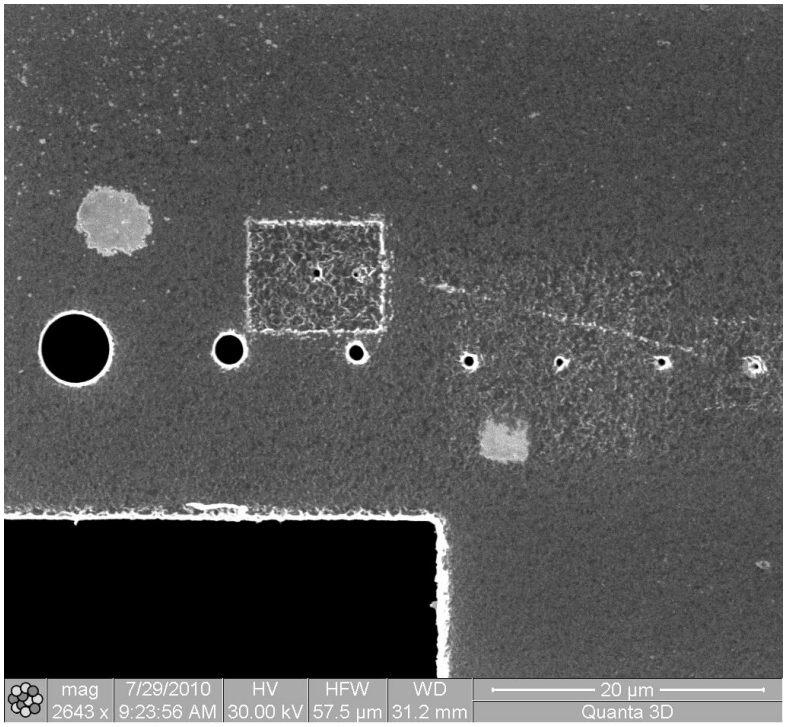

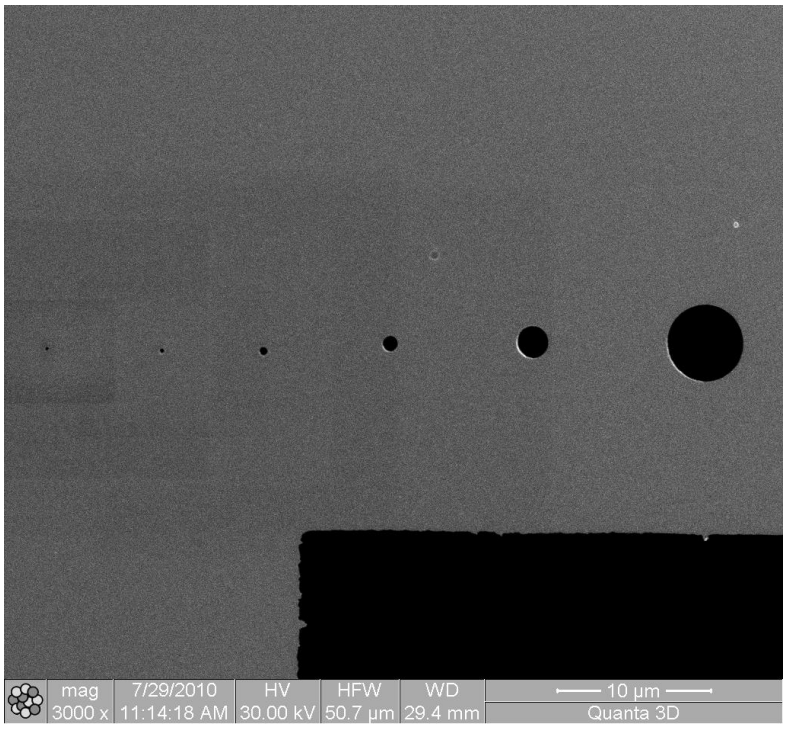

Figure 5.45: The various reference holes for (a) the top side; the diameters from left to right are: 5, 2, 1, 0.5, 0.2 and 0.1 µm. (b) The underside. The reference holes were observable in this instance, because a large 'T' structure was milled through the entire structure, and the reference holes' position known in relation to this structure.

5.10 Conclusion

The branchline at I06 is capable of performing lensless FTH. The custom built holography chamber has several advantages noticeably in its simplicity and its cheapness to build. The obtained holograms were limited by CCD noise and the quality of the sample. The CCD needs to have a high dynamic range so saturation does not occur. The readout noise can be reduced in future experiments by cooling an in-vacuum CCD. Although, the data was affected by these issues, it can be improved by considering the methods discussed in the chapter. Beamline I06 now has a peltier cooled, Princeton CCD. In follow up experiments this will be used and the next step is to motorise the sample, pinholes and photodiode.

The inability of the the phase retrieval algorithms to yield better images of the reconstructions appears to be a result of the imperfect data, where both high and low frequencies are missing from our holograms. The patching of the saturated pixels is also a source of error. The quality of the reconstructions can be improved by scaling the intensities of the estimated hologram to the measured one and replacing the missing regions of the measured hologram with those from the estimate. The features of the object can be observed after approximately 100 iterations but there is no significant with further iterations.

The quality of the samples were greatly effected by the thickness of the gold mask. The thicker gold masks are better at reducing the transmission of X-rays albeit at the expense of an increased number of stubborn grains and severe difficulties in creating the reference holes. Creation of well defined reference holes is guaranteed by measuring the current of the ion beam. If the drift in the FIB can be overcome, then the reference holes will only be limited by the size of the ion beam, which is approximately 10 nm at 30 kV and 1 pA. This would mean that the reference hole would be a factor of five to ten times smaller than current methods; meaning the resolution of lensless FTH would be approaching the diffraction limit. This would allow for the measurement of the magnetism of individual clusters in films instead of just domains.

Chapter 6

Conclusions and Future Work

6.1 Summary

6.1.1 Commissioning of Beamline I07

Beamline I07 at the Diamond Light Source was commissioned by comparing the intensity profile of a CTR measured using various techniques under identical conditions on a (2+3)-type diffractometer with *z*-axis geometry. The three methods used were stationary, rocking and constant velocity scans. The overall discrepancies between the various methods are nearly always within the corresponding statistical error bars. If the systematic error is included, which is typically 10-15%, then the differences all fall within the error. This validates all three modes for crystallographic purposes. The use of an area detector instead of a point detector in X-ray diffraction experiments has greatly improved reliability and greatly improved the data acquisition rate by almost an order of magnitude.

6.1.2 Bicrystal Truncation Rods

An X-ray scattering experiment was performed on beamline I07 at the Diamond Light Source. Previous studies have examined the crystallography the Si Σ13 symmetric tilt GB and several periodic, fully four-fold coordinated GB structures were proposed by Morris et al. In order to ensure physically realistic structures a Keating energy minimisation was performed with over 400 atoms in each simulation. Unlike the first-principle calculations of the GBs, there is no correlation between the Keating energy and structure.

The bicrystallography of the Si Σ13 symmetric tilt GB gave rise to two overlapping CTRs, one from each crystal. The CTR notation was modified to account

for this and a model developed for BCTRs, where the crystals were truncated at the interface. To model X-ray scattering from this interface three regions were considered; bulk like top and bottom Si crystals and an interface region. The simulated scattering was not only sensitive to the atomic coordinates of the GB but also on the interference between the contributions from the two crystals, which depended sensitively on the separation between them. The potential grain boundary structures were discriminated against based on the statistical goodness of fit and we find that structure (a) proposed by Morris ., gives an outstanding agreement with the measured data, proving that this is our GB.

6.1.3 Fourier Transform Holography

A custom built diffraction chamber for performing lensless soft X-ray FTH experiments was designed and commissioned on the branchline of beamline I06 at the Diamond Light Source. Our reconstructions are severely limited by the poor dynamical range and high noise levels of the CCD used, however the observable features have approximately 40 nm resolution.

A hybrid approach, performed by applying phase retrieval algorithms to the measured FTH data, is applied with limited success. The cross-correlation terms are used as a support mask and within a few iterations one of these terms disappears. We are unable to resolve the features of the reconstruction, which are lost due to phase retrieval algorithms inability to deal with high noise levels, unless the missing sections from the measured hologram are replaced by that of the estimated one.

The inconsistencies in creating the reference holes are overcome by using a custom built sample holder that measures the time evolution of a signal that is generated when the ion beam impinges on a copper plate. When the signal plateaus then all of mask-sample has been removed. This signal could be used to create reference holes that are smaller than the resolution limit of the SEM or FIB provided the drift of the microscopes can be overcome.

6.2 Future Work

6.2.1 Soft X-ray Holographic Microscopy

Although the integrated mask-sample design is crucial for lensless FTH it has limited use in microscopy because the object position is fixed and only one region of the sample can be viewed. This limitation has been overcome by Stickler et al. [101]. Their approach is to separate the mask and the sample using two Si_3N_4 membranes, their set-up shown in fig. 6.1. The mask is grown in much the same manner as before: a thick Au film is deposited on the membrane and then the object and reference are machined through it using a FIB. This process has several advantages: the preparation of the mask is much simpler, as the object no longer needs to finish at the membrane, and the object position is no longer fixed and observation is possible anywhere along the sample.

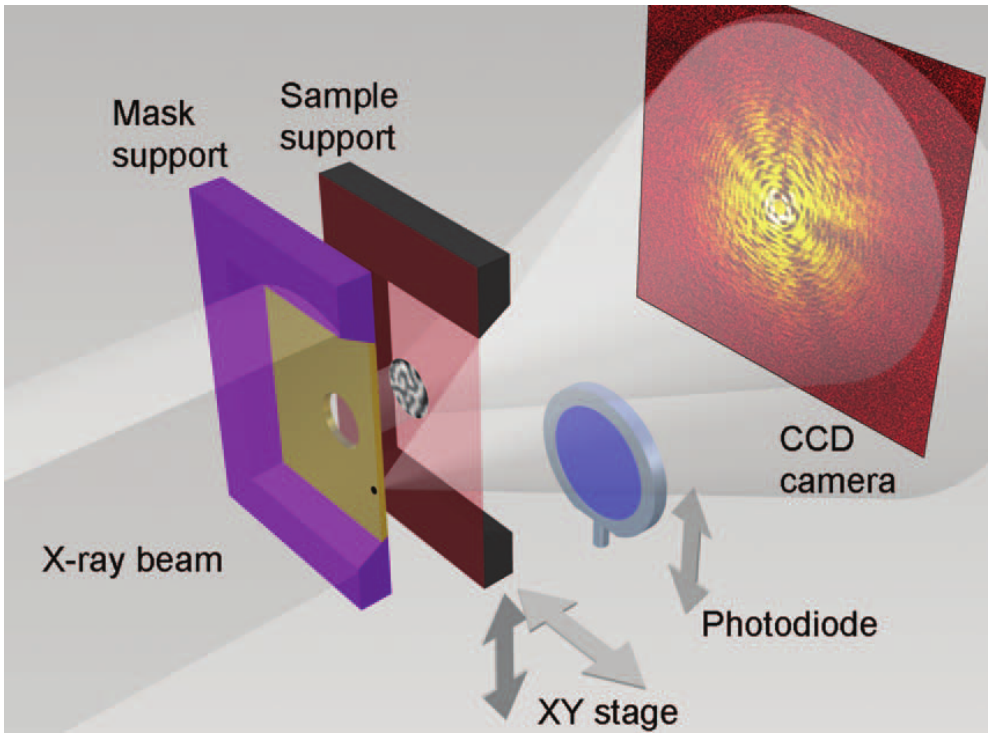

Figure 6.1: Schematic of the X-ray holographic microscopy set-up. The membrane with the mask support is fixed in the centre of the X-ray beam. The second membrane, which has the sample, is free to move in the plane perpendicular to the beam. After [101].

6.2.2 Soft X-ray Ptychography

Despite promising results obtained using phase retrieval algorithms there are limitations when applied to X-ray microscopy. To retrieve a unique set of phases most algorithms require the object to be very small and of a finite extent so that the corresponding highly detailed coherent diffraction pattern can be adequately sampled by the detector. Therefore, obtaining a low-resolution overview of a comparably large area and then zooming into a region of interest – a standard procedure in microscopy- is not feasible [102].

Ptychography is an extension of the iterative phase retrieval methods. The experimental approach of this technique is to collect a number of Fraunhofer diffraction patterns, each of which comes from a different, but overlapping, region of the specimen which is moved laterally across the beam [103]. An aperture is placed in real space over an object. In the Fraunhofer diffraction plane each pattern is now convoluted with the Fourier transform of the aperture function. In one-dimension the aperture acts a top hat function, and the diffracted peaks are convoluted with sinc functions [103]. At their point of overlap the sinc functions add according to the complex values determined by the phase of the underlying diffracted beams. This method is known as ptychography. The pytchographic phase data is pieced together to form a large field of view and by using the ptychographical iterative engine [104] the object is reconstructed within a few iterations

Appendix

A.1 Fourier Transformations

A.1.1. The Fourier Transform

The Fourier transform $F(k)$ of a one-dimensional function $f(x)$ is given by

$$F(k)=\int_{-\infty}^{\infty} f(x)e^{-2\pi ikx}dx=\mathcal{F}\left[f(x)\right] \quad , \text{(A.1.1)}$$

where $\mathcal{F}$ denotes the Fourier transform. The inverse Fourier transform is given by

$$f(x)=\int_{-\infty}^{\infty} F(k)e^{2\pi ikx}dk \quad . \text{(A.1.2)}$$

A.1.2. The Convolution Theorem

The convolution of two functions, $f(x)$ and $g(x)$, where the convolution operator is denoted by *, is given by

$$f(x)*g(x)=\int_{-\infty}^{\infty} f(x)\,g(x'-x)dx \quad . \text{(A.1.3)}$$

If a Fourier transform is applied, then

$$\mathcal{F}\left[f(x)*g(x)\right]=F(k).G(k) \quad . \text{(A.1.4)}$$

A.1.2. Auto- and Cross-Correlations

The correlation operator is denoted by $\star$. The cross-correlation of two functions is given by

$$f(x) \star g(x) = \int_{-\infty}^{\infty} f^*(x) g(x' + x) dx \quad , \text{(A.1.5)}$$

where $f^*(x)$ is the complex conjugate of $f(x)$, or, in terms of the Fourier transform is given by

$$\mathcal{F}\left[f(x) \star g(x) \right] = F^*(k) . G(k) \quad . \text{(A.1.6)}$$

The correlation of a function with itself, the autocorrelation, is given by

$$\mathcal{F}\left[f(x) \star f(x) \right] = |F(k)|^2 \quad . \text{(A.1.7)}$$

A.2 Correction Factors

A.2.1 Differential Cross-Section

Once the integrated intensities have been measured the structure factors, $|F_{hkl}|$, are obtained by applying various correction factors to the integrated intensities that are dependent on the type of diffractometer and the scan type used [43, 44]. The correction factors are derived from first principles by Vlieg (1997) and are are presented by Vlieg (1998) for a (2+3)-type diffractometer. In an ω-scan the integrated intensity can be measured using a sufficiently wide detector acceptance and by rocking the sample over the entire width of the reflection. The detector opening angles are $\Delta\gamma$ and $\Delta\psi$ (fig. A.2.1). The integrated intensity of an ω-scan is

$$I_\omega = \frac{\Phi_0}{\omega_0} \int \left(\frac{d\sigma}{d\Omega} \right) d\gamma \, d\psi \, d\omega \quad , \text{(A.2.1)}$$

where Φ_0 is the incident flux (photon s^{-1} mm^{-2}), ω_0 is the rotation speed and $d\sigma/d\Omega$ is the differential scattering cross-section which is given by

$$\frac{d\sigma}{d\Omega} = r_e^2 \left(\frac{A}{A_u} \right) P\, u(\mathbf{q}) \quad , \text{(A.2.2)}$$

where A is the active surface area, A_u is the area of the unit cell, r_e is the classical electron radius, P is the polarisation factor, $u(\mathbf{q})$ is a function that describes the line shape of a diffraction peak ($\mathbf{q}$ is the momentum transfer) and is normalised in such a manner that integration over h and k is unity.

For a stationary scan the detector accepts the rod over the entire in-plane direction, albeit over a range of l values. It is assumed that the structure factor is approximately constant over the probed l range. The integrated intensity for the stationary scan is given by

$$I_s = \Phi_0 T \int \left(\frac{d\sigma}{d\Omega} \right) d\gamma\, d\psi \quad \text{(A.2.3)}$$

where T is the counting time.

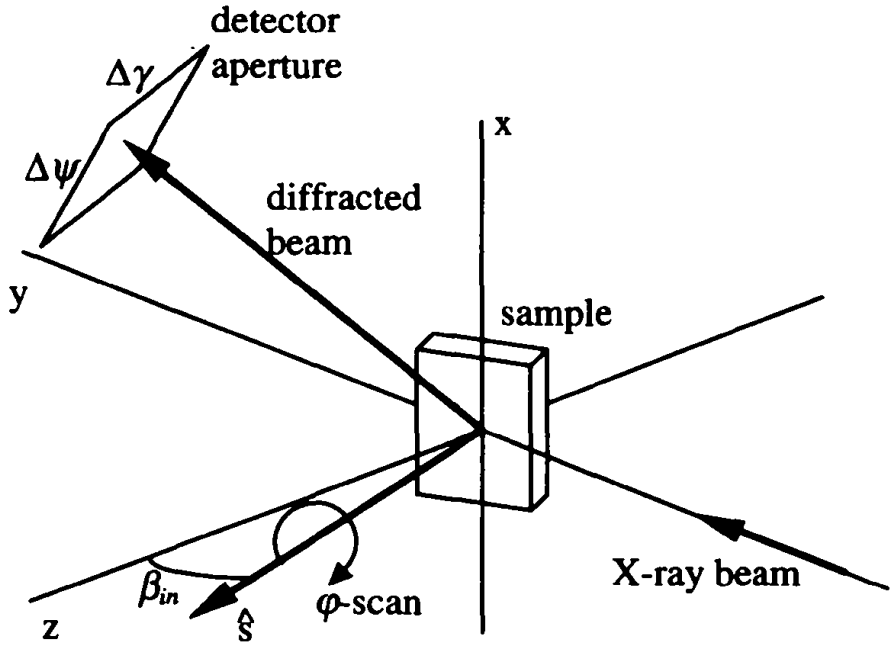

(*a*)

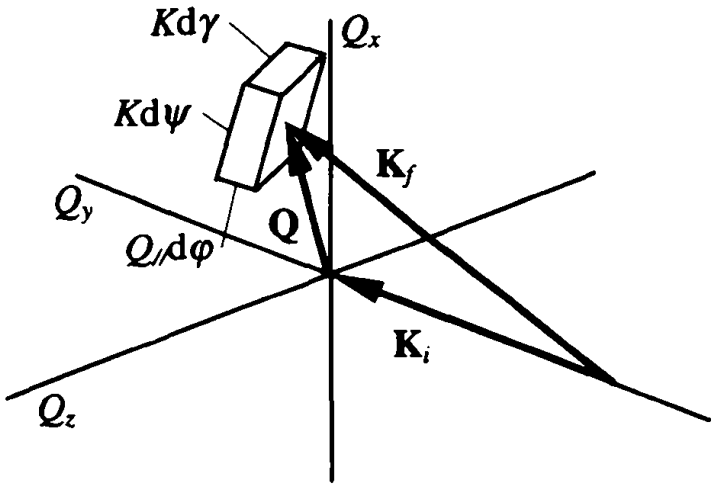

(*b*)

Figure A.2.1: A schematic picture of a rocking scan. (a) The situation in real space. The detector has opening angles $\Delta\gamma$ and $\Delta\psi$. The surface normal $\hat{\mathbf{s}}$ lies in the *yz* plane and makes an angle β_{in}, with the *z* axis of the laboratory frame. A rocking scan is performed by a φ rotation about $\hat{\mathbf{s}}$. (b) The integration volume shown in reciprocal space. After [43].

A.2.2 Lorentz Factor

Since $d\sigma/d\Omega$ is expressed in terms of **q** the angular integration variables in (A.2.1) and (A.2.3) need to be changed into reciprocal space ones. The geometrical correction in integration volume is the Lorentz factor. After some derivation Vlieg obtains the following reciprocal space integration variables:

$$d\gamma\, d\psi\, d\omega = \left(\frac{\lambda^3}{V_u}\right)\left(\frac{1}{\sin\delta_z \cos\gamma_z}\right) dh\, dk\, dl \quad , (A.2.4)$$

and

$$d\gamma\, d\psi = \left(\frac{\lambda^2}{A_u}\right)\frac{1}{\sin\beta_{out}}\, dh\, dk \quad , (A.2.5)$$

where V_u is the volume of the unit cell and λ is the wavelength. The Lorentz factor of the rocking and stationary scans is the angle-dependent parts of equations (A.2.4) and (A.2.5) respectively, and are shown below in the z-axis and (2+2)-circle geometries

$$L_\omega = \frac{1}{\sin\delta_{2+2}} = \frac{1}{\sin\delta_z \cos\gamma_z} \quad , (A.2.6)$$

$$L_s = \frac{1}{\sin\beta_{out}} = \frac{1}{\cos\delta_{2+2}\sin\gamma_{2+2}} = \frac{1}{\sin\gamma_z} \quad , (A.2.7).$$

A.2.3 Rod Interception

Vlieg assumes that F_{hkl} is approximately constant over the integration intervals in *h*, *k* and *l*. Along the *h* and *k* directions this is always true, since the profile is sharp along these directions (this is determined by $u(\mathbf{q})$). Along *l* the diffraction features are rod-like and it is necessary to restrict the experimental integration interval such that a meaningful measurement is made. In (A.2.1) the integration range has the constant

value $\Delta\gamma$ regardless of the angular settings of the diffractometer. However, when the integration variables are changed there is also a change in the integration range and Δl is not constant. In the general case we need to evaluate exactly which range of l values is accepted by the detector. This is determined by calculating for which l values the (hk) diffraction rod cuts the detector acceptance at the values $\pm\Delta\gamma/2$. During a rocking scan the (hk) rod will trace a plane so the intersection of this plane with the lines defining the detector aperture at $\pm\Delta\gamma/2$ needs to be calculated. After some lengthy derivation the following is obtained

$$\Delta l = C_{rod}\,\Delta l_0 \quad , \text{(A.2.8)}$$

where Δl_0 is the l range for zero incoming and outgoing angles (fig. A.2.2) and

$$C_{rod} = \cos\beta_{out} \quad . \text{(A.2.9)}$$

There is no correction for the interception of the rod in the stationary mode as the detector accepts the rod over the entire in-plane direction.

A.2.4 Area Correction

The equations for the integrated intensities contain an active surface area A. This area is determined by slits in the incoming beam and in front of the detector (fig A.2.3). The area correction is

$$C_{area} = \frac{\cos\beta_{out}}{\sin\delta_{2+2}} = \frac{\cos\beta_{out}}{\sin\delta_z \cos\gamma_z} \quad , \text{(A.2.10)}$$

and the illuminated area is this multiplied by s_1 and s_2.

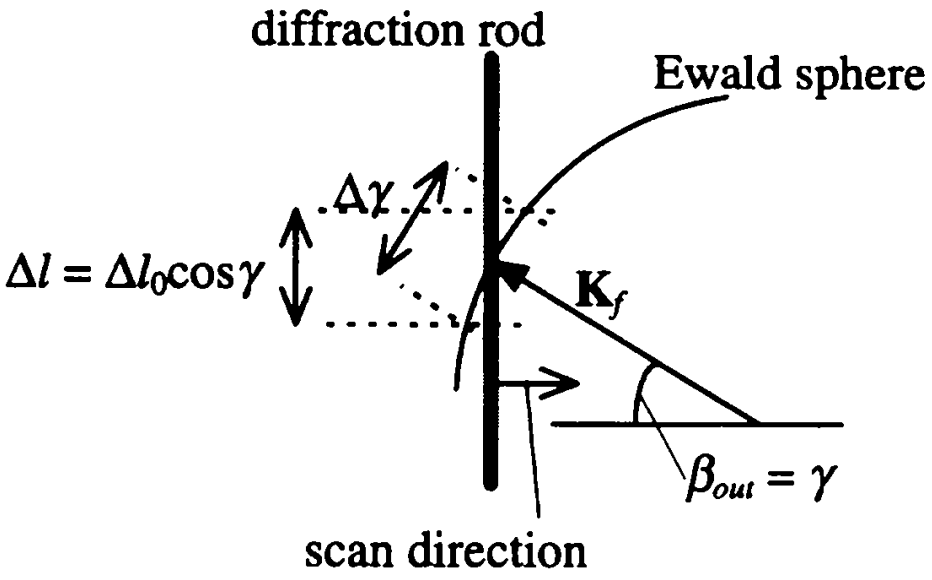

Figure A.2.2: The effect of the outgoing angle β_{out} in the z-axis mode on the amount of integrated rod. In this mode $\Delta l = \Delta l_0 \cos\gamma$, with Δl_0 the l range for zero incoming and outgoing angles. After [43].

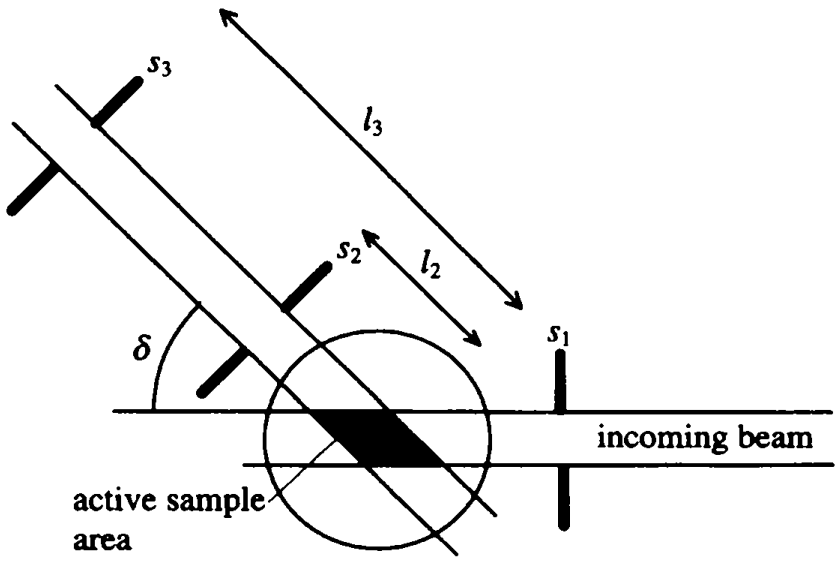

Figure A.2.3: View of the surface plane to showing the illuminated area defined by the slits in the incoming and outgoing beams. After [43]

A.2.5 Polarisation Factor

The polarisation factor, *P*, assuming complete horizontal polarisation is

$$P = 1 - \sin^2 \gamma_{2+2} \cos^2 \delta_{2+2} = 1 - \sin^2 \gamma_z \quad . \text{(A.2.11)}$$

A.2.6 Absorption correction

The X-ray beam is attenuated as it passes through the sample. The sample has a total thickness of *D* (fig. A.2.4). Before the X-rays are scattered they a distance *X* through the bicrystal. From the Beer-Lambert law the intensity of the beam, *I*, has decreased by the following amount

$$I = \exp(-\mu X) \quad , \text{(A.2.12)}$$

where is μ the attenuation coefficient. The X-rays scatter from the sample at a thickness of *D*-*X*. The direction of the beam then changes and the length the X-rays travel before they exit the bicrystal is (*D*-*X*)/cosβ_{out}. The attenuation after the beam has been scattered is then given by

$$I = \exp\left(\frac{-\mu(D-X)}{\cos\beta_{out}}\right) \quad . \text{(A.2.13)}$$

The total attenuation is the product of the attenuation of the beam before and after scattering and is integrated over the entire width of the bicrystal:

$$I = \exp\left(\frac{-\mu D}{\cos\beta_{out}}\right) \int_0^D \exp\left(-\mu X\left(1 - \frac{1}{\cos\beta_{out}}\right)\right) dX \quad . \text{(A.2.14)}$$

After integrating this and after some rearrangement the absorption correction is obtained and is given by the following:

$$C_{atten} = \frac{\exp\left(\frac{-\mu D}{\cos\beta_{out}}\right)}{\mu\left(1-\frac{1}{\cos\beta_{out}}\right)}\left[1-\exp\left(-\mu D\left(1-\frac{1}{\cos\beta_{out}}\right)\right)\right] \quad . \text{(A.2.15)}$$

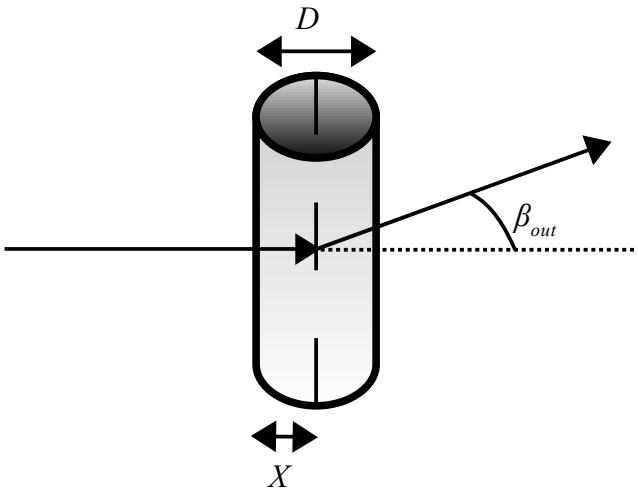

Figure A.2.4: Illustration of the path (denoted by the arrows) the X-ray beam takes through the bicrystal before and after it is scattered.

The structure factors are extracted from the integrated intensities by using either equation (3.4) or (3.5) depending on the scan type used.

A.3 Reciprocal Lattices

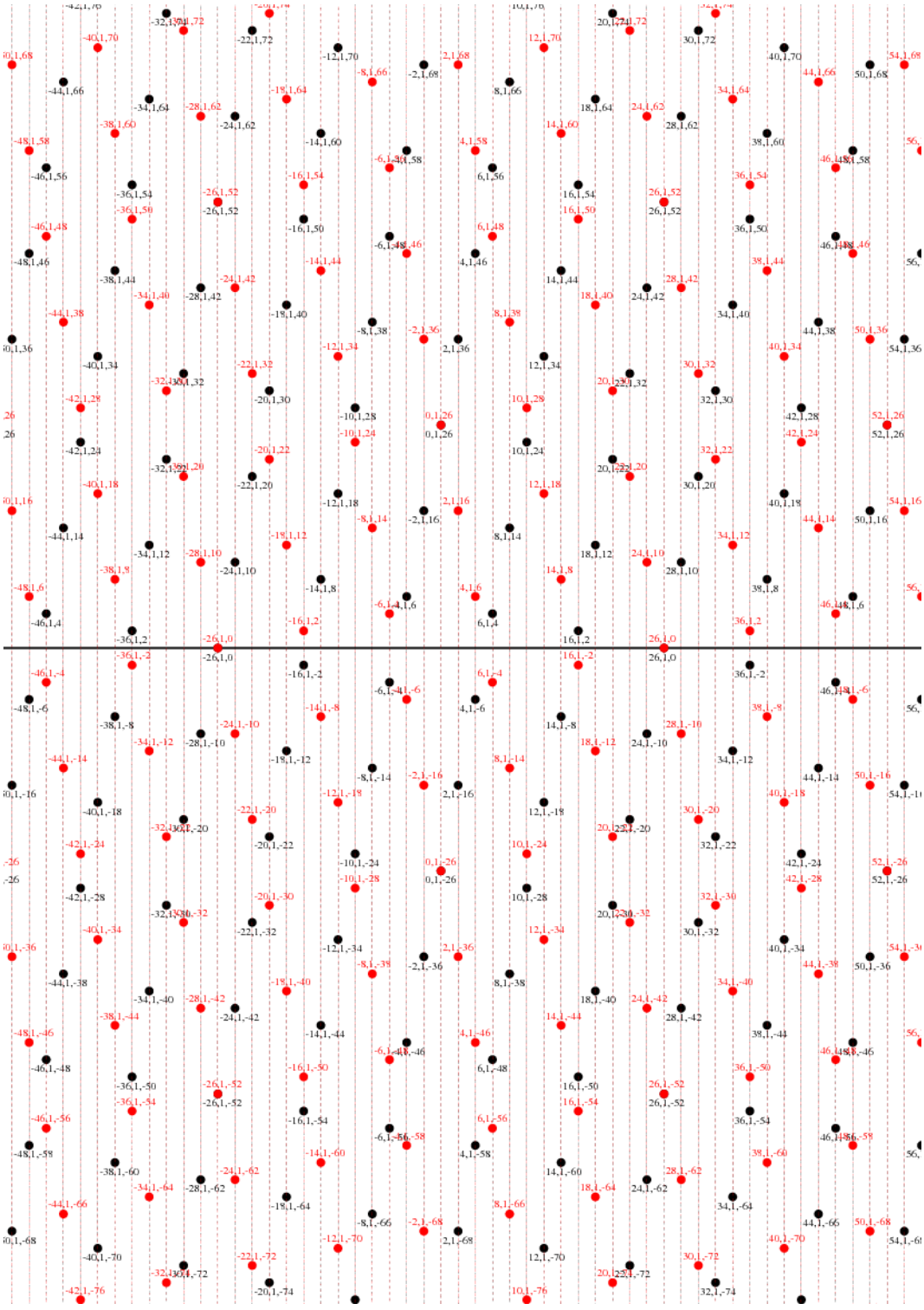

Figure A.3.1: Reciprocal lattice for the $K = 1$ plane. The black and red dots represent the Bragg peaks from the top and bottom crystals respectively.

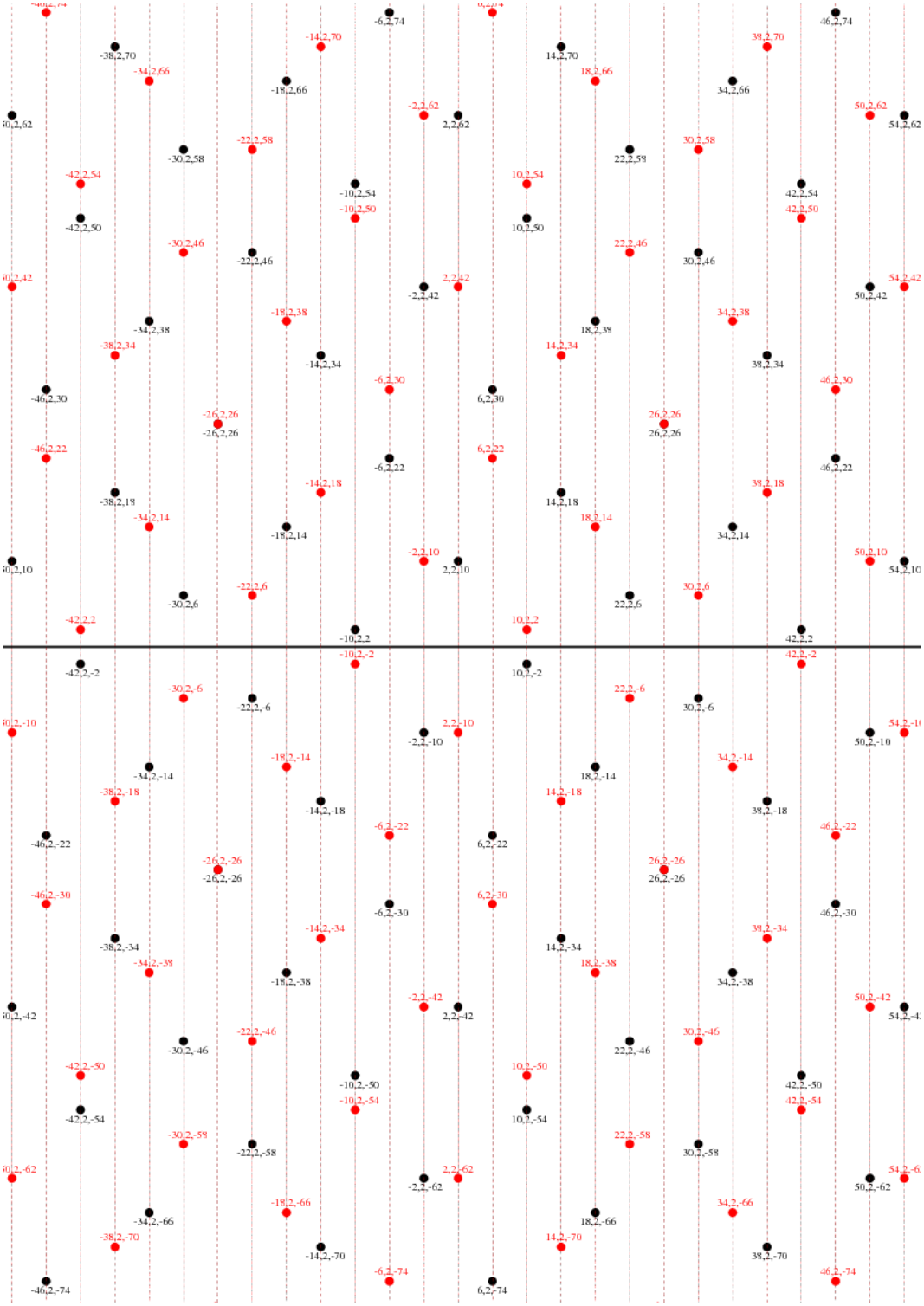

Figure A.3.2: Reciprocal lattice for the $K = 2$ plane.

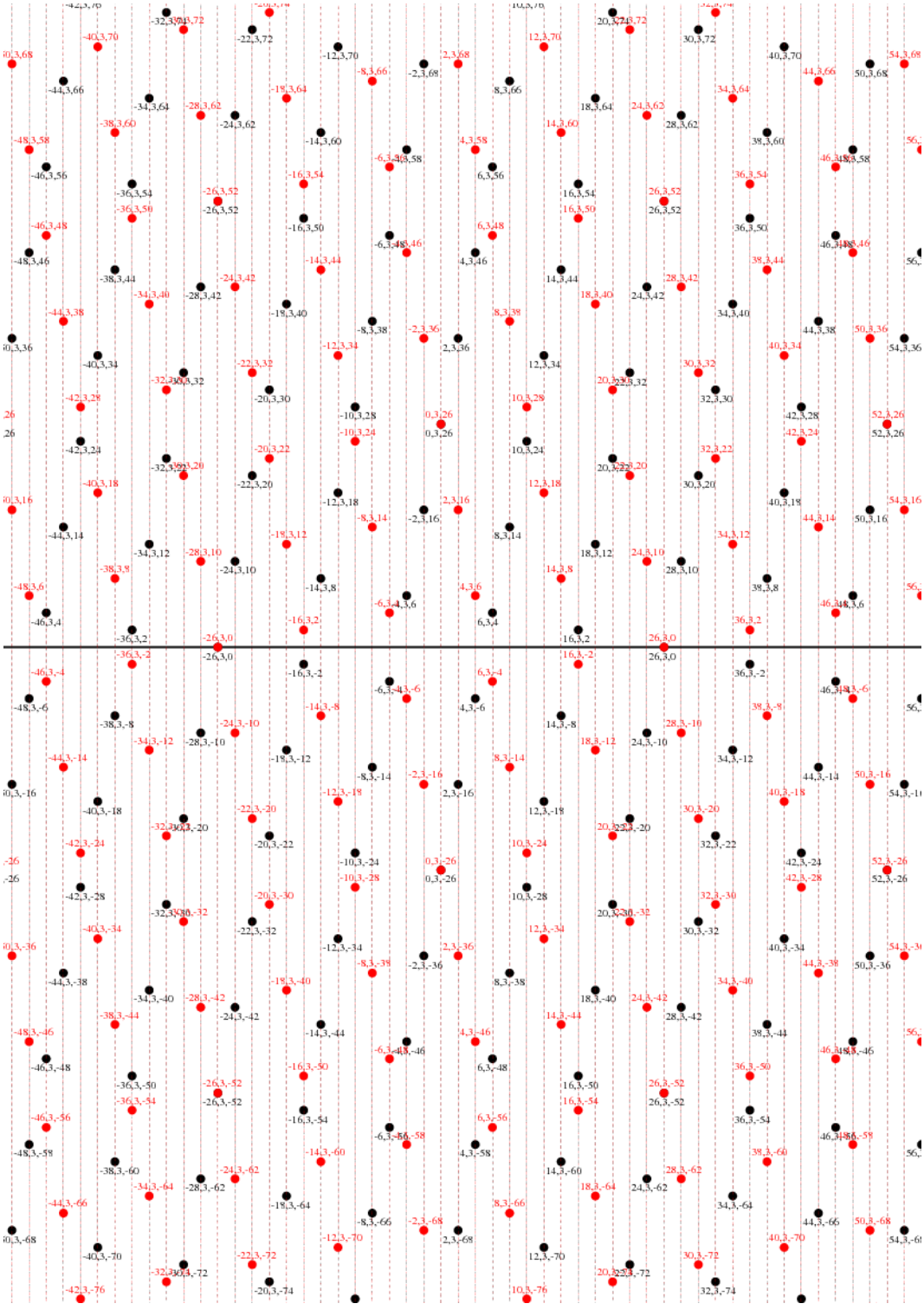

Figure A.3.3: Reciprocal lattice for the $K = 3$ plane.

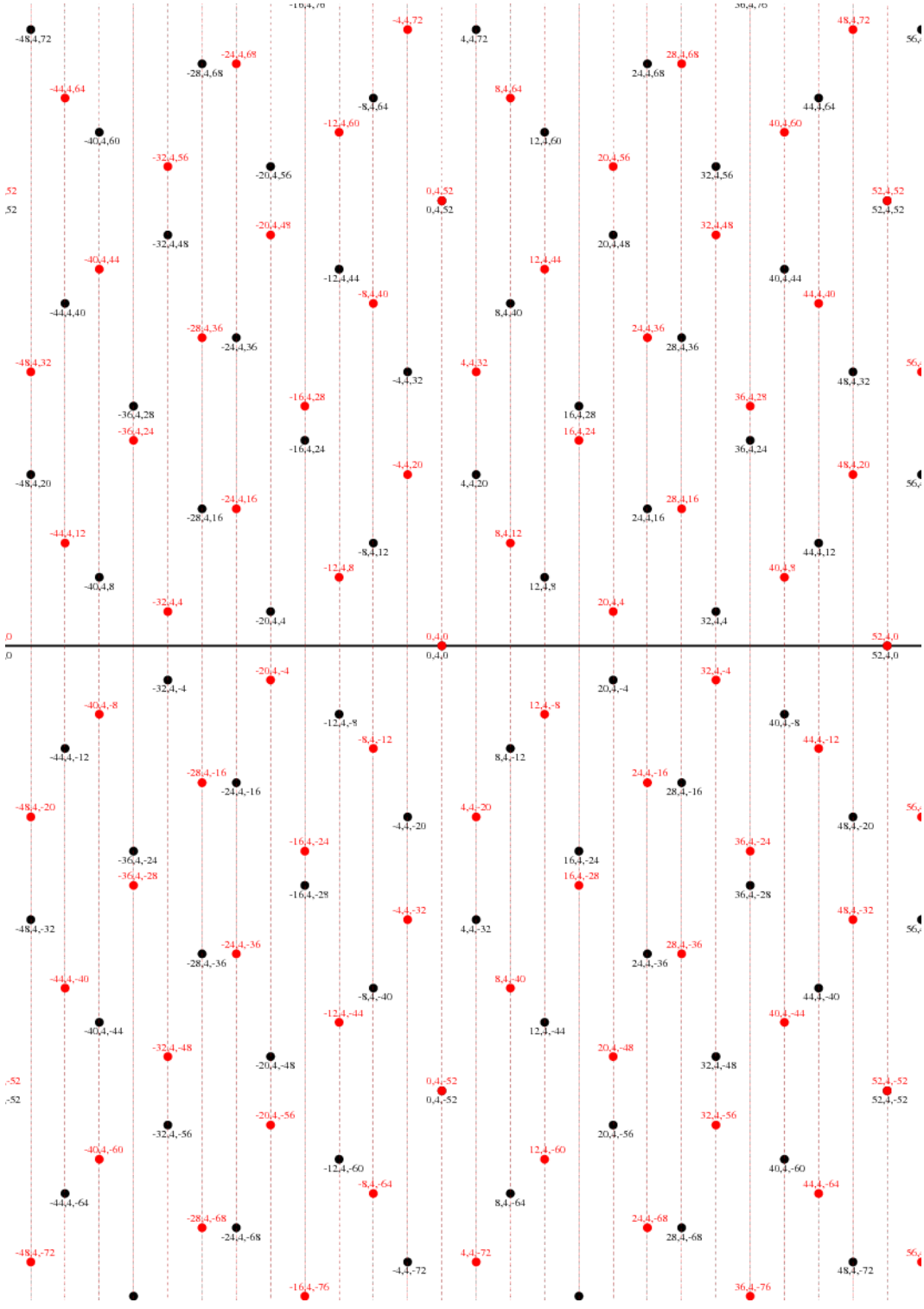

Figure A.3.4: Reciprocal lattice for the $K = 4$ plane

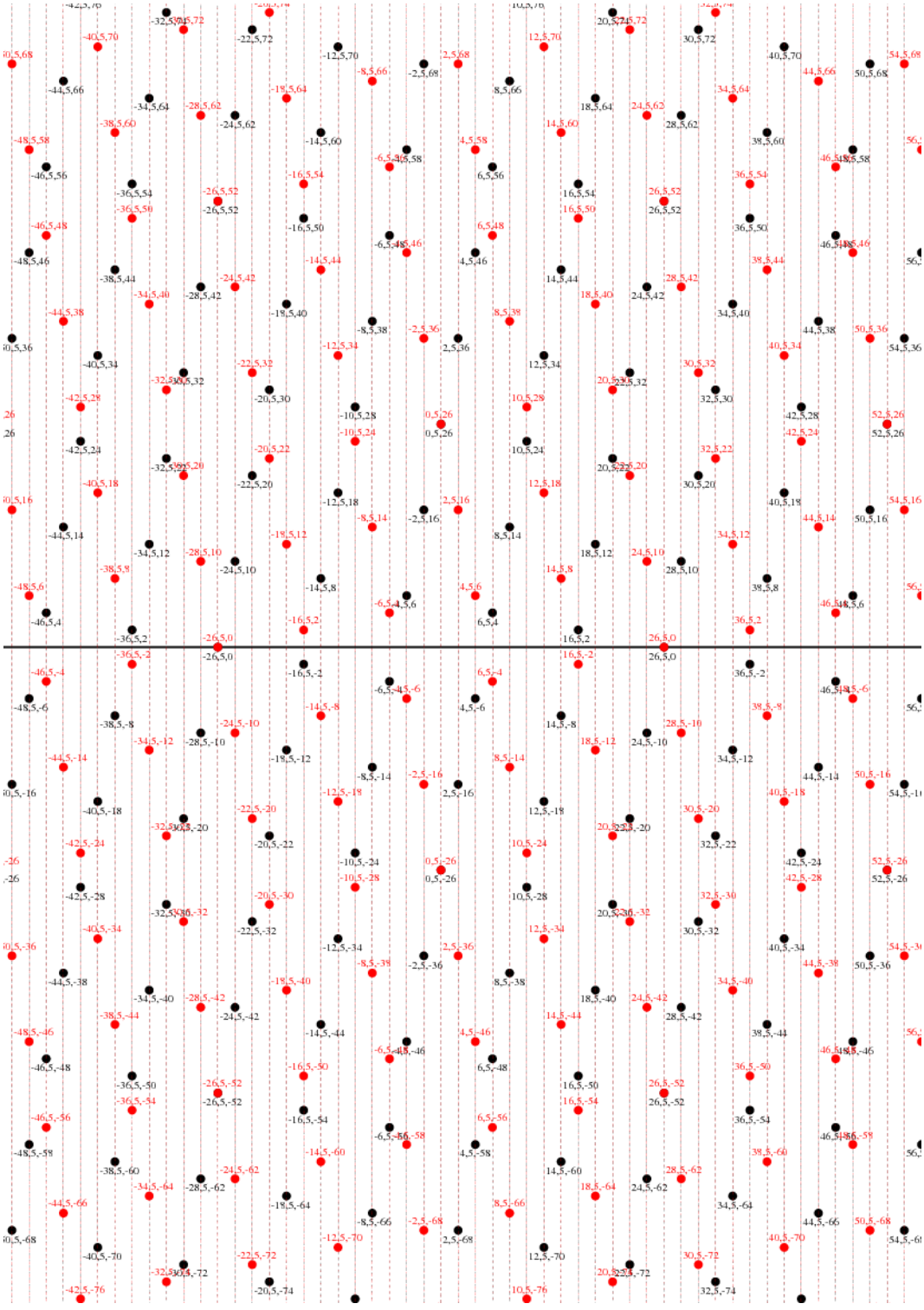

Figure A.3.5: Reciprocal lattice for the $K = 5$ plane.

A.4 Model Evaluation

The calculated scattering is given on a relative scale as the incoming flux of photons I_0 in equations (3.4) and (3.5) is not known accurately. The quality of the proposed scattering can be evaluated by comparing the calculated scattering with observed, allowing a scale-factor to vary. This is often done by calculating

$$\chi^2 = \frac{1}{N-p} \sum_L \frac{\left(a\left|F_{HKL}^{calc}\right| - \left|F_{HKL}^{expt}\right|\right)^2}{\sigma_{HKL}^2} \quad , \text{(A.4.1)}$$

where N is the number of measured points, p is the number of free parameters, σ_{HKL} the experimental uncertainty and a is the scale-factor to be varied. The scale factor that minimises χ^2 is found by differentiating χ^2

$$\frac{d\chi^2}{da} = \frac{1}{N-p} \frac{\sum_L 2a\left|F_{HKL}^{calc}\right|^2 - 2\left|F_{HKL}^{expt}\right|\left|F_{HKL}^{calc}\right|}{\sigma_{HKL}^2} = 0 \quad , \text{(A.4.2)}$$

which after some rearranging gives

$$a = \frac{\sum_L \left|F_{HKL}^{expt}\right|\left|F_{HKL}^{calc}\right|}{\sum_L \left|F_{HKL}^{calc}\right|^2} \quad . \text{(A.4.3)}$$

Equation (A.4.1) is minimised upon insertion of equation. (A.4.3). When $\chi^2 \approx 1$ the experimental scattering is within uncertainties equal to the calculated, and the model is considered satisfactory.

Bibliography

[1] J. Hornstra, Physica **25**, 409 (1959).

[2] J.R. Morris, Z.-Y. Lu, D.M. Ring, J.-M Xiang, K.-M. Ho and C.Z. Wang, Physical Review B **58**, 11241 (1998).

[3] A.P. Sutton and R.W. Balluffi, *Interfaces in Crystalline Materials,* (Oxford University Press, Oxford, 1995).

[4] C.R.M. Grovenor, J. Phys. C: Solid State Phys. **18**, 4079 (1985).

[5] A. Maiti, M.F. Chisholm, S.J. Pennycook and S.T. Pantelides, Phys. Rev. Lett. **77**, 1306 (1996).

[6] J.J. Bacmann, A.M. Papon, M. Petit and G. Silvestre, Philos. Mag. A **51**, 697 (1985).

[7] A.P. Sutton, Polycrystalline Semiconductors II **54**, 116 (1991).

[8] A. Lamzatouar, M. El Kajbaji, A. Charai, M. Benaissa, O.B.M. Hardouin Duparc and J. Thibault, Scripta Materialia **45**, 1171 (2001).

[9] H. Sawada, H. Ichinose and M. Kohyama, Journal of Electron Microscopy **51**, 353 (2002).

[10] H. Sawada, H. Ichinose and M. Kohyama, Scripta Materialia **51**, 689 (2004).

[11] M.J. Kim, R.W. Carpenter, Y.L. Chen and G.H. Schwuttke, Ultramicroscopy **40**, 258 (1992).

[12] M. Kohyama and R. Yamamoto, Physical Review B **49**, 17102 (1994).

[13] M. Kohyama, Phys. Status Solidi B **141**, 71 (1987).

[14] A.T. Paxton and A.P. Sutton, J. Phys. C **21**, L481 (1988).

[15] A.A. Levi, D.A. Smith and J.T. Wetzel, J. Appl. Phys. **69**, 2048 (1991).

[16] J. Miao, P. Charalambous, J. Kirz and D. Sayre, Nature **400**, 342 (1999).

[17] W. Chao, B.D. Harteneck, J.A. Liddle, E.H. Anderson ans D.T. Attwood, Nature **435**, 1210 (2005).

[18] D. Sayre and H. Chapman, Acta Cryst. **51**, 237 (1995).

[19] J. Kirz, C. Jacobsen and M. Howells, Q. Rev. Biophys. **28**, 33 (1995).

[20] S. Eisebitt, J. Lüning, W.F. Schlotter, M. Lörgen, O. Hellwig, W. Eberhardt and J. Stöhr, Nature **432**, 885 (2004).

[21] W.F. Schlotter, PhD Thesis, Department of Applied Physics, University of Stanford, America (2007).

[22] B.E. Warren, *X-Ray Diffraction*. Addison-Wesley, Reading, MA. (1969)

[23] J. Als-Nielsen and D. McMorrow, *Elements of modern X-ray physics.* Wiley, Chichester (2001).

[24] R. Feidenhans'l, Surface Science Reports, **10**, 105 (1989).

[25] *International Tables for Crystallography*, Volume C, edited by A.J.C. Wilson and E. Prince, Kluwer Academic Publishers, Dordecht (1999).

[26] I.K. Robinson, Physical Review B, **33**, 3830 (1986).

[27] R.C. Pond and W. Bollmann, Phil. Trans. R. Soc. Lond. A, **292**, 449 (1979).

[28] R.C. Pond, *Dislocations and Properties of Real Materials* (The institute of metals), 71 (1985).

[29] R.C. Pond and D.S. Vlachavas, Proc. R. Soc. Lond., A**386**, 95 (1983).

[30] L. Sagalowics and W.A.T. Clark, Philosophical Magazine A, **72**, 545 (1995).

[31] R.C. Pond, *Dislocations in Solids*, edited by F.R.N. Nabarro, Vol. 8 (New York: North-Holland), chap. 38 (1989).

[32] S. Ranganathan, Acta Cryst., **21**, 197 (1966).

[33] J.M. Burgers, Proc. Phys. Soc., **52**, 23 (1940).

[34] W.T. Read, *Dislocations in Crystals*, McGraw-Hill Publishing, New York (1953).

[35] http://www.tf.uni-kiel.de/matwis/amat/def_en/kap_5/backbone/r5_1_3.html

[36] J. Weertman and J.R. Weertman, *Elementary Dislocation Theory*, the Macmillan company, New York (1964).

[37] R.J. Collier, C.B. Burckhardt and L.H. Lin, *Optical Holography*, Academic Press, New York (1971).

[38] J.B. DeVelis and G.O. Reynolds, *Theory and Applications of Holography*, Addison-Wesley, Reading, Massachussetts (1967).

[39] H.M. Smith, *Principles of Holography,* Wiley-Interscience, New York (1969).

[40] M. Born and E. Wolf, Principles of Optics, 7th edition, Cambridge University Press (1999).

[41] I.K. Robinson and D.J. Tweet, Rep. Prog. Phys. **55**, 599 (1992).

[42] E. Vlieg and I.K. Robinson, *Synchrotron Radiation Crystallography*, edited by P. Coppens, 255-299. London: Academic Press (1997).

[43] E. Vlieg, J. Appl. Cryst., **30**, 532-543 (1997).

[44] E. Vlieg, J. Appl. Cryst., **31**, 198-203 (1998).

[45] S. Brennan and P. Eisenberger, Nucl. Instr. Methods A, **222** 164 (1984).

[46] http://www.diamond.ac.uk/Home/Beamlines/I07/beamline/optics.html.

[47] O. Bunk and M.M. Nielsen, Journal of Applied Crystallography 37, 216 (2004)

[48] http://adweb.desy.de/~detuser/oxford-scintillation.pdf.

[49] Ch. Broennimann, E.F. Eikenberry, B. Henrich, R. Horisberger, G. Huelsen, E. Pohl, B. Schmitt, C. Schulze-Briese, M. Suzuki, T. Tomizaki, H. Toyokawa and A. Wagner, Journal of Synchrotron Radiation, **13**, 120 (2006).

[50] J. Marchal, N. Tartoni and C. Nave, Nuclear Instruments and Methods in Physics Research A, **604**, 123 (2009).

[51] http://www.dectris.com/sites/pilatus100k.html.

[52] http://sls.web.psi.ch/view.php/beamlines/ms/sd/manuals/index.html.

[53] C.M. Schlepütz, R. Herger, P.R. Willmott, B.D. Patterson, O. Bunk, Ch. Brönnimann, B. Henrich, G. Hülsen and E. F. Eikenberry, Acta Cryst., **61**, 418-425 (2005).

[54] E. Vlieg, http://www.esrf.eu/computing/scientific/joint_projects/ANA-ROD/index.htm

[55] J.W. Pflugrath, Acta Cryst., **55**, 1718-1725 (1999).

[56] O. Bunk, PhD thesis, Department of Physics, University of Hamburg, Germany (1999).

[57] X. Torrelles and J. Rius, J. Appl. Cryst. **37**, 395-398 (2004).

[58] M.F. Chrisholm, A. Maiti, S.J. Pennycook and S.T. Pantelides, Physical Review Letters **81**, 132 (1998).

[59] J.-L. Rouviere and A. Bourret, Colloque de Physique **51**, 329 (1990).

[60] A. Bourret, Colloque de Physique, **51**, C1-1 (1990).

[61] J. Czochralski, Z. Phys. Chem., 92, 219 (1918).

[62] Y.C. Lu, Journal of Crystal Growth **79**, 322 (1986).

[63] J.J. Aubert and J.J. Bacmann, Revue Phys. Appl. **22**, 515 (1987).

[64] P.N. Keating, Physical Review **145**, 637 (1966).

[65] A. Steif, S.C. Tiersten and S.C. Ying, Physical Review B **35**, 857 (1987).

[66] *GNU Scientific Library*, http://www.gnu.org/software/gsl/ (accessed 14 September 2010).

[67] O.A.Shenderova, D.W. Brenner and L.H. Yang, Phys. Rev. B, **60**, 7043 (1999).

[68] E. Vlieg, Journal of Applied Crystallography **33**, 401 (2000).

[69] I.K. Robinson, R.T. Tung and R. Feidenhans'l, Physical Review B **38**, 3632 (1988).

[70] E. Vlieg, J.F. Van der Veen, S.J. Gurman, C. Norris and J.E. Macdonald, Surface Science **210**, 301 (1989).

[71] http://www.icdd.com/index.htm.

[72] I. McNulty, J. Kirz, C. Jacobsen, E.H. Anderson, M.R. Howells and D.P. Kern, Science **256**, 1009 (1992).

[73] http://www.diamond.ac.uk/Home/Beamlines/I06/specs.html

[74] O. Hellwig, S. Eisebitt, W.F. Schlotter, J. Lüning and J. Stöhr, Journal of Applied Physics, **99**, 08H307-1 (2006).

[75] W.T. Cathey, J. Opt. Soc. Am, **55**, 1035 (1965).

[76] J.V. Cornacchio and R.P. Soni, Nuovo Cimento, **38**, 1169 (1965).

[77] R.A. Shore, B.J. Thompson and R.E. Whitney, J. Opt. Soc. Am., **56**, 733 (1966).

[78] R.L. Mitchell, IEEE Trans., **AP-14**, 324 (1966).

[79] A. Consortini, Opt. Acta, **14**, 323 (1967).

[80] B.A. Sotskii, Opt. Sectry., **23**, 238 (1967).

[81] R.A. Shore, Opt. Acta, **16**, 131 (1969).

[82] S.C. Som and B.C Biswas, Opt. Acta, **17**, 925 (1970).

[83] T. Asakura, Optics Communications, **5**, 279 (1972).

[84] K. Singh and B.N. Gupta, Nouv. Rev. d'Optique appliquée, **2**, 97 (1971).

[85] K. Singh and B.N. Gupta, Journal of Modern Optics, **17**, 609 (1970).

[86] A.C. Schell, PhD thesis, MIT (1961).

[87] J.G. Meadord, Journal of Modern Optics, **12**, 379 (1965).

[88] D.J. Carpenter and C. Pask, Optica Acta, **23**, 279 (1976).

[89] E. Gullikson , X-ray Interactions with Matter, http://henke.lbl.gov/optical_constants/, (2009).

[90] M.A. Cerdeira, A.V. Svalov, A. Fernandez, V.O. Vas'kovskiy, M. Tejedor and G.V. Kurlyandskaya, Journal of Optoelectronics, **6**, 599 (2004).

[91] S. Konings, J. Miguel, J. Luigjes, H. Schlatter, H. Luigjes, J. Goedkoop and V. Gadgil, Journal of Applied Physics, **98**, 054306 (2005).

[92] J. Miguel, J.F. Peters, O.M. Toulemonde, S.S. Dhessi, N.B. Brookes and J.B. Goedkoop, Physical Review B, **74**, 094437 (2006).

[93] C.A. Volkert, A.M. Minor and guest editors, MRS Bulletin **32**, 389 (2007).

[94] J. Miao, J. Kirz and D. Sayre, Acta. Crysta., D**56**, 1312-1315 (2000).

[95] J. Miao, D. Sayre and H.N. Chapman, J. Opt. Soc. Am. A, **15**, 1662-1669 (1998).

[96] S. Eisebitt, M. Lörgen, W. Eberhardt, J. Lüning, J. Stöhr, Appl. Phys. A., **80**, 921-927 (2005).

[97] T. Beetz, *Soft X-ray Diffraction with and without lenses*, PhD thesis, State University of New York at Stony Brook (2004).

[98] J. R. Janesick, *Scientific Charge-Coupled Devices*, SPIE Press, 2001.

[99] J.R. Fienup, Applied Optics, **21**, 2758 – 2769 (1981).

[100] S. Marchesini, H. He, H.N. Chapman, S.P. Hau-Riege, A. Noy, M.R. Howells, U. Weierstall and J.C.H. Spence, Phys. Rev. B, **68**, 140101 (2003).

[101] D. Stickler, R. Frömter, H. Stillrich, C. Menk, C. Tieg, S. Streit-Nierobisch, M. Sprung, C. Gutt, L.-M. Stadler, O. Leupold, G. Grübel and H.P. Oepen, Applied Physics Letters **96**, 042501 (2010).

[102] M. Dierolf, O. Bunk, S. Kynde, P. Thibault, I. Johnson, A. Menzel, K. Jefimovs, C. David, O. marti and F. Pfeiffer, Europhysics News **39**, 22 (2007).[6.3]

[103] J.M. Rodenburg, A.C. Hurst, A.G. Cullis, B.R. Dobson, F. Pfeiffer, O. Bunk, C. David, K. Jefimovs and I. Johnson, Physical Review Letters **98**, 034801 (2007).

[104] H.M.L. Faulkner and J.M. Rodenburg, Applied Physics Letters **85**, 023903 (2004).